Imperial College London

Generation of High-Contrast, Terawatt to Petawatt OPCPA Laser Pulses

NICHOLAS STUART

Department of Physics

Quantum Optics and Laser Science Group

Imperial College London

Submitted in partial fulfilment of the requirements for the degree of Doctor of Philosophy of Imperial College London and for the Diploma of Imperial College.

September 2016

All of physics is either impossible or trivial. It is impossible until you understand it, and then it becomes trivial.

— Ernest Rutherford

Declaration

I hereby certify that the material of this thesis, which I now submit for the award of Doctor of Philosophy of Imperial College London, is entirely my own work unless otherwise cited or acknowledged within the body of the text.

Copyright

The copyright of this thesis rests with the author and is made available under a Creative Commons Attribution Non - Commercial No Derivatives licence. Researchers are free to copy, distribute or transmit the thesis on the condition that they attribute it, that they do not use it for commercial purposes and that they do not alter, transf orm or build upon it. For any reuse or redistribution, researchers must make clear to others the licence terms of this work

NICHOLAS STUART

Nicholas Stuart: *Generation of High-Contrast, Terawatt to Petawatt OPCPA Laser Pulses*, © September 2016

ABSTRACT

Laser-matter experiments using >10^{18} W cm^{-2} focused light intensities from terawatt to petawatt peak-power laser systems are highly sensitive to the optical noise sources that are generated and amplified in conjunction with the primary high-power laser pulse. This limits the temporal intensity contrast, the signal to noise of the primary pulse intensity in time.

This thesis presents a detailed investigation into the noise sources that degrade the contrast of high-power laser pulses created for laser-matter interaction experiments. To achieve this, a high-contrast multi-terawatt peak-power laser system, named Cerberus, has been developed to deliver up to 5 J, 500 fs pulses (10 TW) using an optical parametric chirped pulse amplification (OPCPA) front-end and Nd:Glass laser rod power amplifiers. To compliment this study, >10^{10} dynamic range diagnostics have been developed that measure these noise sources in the presence of the intense primary pulse. Parametric fluorescence noise from parametric amplifiers was measured with a diagnostic able to observe the real-time seeded OPCPA fluorescence noise emission and determined the fluorescence emission to be directly linked to the level of pump-depletion, with a ~500 times contrast enhancement from the undepleted to maximum pump depletion modes of operation. A combination of picosecond-pumped OPCPA and nanosecond-pumped OPCPA amplifiers effectively suppresses the longer timescale parametric fluorescence to >10^{8}-10^{10} contrast.

A scanning third-order autocorrelator diagnostic (TOAD) was developed to characterise the compressed pulses emitted from a range of mode-locked laser oscillator sources and the compressed high-power laser pulses from major laser laboratories in the UK. We found the commonly used chirped pulse amplification architecture limits the temporal contrast from formation of an incoherent noise pedestal that can extend many hundred of picoseconds before the arrival of the primary laser pulse. We also observed non-linear generation of pre-pulses from internal reflections inside parallel-faced OPCPA crystals incident with long duration pump pulses.

CONTENTS

1 INTRODUCTION 1

1.1 Optically Driven Ionisation Mechanisms 1

1.1.1 Requirement for High-Contrast High-Power Laser Pulses 3

1.2 Laser Amplification Methods 4

1.2.1 Gain-Storage Laser Amplification 6

1.2.2 Chirped Pulse Amplification 7

1.2.3 Optical Parametric Chirped Pulse Amplification 13

1.3 Organisation of Thesis 16

1.4 Contributors, Publications and Other Outputs 18

1.4.1 Outputs Related to Thesis Work 20

2 IMPERIAL COLLEGE CERBERUS MULTI-TERAWATT OPCPA / ND:GLASS LASER SYSTEM 26

2.1 Choice of Solid-State Gain-Storage Laser Media 31

2.1.1 Ti:Sapphire 32

2.1.2 Nd:Glass 33

2.1.3 Nd:YLF 33

2.2 Numerical Modelling of Optical Parametric Amplifiers 34

2.2.1 Pump Depletion Effects 38

2.3 Pulse Duration Measurements with a Single-Shot Autocorrelator 42

2.4 Optical Damage Mechanisms 44

2.4.1 Self-Focussing (B-Integral) 46

2.5 Mode-locked Nd:Glass Master Oscillator 47

2.5.1 Optical Stabilisation for Low-Drift OPCPA Synchronisation 49

2.6 Picosecond Pumped OPAs 51

2.6.1 OPA Pump Beamline 51

2.6.2 Picosecond OPA Results 56

2.7 Nanosecond Pumped OPAs 61

2.7.1 OPA Pump Beamline 63

2.7.2 Nanosecond OPA Results 65
2.8 Nd:Glass Amplification and Compression 67
2.9 Summary 69

3 HIGH-DYNAMIC RANGE DIAGNOSTICS FOR CONTRAST CHARACTERISATION 70
3.1 Third-Order Autocorrelator Diagnostic (TOAD) 70
3.2 Seeded OPA Fluorescence Diagnostic 74
3.2.1 Experimental Setup 78
3.2.2 Key Seeded OPA Fluorescence Results 80
3.2.3 Analysis: Seeded OPA Fluorescence Contrast 83
3.2.4 Analysis: Parametric Fluorescence Input Noise 85
3.2.5 Analysis: Shot-to-Shot Fluorescence Intensity Statistics 86
3.2.6 Conclusions 87

4 CONTRAST CHARACTERISATION OF OSCILLATORS THAT SEED HIGH-POWER LASERS 89
4.1 Short Pulse Generation via Mode-locking 92
4.1.1 Saturable Absorber Mode-Locking 92
4.1.2 Kerr Lens Mode-Locking (KLM) 95
4.1.3 Non-linear Polarisation Evolution (NPE) Yb-Fibre Laser 99
4.1.4 Optical Parametric Oscillators (OPOs) 102
4.2 Conclusions 105

5 CONTRAST CHARACTERISATION OF UK TERAWATT AND PETAWATT LASER SYSTEMS 106
5.1 Cerberus (IC) 107
5.2 Orion (AWE) 110
5.3 Vulcan (STFC) 114
5.4 TARANIS (QUB) 118
5.4.1 Contrast Enhancement from a Low Gain, Self-Pumped OPA 120
5.5 Discussion: Non-linear Pre-Pulse Synthesis from Post-Pulses 122
5.5.1 Improved Cerberus Nanosecond OPAs 125
5.6 Discussion: Mid-Range CPA Pedestal 128
5.6.1 Phase Conjugate OPCPA 131

5.7 Conclusions 133

6 CERBERUS LASER-MATTER INTERACTION EXPERIMENTS 135
6.1 High-Intensity Laser-Matter Interactions 135
6.1.1 Free Electron Interaction in an Intense Electromagnetic Field 135
6.1.2 Laser Propagation Through a Plasma 136
6.1.3 Contrast Sensitive Plasma Heating Mechanisms 138
6.1.4 Contrast Insensitive Plasma Heating Mechanisms 140
6.2 Cerberus Short-Pulse: Optically Levitated Microdroplet Target 140
6.2.1 Experimental Set Up 142
6.2.2 Results 146
6.2.3 Conclusions and Outlook 148
6.3 Diagnosing MAGPIE Z-Pinch Interactions with Cerberus 148
6.3.1 X-ray Backlighter 151
6.3.2 Optical Polarimetry Probe of Magnetic Fields 154

7 CONCLUSIONS 158
7.1 Future Work 160
7.1.1 Removing Pre-pulse Artefacts with X-TOAD 160
7.1.2 Scaling of OPCPA Contrast Studies to the Mid-IR 164
7.1.3 High Energy OPCPA and Cerberus 100TW Design 166

BIBLIOGRAPHY 172

LIST OF FIGURES

Figure 1.1 Intensity thresholds for laser-matter interaction processes against the potential optical noise sources of a focused high-intensity laser pulse. 4

Figure 1.2 Mode-locking of seven discrete continuous wave frequencies to create a train of short pulses, with a peak-amplitude when all of these frequencies/modes constructively interfere. 5

Figure 1.3 Diagram of gain narrowing of a pulse from a non-uniform gain-spectrum. 7

Figure 1.4 Simple cartoon of the chirped pulse amplification (CPA) method. . . . 8

Figure 1.5 Electric field of a transform-limited 5 fs FWHM pulse stretched/chirped to 40fs by addition of $\phi'' = 72$ fs^2 second-order phase in 1.7. 9

Figure 1.6 Effect of third-order spectral phase on the temporal contrast of a laser pulse. 10

Figure 1.7 Layout of a simple two parallel grating optical setup that adds anomalous dispersion. 11

Figure 1.8 Optical layout of a Martinez stretcher for producing positive GDD. . . 12

Figure 1.9 Schematic energy levels involved in SHG, OPA and a four-level LASER. 14

Figure 1.10 Operation of an optical parametric amplifier using a chirped seed pulse. An intense pump pulse (another laser) is temporally and spatially overlapped in the non-linear medium that is phase-matched to amplify the seed. 15

Figure 1.11 Parametric fluorescence from an OPA. This is emitted in a cone of angles, which represent the phase-matching angles and frequencies of the crystal to the pump. 16

Figure 2.1 Front-end of Cerberus laser system that produces the long-pulse Nd:YLF seed and short-pulse OPCPA seed for large-aperture Nd:Glass amplification. 26

Figure 2.2 Simplified component diagram of the Cerberus long-pulse and terawatt short-pulse beamlines in the Terawatt lab. 27

Figure 2.3 Laboratory layout of the Cerberus laser system and target areas. . . . 30

Figure 2.4 Excessive gain of the signal pulse in an OPA results in back conversion and intensity modulations at the peak of the signal to the pump. . 38
Figure 2.5 Pump energy versus bandwidth gain in an OPCPA stage for Gaussian temporal profiles in the pump and seed, demonstrating the potential benefits to be gained from pump deletion of OPCPA stages, leading to increased bandwidth at the output as well as high gain. 39
Figure 2.6 Seed chirp optimisation of the amplified signal bandwidth (blue crosses and line) and energy (red circles and line) for a pair of OPAs operated at maximum pump-depletion and calculated using the OPA.FOR numerical model. 40
Figure 2.7 Example of over-saturation of the OPA signal produces a region of signal energy gain stability against fluctuations in the input pulse intensity. 41
Figure 2.8 Optical layout of a single-shot second-order autocorrelator. 43
Figure 2.9 Fused silica damage fluencies for varying time duration pulses and wavelengths, showing the deviation from for pulses shorter than 10ps due to onset of multi-photon ionisation. 45
Figure 2.10 Self-focussing of an intense Gaussian pulse from non-linear refractive index. 46
Figure 2.11 Optical layout of the SESAM mode-locked Nd:Glass laser oscillator that seeds the Cerberus laser system. 47
Figure 2.12 Measured single-shot second-order autocorrelation (left) and spectrum (right) of the mode-locked 1054nm pulses from the Cerberus Nd:Glass oscillator (Time-Bandwidth Products GLX200HP). 48
Figure 2.13 A cartoon showing how frequency drift of the oscillator shifts the temporal overlap when selecting different pulses from the oscillator pulse train for the seed and pump pulses. 49
Figure 2.14 Cerberus Nd:Glass oscillator frequency locking stability over a full operational day period. 50
Figure 2.15 Optical layout of the Cerberus OPCPA pump regenerative amplifier stretcher. 52

Figure 2.16 Photodiode trace of the regenerative amplifier output monitored on an oscilloscope. Each successive round trip sees low amounts of gain and eventually saturates at ~3mJ output. Around this saturation point the available laser gain becomes comparable to the cavity loss, producing a stable output from successive round trips. 53
Figure 2.17 Intra-cavity etalon spectral shaping method to suppress gain narrowing effects. 54
Figure 2.18 Cerberus OPCPA pump beamline layout, with amplification in Nd:YLF using the stretched oscillator pulses. 55
Figure 2.19 Third-order autocorrelation of the temporal intensity profile of the 1053 nm compressed pump pulses of the ps-OPAs. 56
Figure 2.20 Optical layout of the Cerberus ps-OPAs. 59
Figure 2.21 Spectral gain profiles of the optimised model and experimental results of the ps-OPAs. 60
Figure 2.22 Cerberus Öffner reflective doublet stretcher side and top view ray diagram for injection/ejecting and guiding of the ps-OPA output to produce ~200 ps/nm stretched pulses to seed the ns-OPAs. 62
Figure 2.23 Bandwidth acceptance of the Cerberus Öffner stretcher, whose output seeds the ns-OPAs, and temporal contrast modelling from this effect on various bandwidths able to be generated. 63
Figure 2.24 Optical layout of nanosecond OPA pump beamline. 64
Figure 2.25 Measured 1.46 ns FWHM pulse duration of the Nd:YLF CPA beamline after stretching in a parallel grating pair stretcher and amplified to 200 mJ at 1053 nm. 65
Figure 2.26 Optical layout of the ns-OPA beamline that uses the 180 mJ, 1053 nm pulses from the Nd:YLF CPA beamline to pump a pair of OPA crystals (BBO) seeded with the stretched output from the ps-OPAs. 66
Figure 2.27 Measured compressed pulse duration scan of amplified 3.7nm bandwidth front-end pulses through the complete short-pulse optical system using a single-shot autocorrelator and adjusting grating separation to identify the optimum grating position. 68

Figure 2.28 Measured focal spot of the Cerberus Laser System with an f/5 GRIN (Gradient-Index) lens, which minimises spherical aberration, and using a calibrated microscope objective for image magnification onto a CCD camera. A 600 mJ, 500 fs pulse focused to this small area will produce ~1.8 $\times$ 10^{18} W cm^{-2} peak-intensities. 68
Figure 3.1 Simplified illustration of the sum frequency process used in third-order autocorrelators. Post-pulses in the input beam may still produce "ghost" pre-pulse artefacts in the retrieved third-harmonic signal, which will need to be analysed after the measurement scan to determine if they are real pre-pulses or diagnostic artefacts. 71
Figure 3.2 Optical layout of the third-order autocorrelator diagnostic (TOAD) for high-dynamic range characterisation of laser pulses. 73
Figure 3.3 a) Optical layout of the parametric fluorescence diagnostic. 76
Figure 3.4 Simplified setup of the Cerberus OPCPA laser front-end used for the parametric fluorescence characterisation. 78
Figure 3.5 Unseeded parametric fluorescence spectrum emitted in the seed direction of the ps-OPAs with a 0.6 non-collinear angle. 80
Figure 3.6 Parametric fluorescence energy generated from the ps-OPAs as a function of the total pump energy for the unseeded amplifier and the fully seeded case. 81
Figure 3.7 Measured parametric fluorescence in competition with the OPA seed and energy contrast between the ps-OPA signal and fluorescence as a function of the seed energy. 82
Figure 3.8 Cross-correlation as a function of time-delay between the OPA2 pump and parametric fluorescence generated in OPA1. A 2.1 ps FWHM pulse is retrieved after a $\sqrt{2}$ deconvolution factor for Gaussian pulses is applied. 84
Figure 3.9 Modelling of the temporal profile on a log scale of an ideal 500fs compressed high-power laser pulse from the Cerberus laser against the parametric fluorescence intensity envelope. The combined intensity envelope shows the contrast to be limited to ~7x10 at ~1.3ps before the arrival of the primary pulse. 85

Figure 3.10 Measured photon statistics of the parametric fluorescence producing a Poisson distribution, demonstrating the random nature of the fluorescence seed, which can occasionally produce much brighter fluorescence background from shot-to-shot as a result. 87
Figure 4.1 Non-linear saturable absorption method to produce mode-locked laser pulses. (a) Valence electrons are excited to the conduction upon absorption of laser light. Limited carriers in conduction band produce saturable absorption effect, which quickly decay of order 10-200 fs via intra-band relaxation and more slowly over 1-10 ps from recombination back to the valence band. (b) The effect over multiple round trips to gradually accentuate the formation of a short-pulse. 93
Figure 4.2 Measured third-order autocorrelations of SESAM mode-locked Nd:Glass oscillators. 94
Figure 4.3 Measured third-order autocorrelations of Kerr-lens mode-locked (KLM) laser sources. 97
Figure 4.4 Measured third-order autocorrelation of a KLM Yb:KGW oscillator. . . 98
Figure 4.5 Schematic of an all-normal dispersion Yb-doped fibre laser. 101
Figure 4.6 Measured third-order autocorrelations of an NPE mode-locked Yb-doped fibre laser. 102
Figure 4.7 Measured third-order autocorrelation of an optical parametric oscillator104
Figure 5.1 Simplified system design of the Cerberus laser. 107
Figure 5.2 High dynamic range scan of the compressed ps-OPA. 108
Figure 5.3 Contrast of Cerberus OPCPA front-end. 109
Figure 5.4 Orion short-pulse front end (Room OPG2) block diagram. 112
Figure 5.5 Measured contrast of the Orion front-end of the compressed ns-OPA pulses from the “SP1” beamline. 113
Figure 5.6 Measured contrast of the Orion front-end of the uncompressed ps-OPA pulses and the compressed ns-OPA pulses from the “SP2” beamline using the TOAD. 114
Figure 5.7 Simplified block diagram layout of the Vulcan petawatt laser and position of the TOAD for the compressed pulse contrast characterisation. 115
Figure 5.8 Measured contrast of the compressed 2 Hz full-system throughput and bypass beamlines of the Vulcan petawatt laser (TOAD: grey, SEQUOIA: green). 117

Figure 5.9 Measured contrast of the TARANIS compressed regenerative amplifier using the TOAD. . . . 119
Figure 5.10 Optical setup of the low-gain OPA for contrast enhancement of compressed ~500 μJ pulses from a Ti:Sapphire regenerative amplifier . . . 121
Figure 5.11 Measured contrast enhancement to a Ti:Sapphire regenerative amplifier (red) from a self-pumped low-gain degenerate OPA (blue) to produce a high-contrast idler pulse that can be stretched and injected by into the high-energy amplification beamline. . . . 122
Figure 5.12 Contrast the compressed ns-OPAs with different length amplifier crystals. . . . 123
Figure 5.13 Schematic overview showing the mechanism of generation of additional collinear post-pulses in an OPCPA process that may then interact with the main pulse to produce pre-pulses after compression. . . . 125
Figure 5.14 Non-linear crystal configuration that negates/minimises non-linear pre-pulse generation. . . . 126
Figure 5.15 Improve Cerberus compressed ns-OPA that removes the interference between the internally reflected post-pulses generated in the OPA crystal, which has removed the non-linear pre-pulse formation. . . . 127
Figure 5.16 Diffracted ray intensities for a near octave spanning spectrum centred at 1053nm using 1740lines/mm groove density and influence of increased number of slits participating in diffraction grating operation. . 130
Figure 5.17 Phase-conjugate OPCPA schematic. . . . 132
Figure 6.1 Optical layout of the levitation trap beam handling and trapping optics. . . . 142
Figure 6.2 Photograph of a trapped microdroplet under vacuum inside the Cerberus Terawatt Lab target chamber. . . . 143
Figure 6.3 A schematic of the target chamber, alignment, and diagnostic-layout for the high-intensity laser droplet interaction experiments. . . . 145
Figure 6.4 Radio-frequency signal measurements for oil droplet and carbon wire shots. . . . 147
Figure 6.5 Cartoon drawing of the MAGPIE pulsed power generator main components. . . . 149
Figure 6.6 Z-pinch interaction from a cylindrical wire array load. . . . 150

Figure 6.7 Optical layout in the MAGPIE Amplification Lab to amplify pulses from the Cerberus front-end up to 20 J energy for injection into the MAGPIE target chamber. Second-harmonic light is used for the X-ray backlighter source, while the 1054 nm beamline is used for the Faraday rotation diagnostic of magnetic fields, described in 6.3.2. . . . 151
Figure 6.8 The X-ray Bragg imaging system of MAGPIE interactions. 152
Figure 6.9 False colour X-ray backlit image of a resolution grid using the long pulse laser beam of the Cerberus system. 153
Figure 6.10 Cerberus X-ray backlit image of a live MAGPIE tungsten wire array shot. 154
Figure 6.11 Optical Faraday rotation plasma diagnostic to characterise magnetic fields in the MAGPIE chamber. 155
Figure 6.12 Electron density map and retrieved Z-pinch magnetic field analysis from Cerberus-MAGPIE polarimetry diagnostic. 156
Figure 7.1 Experimental setup to test the XPW efficiency for the second harmonic of the ~500fs, few millijoule, 10Hz pulses emitted from the complete optical chain of Cerberus. 162
Figure 7.2 XPW efficiency of 527nm pulses as a function of distance from the focussing lens. We observe an exponential behaviour, indicating self-phase modulation is likely acting within the XPW interaction to improve efficiency. 163
Figure 7.3 Proof-of-principle operation of XPW filtering of the probe pulses in a third-harmonic autocorrelator to effectively identify and remove diagnostic artefacts from the autocorrelation signal. (Blue line) A post-pulse introduced into the probe beamline produces a diagnostic artefact ~50 ps ahead of the primary pulse. (Red line) With no change to the optical configuration, the XPW filter is engaged (by crossed-polarisers and a BaF_2 XPW polarisation rotator moved into the focus of the probe pulse), removing the diagnostic artefact from the autocorrelation trace. All other pre-pulses remain and are therefore real features in the temporal profile of the laser pulse. 164
Figure 7.4 Compressor spectral clipping impact on the compressed pulse contrast for varying pulse durations 200fs FWHM Gaussian bandwidth. . 167

Figure 7.5 OPA.FOR Temporal profiles of pump and signal from optimised ns-OPAs. 170

LIST OF TABLES

Table 2.1 Physical properties of common laser gain-storage media used for high-power amplification at 1054nm central wavelength. 31
Table 4.1 Oscillator sources characterised by the TOAD for contrast investigations described in [37]. 91
Table 6.1 Filtered source size measurements for various targets irradiated with 7 μm FWHM ~10^{18} W cm^{-2} intensity pulses from the Cerberus laser. . 146
Table 7.1 Pulse parameters for re-optimised ns-OPAs using an improved pump pulse stretcher and additional amplification. 170
Table 7.2 Required pump intensities and beam diameters for optimal ns-OPA gain. 171

1

INTRODUCTION

The field of high peak-power laser-matter interactions was born shortly after the demonstration of the first laser pulses in 1960 [1]. The MOPA (master oscillator, power amplifier) laser systems that typically underpin this research today include an amplification chain that delivers a modest $\gtrsim$1 J pulse energies confined in an ultrafast, sub-picosecond, pulse envelope. The very largest present day high-power laser systems are capable of generating multi-petawatt peak-powers using metre-scale optics, that are necessary to reduce the optical intensities within the laser to prevent self-damage. The output from these lasers can then be focused into a small volume, of order a few wavelengths cubed, to produce extremely high energy densities that exceed 10^{21} W cm^{-2} at the Vulcan, Astra Gemini and Orion Petawatt national laser facilities in the UK [2–4], whilst >10^{19} W cm^{-2} intensities are possible with medium-sized university scale laser systems. This 10^{21} W cm^{-2} energy density is equivalent to a 10 keV (~110 million degrees Kelvin) black-body, over five times brighter than the centre of the Sun, with a light pressure of 300 Gbar. These extreme light sources are capable of producing highly exotic states of matter, enabling fundamental research in plasma physics [5, 6], compact particle accelerators [7, 8], laboratory astrophysics [9, 10] and nuclear fusion ignition schemes [11, 12].

1.1 OPTICALLY DRIVEN IONISATION MECHANISMS

Depending on its wavelength, intensity and duration, light can couple energy into matter through a number of distinct mechanisms. The nature of these energy coupling mechanisms will greatly influence the state of matter that can be accessed, for example its density, temperature and ionisation state. Energy coupling from light to matter in an experiment or application may be “intentional”, i.e. the goal of an experiment is to heat or compress matter, or “unwanted”, e.g. early-time optical “noise” from the laser may begin to heat or ionise a target before the arrival of the primary laser pulse. A key goal of the work presented in this thesis is to develop laser systems able to drive high-quality experimental programmes, and this requires one to understand, characterise and control optical noise

in high-power lasers. As a prelude to this, it is pertinent to describe processes such as the ionisation of matter by light, to set the scene for discussions of the permissible levels of laser pre-pulse on target.

The first light-matter interactions that can irreversibly change the physical state of matter of the target will involve ionisation processes via the photoelectric effect. Electrons bound to the Coulomb potential field of the atom will have an ionisation potential $E_i$required to excite and free the electron into the continuum. The single photon energy from a typical 1054 nm central wavelength laser is ~1.2 eV, compared to the typical 5-10 eV ionisation potential energy of the outermost electrons in most elements, increasing up to >1 keV for innermost electron orbitals and heavier atoms. Single photon ionisation is thus a very low probability process with infra-red or visible laser sources. However, multiple, n, laser photons of wavelength λ can combine via short-lived virtual energy levels to ionise an atom to release an electron with kinetic energy $E_k = {}^{nh\lambda}/_{c} - E_i$, producing an intensity dependent mechanism. For example, the multi-photon ionisation threshold of aluminium foils have been measured to be ~2x10^{12} W cm^{-2} when irradiated with 1053 nm, picosecond duration pulses [13].

An important quantity to consider for high-intensity light interacting with matter is the ponderomotive energy U_p, which is the average kinetic energy a free electron acquires oscillating in the electromagnetic field of the laser pulse of wavelength λ and intensity I,

$$U_p = \frac{e^2\lambda^2 I}{8\pi^2 c^3 m_e \varepsilon_0} \tag{1.1}$$

where e is the electron charge, m_e is the electron mass and ε_0 the vacuum permittivity. As a general rule, so called "strong-field" ionisation processes become dominant when $U_p > E_i$, which corresponds to ~5x10^{13} W cm^{-2}, although multi photon processes can occur below this level. These strong-field ionisation processes can also involve tunnelling ionisation between 10^{14}-10^{16} W cm^{-2}, where the electron has a probability/cross-section to pass through the potential well below the barrier height and becomes important, and barrier suppression ionisation at intensities around 10^{16} W cm^{-2}, where the potential well is appreciably perturbed by the local electric field of the intense laser pulse, reducing the required energy to ionise the trapped electron [14, 15]. The key point is that generally ultrafast optical intensities greater than 10^{12} W cm^{-2} lead to a variety of ionisation mechanisms that will ionise and heat the target material and eventually form a plasma state of matter for highly ionised targets.

1.1.1 *Requirement for High-Contrast High-Power Laser Pulses*

The state of the target before arrival of the primary laser pulse can adversely affect the energy coupling into the target medium and reduce the plasma electron temperature and dynamics for efficient X-ray, electron and ion generation. We have identified ionisation and plasma formation mechanisms that begin at 10^{12} W cm^{-2} intensities, however the peak intensity able to be produced from terawatt to petawatt laser system are between 10^{18} to 10^{21} W cm^{-2} respectively, with designs and aspirations in the community to reach 10^{24} W cm^{-2} intensities [16, 17]. Large amounts of "pre-pulse" will create a "pre-plasma" on the front of a target, which will expand over time and significantly alter the plasma heating mechanisms and coupling efficiency from the primary laser pulse to the target. If the pre-pulse is significantly ahead of the arrival of the primary pulse, the target material can even be completely disintegrated before its arrival. For materials and ultrafast pump-probe techniques, pre-pulse can detrimentally alter the state of matter before the arrival of the main pulse and detrimentally alter the state of matter and dynamics under examination. We therefore define the laser contrast as the signal-to-noise ratio of the primary high-power laser pulse to any other resolvable optical noise source ahead of the primary pulse envelope. As earlier pre-pulse is more detrimental for the same optical intensities, we may also differentiate between the different timescales of the physical mechanisms that create pre-pulse in their observation and analysis.

For high-intensity laser sources a contrast of $>10^{8}$ is typically acceptable and $>10^{10}$ is more ideal for petawatt systems. However, a variety of noise sources with varying temporal extents are likely to be generated at various stages of the laser amplification process. These sources can be long duration sources such as amplified spontaneous emission from the initial lower power laser seed, shorter range noise pedestals specific to the amplification processes we describe in §6.1 or co-propagating pulse replicas from internal reflections of optics of various thicknesses and their non-zero surface reflectivity.

Determining the detailed temporal structure of a laser pulse over many orders of magnitude, and using this to inform both laser development and the interpretation of laser-matter interaction experiment results is of critical importance.

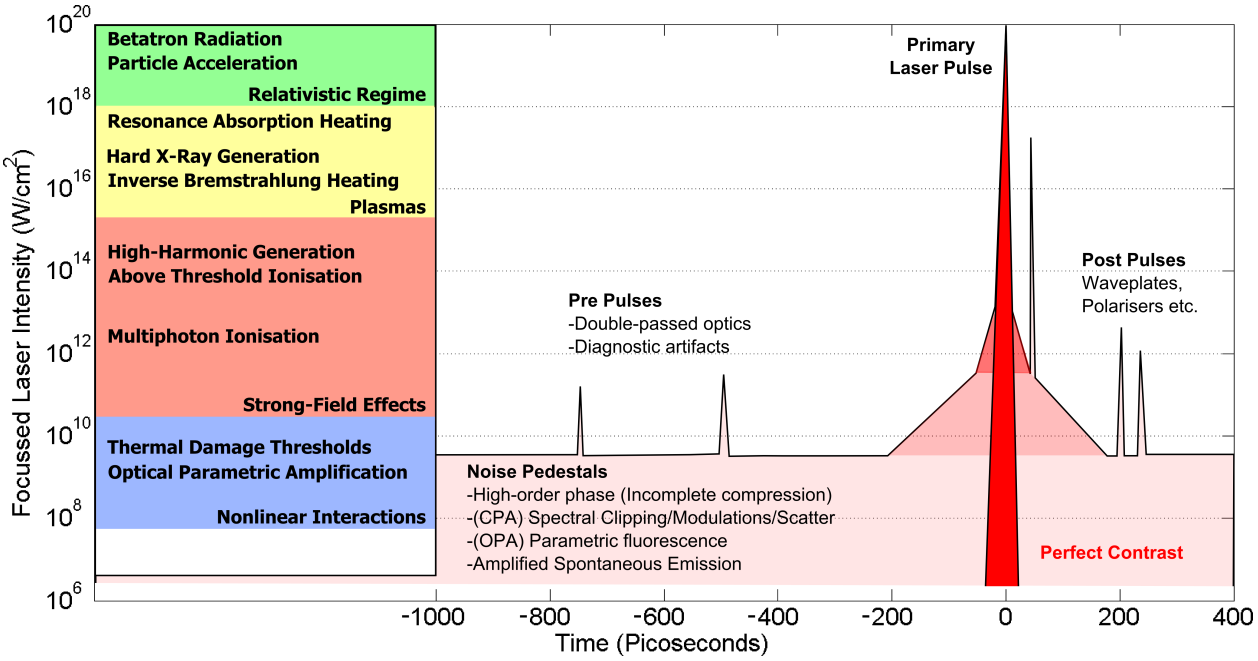


Figure 1.1: Intensity thresholds for laser-matter interaction processes against the potential optical noise sources of a focused high-intensity laser pulse, highlighting the "ideal" laser pulse envelope on a logarithmic intensity scale and the likely "real world" behaviour of a high peak-power laser system, which may ionise and form a pre-plasma many hundreds of picoseconds to nanoseconds ahead of the primary pulse that expands and alters the dynamics of the laser-matter interaction under investigation.

1.2 LASER AMPLIFICATION METHODS

The generation of terawatt-petawatt intensities requires laser amplification methods that amplify nanojoule, ultrashort pulses from laser oscillator sources to many joules for application in high-intensity light-matter interaction studies. Apart from high energy, short duration and high contrast, a "useful" laser system should also output stable energy, typically <1-2% RMS (root mean square) stability for reliable and reproducible results, and high waveform quality and to be focused into a small volume approximately a few wavelengths cubed.

Crucially, the coherent bandwidth of the laser pulse must be preserved to maintain the short-pulse width at the output of the system. This follows a the Fourier relationship between the phase-locked spectral components that constructively interfere at a single point to produce a short-pulse, in a scheme known as "mode-locking" and conceptually demonstrated in figure 1.2. Larger bandwidths produce a sharper interference effect and therefore shorter pulses, whose minimum value is given by the relation

$$\triangle t = TBP\frac{\lambda}{\triangle\lambda^2\triangle tc} \tag{1.2}$$

where $\triangle t$ is the Fourier transform-limited duration of the laser pulse for a given bandwidth, whose bandwidth shape determines the time-bandwidth product (TBP) Fourier transform factor, which is ~0.44 for Gaussian and ~0.315 for sech^2 pulse shape.

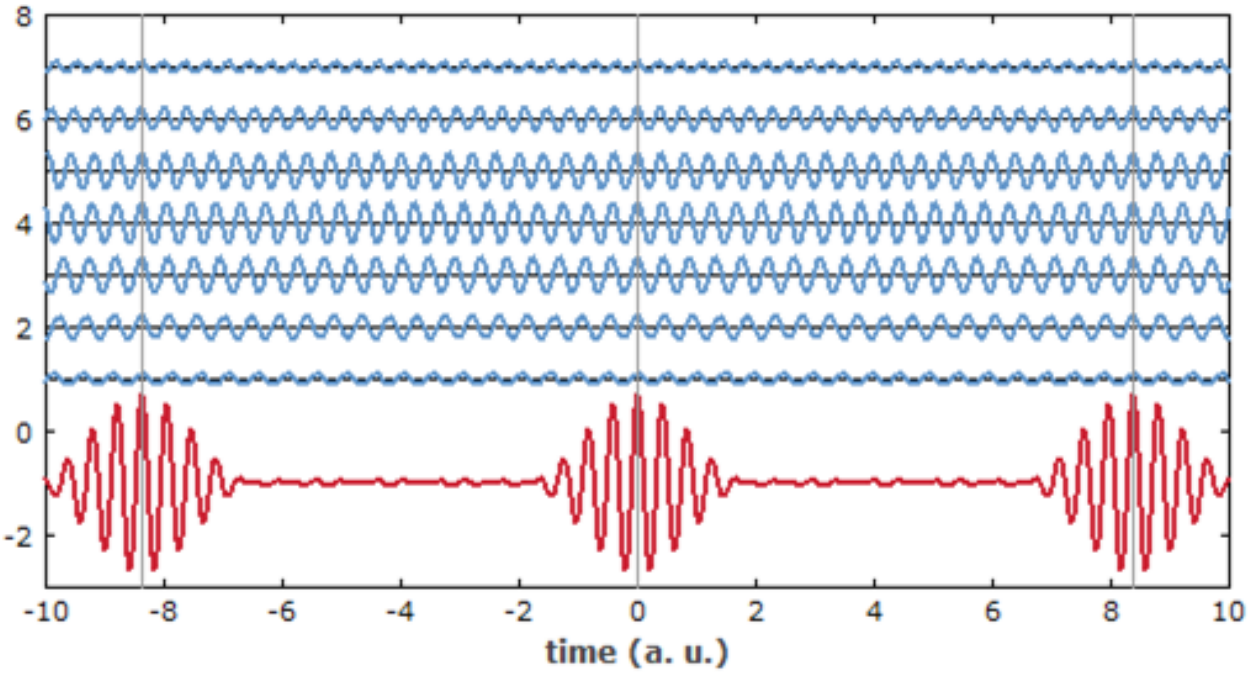


Figure 1.2: Mode-locking of seven discrete continuous wave frequencies to create a train of short pulses, with a peak-amplitude when all of these frequencies/modes constructively interfere. Image from rp-photonics.com.

For the generation of a 250 fs pulse, more than 10^4 discrete spectral or longitudinal modes of a laser cavity are required. For laser oscillators, a population inversion will exist at all times for stable laser operation. Continuous pumping will produce steady spontaneous emission in all directions, with a portion of this within the alignment tolerance of the oscillator cavity and will be successively amplified with each round trip. For ultrafast laser oscillators, some of this emission will form the basis of the mode-locked pulse and discussed in further detail in §4.1.

The laser gain medium must be able to support and amplify the required bandwidth with very little loss of frequency components in order to support the ultrashort pulse. At 1054 nm central wavelength, ~3.3 nm bandwidth is required to support a 500 fs pulse and ~165 nm bandwidth to support a 10 fs pulse, greatly limiting the available gain media and amplification techniques for creating high-energy short pulses, primarily to either

Ti:Sapphire lasers and/or non-linear methods such as optical parametric chirped pulse amplification (OPCPA), which will be described in 1.2.3.

1.2.1 *Gain-Storage Laser Amplification*

Conventional laser amplification utilises the population inversion of an excited atomic state that can relax to the ground state via either coherent stimulated emission or incoherent spontaneous emission. The upper-state lifetime of the laser transition determines the duration of spontaneous emission, as well as the effective gain window in which significant stimulated emission may occur. The >10^{10} total gain available from high-power multi-stage laser systems that only utilise gain-storage amplification techniques can be particularly susceptible to amplified spontaneous emission (ASE), where the spontaneous emission process is seeded near the start of the laser system and propagates through the optical chain and subsequent gain stages to be further amplified, producing a system gain-dependent noise term. Spontaneous emission is ultimately a quantum mechanical process that can be considered as stimulated emission of the zero-point ground-state energy fluctuations of the vacuum. These fluctuations arise from the energy uncertainty principle $\Delta E \Delta t > h/4\pi$, which states that in any small localisation in time there is an associated large fluctuation in energy, leading to generation of incoherent photons that will be amplified, via stimulated emission, to appear as ASE. If the ASE intensity on target is above the ionisation threshold, the very long >1-100 μs ASE lifetimes represent a significant limiting factor towards ensuring good laser contrast with the potential to produce very long plasma scale lengths. The ASE intensity in the limit of high gain has been shown to approximate to [18]

$$I_{ASE} = \frac{hc}{16\lambda\sigma\tau F^2}\frac{\triangle\lambda_{ASE}}{\triangle\lambda}G \tag{1.3}$$

where λ and $\triangle\lambda$laser are the laser central wavelength and bandwidth, σ is the emission cross-section, τ is the upperstate lifetime, F is the f-number of the final focussing optic, $\triangle\lambda_{ASE}$ the ASE emission bandwidth and G the net signal gain. If we use the example of a 100 TW Nd:Glass 1054 nm central wavelength short-pulse laser system to produce 50 J, 500 fs pulses onto target, a net signal gain of ~5x10^{10} from an laser cavity emitting ~nJ seed pulses and an f/3 focussing parabola the ASE intensity produced will be ~3x10^{13} W cm^{-2}. An Nd:Glass 8 TW system producing 2.4 ps pulses, a pre-cursor to the Vulcan Petawatt

hybrid OPCPA/Nd:Glass beamline, produced an ASE intensity contrast at 10^{-6} level [19], producing ~6x10^{13} W cm^{-2} pre-pulse intensities using an f/3 focussing optic. While this analytical model appears to be reliable, this ASE intensity is still significantly above the threshold for pre-plasma formation.

Another drawback of the use of many types of commonly used laser gain media is the effect of spectral gain narrowing, figure 1.3, where the non-uniform spectral gain profile can reduce the bandwidth of a pulse undergoing amplification and therefore the minimum compressible pulse duration as a function of gain.

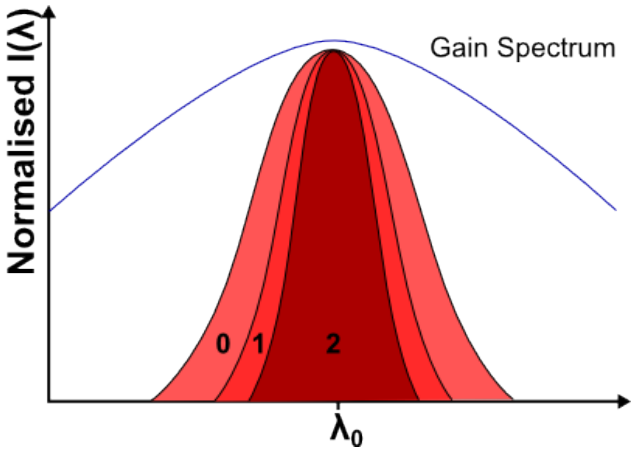


Figure 1.3: Diagram of gain narrowing of a pulse from a non-uniform gain-spectrum, both with central wavelength λ_0. The pulse spectrum is shown before amplification (0), after a single amplifier pass (1) and after two passes (2).

For Nd:Glass systems, the effects of gain narrowing can be reduced to some extent by using a mix of different glass types in the amplifiers; for instance silicate and phosphate glass, which have slightly different gain central wavelengths and gain profiles. Even with these corrections, gain-narrowing is still one of the main limiting factors in achieving high-power <500 fs pulse-durations.

1.2.2 *Chirped Pulse Amplification*

Direct amplification of an ultrashort pulse will typically lead quite rapidly to intensities sufficient to cause laser-induced damage to optical components; which is driven by multi-photon ionisation and plasma formation for sub-picosecond pulses and thermal processes i.e. lattice deformation, for pulses above tens of picoseconds [20]. The chirped pulse amplification (CPA) technique was first applied to optical systems in the 1980s and has led to a dramatic reduction in the size and cost of the optical components required to access

multi-gigawatt to multi-terawatt laser powers [21, 22]. It utilises "stretching" the bandwidth of the pulse in time to propagate through the laser amplification optics, reducing the instantaneous peak-power and allows greater energy extraction whilst also avoiding optical damage. After amplification, the pulse bandwidth is "compressed" as close as possible to its Fourier transform-limited duration, determined by (1.2), for interaction with targets. The compressor optics and focussing elements onto target will still need to have a large area to handle high-power pulses after compression. For the largest systems operating today, approximately one metre diameter optics are required to handle pulse energies of order 1 kJ to create petawatt optical peak-powers.

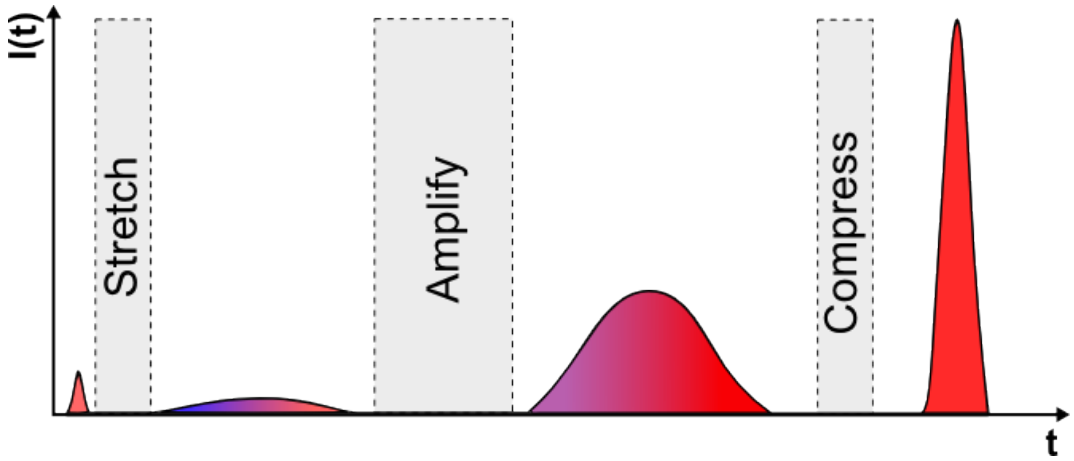


Figure 1.4: A cartoon of the chirped pulse amplification method. Short pulses from a low-power laser oscillator are first stretched in time before amplification to avoid optical damage from high optical peak-power, allowing greater energy extraction. The pulses are finally compressed back to their shortest duration for interaction with targets.

Ignoring its weak magnetic field for sub relativistic intensities, a linearly polarised laser pulse can be usefully described as a rapidly time-varying co-sinusoidal electric carrier wave with fixed phase relationship ϕ confined within a temporal pulse envelope $A\,(t)$,

$$E\,(t) = A\,(t) \exp\left(i\left(\omega t + \phi\right)\right) \tag{1.4}$$

where Gaussian

$$A\,(t)_{Gauss} = \exp\left(-2\ln 2\left(\frac{t}{\triangle t}\right)^2\right) \tag{1.5}$$

and hyperbolic secant

$$A\,(t)_{Sech^2} = sech^2\left(\frac{1.76t}{\triangle t}\right) \tag{1.6}$$

envelope shapes are most typically observed and modelled, with $\triangle$t denoting the full-width at half-maximum (FWHM) of the temporal profile. If the pulse propagates through an optical material, the wavelength-dependent refractive index of the material produces a frequency-dependent phase term $\phi(\omega) = k(\omega)z = {}^{n(\omega)\omega z}/_{c}$ that is accumulated from the propagation though an optical material, of length z. This can be expanded as a Taylor series in the spectral domain as

$$\phi^{(j)} = \left.\frac{\delta^j(\omega)}{\delta\omega^j}\right|_{\omega_0}, \phi(\omega) = \phi + \phi'(\omega-\omega_0) + \frac{\phi''}{2}(\omega-\omega_0)^2 + \frac{\phi'''}{6}(\omega-\omega_0)^3 \tag{1.7}$$

The zeroth-order term determines the absolute phase of ω_0 and the first-order term containing ϕ' translates only the envelope of the laser pulse in the time domain i.e. it represents group delay, where positive phase leads to a later time of arrival. The combination of these two terms create the absolute carrier-envelope phase (CEP) of the pulse. Higher order terms are responsible for the temporal structure of the electric field, where the ϕ'' term creates a linearly varying frequency change across the field i.e. group delay dispersion (GDD) or "chirp".

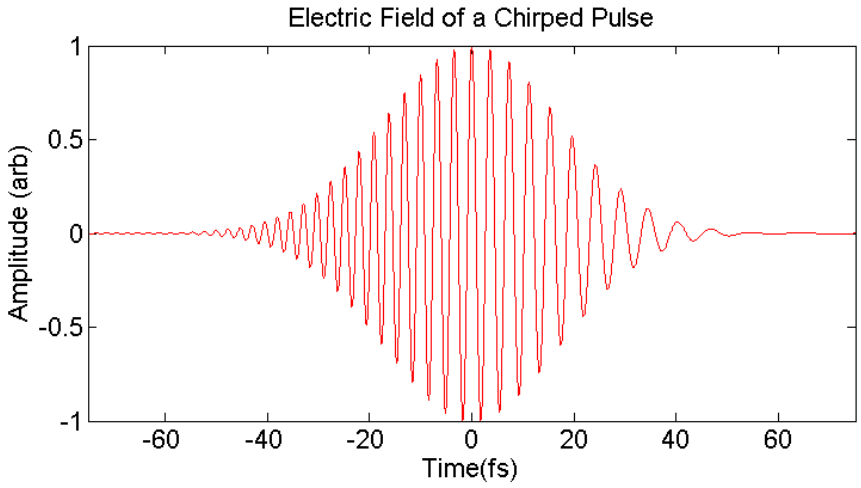


Figure 1.5: Electric field of a transform-limited 5 fs FWHM pulse stretched/chirped to 40fs by addition of ϕ''= 72 fs^2 second-order phase in 1.7.

The shape of the envelope is not adversely affected by GDD; however, the duration of the pulse $\triangle t_2$ after linear chirp is applied across its field can be calculated as

$$\triangle t_2 = \sqrt{\triangle t_1 + \left(\frac{4\phi''}{\triangle t_1}\ln 2\right)^2}. \tag{1.8}$$

Chirped pulse amplification therefore ideally refers to the manipulation of the second-order spectral phase, without losing its spectral content, with stretchers and compressors

adding approximately opposite amounts of chirp so that pulses are compressed back towards the Fourier-transform pulse duration limit of the pulse bandwidth.

Higher-order phase terms also occur in real-world CPA laser systems and typically lead to changes in the shape of the pulse envelope. Figure 1.6 shows how small amounts of positive third-order phase causes the front of the pulse to extend further out in time, reducing contrast, whilst temporal modulations are created on the rear of the pulse. For significantly greater amounts of third-order phase the modulation amplitudes become stronger and therefore significant negative third-order phase has the potential to create a large asymmetric pre-pulse pedestal.

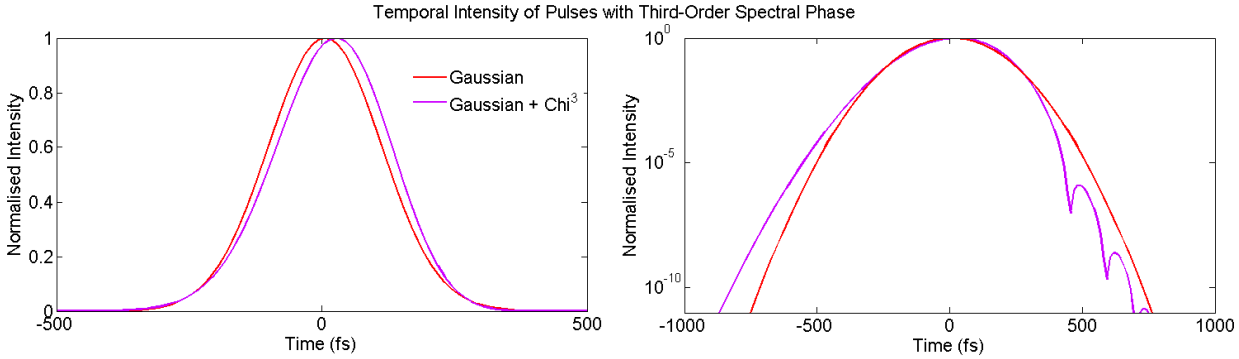


Figure 1.6: Linear (left) and logarithmic (right) plots of the temporal Intensity of a 250 fs pulse with zero spectral phase and with ϕ''' =1x10^6 fs^3 third-order phase, equivalent to 2.15 m propagation through SF10 glass or 7.7 m of BK7. On a log scale it is clear that the pulse envelope becomes skewed and pre-pulses at 10^{-6} and 10^{-8} relative intensity are generated on the rising edge of the pulse envelope with this amount of spectral phase. This model also highlights the need for high-dynamic range measurements when assessing the impact of high-order phase on a laser pulse used to drive experimental systems sensitive to pre-pulse.

For chirped pulse amplification, the easiest method to add GDD to a pulse is to use the wavelength-dependent refractive index transparent dielectric materials, which typically produces a ϕ''term of order 20-100 fs^2 mm^{-1}. However, unwanted higher-order spectral phase accumulation limits this method of stretching to a few picoseconds. For larger stretch factors, angular dispersion from prisms or diffraction gratings can be used in optical setups with less higher-order phase accumulation.

The wide angular dispersion from diffraction gratings is typically used to stretch pulses over timescales from above a picosecond to many nanoseconds in duration. The condition

for constructive interference from a reflective diffraction grating is given by the grating equation

$$m\lambda = d\,(\sin\theta + \sin\gamma) \tag{1.9}$$

where m is the diffraction order, d is the slit/groove separation, θ is the incidence angle from the diffraction grating normal and γ is the diffracted ray angle from the grating normal. The zeroth-order beam is the mirror-like reflected beam from a diffraction grating and contains no angular dispersion. In real-world CPA systems it represents an energy loss mechanism.

The simplest stretcher/compressor configuration comprises two parallel gratings that produces negative GDD and is shown in figure 1.7.

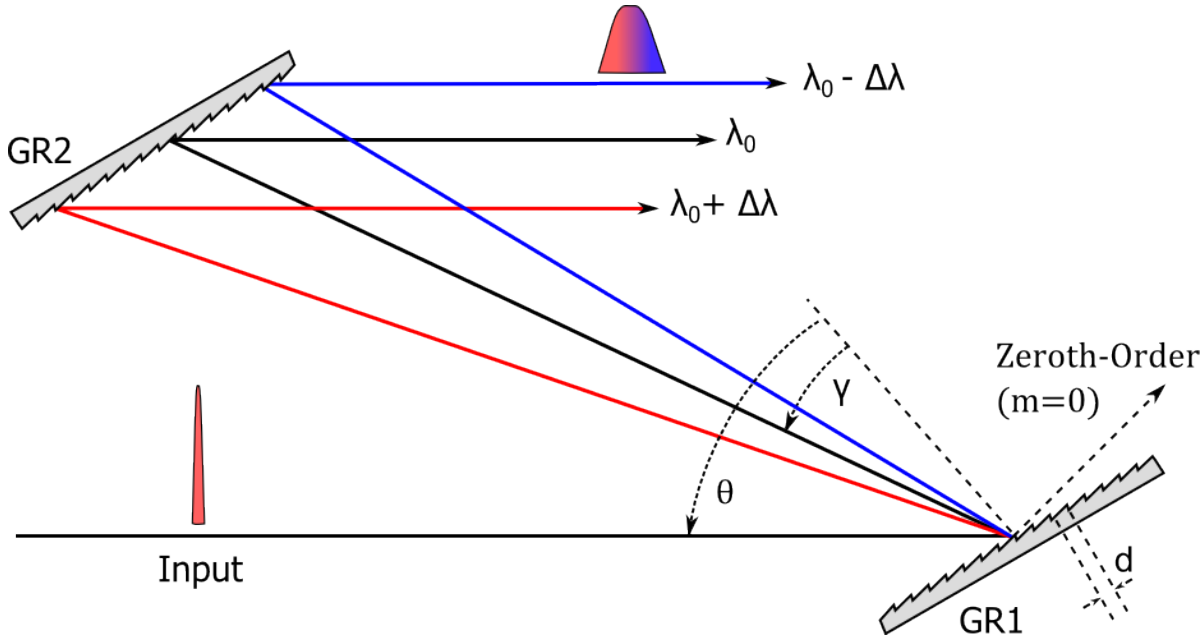


Figure 1.7: Layout of a simple two parallel grating optical setup that adds anomalous dispersion. This geometry is typically used for compressors due to simplicity, zero transmission though glass and large area beam acceptance to avoid optical damage.

The output of this simple compressor layout will have an unavoidable spatial chirp. The system may however be double-passed with a near normal incidence mirror or roof prism placed at the spatially chirped output. The input and output beams can be spatially separated by either tilting the beam in the non-dispersion plane or adding a retro-shift of the beam at the spatially chirped output, typically in the non-dispersed plane as well. When well aligned, this two-pass geometry can compensate for spatial chirp while doub-

ling the temporal compression factor, though at the expense of additional energy loss from multiple bounces off the gratings.

The pulse duration per pass of a diffraction grating stretcher/compressor with effective grating separation G can be analytically calculated as [23]

$$\triangle t = \frac{G\lambda_0 \triangle \lambda}{c\left(d\cos\left(\gamma_{\lambda_0}\right)\right)^2} \tag{1.10}$$

where γ_{λ_0} is the central wavelength diffracted ray angle. A diffraction grating setup that adds positive GDD was first proposed by Martinez [24] is shown in figure 1.8. This setup has a unit magnification telescope placed between two anti-parallel diffraction gratings.

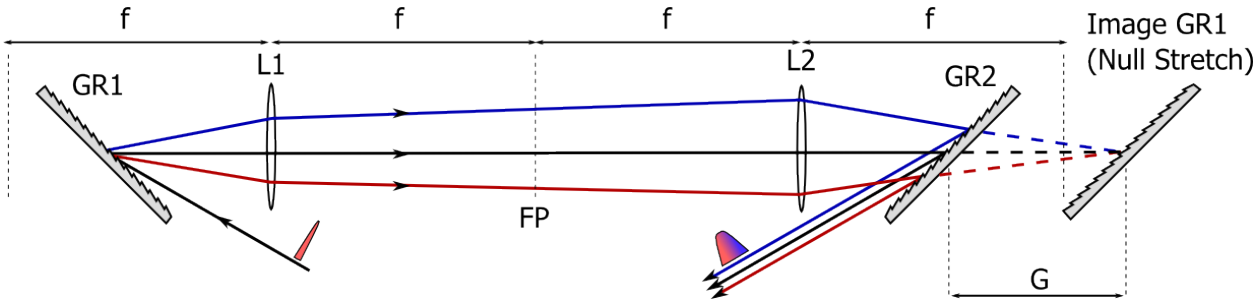


Figure 1.8: Optical layout of a Martinez stretcher for producing positive GDD. In this geometry the first grating can be placed a focal length away from the first lens L1. If the optical system is folded on the Fourier plane of L1 (FP), the first grating can be moved away from this position to produce the required chirp from effective grating separation G from the null stretch position.

The second grating is placed either in front or behind the image of the first grating to add either positive or negative GDD respectively. For unit magnification, the object-image distance of the first grating will be fixed and therefore the effective grating separation is simply $G = 2(f - l)$ per pass, where l is the grating-lens distance. For maximum chirp, the grating-lens distance is usually minimised as much as possible until the input and dispersed beams are close to clipping. The setup can be folded at the focal length of the first lens to use a single grating and lens, which has the advantage of using only a single grating, ensuring exact matching of the grating angle for each pass. This optical setup should also be double-passed to minimise spatial chirp, which can be achieved in a number of ways, including use of image inversion (using a long focal length lens and zero degree mirror) to partially compensate for geometric aberrations in the stretcher optics.

1.2.3 *Optical Parametric Chirped Pulse Amplification*

The refractive index of optical media forms the basis of geometric and physical optics, whose output depends linearly upon the input electric field amplitude. At higher-intensities, non-linear optical phenomena can also become important. The first observation of the non-linear interaction of the light field with matter was made by Franken et al. with the discovery of second-harmonic generation (SHG) from optical pumping of a ruby crystal [25]. Since then, the field of non-linear optics has grown to encompass an extensive range of processes and applications. The strength of the material response is related to the polarisability $\overrightarrow{P}$ of the material, which is expanded as a power series to

$$\overrightarrow{P} = \varepsilon_0 \overrightarrow{\chi^{(1)}} \overrightarrow{E} = \epsilon_0 \left(\chi^{(1)} \overrightarrow{E} + \chi^{(2)} \overrightarrow{E}^2 + \chi^{(3)} \overrightarrow{E}^3 + ... \right). \tag{1.11}$$

Here ε_0 is the vacuum electric permittivity and the optical susceptibilities $\chi^{(n)}$ are nth-rank tensors. For a monochromatic plane wave travelling along the z-axis, with the form $E(t) = A\cos(\omega t - kz)$ substituted into (1.11), a variety of optical non-linear responses are possible, as shown in (1.12)

$$\overrightarrow{P} = \varepsilon_0 \chi^{(1)} A \cos\left(\omega t - \overrightarrow{k} z\right) + \tag{1.12}$$

$$\epsilon_0 \chi^{(2)} \left(\frac{A^2}{2} \left(1 + \cos\left(2\omega t - 2\overrightarrow{k} z \right) \right) \right) + \tag{1.13}$$

$$\epsilon_0 \chi^{(3)} \left(\frac{A^3}{4} \left(3\cos\left(\omega t - \overrightarrow{k} z\right) + \cos\left(3\omega t - 3\overrightarrow{k} z \right) \right) \right) + ... \tag{1.14}$$

All media, crystalline and non-crystalline, have non-zero odd susceptibilities. In weak fields, the polarisation of the material will approximate the first term, producing a linear response proportional to the strength of the input electric field i.e. the "ordinary" material refractive index.

Non-centrosymmetric media have non-zero second-order susceptibilities whose second-order response depends upon the squared amplitude i.e. intensity of the input field. The first term in (1.11) represents the DC polarisability, known as optical rectification, of a material from the alternating field of the laser. The second term is the two-photon sum frequency process, here second-harmonic generation where the input electric field is considered to be monochromatic.

Optical parametric amplification (OPA) is based upon a second-order non-linear difference frequency process where "pump" photons are converted into "signal" and "idler" photons in a non-centrosymmetric crystal such that

$$\omega_p = \omega_s + \omega_i \tag{1.15}$$

Where ω_p ,ω_s and ω_i are the pump, signal and idler frequencies respectively. Optical parametric amplification (OPA) refers to a version of this process that is initially seeded with a "weak" beam at ω_s, thereby providing a method for amplification via energy transfer from the more intense pump pulse to the amplified seed/signal and idler. For efficient and broadband amplification, this process must also be well phase-matched i.e. momentum must be conserved, via the relation $k_p = k_s + k_i$, which can be achieved using appropriate birefringent crystalline media. The crystal material, length and pulse parameters also have an effect on bandwidth generation. OPA is able to amplify a very broad range of signal frequencies and is not limited to the discrete energy level differences in atomic structure, as seen in traditional gain-storage amplifiers.

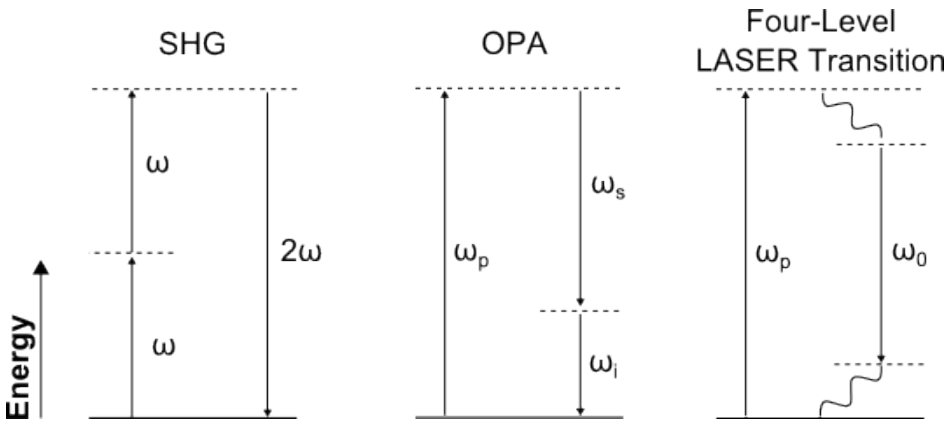


Figure 1.9: Schematic energy levels involved in SHG, OPA and a four-level LASER.

Optical parametric chirped pulse amplification (OPCPA) refers to the use of a chirped seed in the OPA process which can take the place of a traditional gain storage amplifier in a CPA laser system [18, 26]. In addition to avoiding optical damage during amplification, a chirped seed is a crucial degree of freedom that allows spectral management of the pulse, such that gain broadening can be achieved if the seed pulses are shorter than the pump pulses of Gaussian temporal shape and a high-degree of pump energy depletion.

In a parametric amplifier the gain is instantaneous and the system immediately returns to its ground state after amplification with zero quantum defect, and therefore very little

energy is transferred to the crystal during amplification (limiting thermal stress and defocusing), allowing construction of high repetition rate amplifiers based on this process.

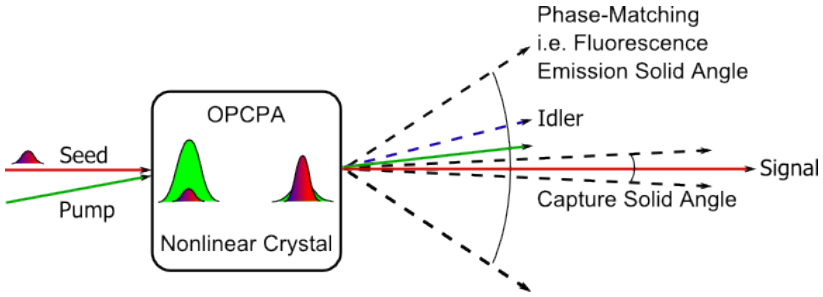


Figure 1.10: Operation of an optical parametric amplifier using a chirped seed pulse. An intense pump pulse (another laser) is temporally and spatially overlapped in the non-linear medium that is phase-matched to amplify the seed.

Very high single-pass gains of up to 10^5 using 5-10 mm beta-barium borate (BBO) crystal lengths are possible with OPCPA versus a typical 10 cm rod amplifier lengths providing ~x10 single-pass gain from gain-storage amplifiers. This helps to reduce the optical system complexity in the primary laser chain and also reduces the accumulation of higher order spectral phase terms through dispersive media that act to degrade the compressibility of the pulse. This does however come at the cost of a pump system that is itself a complex laser rather than a simple flash-lamp or diode bar.

The spontaneous down-conversion of phase-matched signal and idler pairs in the presence of the high intensity pump in an OPA process is a source of incoherent noise, analogous to ASE in gain-storage amplification. While an OPA process is fundamentally quantum mechanical in behaviour [27], the generation and further amplification of fluorescence can be modelled semi-classically as zero-point fluctuations of the electromagnetic field [28] contributing an initial seed term to the OPA process that is then amplified in parallel with the main laser seed.

The fluorescence intensity on target in the limit of high gain is given by [18, 27]

$$I_{PF} = \frac{\pi}{4F^2}\frac{hc^2\triangle\lambda}{\lambda^5}G \tag{1.16}$$

where is $\triangle\lambda$ the fluorescence emission bandwidth or the spectral acceptance of the optical system, whichever is smaller. The duration of fluorescence will be of order the pump pulse duration. Using a similar example of a 100 TW laser system, this time using OPCPA with a spectral acceptance of 20 nm and 1 ns pump duration, the fluorescence intensity will be ~3x10^{13} W cm^{-2}. This produces a negligible improvement in intensity contrast

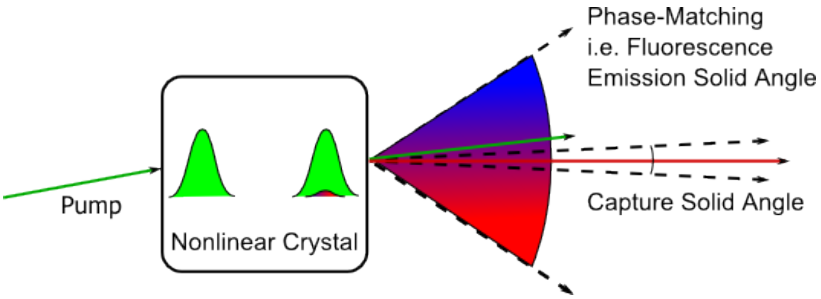


Figure 1.11: Parametric fluorescence from an OPA. The pump photons also have a probability to decay into signal and idler pairs across the phase-matching space of the amplifier. This is emitted in a cone of angles, which represent the phase-matching angles and frequencies of the crystal to the pump.

compared to a gain storage amplifier based system. However, the temporal duration of the noise feature can be reduced by >1000 using picosecond duration pump pulses. The first generation of OPCPA systems used such picosecond duration pump pulses to amplify up to ~20 mJ before seeding a Nd:Glass amplifier chain. Pulse pedestals at ~10^{-8}-10^{-6} relative intensity level were seen at the Vulcan [29] and Orion Petawatt facilities [30]. More recently. the use of picosecond pumping schemes up to the μJ-mJ level has significantly improved the long-timescale pedestal to <10^{-8} level [29–31].

1.3 ORGANISATION OF THESIS

The primary aim of this project was to investigate high-contrast amplification techniques for high-intensity laser systems. The preceding sections briefly outlined the motivation for generation high-contrast, high-intensity laser pulses and the available amplification methods to achieve this, with particular emphasis on the benefits of OPCPA both for high-contrast and high repetition rate, gain broadened laser pulses.

Chapter 2 documents the development of the hybrid OPCPA/Nd:Glass Imperial College Cerberus laser system, which will be used as a source for the experimental investigations to achieve high-contrast pulses for laser-matter experiments. This laser is currently which capable of producing 5 J, 500 fs i.e. 10 TW pulses and a 20 J, 1.4 ns long-pulse driver to use between three target areas for laser-matter and plasma probing experiments. The design, modelling and experimental results from this laser system are documented in this chapter.

Chapter 3 introduces the high-dynamic range optical diagnostics developed to measure and understand the physical processes and origins behind optical noise sources that impact the temporal contrast of the high-power laser pulse. These instruments include an extremely sensitive high-dynamic range scanning third-order autocorrelator diagnostic (TOAD) that can be used for complete characterisation of the laser contrast from the short-pulse oscillator to the complete high-power operation. Additionally, a new optical diagnostic for characterisation of the parametric fluorescence background signal from a high-gain OPA was developed during this project. We present our findings on the seeded OPA parametric fluorescence from the Cerberus picosecond pumped OPCPA stages. The ability of this diagnostic to measure the weak fluorescence emission in real-time when the OPAs are amplifying a significantly more intense laser pulse produced the first experimental verification of the behaviour of parametric fluorescence amplification in competition with the laser pulse. The technique is widely applicable to all high-intensity OPCPA laser systems, where the Cerberus picosecond pumped OPA stages were found to produce a fluorescence pedestal 2.1 ps in duration that would impact the compressed short-pulse laser contrast at $7\text{x}10^{-9}$ relative intensity at 1.3 ps ahead of the primary pulse. The investigation was also able to experimentally determine the semi-classical parametric fluorescence seed term, which will a useful quantity to insert into numerical models of OPAs for future developments.

Chapter 4 presents a unique investigation into the temporal contrast performance of a wide range of short-pulse oscillators used for seeding Nd:Glass terawatt-petawatt laser systems in a number of major UK laboratories. This includes saturable absorber, Kerr lens, and elliptical polarisation rotation mode-locking techniques in addition to an optical parametric oscillator source at the Orion petawatt laser facility (AWE), Vulcan laser facility (STFC) and TARANIS laser (QUB) as well as sources at Imperial College. The conclusions from this investigation yielded significant insight into the relative contrast performance between these mode-locking methods and may guide the choice of oscillator systems needed to underpin contrast sensitive experiments in the future.

Chapter 5 documents the contrast results obtained using the TOAD diagnostic on a range of UK terawatt and petawatt laser systems that collaborated with this project, who also contributed the laser oscillator sources characterised in chapter 4. Initial investigations using the TOAD found anomalous pre-pulses on the TOAD contrast scans, which lead this collaboration to investigate whether other laser systems produced similar features. The results from this investigation has produced valuable insights into techniques

that avoid potential pre-pulse generation from OPCPAs in addition to a general overview of the current contrast limitations of a medium-range ~10^{-5} intensity pedestal common to both CPA and OPCPA laser systems worldwide. This pedestal is thought to originate from optical scatter or incoherent diffractive effects in the pulse stretcher optical system. We identify a method of verifying this claim and present preliminary results, whose conclusions are so far limited by other factors.

A high-intensity laser will be of little benefit without matching it to applications such as laser-matter experiments that use the laser as a source for plasma physics investigations. Chapter 6 introduces plasma physics concepts and documents the experiments that have so far used the Cerberus laser system high-power laser pulses. This includes the X-ray backlighter and plasma Faraday rotation diagnostics using the Cerberus long-pulse beamline for MAGPIE, a stand-alone terawatt pulsed-power Z-pinch plasma generator, and short-pulse laser-matter interactions on levitated droplets.

Finally, chapter 7collects the results and conclusions from preceding chapters to form a complete perspective on current state of high-contrast laser sources, CPA and OPCPA laser systems. We conclude that whilst much has been achieved in this project in the understanding of laser contrast and methods to mitigate noise sources, further work is still required to, hopefully, one day achieve the ideal noise-free pulse. Future work on contrast diagnostic improvements and Cerberus laser upgrades are also presented.

1.4 CONTRIBUTORS, PUBLICATIONS AND OTHER OUTPUTS

This PhD project would certainly not have been so fruitful without the close cooperation within research team that exists at Imperial College.

Many CPA components of Cerberus laser design were designed carried out by Dr Siddharth Patankar and parts of the design are either quoted or reiterated here [32]. The author has been responsible for the modelling, commissioning, operation and maintenance of the picosecond and nanosecond OPA stages of Cerberus, the primary amplification mechanism of this complex laser system. Dr Damien Bigourd was responsible for the initial technical design and installation of the picosecond OPA stages (based on previous MSc modelling projects by Krystallo Hadjicosti [33] and Nicolas Leblanc[34]) and this has been significantly redesigned by the author to provide greater energy output (70 μJ to 300 μJ), bandwidth and stability. The short-pulse oscillator and much of the OPA pump

chain optics were installed by Prof Roland A. Smith; however many small optimisations and upgrades have been made by the author and the author has been responsible for its characterisation, development, operation and maintenance of system and laser beam delivery to multiple experiments. The pump chain of Cerberus is also the seed for a high-energy long-pulse beamline and the author has been responsible for the final commissioning steps, operation and maintenance of the Cerberus-MAGPIE beam used for experiments such as Faraday rotation B-field imaging in pulsed power driven plasmas [35]. The initial Nd:Glass amplifier installation was carried out by Dr Siddharth Patankar and the author continued its development, maintenance and delivery to multiple high-power, short-pulse experiments.

The author has been responsible for the contrast characterisation and contrast development of the Cerberus laser contained within this thesis, including the novel parametric fluorescence diagnostic concept, design and measurements [36], the third-order autocorrelator development and measurements, both on the Cerberus laser system and other laser system characterised [37] that will be used to inform further laser development at these external labs and researchers requiring detailed knowledge of the temporal profiles and noise terms for high-quality multi-terawatt-petawatt experiments.

The design, development and experiments that used the Cerberus laser system were the primary responsibility of other members in the research group. However, the author was responsible for delivery of the Cerberus high-power laser-pulses onto the targets and general support including target alignment and the design of optical diagnostics and for characterisation of the laser-matter interactions. This resulted in a need to work closely with multiple "users" of the laser system and is linked to a number of resulting publications [5, 35, 38, 39]

This work was in part supported by EPSRC grant (#EP/G001324/1) and the AWE contract (#30242504) for "Advanced technologies for high-contrast short-pulse operation on the Orion Laser Facility" with the intention of enabling transfer of expertise and techniques in laser systems and metrology between AWE Aldermaston and Imperial College to the mutual benefit of both institutions.

1.4.1 *Outputs Related to Thesis Work*

The following peer-reviewed journal publications resulted from the work described in this PhD project:

- D. Bigourd, S. Patankar, S. I. Olsson Robbie, H. W. Doyle, K. Mecseki, N. Stuart, K. Hadjicosti, N. Leblanc, G. H. C. New and R. A. Smith, "Spectral enhancement in optical parametric amplifiers in the saturated regime" Appl. Phys. B. 113 (2013) 627–633 [40].
  - This article presented the modelling and experimental performance of the picosecond OPA stages of Cerberus driven in a strong pump-depleted regime to produce spectra broadening and enhanced stability from "saturation" of the OPA process. The early PhD works of the author assisted with numerical modelling and discussions on optimal OPCPA operation.
- N.H. Stuart, D. Bigourd, R.W. Hill, T.S. Robinson, K. Mecseki, S. Patankar, G.H.C. New and R.A. Smith, "Direct fluorescence characterisation of a picosecond seeded optical parametric amplifier", Opt. Commun. 336 (2014) [36].
  - This publication reports on the new diagnostic technique developed and used to characterise the parametric fluorescence emission from an OPA stage. Critically, this setup is able to measure the weak fluorescence emission simultaneously with the presence of the amplified laser signal. This new measurement technique provided significant insights into the behaviour of fluorescence through different levels of pump depletion and found that strong pump depletion drastically reduces the fluorescence generated a delivered to target, a result that was not widely hypothesised or verified previously. The semi-classical "vacuum fluctuation" driven noise term seeding the OPA fluorescence was determined to be 0.7 ± 0.4 photons ps^{-1} nm^{-1} bandwidth, which will be a useful term to employ in OPA modelling codes.
- N. H. Stuart, T. Robinson, D. Hillier, N. Hopps, B. Parry, I. Musgrave, G. Nersisyan, A. Sharba, M. Zepf and R. A. Smith. “Comparative Study on the Temporal Contrast of Femtosecond Mode-Locked Laser Oscillators”, Opt. Lett. 41.14 (2016) [37].
  - This paper documents a temporal contrast survey, using the third-order autocorrelator system described in §3.1, of a wide-range of mode-locking meth-

ods used to produce short-pulse, sub-picosecond, laser sources that seed high-power laser systems. Saturable absorber (SESAM), Kerr lens (KLM), non-linear polarization evolution (NPE) in optical fibres and synchronously pumped optical parametric oscillator (OPO) mode-locked sources were measured with up to 10^{10} dynamic range. We found additional non-linear terms and residual higher-order dispersion limits the performance of KLM and NPE sources up to the 10^5 contrast level and $>10^8$ contrast was observed from the SESAM and OPO laser pulse trains. These findings will serve to inform the high-power laser community which laser oscillator seed sources methods to build or purchase, as it was not clear previously which mode-locking methods were best suited for high-contrast seeding of laser amplification chains.

- A. Sharba, N. H. Stuart, G. Nersisyan, M. Zepf, R. A. Smith, M. Borghesi and G. Sarri, "Generation of High-Contrast and High-Spatial Quality Idler from A Low-Gain Optical Parametric Amplifier", Submitted to (QUB) Low Gain OPA Paper (2016) Submitted to Appl. Opt. (2016).
  - This work, based at Queen's University Belfast, improved the ~10^5 ASE temporal contrast from a Ti:Sapphire regenerative amplifier with a low-gain, self-pumped degenerative OPA. The idler pulse contrast from this process is proportional to the non-linear gain window of the OPA, whose pump pulse contrast is also enhanced from SHG. The idler contrast from this low-gain OPA was observed to be greater than the 10^{10} dynamic range of the third-order autocorrelator used to characterise these pulses. The author developed and carried out the contrast measurements with the third-order autocorrelator used to measure the idler pulse contrast from this source.

- K. Mecseki, D. Bigourd, S. Patankar, N. H. Stuart, and R. A. Smith , "Flat-top picosecond pulses generated by chirped spectral modulation from a Nd:YLF regenerative amplifier for pumping few-cycle optical parametric amplifiers", Appl. Opt. 53 (2014) 2229–2235 [41].
  - This paper presented the use of a custom etalon inside a Nd:YLF regenerative amplifier to introduce a frequency modulation on the transmitted pulse. This can be used to partially counteract gain narrowing to produce temporally a longer amplified pulse, which reduce B-integral in the pump beamline of the OPCPA laser this is source used for. We found the use of an etalon opposed

to use of a spectral mask in the pre-stretcher greatly improved the spectral width, smoothness and energy stability of the regenerative amplifier, which is the dominant amplification source for the pump laser in the Cerberus laser. The author was involved with these comparisons, regenerative amplifier characterisation and evaluating their use to enhance pumping of the ps-OPAs in the Imperial College Cerberus laser.

- Christopher Price et al., "An in-vacuo optical levitation trap for high-intensity laser interaction experiments with isolated microtargets", Rev. Sci. Instrum. 86 (2015) 033502 [39].
  - This paper presents the first design, characterisation and use of an in-vacuo optical levitation trap for application as a target source for high-intensity laser-matter interactions. With a large working distance of ~4 cm, the trapped droplets are highly accessible by many diagnostics as well as the primary heating beam. This is the first time a completely isolated target has been "shot" with a high-intensity laser and was the first short-pulse experiment using the Cerberus laser, with an estimated intensity on target of 10^{17} W cm^{-2}. The author was involved with developing the high-power laser system, delivering high-power laser shots to targets and development of the optical alignment system onto these unsupported ~10 μm targets.

- Gareth Hall et al, "Monochromatic radiography of high energy density physics experiments on the MAGPIE generator", Rev. Sci. Instrum. 85 (2014) [5].
  - This was a joint Cerberus-MAGPIE experiment employing the 20 J long-pulse beamline to produce a bright incoherent plasma based X-ray source (1.865 keV Si K-α transition) to image the plasma dynamics inside the MAGPIE chamber. A wide range of standard target geometries were used during this campaign and features of the plasma dynamics were observed.

- George Swadling et al., "Diagnosing collisions of magnetized, high energy density plasma flows using a combination of collective Thomson scattering, Faraday rotation, and interferometry", Rev. Sci. Instrum. 85 (2014) [35].
  - This publication presented the use a newly developed diagnostic using the Cerberus long-pulse beamline to more precisely and accurately determine the electron density and dynamic magnetic fields of MAGPIE experiments using

a combination of interferometry and a newly developed Faraday rotation diagnostic, detailed in §6.3.2, to measure the polarisation rotation of the long-pulse laser as it traverses through the magnetic fields embedded in a plasma within the experiment.

- S. Patankar, E. T. Gumbrell, T. S. Robinson, H. F. Lowe, S. Giltrap, C. J. Price, N. H. Stuart, P. Kemshall, J. Fyrth, J. Luis, J. W. Skidmore, and R. A. Smith, "Multi-wavelength interferometry system for the Orion laser facility", Appl. Opt. 54, 10592 (2015) [42].
  - This article reports on the design and testing of a multi-wavelength (1054 nm, 527 nm and 263 nm) interferometry system for the Orion laser facility based upon the use of self-path matching Wollaston prisms, which provide timing-free alignment of femtosecond pulses that are highly difficult to achieve on single-shot systems. Features as small as 5 μm can be resolved for 15×10 mm object sizes. Results are also shown for an off-harmonic wavelength that will underpin a future capability. The primary optics package is accommodated inside the footprint of a ten-inch manipulator to allow the system to be deployed from a multitude of viewing angles inside the 4 m diameter Orion target chamber. The author was involved with the characterisation work and operation of the Cerberus laser used to characterise this imaging system before deployment on the Orion petawatt laser.

- S. Patankar, E. Gumbrell, T. Robinson, J. Fyrth, E. Floyd, N. Stuart, A. Moore, J. Luis, J. Skidmore and R. A. Smith, "Absolute Calibration of Optical Streak Cameras on Picosecond Time-scales using Supercontinuum Generation", Submitted to Rev. Sci. Instrum. (2016)
  - This paper reports a new method using high stability, laser-driven super-continuum generation in a liquid cell to calibrate the absolute photon response of fast optical streak cameras as a function of wavelength when operating at full sweep speeds. A stable, pulsed white light source (400-1000 nm) based around the use of self-phase modulation in a salt solution (K_2ZnCl_4) was developed to provide the required brightness on picosecond timescales, enabling streak camera calibration in fully dynamic rather than slow or static modes of operation. The measured spectral brightness allowed for absolute photon response calibration

over a broad spectral range between 425 nm and 650 nm of wavelengths. Despite good agreement between two identical streak cameras at the same sweep speed, the camera systems showed some significant deviations from the shape of the static photocathode response towards both ends of the spectrum. This new calibration technique is generally applicable to calibrating other fast optical and near-infra-red detectors across broad spectral ranges. The author was involved with developing a highly stable (1% standard deviation), high-energy (20 mJ), 10 Hz OPCPA short-pulse front-end used to drive the stable white light supercontinuum spectrum.

- L. G. Suttle, J. D. Hare, S. V. Lebedev, G. F. Swadling, G. C. Burdiak, A. Ciardi, J. P. Chittenden, N. F. Loureiro, N. Niasse, F. Suzuki-Vidal, J. Wu, Q. Yang, T. Clayson, A. Frank, T. S. Robinson, R. A. Smith, and N. Stuart, "Structure of a Magnetic Flux Annihilation Layer Formed by the Collision of Supersonic, Magnetized Plasma Flows", Phys. Rev. Lett. 116.22 (2016) [38].
  - This joint Cerberus-MAGPIE publication presents characterisation of the detailed structure of a current layer, generated by the collision of two counter-streaming, supersonic and magnetized aluminium plasma flows. The antiparallel magnetic fields advected by the flows were diagnosed with the Faraday rotation diagnostic detailed in §6.3.2 and were found to mutually annihilate inside the layer, giving rise to two narrow current sheets running along the outside surfaces of the layer with a fast outflow of plasma and high ion temperatures.

- J. D. Hare, L. Suttle, S. V. Lebedev, N. F. Loureiro, A. Ciardi, G. C. Burdiak, J. P. Chittenden, T. Clayson, C. Garcia, N. Niasse, T. Robinson, R. A. Smith, N. Stuart, F. Suzuki-Vidal, G. F. Swadling, J. Ma, J. Wu and Q. Yang, "Anomalous Heating and Plasmoid Formation in a Driven Magnetic Reconnection Experiment", Submitted to Phys. Rev. Lett. (2016).
  - This joint Cerberus-MAGPIE submission presents a detailed study of magnetic reconnection in a quasi-two-dimensional MAGPIE pulsed-power driven laboratory experiment. Oppositely directed magnetic fields (B = 3 T), advected by supersonic, sub-Alfvenic carbon plasma flows are brought together and mutually annihilate inside a thin current layer. The spatial and temporal character-

isation of the magnetic dynamics used the Faraday rotation diagnostic detailed in §6.3.2 to determine the structure and dynamics of this layer.

2

IMPERIAL COLLEGE CERBERUS MULTI-TERAWATT OPCPA/ND:GLASS LASER SYSTEM

In chapter 1 the potential advantages of using OPCPA as the primary amplification technique to achieve high-contrast, broadband amplification were outlined. This chapter details the development of the Cerberus hybrid OPCPA/Nd:Glass multi-terawatt, multi-beam, multi-target area laser system at Imperial College. The laser system was primarily funded by EPSRC (grant number EP/G001324/1) with the aim to deliver both long-pulse (20 J, 1.4 ns) and short-pulses (10 J, 500 fs, 20 TW) into the MAGPIE Z-Pinch [43] interaction chamber to create a unique capability of optical, X-ray and proton diagnostics of high-temperature magnetised plasma flows [5, 35, 44]. Two additional target areas built with funding from Imperial College and the Royal Society provide the capability for stand-alone laser-plasma physics investigations and linking of Cerberus to other experimental systems such as gas gun launchers used to shock compress material to high pressures and densities comparable to planetary cores.

This laser system utilises an OPCPA "front-end" that provides the first ~10^8 gain in order to generate a high-contrast, broadband, energetic and nanosecond duration chirped pulse seed for a large aperture Nd:Glass power amplifier chain, which provides high-energy scaling with modest 10^2 to 10^3 gain to achieve multi-terawatt optical peak-power after compression. The use of Nd:Glass enables future scalability to >100 TW from large-aperture 25 mm and 50 mm rod amplifiers and 108 mm and 150 mm diameter disc amplifiers released by the decommissioning of the HELEN laser system (AWE Aldermaston)

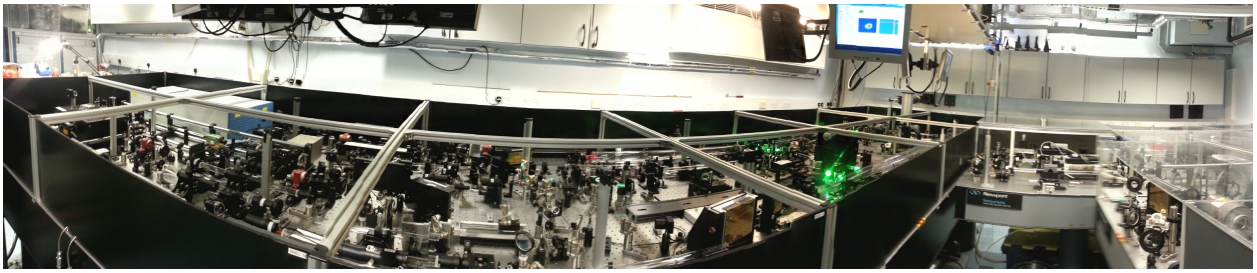


Figure 2.1: Front-end of Cerberus laser system that produces the long-pulse Nd:YLF seed and short-pulse OPCPA seed for large-aperture Nd:Glass amplification.

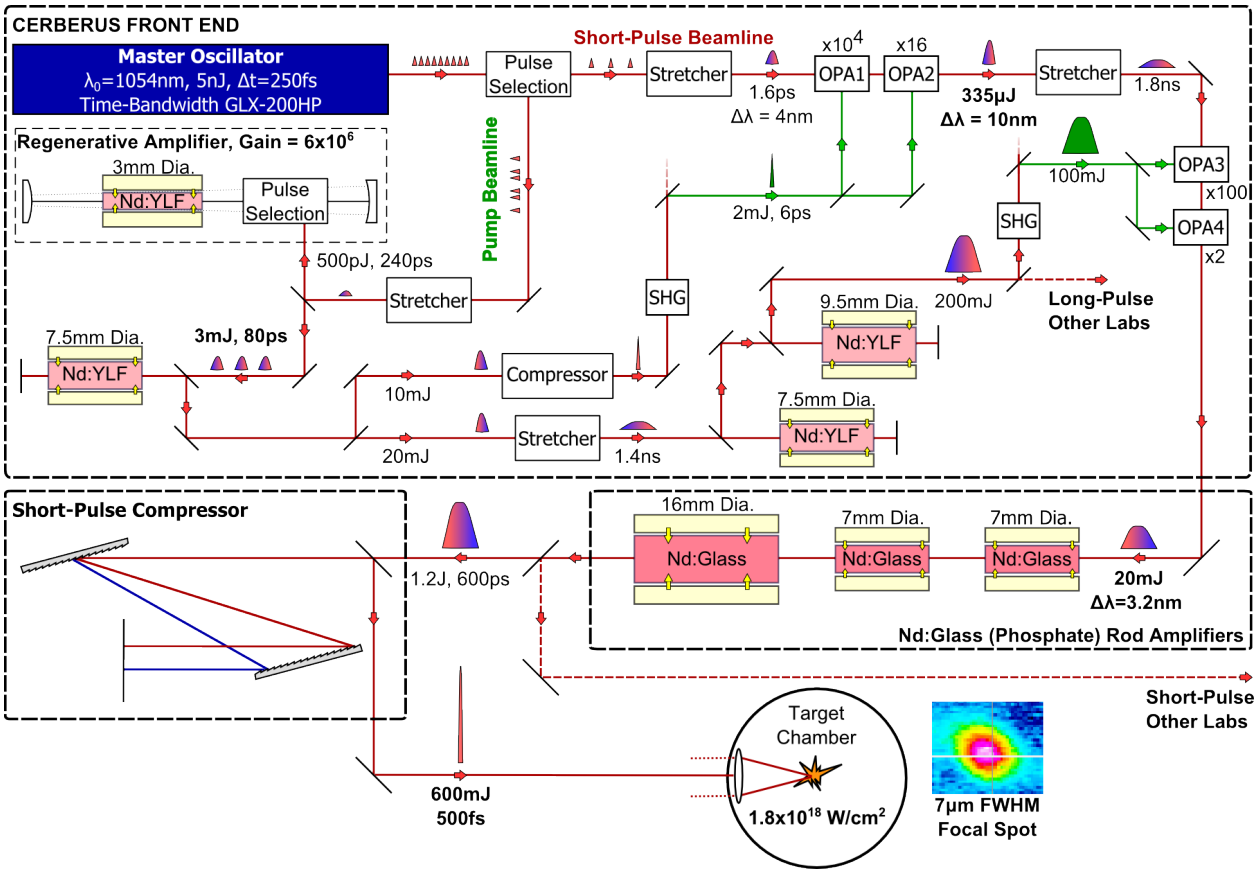


Figure 2.2: Simplified component diagram of the Cerberus long-pulse and terawatt short-pulse beamlines in the Terawatt lab. Seed and pump pulses for the OPCPA beamline are derived from a common Nd:Glass oscillator. Pump pulses are amplified by an Nd:YLF CPA beamline, which pump two pairs of OPA stages with ~6 ps and then ~1 ns pulses that generate an ~20 mJ amplified OPA signal. The OPA signal is then amplified to ~1.2 J through an Nd:Glass rod amplifier chain and compressed to ~600 mJ, 500 fs for interaction with targets with up to 1.8×10^{18} W cm^{-2} peak-intensity from an f/5 focussing optic.

[45]. Although petawatt National facilities have been commissioned using similar hybrid OPCPA/Nd:Glass amplification schemes [2, 4, 46, 47], there still exists a large body of work needed to inform development and optimisation of high-contrast, broadband, high-energy, and stable OPCPA that can benefit the high-power laser community.

A schematic overview of the Cerberus short and long-pulse amplification beamlines is shown in figure 2.2. A common Nd:Glass semiconductor saturable absorber (SESAM) mode-locked laser oscillator (Time Bandwidth Products GLX-200HP) generates a ~5 nJ, 250 fs, 70 MHz pulse train centred at 1054 nm to seed the long-pulse OPCPA pump and short-pulse beamlines. The oscillator is electronically locked to an external high-stability rubidium atomic clock, linked to a piezoelectrically driven mirror in the oscillator cavity,

in order to minimise thermal drift of the 70 MHz pulse train. This in turn limits long term temporal drift between OPA pump and seed pulses which take different routes through the laser system before overlapping in space and time in the OPA crystals. Spatial and temporal drift from differential thermal expansion in other sections of the laser system are minimised through engineering measures; for instance, the regenerative amplifier is mounted on a floating Invar rail assembly (a nickel-iron alloy with a thermal expansion coefficient an order of magnitude less than steel), optical front-end optics mounted on an enclosed, vibration damped, stainless steel surface optical table assembly and the laboratory temperature stabilised.

The long-pulse/OPCPA pump beamline is generated via gain-storage chirped pulse amplification with the 1053 nm laser transition of Nd-doped yttrium lithium fluoride (Nd:YLF, a-cut with 1% dopant concentration). This is very well overlapped with the 4 nm FWHM bandwidth from the 1054 nm Nd:Glass oscillator, which can also be tuned between ~1050-1056 nm if required. After initial stretching to ~240 ps, a Pockels cell selects a 400 Hz component of the oscillator pulse train to inject into a diode-pumped Nd:YLF linear regenerative cavity that amplifies pulses to 3 mJ. The large ~10^6 gain from this regenerative amplifier and narrow emission bandwidth of Nd:YLF creates significant gain-narrowing such that the output pulse is reduced to ~40 ps without additional spectral control, or to ~80 ps in duration with the use of a custom intra-cavity etalon that puts a slight dip into the gain profile at the centre of the YLF line at 1053 nm. The output from the regenerative amplifier is chopped to 10 Hz with an extra-cavity Pockels cell and seeds a double-passed flash-lamp pumped Nd:YLF amplifier that produces 30 mJ. At this point the pulse energy is split, with ~10 mJ compressed to ~10 ps duration and frequency-doubled to pump a set of OPCPA pre-amplifier stages, which are referred to as the "ps-OPAs", and the remainder is stretched again to ~1.4 ns and amplified by two more double-passed Nd:YLF amplifiers to produce up to 400 mJ, usually limited to 200 mJ, to be used as the "ns-OPA" pump and/or a long-pulse seed for high-energy amplification up to ~35 J in Nd:Glass amplifiers for driving experiments or plasma diagnostic systems.

A later pulse in the 70 MHz pulse train from the Nd:Glass oscillator is selected by a Pockels cell and polariser to act as the OPCPA seed. The 250 fs pulse is stretched to 1.6 ps through four passes of a 30 cm long high-index H-ZF7LA (SF6) bulk glass stretcher for optimal bandwidth and energy extraction from a pair of ps-OPAs, detailed in §2.6, that generates ~300 μJ pulses with 1% standard deviation stability and ~8.7 nm bandwidth, which would be compressible to ~190 fs transform-limited duration at this point.

This highly stable ps-OPA output is stretched at ~190 ps/nm in an all-reflective Öffner triplet system [48] to seed a pair of nanosecond pumped OPAs (ns-OPAs) that use the re-stretched, amplified and frequency doubled output of the Nd:YLF beamline to produce ~20 mJ pulses with typical 1% standard deviation energy stability and ~3.7 nm bandwidth that can ideally compress to 440 fs.

The amplified ns-OPA signal then seeds a chain of two 7 mm diameter and single 16 mm diameter Nd:Glass (phosphate) rod amplifiers to produce 1.2 J. This can either be compressed with ~65% efficiency to ~500 fs with a double-passed gold holographic diffraction grating (Jobin Yvon) compressor in the "Terawatt lab" or is diverted for further amplification and compression in the "Multi-Terawatt lab", which houses a 50 mm diameter Nd:Glass rod amplifier that can produce stretched pulse energies up to 25 J and then incident on to a multilayer coated, dielectric substrate diffraction grating compressor (Plymouth Grating Laboratory) with 87% efficiency for up to 35 TW interactions. Currently, the power is limited from compression in air to <5 TW from non-linear self-focussing (B-integral) limits, but a vacuum compressor is planned for the current diffraction grating set which would allow operation at up to 20 J.

Additional laser beamlines exist that use the <400 mJ, 1.4 ns OPCPA pump as a basis for a long-pulse beamline into an intermediary MAGPIE amplification lab that houses a 25 mm and 50 mm diameter Nd:Glass rod amplifiers capable of producing 25 J pulses for MAGPIE experiments.

An additional Q-switched laser system and external 25 mm diameter Nd:Silicate rod amplifier in this laboratory also delivers up to 8 ns, 3 J pulses at 532 nm in the second-harmonic as a Thomson scattering optical probe of MAGPIE experiments [35, 44].

The design and modelling of the stretchers and compressors for the Cerberus laser were performed by Dr Siddharth Patankar and therefore the author directs the reader to [32] for their design.

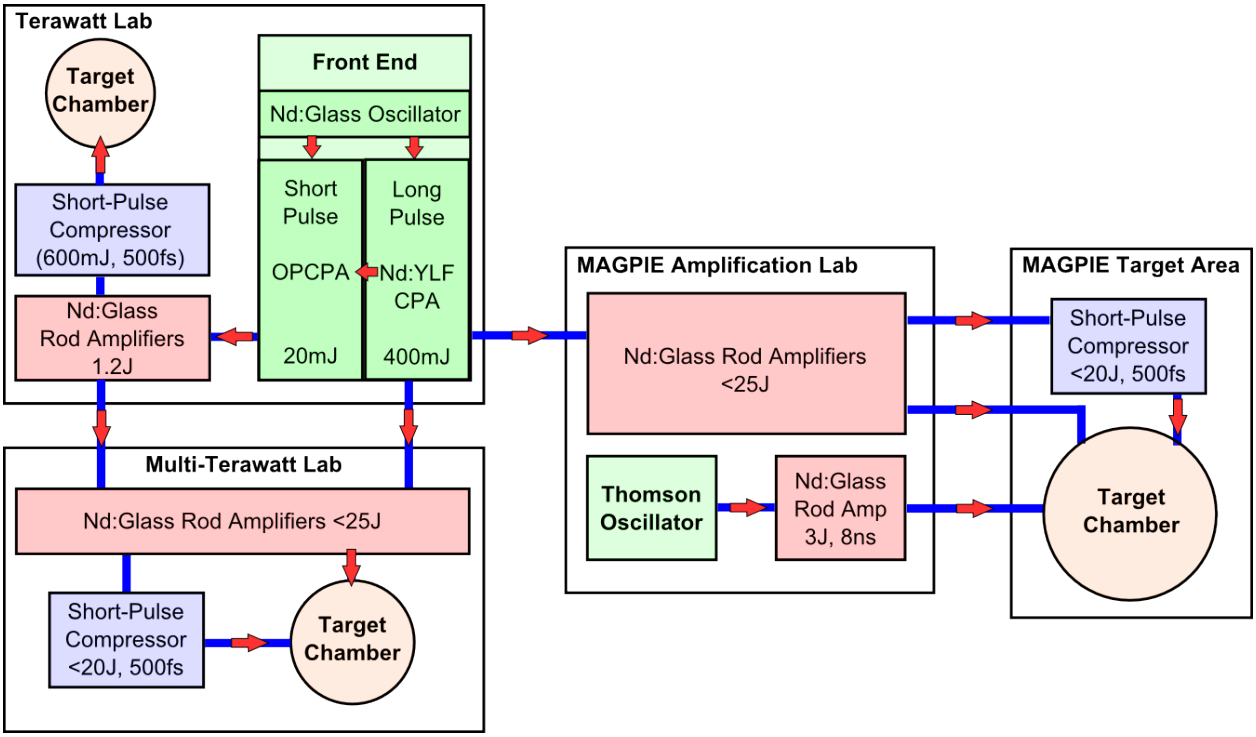


Figure 2.3: Laboratory layout of the Cerberus laser system and target areas. Pulses are generated in the "Terawatt Lab", which houses the OPCPA front-end, long-pulse Nd:YLF CPA laser, that also is used to pump the OPCPA stages, and up to 16 mm aperture Nd:Glass amplifiers that generate up to 1.2 J pulses compressible to 500 fs. These 1.2 J pulses may be diverted with a waveplate-polariser to the "Multi-Terawatt Lab", which amplifies the light further with a single-pass through a 50 mm diameter Nd:Glass amplifier and compressed with larger aperture multilayer coated dielectric gratings that are designed to produce up to 35 TW pulses. Leakage OPCPA pump light from the Nd:YLF CPA beamline can be used as a long-pulse driver, which is amplified further with a double-pass of a 50 mm Nd:Glass amplifier for 20 J, 1.4 ns optical driver in the Multi-Terawatt lab, or up to 25 J with a single-pass of a 25 mm and 50 mm Nd:Glass amplifier in the "MAGPIE Amplification Lab" that are then guided to the MAGPIE Chamber for X-Ray backlighting or magnetic field probing of MAGPIE experiments. A stand-alone 8 ns Nd:YAG laser that is amplified and frequency-doubled to 3 J, 532 nm pulses to be used as a Thomson scattering diagnostic of MAGPIE interactions.

2.1 CHOICE OF SOLID-STATE GAIN-STORAGE LASER MEDIA

The shortest possible pulse durations are achieved with laser materials that can emit the greatest emission bandwidth. Solid-state laser gain media rely upon ion dopants and the energy transition between two energy levels in the same electron configuration, which are usually forbidden transitions in a free ion. The introduction of an ion dopant interacts via Coulomb forces to perturb the spherical symmetry of the neighbouring "crystal-field", producing configurations that allow such laser transitions to occur, especially energy transitions that involve a vibronic state change, where extra degrees of freedom in energy and momentum conservation are allowed through non-radiative phonon transitions in the crystal lattice [49]. Although allowed, the cross-section of these transitions are still small enough such that large lifetimes of the excited state, τ, are possible. The upper-state population lifetime is limited by the spontaneous emission rate and is therefore smaller in gain media with larger cross-sections and emission bandwidths, due to the greater number of routes to the ground state. The pumping method is largely determined by this parameter, where >500 μs lifetimes are well suited to diode pumping technology, flash-lamp pumping may be used between ~100 μs-1 ms lifetimes and shorter lifetimes require shorter pump sources, which typically is another laser source.

	Nd:YLF	Nd:Glass (Phosphate)	Nd:Glass (Silicate)	Ti:Sapphire
λ_0 (nm)	1053	1054	1060	660-1180
$\triangle\lambda$ (nm)	1.4	28	36	150
τ (μs)	525	361	361	3.2
σ (10^{21}cm^2)	142	34	25.4	410
κ (W m^{-1} K^{-1})	6.3	0.8	1.2	33

Table 2.1: Physical properties of common laser gain-storage media used for high-power amplification at 1054 nm central wavelength, where τ is the upper-state lifetime of the laser transition, σ is the gain cross-sectional area and κ is the thermal conductivity. Information obtained from [50] and supported by [49, 51].

The $4f_{3/2}$-$4f_{11/2}$ laser transition in the trivalent neodymium (Nd^{3+}) rare-earth ion emits around 1 μm. The optical absorption and emission bandwidth of the 4f transitions in

Nd^{3+} are strongly dependent on available vibronic transitions as well as phonon collision processes [49]. The laser emission wavelength is weakly dependent on the host medium as the size of the 4f orbital wave-function is relatively small compared to the size of the ion, producing a weak interaction with the crystal field that only slightly perturbs the energy levels of the free ion configuration [49]. For this reason, it is possible to construct a laser system using a mixture of neodymium doped gain media types to take advantage of the various benefits of different host materials, such as the closely matched 1053 nm Nd:YLF emission and 1054 nm Nd:Glass peak-emission. The 4-level laser transition is usually pumped at ~808 nm and can be either flash-lamp or diode pumped due to their >350 μs upperstate lifetimes.

The high thermal conductivity of Nd:YLF and Ti:Sapphire, typical for crystalline hosts, allows higher repetition-rates to be achieved in comparison to Nd:Glass. These host materials also provide high gain per unit length from their large cross-sectional area and are favourable for front-end systems that amplify up to ~1 J. Equally large bandwidths can be obtained from OPCPA and their potential for much improved contrast compared to gain-storage media could produce a higher quality seed for the large aperture Nd:Glass amplifiers.

The energy scalability of a laser system depends largely on the largest optics producible, which typically is limited to the amplification medium or compressor grating size and costs. Nd:Glass is a common amplification route mainly rivalled by titanium-doped sapphire (Ti:Sapphire) for generation of petawatt peak-power laser pulses. Nd:Glass (phosphate) amplifiers can be produced to sizes approaching one metre, with up to 46 cm × 81 cm at the National Ignition Facility [12], whereas the largest Ti:Sapphire laser amplifier crystals are ~10 cm in diameter [3, 52].

2.1.1 *Ti:Sapphire*

When the shortest pulse durations are required, there is little competition with titanium-doped sapphire (Ti^{3+}:AL_2O_3, or "Ti:Sapphire") from other solid state laser gain-storage media and therefore the use of this material has become the standard approach for many years for creating high-power laser systems requiring sub-50 fs duration pulses at ~800 nm central wavelength [3, 52]. However that dominance is now being challenged by OPCPA techniques, which also offer highly tunable, high gain and broad bandwidth amplification

to support bandwidths close to single optical cycles. The laser transition of the Ti^{3+} ion occurs on a single 3d-orbital electron, whose five angular momentum states/orbital shapes are strongly perturbed by Coulombic forces from the surrounding oxygen atoms in the host crystal lattice. A large technical and monetary drawback of Ti:Sapphire is its short τ = 3.2 μs excited state lifetime, a natural consequence of its large emission bandwidth and cross-section, such that achieving a population inversion requires optical pumping from another laser, most usually frequency-doubled Q-switched Nd:YAG.

The broadband emission from Ti:Sapphire permits lasing at around 1 μm wavelength, suitable for seeding larger aperture Nd:Glass amplifiers. Mode-locked oscillator sources using a Ti:Sapphire gain medium are also commercially available. These cavities are typically Kerr lens mode-locked in comparison to saturable absorption mode-locking of Nd:Glass oscillators. Both methods are capable of producing 100 fs pulses at 1054 nm central wavelength from an oscillator source producing nanojoule pulse energies.

2.1.2 *Nd:Glass*

Inhomogeneous broadening of the laser bandwidth can occur from variations of the crystal field within the material volume. This can be caused by crystal defects, impurity ions and strain points in the host medium. This is especially true for amorphous glass structures, which have no periodic crystalline structure. Various glass impurities can be added that alter the laser wavelength and emission bandwidth.

A method to counteract gain-narrowing effects in Nd:Glass petawatt laser systems uses a mix of phosphate and silicate based glass hosts, which have peak emission at 1054 nm and 1060 nm respectively [2, 51, 53]. With careful balancing of the gain from each type of media it is possible to achieve a ~1.5 factor reduction in the final pulse duration [54]. The gain bandwidth of Nd:Glass is substantially less than that of Ti:Sapphire or OPA systems, but the large apertures available and simplicity of flash-lamp pumping make Nd:Glass an attractive gain medium for >10J laser systems.

2.1.3 *Nd:YLF*

The non-linear crystals used in OPCPA laser systems require a pump laser source. Picosecond and nanosecond pumping of OPAs does not necessarily benefit from broadband

Ti:Sapphire emission. The simpler diode and flash-lamp pumping possible with Nd:YLF presents a more practical solution to developing a robust OPA pump source. Nd:YLF laser rods can be grown to high optical quality up to ~12 mm diameter, at which point the transmitted wave-front distortion becomes increasingly more prohibitive for propagation of smooth Gaussian/super-Gaussian pulses. This is true for most crystalline laser hosts, as a single crystal is usually required to prevent boundaries between crystallites that lead to wave-front distortion and scattering losses. Recent advances in polishing techniques that can correct for inhomogeneity's through the bulk have been shown to produce 100 nm ($\lambda/10$) wave-front distortion for up to 25 mm YLF rod diameters [55]. Experimental set-ups should be mindful that the material is birefringent and also has a small negative temperature dependent refractive index that will become more pronounced for multi-pass and regenerative amplifier set-ups. Nd:YLF can also lase at two discrete wavelengths of 1054 and 1047 nm in two different polarisation states, with a trade off to be made between higher gain and higher thermal defocusing at 1047nm and lower gain (by approximately a factor of two) but less problematic thermal defocus at 1053nm. The 1053nm emission is also attractive for the Cerberus system as it allows use of a single front end oscillator that can seed both the short pulse beam line and the OPA pump chain with all-optical synchronisation between the two to sub-picosecond accuracy.

2.2 NUMERICAL MODELLING OF OPTICAL PARAMETRIC AMPLIFIERS

The OPA stages in the Cerberus beamline serve as the main source of gain and bandwidth enhancement in the short-pulse beamline. The broad parameter space and complexities involved with non-linear interactions, such as pump depletion effects can be understood and optimised with numerical modelling of the non-linear interactions based around solving the coupled wave equations for optical parametric amplification. Such a code, named "OPA.FOR" here was made available by Professor Geoff New, with further refinements by Dr Katalin Mecseki [56] and the author. This model uses the "Fourier split-step method", which divides a non-linear crystal of length L into n smaller segments/steps with length L/n and each step the coupled-wave equations are solved in the temporal domain and dispersion is treated by Fourier transform in the frequency domain. The current version (v.391) is a 1D plane-wave code able to model temporal evolution of pump, signal and idler pulses through multiple stages of BBO, LBO and KDP crystals. It is able to simulate

chirped pulses, non-collinear geometry, group-velocity mismatch (GVM) and arbitrary phase, spectral and temporal intensities of the seed and pump. A range of common temporal shapes for the input pulses can be selected; including sech^2, Gaussian and super-Gaussian profiles. Being a 1D code, it does not directly handle spatial information and spatial effects of the pulses, but can be run many times through parameter scans to approximate spatial effects.

To derive the coupled-wave equations, we start by considering a plane-wave travelling in the z-direction with complex form

$$E_n(z,t) = A_n(z)\exp\left(i\left(\omega_n t - k_n z\right)\right) + c.c. \tag{2.1}$$

where the angular wave number $k_n = n_n\omega_n/c$ and n_n is the refractive index at ω_n. This plane wave is a solution of the wave equation propagating in a non-linear medium with induced polarisation P [50]

$$-\frac{\partial E_n}{\partial z} + \frac{1}{c^2}\frac{\partial^2 E_n}{\partial t^2} = -\mu_0\frac{\partial^2 P_n}{\partial t^2} = -\mu_0\frac{\partial^2\left(P_n^L + P_n^{NL}\right)}{\partial t^2} \tag{2.2}$$

where μ_0 is the vacuum permeability and we have separated out the linear and non-linear components of the polarisability to $P_n^L{=}\varepsilon_0\chi^{(1)}E_n$ and to $P_n^{NL}{=}\varepsilon_0\chi^{(2)}E_n^2$ for a second-order non-linear process. If we substitute (2.1) into (2.2), move the linear polarisation term to the left-hand side and use the slowly varying amplitude approximation $\partial^2 E/\partial z^2 \ll 2k_n\partial E/\partial z$, this equation reduces to the general simplified form [50]

$$\frac{\partial A_n}{\partial z} = -i\frac{\omega_n}{2cn_n\varepsilon_0}P_n^{NL} \tag{2.3}$$

In the case of difference frequency generation we have a non-linear interaction $\omega_p = \omega_s + \omega_i$and therefore (2.3) forms the basis of the three-coupled equations, which for plane-waves are

$$\frac{\partial A_p}{\partial z} = i\frac{\omega_p d_{eff}}{cn_p}A_i A_s\exp\left(-i\triangle kz\right)$$

$$\frac{\partial A_s}{\partial z} = -i\frac{\omega_s d_{eff}}{cn_s}A_p A_i^*\exp\left(-i\triangle kz\right)$$

$$\frac{\partial A_i}{\partial z} = -i\frac{\omega_i d_{eff}}{cn_i}A_p A_s^*\exp\left(-i\triangle kz\right) \tag{2.4}$$

and we specified an effective scalar non-linear coefficient $d_{eff} = \chi^{(2)}_{eff}/2$ that the pulse experiences in relation to its propagation to the crystal axes. These equations can be used for both sum frequency and difference frequency second-order processes. The rate and maximum efficiency of the conversion process is closely linked to this non-linear coefficient and the phase-mismatch parameter

$$\triangle k = k_p - (k_s + k_i) \tag{2.5}$$

Dispersion in optical media typically creates non-zero phase-mismatch between the three pulses and therefore forward conversion of pulses is only possible until the phases are π radians out of step. It is common to specify a coherence length that sets the maximum crystal length that should be used

$$L_{coh} = \frac{\pi}{|\triangle k|} \tag{2.6}$$

Operation beyond this point will cause the non-linear interaction to be reversed, a process we shall more generally refer to as "back-conversion". The polarisations of the different OPA wavelengths are typically be aligned to different axes in birefringent crystalline media to achieve phase-matching. "Type I" phase-matching refers to the signal and idler having the same incident polarisation, which can be perpendicular/ordinary (o) or parallel/extraordinary (e) to the optic axis. "Type II" phase-matching refers to the signal and idler having orthogonal polarisations, one ordinary and the other extraordinary.

We will now state the general analytical results from these sets of equations in the case of the low pump depletion regime. For small signal gain and assuming perfect phase-matching, the output signal intensity as a function of crystal length is [57, 58]

$$I_s(L) = I_{s0}\left(1 + \sinh^2(gL)\right) \tag{2.7}$$

where I_{s0} is the initial signal intensity and the gain factor g is given by

$$g = 4\pi d_{eff}\sqrt{\frac{I_p}{2\varepsilon_0 n_p n_s n_i c \lambda_s \lambda_i}}. \tag{2.8}$$

In the limit where the signal gain is very large, the small signal gain simplifies to

$$I_s(L) = \frac{I_{s0}}{4}\exp(2gL). \tag{2.9}$$

From (2.8) and (2.9), increasing the crystal length is more effective to increase gain than stronger pump intensities. However, the crystal length is also restricted by the coherence

length, available manufactured crystal sizes, group velocity mismatch (GVM) in the temporal domain and pulse walk-off in the spatial domain. The pump intensities are usually limited by the non-linear crystal anti-reflective coating damage threshold.

The group-velocity mismatch (GVM) between the pump and amplified field causes the signal and idler pulse to gradually walk-off in time from the pump. This also limits the temporal overlap that can be achieved to

$$\triangle\tau_{GVM} = L\left|\frac{1}{v_g\left(\omega_p\right)} - \frac{1}{v_g\left(\omega_{s,i}\right)}\right| = L.GVM \tag{2.10}$$

where $v_g\left(\omega_p\right)$ and $v_g\left(\omega_{s,i}\right)$ are group-velocities of the pump and signal/idler fields respectively. For femtosecond pulses, this can limit the crystal length to tens of micrometres and which then require higher optical intensities that are closer to the optical damage thresholds to achieve high gain factors.

Spatial walk-off from the mismatched Poynting vector $\overrightarrow{S} = \overrightarrow{E} \times \overrightarrow{B}$, which describes the direction of energy flow, is not collinear with the wave-vector. The use of non-collinear seed and pump pulses can be set up to counter Poynting vector walk-off. This also gives an added degree of freedom on the phase-matching conditions and also allows robust separation of the pump, signal and idler pulses after interaction. Non-linear conversion efficiencies are therefore generally maximised by maximising the optical intensity on the crystal, within sensible damage threshold limits/estimates, and using the minimum required crystal lengths to reduce GVM and Poynting vector walk-off. Smaller beams are more sensitive to walk-off effects. In practice, spatial walk-off is partially compensated in the Cerberus OPCPA operation by steering the pump beam for optimal gain on the seed centroid, which may result in slight reduction of overall gain but the energy distribution is centrally aligned to the remainder of the laser system that is aligned with the oscillator/seed pulse train.

It should be noted that when the pump pulse becomes sufficiently depleted, the analytical solutions become more complex [59]. Accurate modelling that takes into account all of these effects along with pump-depletion typically requires numerical analysis of the coupled-wave equations. While it is possible theoretically to approach >50% conversion efficiency to the signal for plane-wave solutions and flat-top beam profiles, real beams are Gaussian/super-Gaussian in spatial and temporal profiles with intensity modulations/non-uniformities that reduce the total efficiency. Additionally, broadband amplification does not necessarily align well with maximum energy gain, as we shall see in the following

section. The 1D OPA modelling with inferred 2D effects from OPA.FOR therefore serves best as a tool to understand and optimise the OPA pulse and crystal experimental parameters that does not necessarily completely predict overall energy efficiency because of the lack of 2D/3D modelling capability, which are far more computationally intensive (approximately 30 seconds for 1D model versus potentially many hours for a 3D model).

2.2.1 *Pump Depletion Effects*

An ideal laser amplification system should produce maximum energy extraction and bandwidth from the available pump source with high energy stability, where <1 % is typically desirable for reproducible laser-matter experiments. In OPCPA, these output characteristics are significantly affected by the level of pump-depletion i.e. when the amplification to the signal pulse changes the shape of the pump pulse. At high levels of pump-depletion, the amplified signal approaches and exceeds the local electric field intensity of the pump pulse. Such a regime exists when the energy difference between the input pump and seed intensity is less than the small-signal gain of the amplifier. This is illustrated in figure 2.4, where the pulses are temporally overlapped and the available gain causes the intensity centre of the signal to exceed the local pump intensity.

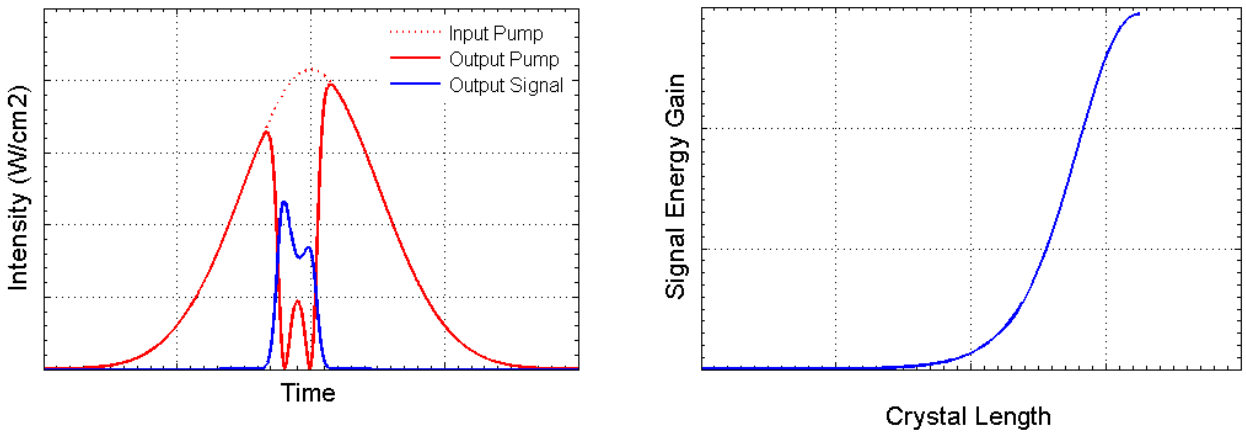


Figure 2.4: Excessive gain of the signal pulse in an OPA results in back conversion from the peak of the signal to the pump. This creates a dipped Gaussian pulse shape that will Fourier-transform to a pulse pedestal after compression and therefore generally avoided in the OPCPA process, except in the case where a dipped spectrum is created in the front-end that is "filled" to counteract gain-narrowing effects in subsequent amplifier stages.

At this point, where the signal has extracted the maximum available energy from the pump, the non-linear process "slows down" and then begins to "back-convert" towards

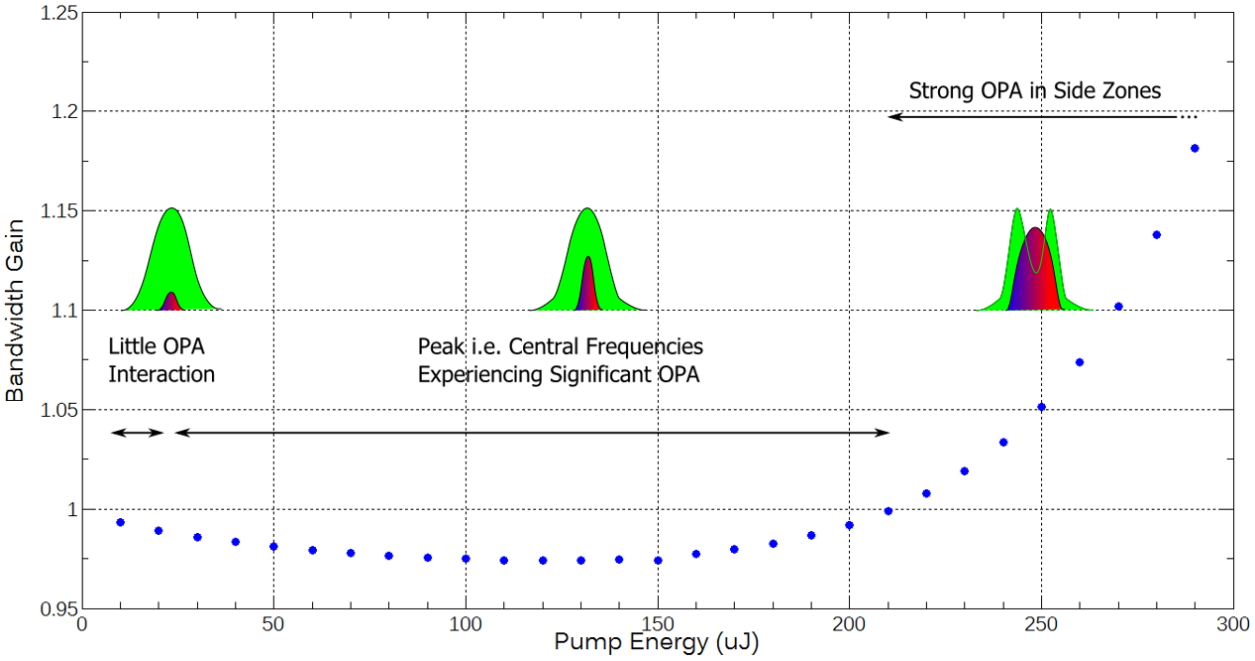


Figure 2.5: Pump energy versus bandwidth gain in an OPCPA stage for Gaussian temporal profiles in the pump and seed, demonstrating the potential benefits to be gained from pump deletion of OPCPA stages, leading to increased bandwidth at the output as well as high gain. At moderate-high pump depletion, the gain in the pump intensity centre slows down, whilst the gain in the wings continues to increase, creating bandwidth amplification.

re-amplification of the pump field, producing modulations onto the amplified signal envelope. In the case of chirped seed/signal pulses, the additional spectral modulations from such an effect will Fourier-transform upon compression to produce short-range pedestals and therefore such effects are generally best avoided in the OPA process.

It is straightforward to see that increasing pump-depletion directly increases signal gain. Non-uniform gain profiles in either the temporal or spatial domain under pump-depletion can produce bandwidth broadening modes of operation that are also highly stable with respect to energy input. We first address bandwidth enhancement with Gaussian pump pulses longer than the chirped seed pulses, such that the seed experiences more uniform gain across the Gaussian peak of the pump pulse, rather than across the entire Gaussian envelope. We have modelled this by linearly increasing the pump energy, which exponentially increases the small signal gain, as shown in (2.8), which in turn increases pump depletion.

For low-depletion pump intensities the non-uniform pump profile produces greater gain at the temporal centre and therefore narrows the signal spectrum. With greater pump

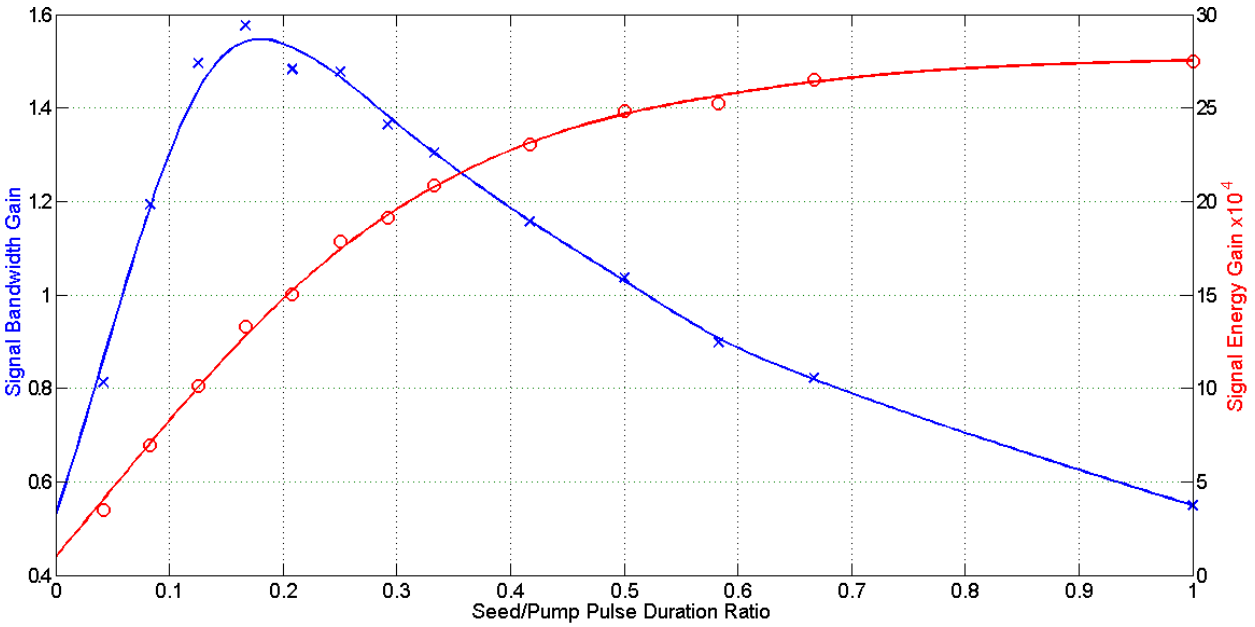


Figure 2.6: Seed chirp optimisation of the amplified signal bandwidth blue cross and line and energy red circles and line for a pair of OPAs operated at maximum pump-depletion and calculated using the OPA.FOR numerical model. Optimal bandwidth amplification exists when the pump pulse are ∼5x longer than the seed pulses whilst increasing seed duration increases energy extraction at the expense of reduced bandwidth enhancement.

intensity, not only do the temporal/spectral OPA signal wings experience significant gain but the envelope centre experiences a slowdown in gain as the signal and pump intensities become comparable, with a net effect of creating bandwidth amplification and the potential to recompress to a shorter pulse duration.

For longer seed pulses, the signal interacts across a larger section of the Gaussian pump envelope. The chirped seed bandwidth towards the temporal edge of the pulse experiences less gain and therefore less bandwidth is able to be amplified. Using seed pulses that fill the available gain window of the pump also improves energy extraction and therefore we can optimise the OPAs between bandwidth and energy gain. For seed pulses that have little or no chirp the temporal broadening of the pulse in the pump-depletion regime directly reduces the transform-limited duration and bandwidth and therefore direct OPA without chirped seeds cannot utilise the benefits of pump-depletion. Figure 2.6 shows modelling results demonstrating optimisation of the chirped seed duration with a fixed pump pulse duration operated at maximum pump-depletion before the onset of back-conversion.

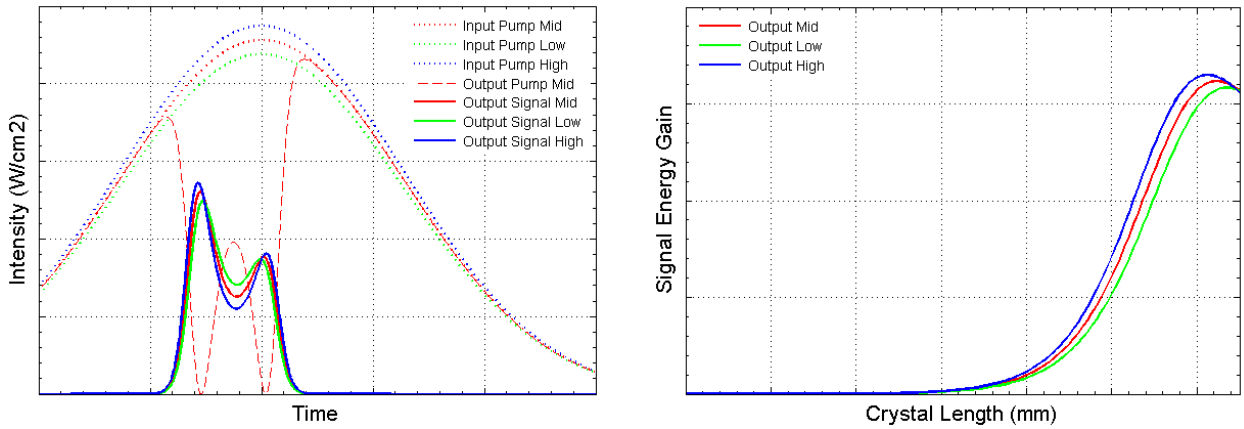


Figure 2.7: Example of over-saturation of the OPA signal produces a region of signal energy gain stability against fluctuations in the input pulse intensities. (Left) Pump and signal time profiles showing equal rise in the wings to decreasing central intensity from back-conversion to the pump for low, normal and high pump (±4%) and signal (±2%) fluctuations. (Right) Signal energy gain as a function of fluctuations in the pump and signal converges towards a common central point.

Just beyond the point of maximum signal gain is a regime where fluctuations in the pump input intensity create very little effect on the output signal intensity. We have modelled this in figure 2.7, with 4% variations in pump energy and 2% variation in seed energy. This is due to almost equal and opposite changes in energy between the wings and back-converting pulse centre. As the amplified signal envelope will be modulated with back-conversion at this point, the Cerberus OPAs are operated close to this point such that back-conversion is not seen on the measured spectra but their performance still benefits from stable operation close to this high-stability point.

The Cerberus short-pulse front-end uses two second harmonic processes to generate picosecond and nanosecond duration pump pulses used to drive four OPA stages. Therefore, the ability to operate in a highly stable regime is critical to minimise fluctuations in energy and bandwidth from multiple cascaded non-linear processes. Pump depletion is therefore a desired process as part of the non-linear amplification that is able to overcome the gain narrowing limitations with gain-storage amplification but also for efficient and highly-stable energy extraction from the pump source.

2.3 PULSE DURATION MEASUREMENTS WITH A SINGLE-SHOT AUTOCORRELATOR

Direct measurement of pulse durations with electro-optic detectors such as photodiodes are unable to accurately determine <100 ps pulse durations. Optical autocorrelators typically utilise one of the non-linear processes described in (1.12) to produce an intensity dependent optical response that is measured as a function of time delay i.e. optical path length, by an alternative observable e.g. frequency-conversion, polarisation rotation, refractive index change. For measurement of the Cerberus laser pulse durations we show in this chapter, a single-shot second-order autocorrelator is described. This uses the second-order non-linear process of second-harmonic generation from spatial and temporal overlapping of two copies of the input pulse in a non-linear crystal and scanned temporally across each other. As one of the pulses is scanned in time, usually a micrometer translation stage, it produces a second harmonic autocorrelation of response equal to

$$I_{ac}(t) = \int P(t)\, P(t+\tau)\, dt. \tag{2.11}$$

The autocorrelation signal is at a maximum when time delay $\tau = 0$ and is a symmetrical process in positive and negative time delay that therefore does not allow one to discern a time-axis direction. Scanning autocorrelators can either use a non-linear crystal or two-photon absorption in semiconductor photodiodes, whose band-gap is larger than the single photon energy at the fundamental laser wavelength but smaller than the second-harmonic photon energy, to produce a direct electrical response that can be read by an oscilloscope [60].

Scanning systems become less practical for lower rep rate, 10 Hz or single-shot, characterisation of systems such as Cerberus. An alternative geometry can be adopted that uses the crossing of the two pulses in a non-linear crystal that produces a spatially dependent temporal overlap of second-harmonic generation. The SHG signal can then be imaged onto a camera to provide a pulse duration measurement after deconvolution of the SHG signal, typically a $2^{1/2}$ factor for Gaussian pulses. The time axis can be calibrated by producing a known temporal delay e.g. a 30 μm optical delay on one of the arms using a micrometer translation stage corresponds to a 100 fs delay, shifting the intensity correlation signal maximum on the camera.

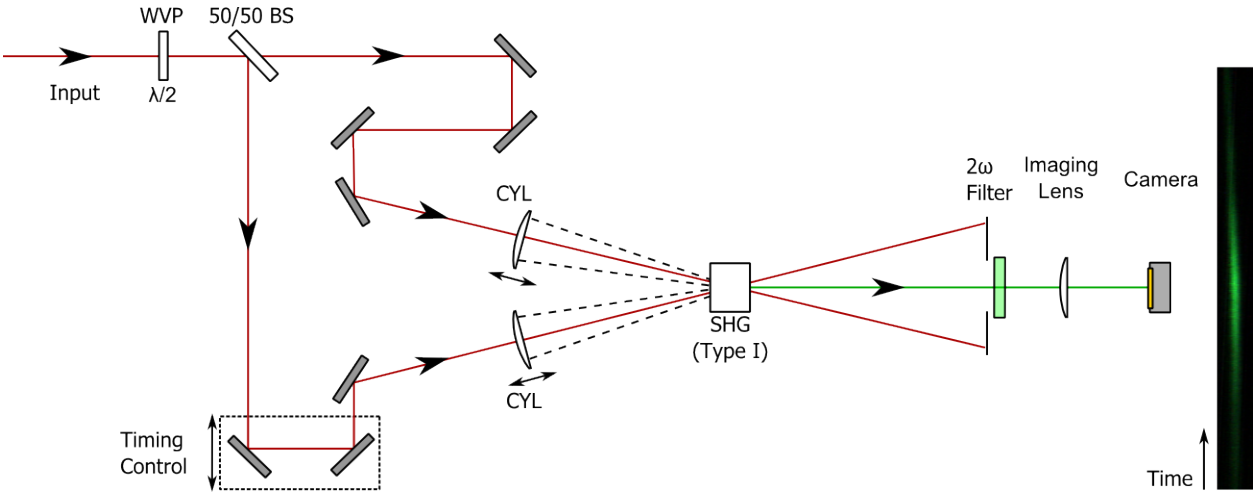


Figure 2.8: Optical layout of a single-shot second-order autocorrelator. The input pulse energy is split with a 50/50 polarisation-insensitive beam splitter with equal path lengths that are non-collinearly focused with cylindrical lenses (CYL) into a non-linear second-harmonic generation phase-matched crystal. The crystal and its second-harmonic autocorrelation signal is imaged onto a camera, which can be calibrated by adding a known temporal delay to one of the input arms.

The non-linear crystal is usually chosen to have large non-linearity and a broad phase matched bandwidth. The crystal can be tuned to achieve optimal phase-matching for a particular set of frequencies, however dispersion can prevent phase-matching across the broad bandwidth. The phase-matched SHG intensity can be shown to be [50]

$$I_{SHG}(L) \propto \left(\frac{d_{eff} I_1}{2}\right)^2 sinc^2\left(\frac{\triangle kL}{2}\right) \tag{2.12}$$

where I_1 is the input field intensity and L is the crystal length. The sinc-squared half-maximum values occur when $\triangle kL = 1.39$ and the FWHM phase-match bandwidth is given by

$$\triangle\lambda = \frac{TBP.\lambda^2}{cL.GVM} \tag{2.13}$$

For the Cerberus single-shot autocorrelator a 1.5 mm thick beta-barium borate (BBO) non-linear crystal provides 12.3 nm of phase-matched bandwidth, which is applicable for measuring pulses as short as 150 fs.

2.4 OPTICAL DAMAGE MECHANISMS

The generation of high-power laser pulses inevitably leads to optical intensities close to the material damage thresholds that bulk materials and optical coatings can handle before being irreversibly damaged. It is therefore necessary to identify these damage thresholds and underpinning physical mechanisms throughout the entire laser system design, with particular attention to the OPA pump laser amplifiers and the pump intensities on the OPA crystals.

For Gaussian laser pulses with a measured FWHM pulse duration $\triangle t$, energy J and $I = {}^{I_{peak}}/_{e^2}$ Gaussian beam radius $w(z)$, the peak-intensity is calculated as

$$I = \frac{0.94}{\triangle t} \frac{2J}{\pi w(z)^2} \tag{2.14}$$

Additionally, for applications that focus the laser light onto a material e.g. autocorrelators and the high-power laser-matter interaction, the ideal diffraction limited spot waist at the focus of a lens for a Gaussian beam can be calculated using the relation

$$w(z = f) = \frac{f\lambda}{\pi w(0)}. \tag{2.15}$$

Where f is the focal length and $w(0)$ is the Gaussian beam waist at the entrance of the focusing optic. For real beams, the focal spot will typically be aberrated e.g. spherical aberration using low f-number lenses or astigmatism from imperfect alignment through singlet lenses, and therefore the real focal spot can be imaged onto a camera if more precise laser beam characterisation is required.

The damage threshold for any medium will be dependent upon the wavelength and pulse duration. Empirical studies by Stuart et al. measured the damage thresholds for surfaces of a variety of dielectric media with varying pulse lengths and determined a strong $\tau^{1/2}$ scaling from nanosecond to picosecond pulse durations in dielectric media [20].

The damage threshold below 10 ps was found to deviate from this empirical scaling law due to a shift in the dominant mechanism responsible for damage. For pulses above 10 ps, the photon energy is able to be absorbed by the lattice phonons of the medium, leading to local heating and the potential for damage by melting or boiling of material. Below this pulse duration, the energy is deposited into the material too quickly to be absorbed by the lattice and instead instantaneous non-linear multi-photon ionisation processes of outer

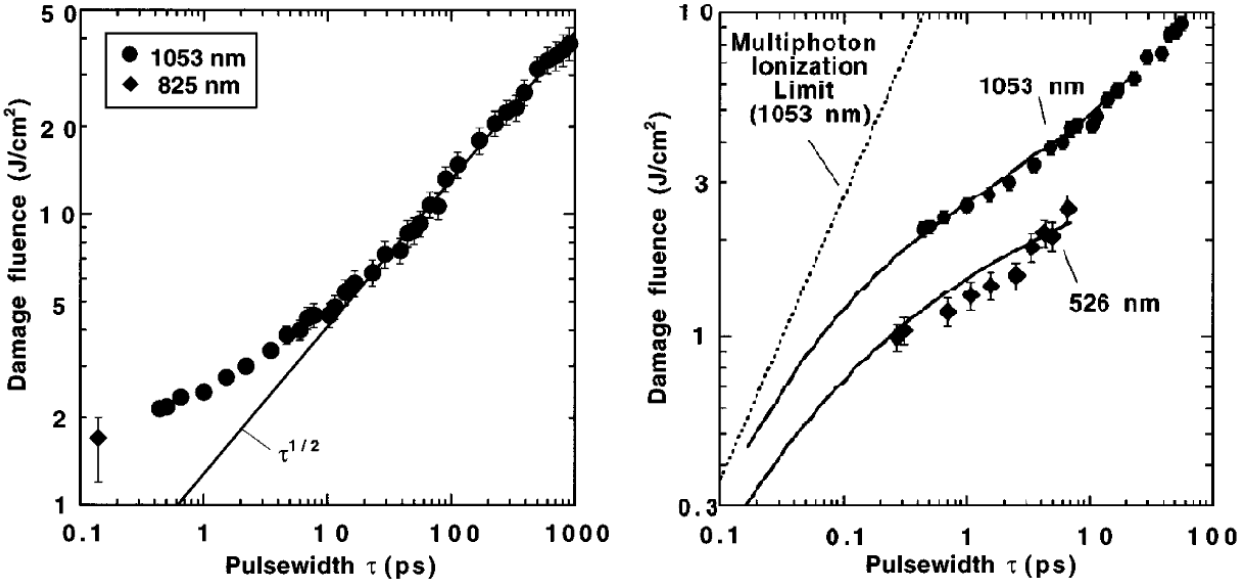


Figure 2.9: Image extracted from [20].(Left) Fused silica damage fluencies for varying time duration pulses showing the deviation from $\tau^{1/2}$ for pulses shorter than 10 ps due to onset of multi-photon ionisation. (Right) Damage fluence relationship between different wavelengths common to the Cerberus OPA setup, where 1053 nm damage fluence is approximately double 526 nm light.

electrons becomes dominant, with prompt ionisation and plasma formation causing damage rather than thermally driven processes. From this empirical study we can determine the damage threshold with any pulse duration $\triangle t_2$ between hundreds of femtoseconds to tens of nanoseconds incident upon dielectric media as long as it has been measured at any other pulse duration $\triangle t_1$ between this range, typically 1 ns-20 ns, 1064 nm (Q-switched Nd:YAG lasers outputs),

$$D\left(\triangle t_2\right) = D\left(\triangle t_1\right).f\frac{\lambda_1}{\lambda_2}\sqrt{\frac{\triangle t_1}{\triangle t_2}} \tag{2.16}$$

where $D\left(\triangle t_1\right)$ is the reference damage threshold data and f is a proportionality factor for pulses shorter than ~10 ps to be decided from 2.9. This scaling law is particularly useful for estimating the performance of optical coatings such as mirrors surfaces and anti-reflection multi-layers which usually represent the lowest damage threshold elements of the laser system.

2.4.1 *Self-Focussing (B-Integral)*

Where the laser pulse passes through bulk optical material at high-intensities, e.g. a laser rod or OPA crystal, an additional damage mechanism must be taken into account. All materials have non-zero odd susceptibilities that produce third-order non-linear responses at strong optical intensities. Terms of the original plane wave form $A\cos(\omega t - kz))$ in (1.14) are linked to the refractive index of the material $n_0 = \sqrt{\varepsilon/\varepsilon_0} = \sqrt{1+\chi^{(1)}}$, where ε is the material electric permittivity. The third-order term in (1.12) identifies an intensity-dependent change of the local refractive index, the optical Kerr effect, experienced by the electric field of the laser pulse as

$$n = n_0 + n_2 I \tag{2.17}$$

where $n_2 = {}^3\chi^{(3)}/2n_0^2\varepsilon_0^2$ is a material property. When propagating a distance L through a medium, the phase accumulation from the non-linear refractive index is

$$\phi = B = \frac{2\pi}{\lambda}\int_0^L n_2 I(z)\,dz \tag{2.18}$$

that is known as the 'B-Integral', B for "break-up". For intense beams the variation of B can be quite large in small spatial regions. This typically causes the wave-front to converge towards a spherical form i.e. one which focuses, as visualised in figure 2.10, which avalanches the effect from increasing local intensity of a focused beam.

Phase accumulation can be reduced by lowering the pulse intensity either temporally through the use of longer chirped pulse durations or by expanding the beam spatially, which requires larger, more expensive optics. Local defects created in the beam e.g. aperture clipping and diffraction rings from dust particles or material defect, create large vari-

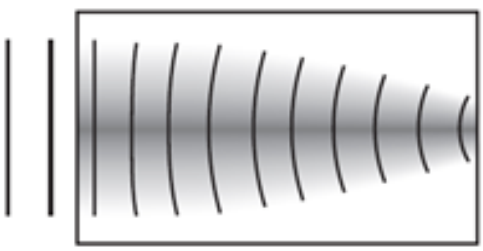


Figure 2.10: Self-focussing of an intense Gaussian pulse from non-linear refractive index. The intensity centre accumulate more phase/refractive index than at the edge, producing a lensing effect that will eventually damage optics.

ations in the local intensity, which will create local areas of self-focussing known as "hot-spots".

A general rule for laser design is to keep the B integral below 1 radian for good compression and reliable tight focussing of the pulse [49] and below π radians to avoid catastrophic damage to optical components from self-focussing effects. The total B-integral for a laser system can be greater than 10 radians but regular spatial filtering after each amplification stage can remove high spatial frequency content of hot-spots and attenuates the onset of self-focussing wave-fronts.

2.5 MODE-LOCKED ND:GLASS MASTER OSCILLATOR

The Cerberus laser system uses a commercial saturable absorber mode-locked Nd:Glass oscillator (Time-Bandwidth GLX200HP [61]) that produces 5 nJ, 250 fs pulses with stable central wavelength tunable between 1050-1056 nm, which is set to 1053.5 nm as a compromise between seeding the 1053 nm Nd:YLF OPCPA pump chain and the 1054 nm design wavelength of the short-pulse optical system.

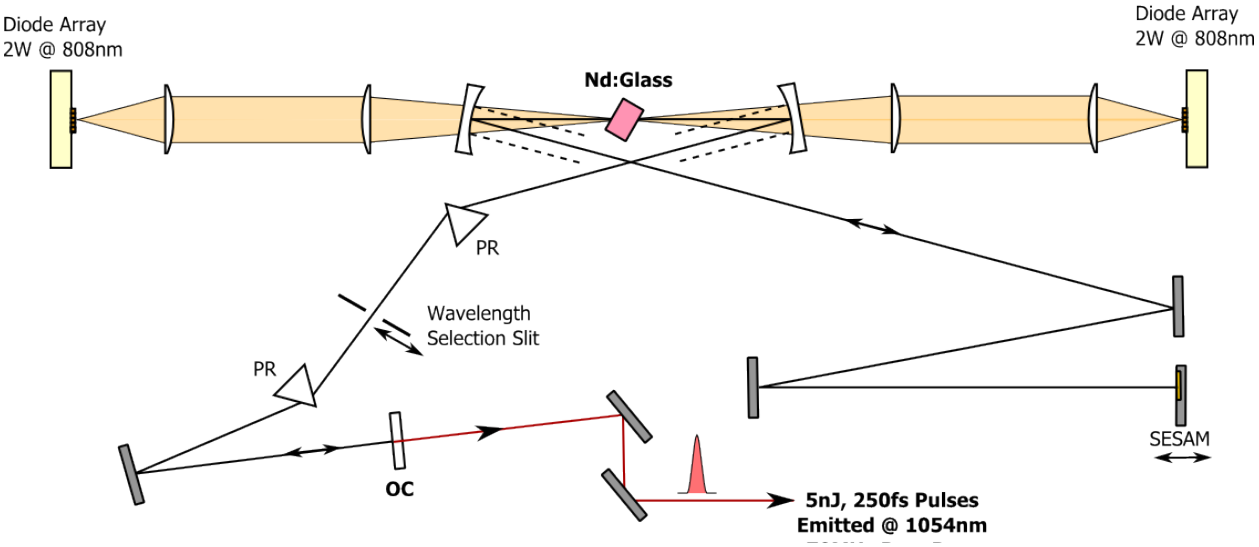


Figure 2.11: Optical layout of the SESAM mode-locked Nd:Glass laser oscillator that seeds the Cerberus laser system.

The optical layout of the cavity is shown in figure 2.11. The output from two individual 2 W, 804 nm central wavelength laser pump diodes are collimated and focused into either side of an Nd:Glass slab a few millimetres thick positioned at Brewster's angle, which minimises Fresnel reflection losses from uncoated surfaces that allow higher damage threshold operation. Continuous pumping will produce steady spontaneous emission

in all directions, with a portion of this within the alignment tolerance of the oscillator cavity that will then be successively amplified with each round trip. It should be noted that the ASE emission is strong enough to align the cavity.

The cavity is formed from two concave mirrors placed either side and a focal length away from the Nd:Glass slab gain medium to collect and collimate this ASE emission. At the rear of the cavity is a semiconductor saturable absorber mirror (SESAM), which has an intensity dependent reflectivity from the finite availability of valence electrons that absorbs the low-power light slightly more efficiently than high-power light [62] and is described further in chapter 4. Towards the front side of the cavity an adjustable prism pair controls the group velocity dispersion accumulation in the cavity that is optimised by monitoring the bandwidth and a variable slot in the dispersed beam between the prisms provides control of the central wavelength.

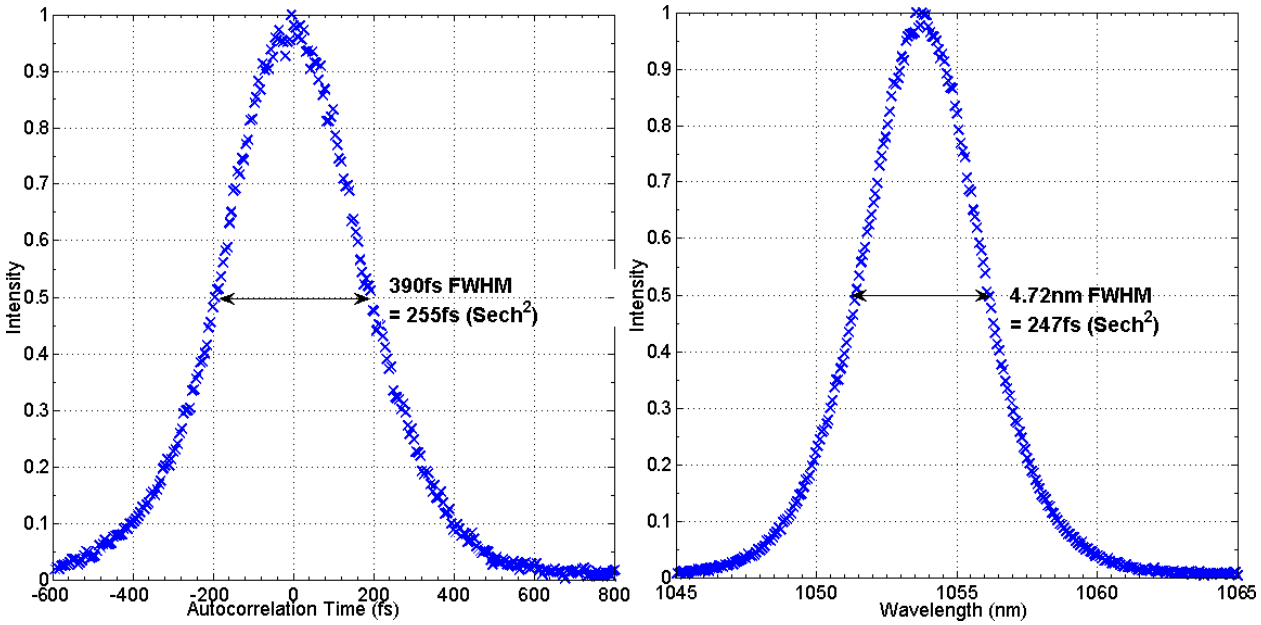


Figure 2.12: Measured single-shot second-order autocorrelation (left) and spectrum (right) of the mode-locked 1054 nm pulses from the Cerberus Nd:Glass oscillator (Time-Bandwidth Products GLX200HP). Pulses as short as 255 fs have been measured, which are very close to the transform limit of the emission bandwidth.

Pulses as short as 255 fs have been measured with 4.7 nm bandwidth. With careful optimisation 5.2 nm has been achieved and as little as 3.5 nm is produced after long periods without maintenance (typically several months) as the power in the cavity gradually falls from misalignment, dirty optics or pump diode degradation. Fortunately, the OPA stages are relatively insensitive to the input seed bandwidth and can easily recover any lost bandwidth.

2.5.1 *Optical Stabilisation for Low-Drift OPCPA Synchronisation*

The OPCPA seed from the Nd:Glass oscillator must be timed within a few picoseconds of the ps-OPA pump to obtain gain. This is achieved by seeding the pump optics chain with an earlier oscillator pulse and then selecting a later pulse for the OPCPA seed in the 70 MHz oscillator pulse train, as the short-pulse beamline has significantly less optical path than the pump beamline. Pulse selection is achieved using a half-wave Pockels cell and polariser. Fine tuning of the temporal overlap is then achieved from adding/removing optical path and micrometer translation stages on the pump beamline to achieve absolute overlap in the OPA crystals. A common oscillator allows highly robust optical synchronisation between the pulses, which would be very difficult to achieve using electronic synchronisation between two independent oscillators.

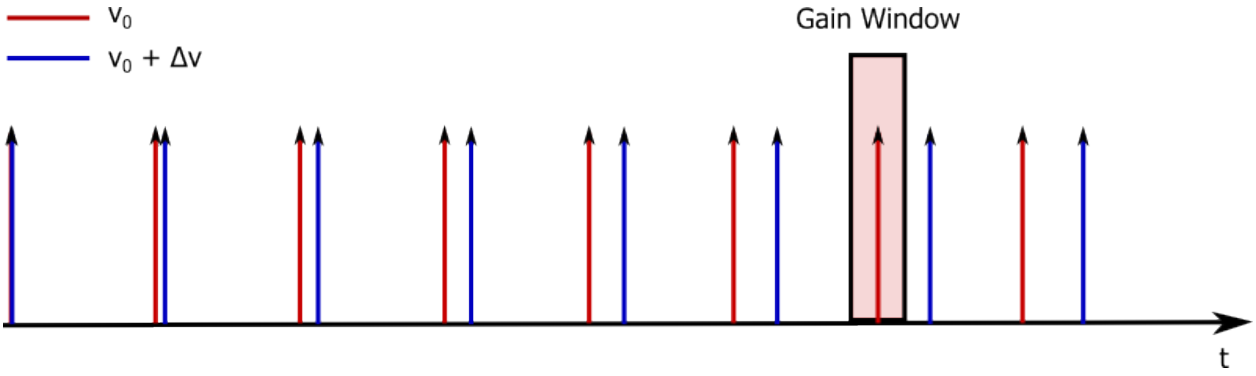


Figure 2.13: A cartoon showing how frequency drift of the oscillator shifts the temporal overlap when selecting different pulses from the oscillator pulse train for the seed and pump pulses. A frequency drift of $\triangle\nu$ is shown to shift the relative timing outside the "Gain Window" of the OPA.

Long-term drift between the pump and seed is still possible if the repetition rate of the master oscillator is not well stabilised from temperature changes of the cavity optics, which generally rise throughout the day from the laser pump diodes and the lab temperature. The Cerberus ps-OPA temporal gain window is defined by the pump pulse optical path length from the initial seed/pump split. The OPA temporal overlap is then aligned at oscillator repetition rate ν_0, where a later pulse in the oscillator train is used to achieve temporal overlap. The OPCPA pump and seed are temporally separated by $n\left(1/v_{rep}\right)$, where n is the number of pulses separating the pump and seed and v_{rep} is the repetition rate of the oscillator pulse train.

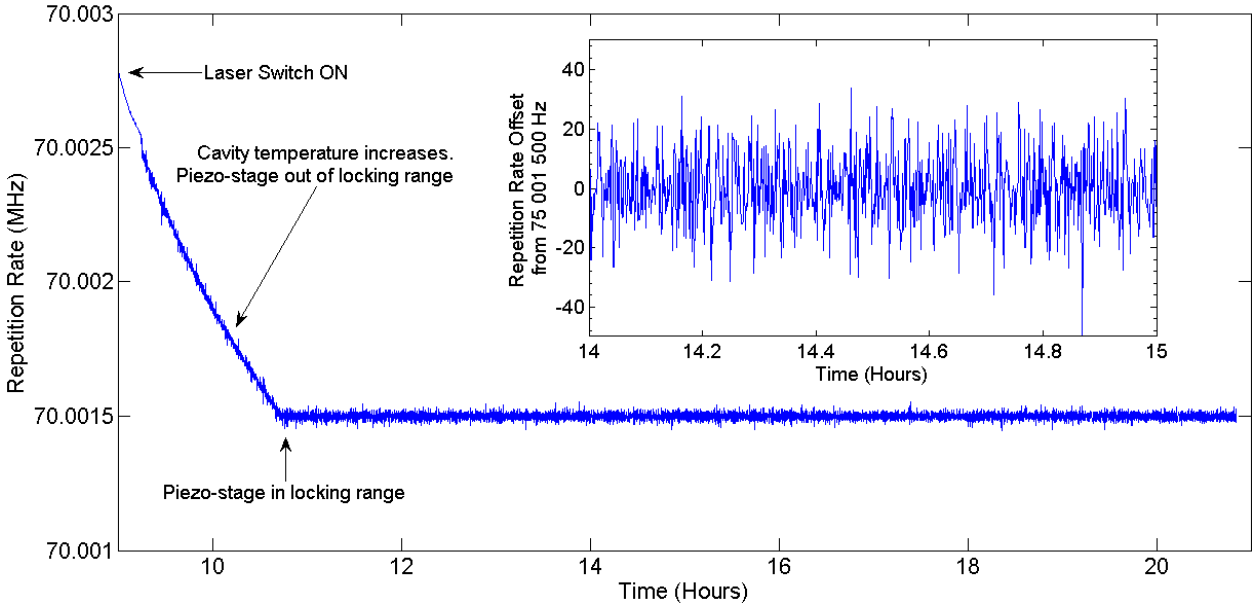


Figure 2.14: Cerberus Nd:Glass oscillator frequency locking stability over a full operational day period. After initial switch on at the start of the day, a sharp temperature rise lowers the oscillator repetition rate closer to the locking range of the piezoelectric stage. Once within range, after ~1.5 hours, the repetition rate is locked with 70,001,500±10 Hz stability. This initial warm up period is a consequence of non-optimal heating control of the temperature stabilisation, as the laser diodes significantly increase the ambient temperature of the cavity. This is an acceptable mode of operation given the approx. one hour warm up time of the Nd:YLF regenerative and power amplifiers, but has since been improved by addressing a problem with the temperature control system.

For the Cerberus OPCPAs, $n \cong 50$, which accommodates the from the regenerative amplifier and multi-pass amplification of the pump pulse with ~10^7 gain. Therefore, a frequency drift of 70,001,500±500 Hz is sufficient to offset the OPA gain window by 5.4 ps, which would significantly affect the ps-OPA gain with ~6 ps FWHM pump pulse durations. In addition to active temperature stabilisation of the cavity (retrofitted to the GLX200HP by Imperial College), the cavity repetition rate is continuously monitored on a photodiode and frequency counter (Stanford Research Systems SR400) and the cavity length readjusted with a cavity mirror mounted on a piezoelectric driven translation stage. This currently achieves a stability of 70,001,500±10Hz or better i.e. 90 fs random drift between the pump and seed, which is sufficient to maintain robust synchronisation of the 6 ps pump of the ps-OPAs.

The electronic triggering system that synchronises the laser system amplifiers, Pockels cells and diagnostic equipment is derived from the laser repetition rate signal that is

monitored against a rubidium atomic clock timing module (Stanford Research Systems DG645, Rb timebase option). Equipment such as streak cameras that require triggers hundreds of microseconds to tens of nanoseconds in advance will be fundamentally limited to a triggering jitter of order 15 ps per 100 μs trigger delay from the locked repetition rate stability.

2.6 PICOSECOND PUMPED OPAS

The first demonstrations of OPCPA front-ends used for seeding Petawatt lasers performed amplification solely with nanosecond duration pump pulses with more than 10^7 gain [2, 4]. However, these systems reported 10^6-10^8 intensity contrast to the nanosecond duration pedestals attributed to parametric fluorescence from these amplifiers [29, 30, 63]. Limiting the parametric fluorescence generation to a narrower temporal window with picosecond pumped OPAs has been experimentally demonstrated by Dorrer et al. on the Omega EP system in the US and by Musgrave et al. on the Vulcan laser in the UK and has been shown to significantly reduce the nanosecond fluorescence pedestal to achieve >10^{10} contrast from the 10^4-10^5 gain using picosecond pump pulse duration OPAs (ps-OPAs) [29, 64].

The Cerberus laser uses pre-amplification with ps-OPAs with optically locked generation of high energy pump pulses using regenerative amplification in diode-pumped Nd:YLF, a technique broadly similar to the methods used by Dorrer and Musgrave et al. We demonstrate independent numerical modelling and experimental optimisation for the Cerberus ps-OPA stages as a high-contrast amplification technique, which we detail in chapters 5 & 6.

2.6.1 *OPA Pump Beamline*

The signal gain, beam quality, pulse bandwidth and energy stability of an OPCPA laser system are all critically dependent upon the quality of the pump pulses. A 400 Hz component of the ~70 MHz pulse train from the short-pulse Nd:Glass oscillator is used to seed the Nd:YLF pump beamline. These pulses are first stretched by a four-pass folded Martinez stretcher with 2.8 m total effective grating separation, using a 1740 lines/mm

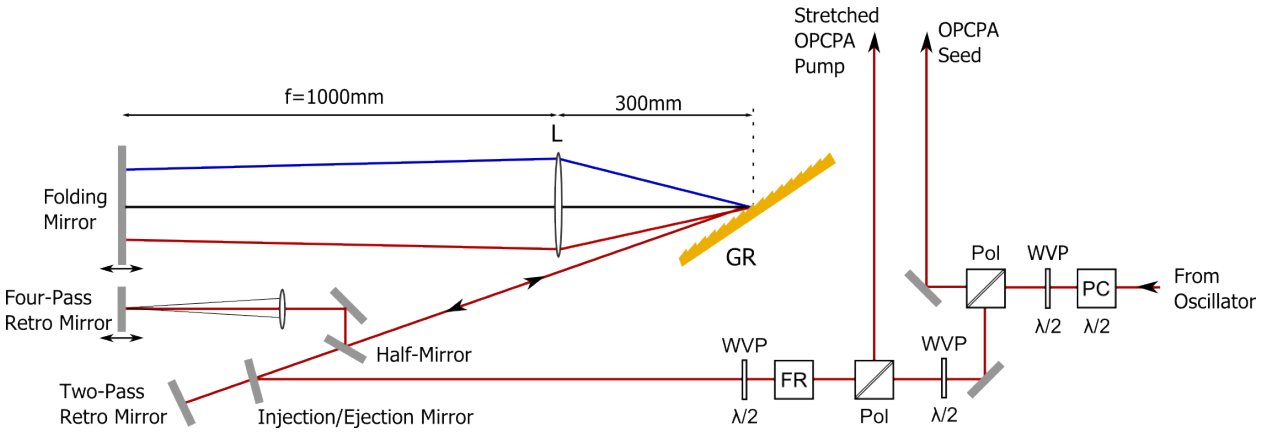


Figure 2.15: Optical layout of the OPCPA pump regenerative amplifier stretcher. After seed/pump pulse selection from a Pockels cell, pulses are incident onto a folded geometric four-pass Martinez grating stretcher configuration. Pulses enter "low" and the first pass exits "high" from vertical translation of the imaging lens L. A retro-periscope mirror behind the injection mirror adds a small vertical translation upwards to the retro-beam, which causes the second pass to exit lower than the initial injection beam. A half-mirror picks off this lower ejected beam and an image inversion using a singlet lens and a normal incidence mirror at the focus aids collimation over the long traversal length as well as producing more uniform output through partial cancellation of asymmetric stretcher optic aberrations. The mirror at the focus sends the whole process in reverse, producing a four-pass stretcher. The output is separated from the spatially overlapped input by a Faraday isolator assembly.

gold holographic reflective diffraction grating (Spectrogon) at 70.2°incidence angle. From use of (1.10), this produces a 147 ps/nm chirp.

The stretched pump pulses are then injected by a Pockels cell, triggered at 400 Hz, and polariser into a linear regenerative amplifier cavity, which uses a CW diode-pumped 3 mm rod diameter Nd:YLF module (Northrop Grumman RBA35-1C2, a-cut, 0.9% doping) operating at 1053 nm amplification.

The Nd:YLF gain bandwidth is much narrower than the Nd:Glass oscillator, causing significant gain narrowing of the ~4 nm oscillator pulses to produce ~0.4 nm after amplification to ~3 mJ from 43 round trips in the regenerative amplifier, with a single-pass gain of ~1.25. Typical energy stabilities of <1% are achieved and up to 0.3% standard deviation over 500 pulses has been observed. Optimal operation of the amplifier is found by increasing the number of round trips for a given diode current, chosen to be slightly less than manufacturer operating maximum to maximise the diode lifetime, and observing

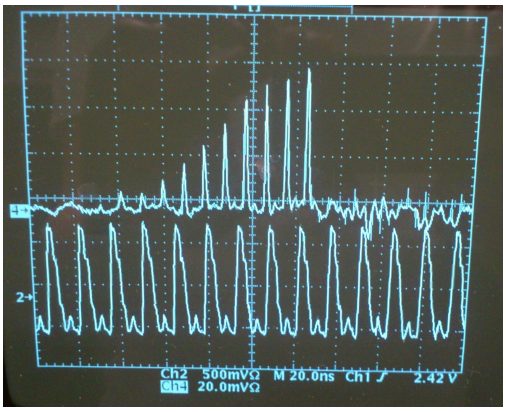


Figure 2.16: Photodiode trace of the regenerative amplifier output monitored on an oscilloscope. Each successive round trip sees low amounts of gain and eventually saturates at ~3 mJ output. Around this saturation point the available laser gain becomes comparable to the cavity loss, producing a stable output from successive round trips. (Bottom) Photodiode trace of the mode-locked oscillator pulse train.

the saturation roll-off in the pulse energy on a photodiode trace. At the saturation point, the regenerative amplifier is much less sensitive to energy fluctuations on the seed pulses.

The regenerative amplifier cavity includes a custom low finesse (low reflectivity) intracavity etalon was fabricated to introduce a tunable co-sinusoidal loss term that can be centred on the 1053 nm peak gain of Nd:YLF. This reduces gain narrowing effects from ~0.4 nm to 0.6 nm amplified output, corresponding to ~88 ps FWHM pulses, and improves the compressibility of the output pulse for pumping the ps-OPAs. The periodicity of the co-sine loss term is a function of the etalon thickness whilst the amplitude is dependent on the reflectivity. The phase of the loss term can be tuned with small angle adjustments of the etalon, producing more pronounced gain narrowing or, in our case, suppression of gain narrowing to produce shorter compressed pump pulses for the ps-OPAs.

The anti-reflection coatings were produced in-house utilising available thermal deposition optical coating equipment. For <1% reflectivity and high-damage threshold (14 J cm^{-2}, 1.4 ns, 1053 nm), a titanium dioxide (TiO_2) + magnesium fluoride (MgF_2) coating was developed by Roland Smith that optimally achieves > 0.02% surface reflectivity. From gradual addition of thin layers of MgF_2, precise engineering of the etalon finesse can be iteratively optimised in experimental conditions, leaving only the etalon thickness to be initially decided by modelling. A 500 μm thick etalon was found to create a suitably wide spectral loss profile, whose reflectivity was then optimised experimentally by adding incremental amounts of MgF_2 (~5 nm for the smallest increments) after recording the amplified spectrum after each test.

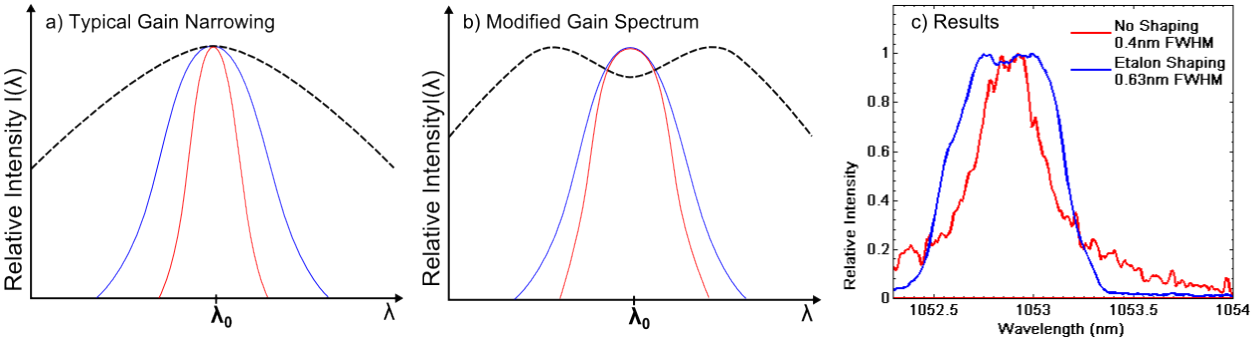


Figure 2.17: Intra-cavity etalon spectral shaping method to suppress gain narrowing effects. a) Typical gain narrowing where a (blue) seed spectrum is narrowed upon amplification (red) by a non-uniform gain spectrum (black dashes). b) Modification of the spectral gain from a co-sinusoidal modulation from an etalon reduces suppresses gain narrowing. c) Experimental results from incorporation of etalon shaper, which increased the pulse bandwidth by ~57%.

This etalon produced significant improvements in amplified pulse bandwidth from 0.4 nm to 0.63 nm with a more pseudo flat-top spectrum, which helped to improve energy saturation and hence the maximum stability of the regenerative amplifier from ~1% to <0.5% without significantly impacting the extracted output energy. Consequently, shorter compressed pump pulse durations were measured, improving the ps-OPA amplified signal gain and energy stability from 7.4% to 1.25%. Other spectral shaping methods that involved modifying the input spectrum were explored and found limited improvements in comparison. These results formed part of a publication [41].

A pulse energy of ~10 mJ is required from the Nd:YLF CPA pump beamline for injection into the first set of OPCPA stages. A flash-lamp pumped Nd:YLF amplifier with 7.5 mm rod diameter in double-pass operation was used to amplify to 30 mJ, limited to this energy from the high B-integral accumulation of the Terbium Gallium Garnet (TGG) Faraday rotator used to double-pass the YLF rod. This rotator is used to separate the input and output beams as well as setting the input polarisation for the birefringent Nd:YLF crystal. This 30 mJ output is then spatially filtered in vacuum to suppress self-focussing and remove high spatial frequencies to "clean up" beam imperfections from dust particles and minor clipping effects. This output is split by a half-waveplate and polariser combination into 10 mJ and 20 mJ pulses for the pumping the ps-OPAs and the seeding the remaining Nd:YLF amplifier chain for generation of the ns-OPA pump pulse.

The 10 mJ pulses for the ps-OPAs are compressed with anomalous dispersion from a two-pass parallel grating pair, using only a single grating in a folded geometry to reduce

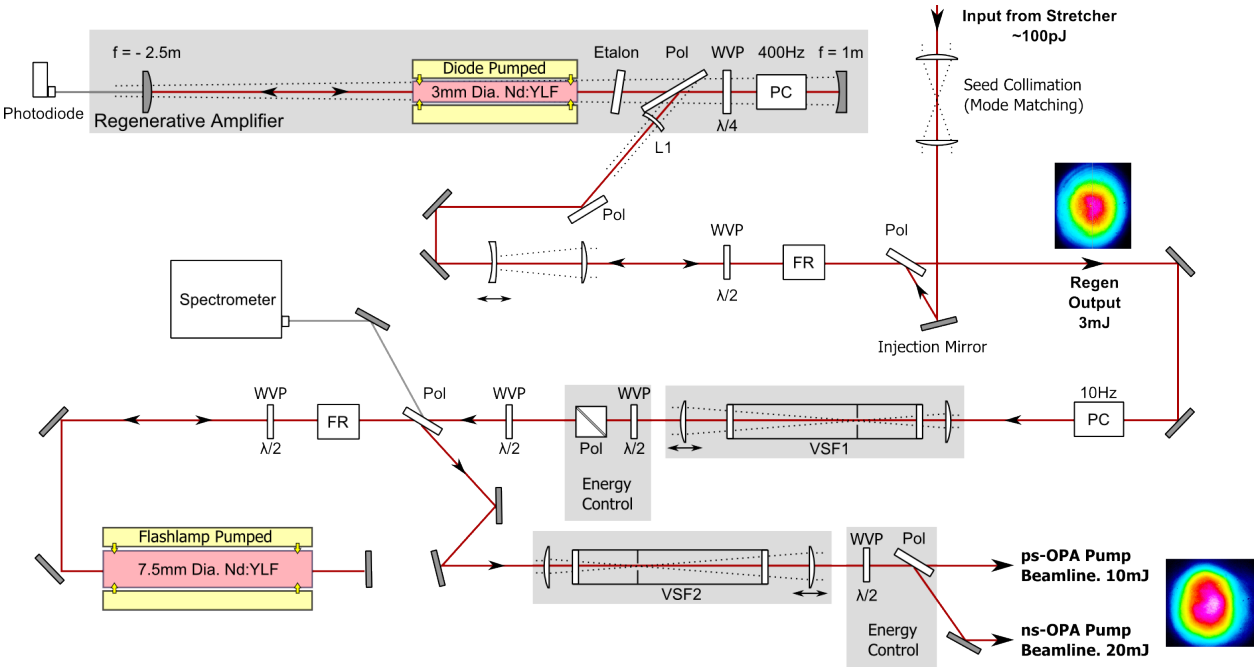


Figure 2.18: Pump Cerberus OPCPA pump beamline layout, with amplification in Nd:YLF using the stretched oscillator pulses. Pulses are amplified from 0.1 nJ to 3 mJ energy after 43 round trips inside a regenerative amplifier cavity. Pulses are injected and ejected from a Faraday isolator assembly and the B-integral kept low by expanding the amplified output pulse from the regenerative amplifier. Pulses are injected in s-polarisation and a Pockels cell selects a 400 Hz pulse train to be amplified and ejected from the cavity. The output pulses then enter a spatial filter, optional Pockels cell 10 Hz selection and static power control before injection into a double-passed 7.5 mm diameter, 10 Hz flash-pumped Nd:YLF rod amplifier to produce ~30 mJ that is spatially separated from the input beam with another Faraday isolator setup. This pulse is then spatially filtered and split into ~10 mJ and 20 mJ portions for the ps-OPA and ns-OPA pump beamlines respectively.

table space and cost. The ps-OPA pump stretcher and compressor incidence angle both use a 1740 lines/mm gold holographic diffraction grating (Spectrogon) and a minimum pulse duration of 10 ps in figure 2.19 has been measured using a scanning third-order autocorrelation, see §3.1 for details on this diagnostic.

The pulses are then frequency-doubled using a 2.5 mm thick BBO (type-I) non-linear crystal, achieving ~60% conversion efficiency to 2 mJ, 526.5 nm, 6 ps duration pulses. In figure 2.19 there exists a non-uniformity in the pulse envelope of the compressed regenerative amplifier pulse. This modulation lies outside the gain window of the ps-OPAs, which has been measured via temporal delay of the pump pulses to have an absolute width of ± 4.5 ps, with zero gain at these edges. This modulation was found to be in-

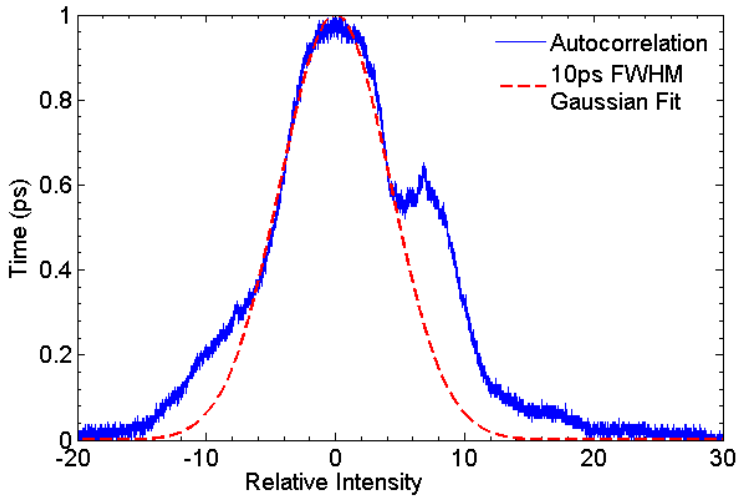


Figure 2.19: Third-order autocorrelation of the temporal intensity profile of the 1053 nm compressed pump pulses of the ps-OPAs. The asymmetry of the compressed pulse is believed to be due to the use of an intra-cavity etalon used to increase the available bandwidth of the pump pulse during amplification in Nd:YLF.

troduced from the etalon spectral shaper after third-order autocorrelations of the pulse showed no presence of these modulations with the etalon removed from the regenerative amplifier. This modulation broadens the temporal gain window for parametric fluorescence in the ps-OPAs; however, the advantages of energy stability, shorter pulse length and a flatter-topped pulse envelope outweighs this effect in this case.

2.6.2 *Picosecond OPA Results*

The design of the ps-OPAs involved extensive modelling prior to the experimental build to optimise crystal lengths, gain factors and seed chirp durations with the fixed 2 mJ, 6 ps, 526.5 nm pump pulses available from the ps-OPA pump beamline. A number of masters students over the course of several projects identified and cross-checked the required crystal lengths for the ps-OPAs and ns-OPAs [33, 34]. However, these studies did not optimise the chirped seed duration or identify optimal operation at maximum pump depletion close to the high stability point for bandwidth enhancement. In this section we present side-by-side experimental and modelling results of the ps-OPAs. These results have also contributed towards a publication documenting the ps-OPA modelling and experiment to create bandwidth enhancement in the strongly pump-depleted regime [40].

The design of the Cerberus laser system limits the gain of each amplifier to be below 10^4 to reduce parametric fluorescence generation [65] and spreads the gain across a pair

of OPAs. The first OPA is a high gain (<10^4) stage whilst the second has significantly less gain (~20) and is responsible for producing additional bandwidth and energy stability from pump depletion effects. Parametric fluorescence is further suppressed by ensuring the seed pulse slightly overfills the spatial profile of the pump.

Beta barium borate (BBO) is an ideal non-linear crystal that can provide efficient non-linear gain with a large non-linear coefficient, long coherence length and low group velocity mismatch with high damage thresholds for the phase matched wavelengths concerned with the Cerberus OPCPA front-end. Type-I interactions in BBO minimise group velocity dispersion of the pulses. If dispersive effects such as pulse walk-off become a significant degrading factor, LBO crystals offer significantly less dispersive effects, whilst still providing moderate rates of non-linear gain.

In §2.2.1 we identified bandwidth enhancement and high stability operation of OPCPA in the strongly pump-depleted regime as being a highly desirable feature for bandwidth enhancement, high energy gain and stability. We also identified suitable seed/pump pulse durations for optimal bandwidth and energy extraction. For the Cerberus ps-OPAs, the generation of a broad bandwidth is a priority to ensure good compressibility to <500 fs and therefore a chirped seed FWHM duration of 1.65 ps was chosen to provide ~1.5x bandwidth enhancement per non-linear stage.

The original design intended to use a two grating Martinez stretcher and the use of a programmable spatial light modulator at the Fourier/folding plane to address fine spectral-phase control to optimise compression and nullify higher-order phase components accumulated through the beamline. Unfortunately, the multilayer dielectric gratings (1740 lines/mm, Plymouth Grating Laboratory) purchased for this pre-stretcher were found to produce significant diffraction grating "ghosts" as a result of a ruling error periodicities in the manufacturing process [66]. Additionally, the spatial light modulator bought for this application was found to have dead pixels, rendering the instrument unusable for a high contrast system. To avoid any potential contrast impact from non-ideal diffraction gratings, a monolithic glass stretcher was designed to stretch the seed pulses to the few-ps level required for optimal seeding of the ps-OPAs.

We introduced the concept of chirped pulse amplification in §1.2.2 and showed the spectral phase can be expanded as a series of higher-order terms that correspond to the group delay (GD), group delay dispersion (GDD), and higher phase terms. Addition of GDD will create a frequency chirp that increases the pulse duration without reducing the spectral bandwidth of the pulse.

Modelling of the bulk glass stretcher started with plotting the wavelength dependent refractive index, given by the well-known Sellmeier formula

$$n(\lambda) = \left(1 + \frac{B_1\lambda^2}{\lambda^2 - C_1} + \frac{B_2\lambda^2}{\lambda^2 - C_2} + \frac{B_3\lambda^2}{\lambda^2 - C_3}\right)^{1/2} \tag{2.19}$$

where $B_{1,2,3}$ and $C_{1,2,3}$ are empirically determined coefficients. With suitable spectral resolution it is easily possible to determine the spectral phase components $\phi^{(j)} \propto {}^{\delta^j n}/_{\delta\lambda^j}$ in (1.7). The stretched pulse duration may be calculated with (1.8) whilst the distortion to the intensity envelope from higher-order spectral phase contributions were modelled via the Fourier transformation back into the temporal domain. A high refractive index H-ZF7LA (SF6 equivalent) glass block was chosen as a balance between performance and material availability, where 1.2 m of propagation though this material is required to stretch the bandwidth of a 250 fs pulse to 1.2 ps. Modelling of unwanted high-order spectral phase estimated 10^{-12} intensity temporal ripples that will be of negligible impact to contrast. This long propagation length was achieved with a four-pass of a 30 cm long glass block that has been coated with aluminium HR coatings and magnesium fluoride AR coatings, which also protect the aluminium coatings from environmental deterioration. The coated glass block allows an even number of passes. The use of a static stretcher provides a robust optical setup with a well defined chirp, time delay and high transmission (73%) in a four-pass geometry. The pulse durations for a number of passes through the stretcher were measured using a scanning second-order autocorrelator and found to agree with the modelling. The optical quality of the glass for this application was found to have internal stress that produced astigmatism on the beam profile, which has been partially corrected from in-house thermal annealing to relieve the internal stress. The residual stress still creates an effective f = -20 m cylindrical defocus in the vertical plane. At present, this astigmatic aberration has been well corrected for by tilting a telescope lens used to set the OPA1 seed size.

An optical diagram of the ps-OPA signal amplification is shown in figure 2.20. Seed pulses are first stretched to 1.2 ps with the four-pass monolithic H-ZF7LA glass block stretcher and the beam size is set with a positive-positive telescope before injection into the first 6.5 mm BBO OPA stage through a dichroic mirror/beam combiner. The pump pulses are generated with a 2 mm thick BBO phase-matched for type-I SHG, with ~65% conversion efficiency from the available 4 mJ, 1053 nm compressed pulses from the Nd:YLF

CPA beamline, which is then attenuated after SHG to provide a fixed and stable 2 mJ, 6 ps duration, 526.5 nm pump pulse, with spare energy budget if required.

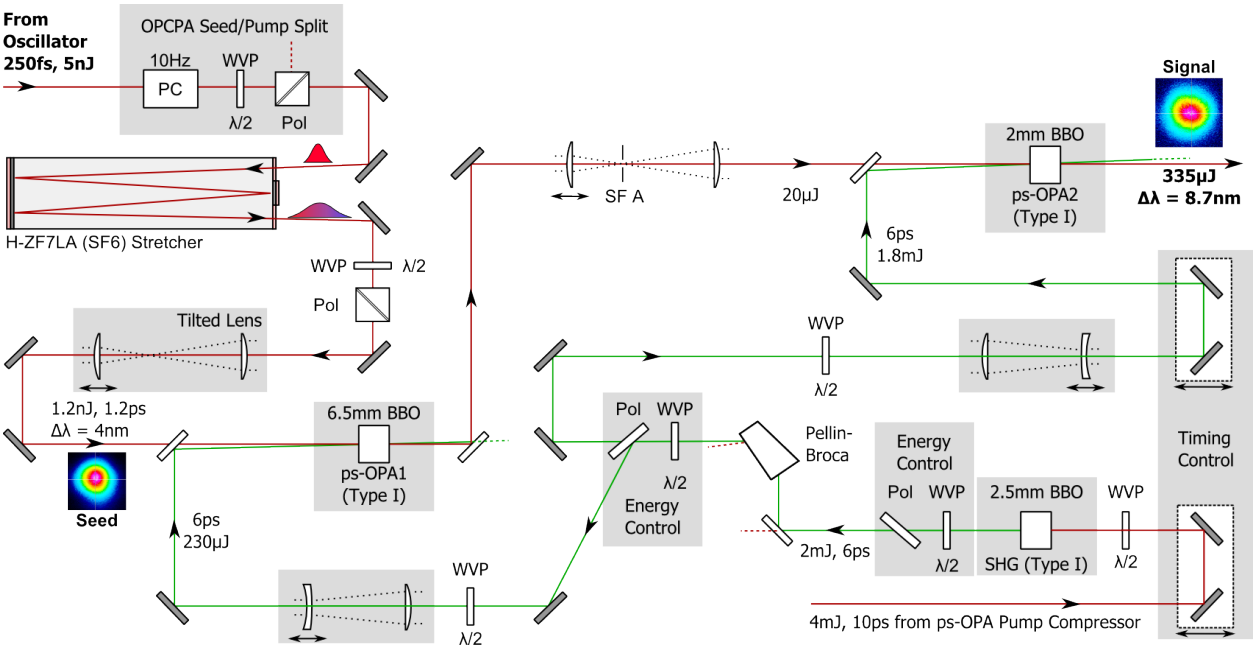


Figure 2.20: Optical layout of the Cerberus ps-OPAs. The pump pulses are frequency-doubled from the compressed 4 mJ portion allocated from the Nd:YLF CPA beamline. The 2 mJ, 6 ps pump pulses are then split with a waveplate and polariser combination for pumping each ps-OPA stage, with individual beam size and polarisation control. Fine tuning of the pulse temporal overlap in the OPAs is achieved with a shared timing stage before SHG and an individual translation on ps-OPA2. The seed pulses are stretched to ~1.2 ps duration through a H-ZF7LA glass block stretcher. The seed is injected into the ps-OPA1 stage through the rear of a dichroic mirror beam combiner. The idler and residual pump pulses are filtered in the near-field and a spatial filter telescope is designed to filter parametric fluorescence, idler scatter and set the seed beam size into ps-OPA2.

Optimal energy, bandwidth and stability is achieved when each stage saturates the available pump energy at the temporal intensity centre. Beyond this point, further amplification will result in back-conversion of energy from the signal to the pump, which is monitored with a spectrometer. Spatial and temporal overlap of pulses in all the Cerberus OPAs are achieved with adjustment on the pump beamline, where spatial overlap is achieved with the dichroic mirror beam combiner (HR at 527 nm, AR at 1054 nm) and temporal overlap achieved with two-mirror translation stages. Residual 1053 nm light on the pump beamline is removed with a combination of narrow bandwidth HR mirrors and

also with angular dispersion from a Pellin-Broca prism to prevent any self-seeding of the OPAs.

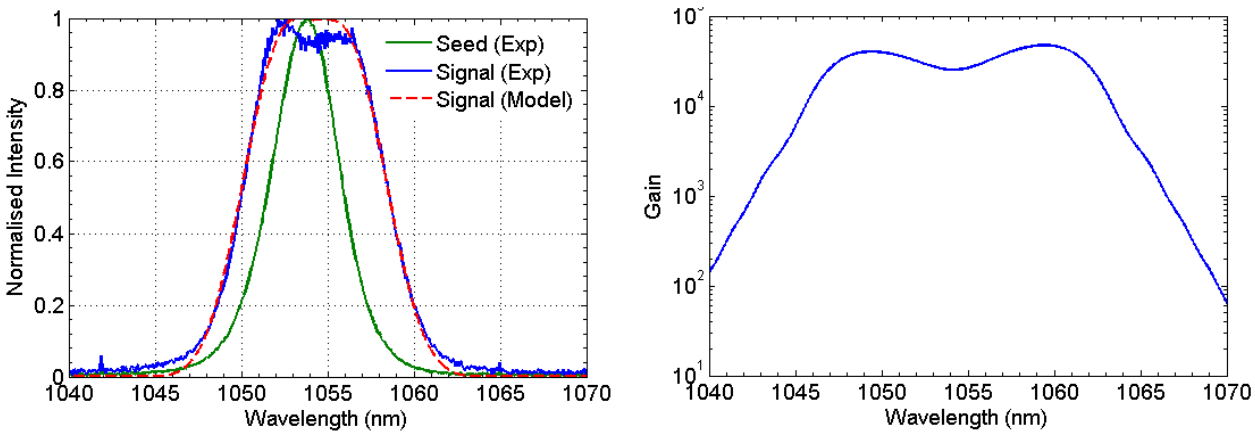


Figure 2.21: Spectral gain profiles of the optimised model and experimental results of the ps-OPAs. A stable, high gain bandwidth broadening mode of operation is achieved with careful design of pump/seed pulse durations and strong pump-depletion, which achieves ~8.7 nm FWHM bandwidth in the amplified signal pulse from only 4 nm FWHM bandwidth in the oscillator seed.

The first OPA stage amplifies the seed pulses in BBO with a 6 ps, 230 μJ portion of the available 527 nm pump energy and intersect the seed pulse with a 0.6 $^\circ$ non-collinear angle, which permits effective separation of the signal, pump and idler pulses without affecting phase-matching. This OPA stage routinely generates 20 μJ signal energy with a gain broadened bandwidth of 6 nm from the 4 nm FWHM seed. The beam is expanded with a spatial filter, which was included to eliminate wide-angle parametric fluorescence emission that may seed the remaining down-stream amplifiers, and injected into the second ps-OPA that is pumped with the remaining 1.8 mJ, 6 ps pulse. This final ps-OPA stage generates 335 μJ, 8.7 nm bandwidth, shown in figure 2.21, with 1% standard deviation in output energy, which is a consequence of strong OPA pump-depletion and a high stability pump beamline.

Using the input pulse durations and crystal configuration in the OPA.FOR model, there is strong agreement between experiment and simulation of the ps-OPAs, which both produce bandwidth broadening and are able to produce 8.7 nm bandwidth at maximum pump-depletion. The contrast characterisation of these pulse is presented in §5.1.

2.7 NANOSECOND PUMPED OPAS

The amplified signal from the ps-OPAs is stretched again with ~200 ps/nm chirp from a modified reflective "Öffner" triplet stretcher setup. This stretcher was initially designed by Dr Mike Mason for a Ti:Sapphire laser [48], who used 3D ray tracing to minimise optical aberrations using $\lambda/30$ flatness reflective optics and achieving aberration-free operation away from the null-stretch position. The optical setup was later adapted for use on Cerberus by Dr Siddharth Patankar, using 1740 lines/mm multilayer dielectric coated reflective diffraction gratings (Plymouth Grating Laboratory) [32]. The design of the stretcher assumed a 4.7 nm input bandwidth from the Cerberus oscillator uses a grating angle of 77 ° with effective grating spacing of 1142 mm that is optimised between the stretched pulse duration and minimal contrast degradation from spectral clipping effects given the cost limits on finite sized optics. A double-passed implementation would only achieve ~100 ps/nm, which was not envisioned to be sufficient with the ~4.7 nm oscillator bandwidth to allow for low B-integral operation at multi-joule energies in the glass amplifier chain. Therefore a four-pass configuration has been implemented that produces ~200 ps/nm chirp whose output seeds a pair of nanosecond-regime OPAs (ns-OPA) that aim to generate a high-energy OPCPA seed for the Nd:Glass amplifiers.

The optical layout of the Öffner stretcher is shown in figure 2.22. The Öffner design is essentially a folded Martinez stretcher that uses on-axis reflective imaging optics to minimise chromatic aberration and off-axis aberrations, such as coma and astigmatism, and of large f-number to minimise spherical aberration.

The amplified signal from the ps-OPAs transmits through a Faraday rotator/polariser combination and is injected slightly low into the Öffner stretcher. After the first pass (blue ray on side view in figure 2.22) the beam is shifted downwards such that the output of the second-pass is output high. This beam is collected with a half-mirror and re-injected with an image inversion that cancels out asymmetric aberrations from the stretcher optics and produces a more uniform output beam from the third and fourth pass. The fourth pass propagates in the reverse direction on exactly the same path as the first-pass injected beam and is separated using the Faraday isolator rejection and is guided directly to seed the first ns-OPA stage.

The primary contrast limitation of the stretcher is governed by the amount of spectral clipping i.e. stretch factor/dispersion versus the finite optical aperture. This has been

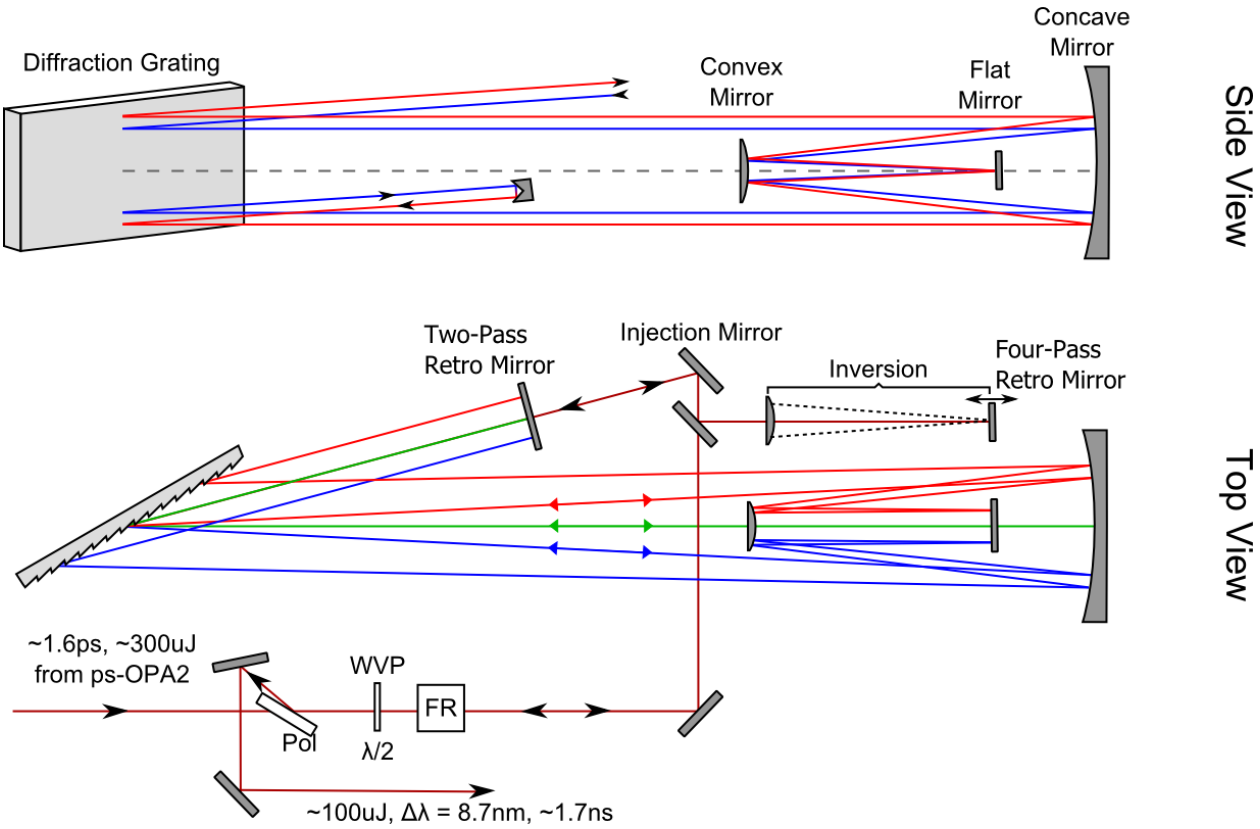


Figure 2.22: Cerberus Öffner reflective doublet stretcher side and top view ray diagram for injection/ejecting and guiding of the ps-OPA output to produce ~200 ps/nm stretched pulses to seed the ns-OPAs.

measured experimentally to be 20.5 nm, limited to the grating width, by over-driving the ps-OPA conversion to produce much broader spectra than generated from the GLX oscillator alone and either red/blue-shifting the central wavelength by temporal delay of the pump pulses into the ps-OPAs. Modelling the impact on the temporal contrast from the measured spectral clipping is shown in figure 2.23, where the measured spectral clipping envelope of the full stretcher system was fitted well with a 20.5 nm wide 5^{th}-order super-Gaussian attenuation mask on the 8.7 nm FWHM bandwidth of the ps-OPAs. The contrast impact was calculated by Fourier-transform of the 200-500 fs bandwidth that is spectrally clipped with this 20.5 nm wide 5^{th}-order super-Gaussian attenuation mask.

We see from figure 2.23 that, in the existing 500 fs design, spectral clipping should not an issue through this stretcher for contrast degradation down to the 10^{-15} level. However, the 8.7 nm available from the ps-OPAs may contribute a 10^{-4} intensity short-range pedestal after amplification that should be weakened by the gain factor of the ns-OPAs, as they currently amplify over a narrower bandwidth. This highlights that spectral clipping in the Cerberus stretcher is not currently a limiting factor in delivering high contrast pulses.

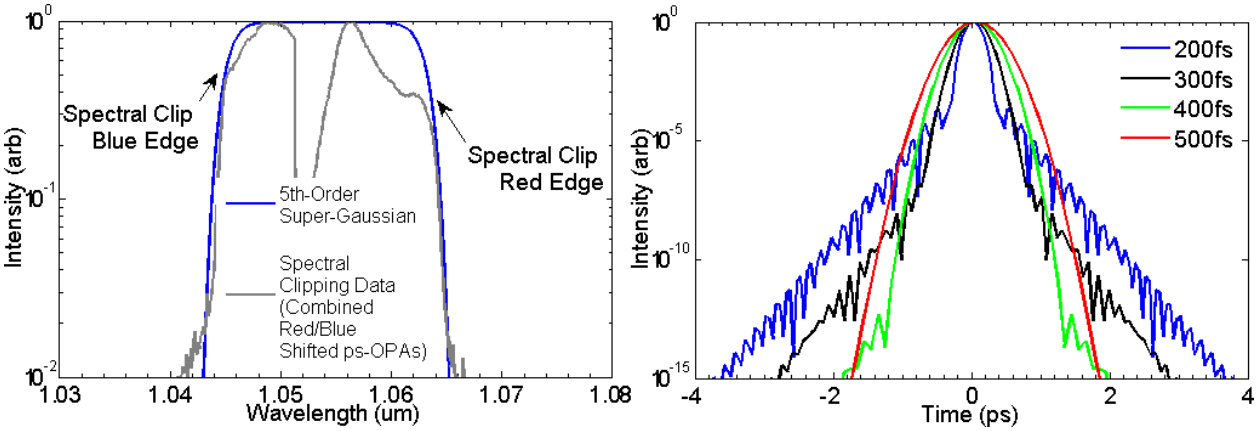


Figure 2.23: (Left) Bandwidth acceptance of the Cerberus Öffner stretcher whose output seeds the ns-OPAs. The acceptance is 20.5 nm wide and approximates a 5^{th}-order super-Gaussian profile. Additional bandwidth was producing from over-driving and spectrally shifting the ps-OPA output. (Right) Impact of the stretcher spectral clipping function on various transform-limited pulse-duration bandwidths, showing increasing intensity noise pedestals for shorter pulses/larger bandwidths.

However, using it unmodified for pulses below ~300 fs may result in some contrast degradation, which could be addressed by use of a wider diffraction grating.

2.7.1 *OPA Pump Beamline*

The pump pulses for the nanosecond OPAs are seeded using the remaining 20 mJ, 80 ps pulses from the ps-OPA pump generation we described in §2.6.1. The optical layout of the ns-OPA pump beamline is shown in figure 2.24. Approximately 23 ns of optical path is first added to achieve temporal overlap of OPA seed and pump pulses before stretching with a two-pass parallel grating pair. Although this stretcher adds anomalous dispersion that acts oppositely to the Martinez stretcher for the pulses injected into regenerative amplifier, a parallel grating pair was chosen to avoid a high-power line focus in the folded Martinez geometry. Pulses of ~1.4 ns duration are output when injected at ~59 ° incidence angle and using a ~5.6 m grating separation.

The grating incidence angles are unmatched due to fast decline in diffractive beam efficiency with these large gold holographic gratings (Jobin Yvon), made available from an old Nd:Glass laser system. The beam is also elliptically up-expanded from a cylindrical positive-negative lens pair that reduces the intensity below the particularly low damage threshold of the holographic gold gratings used and also were necessary to project a more

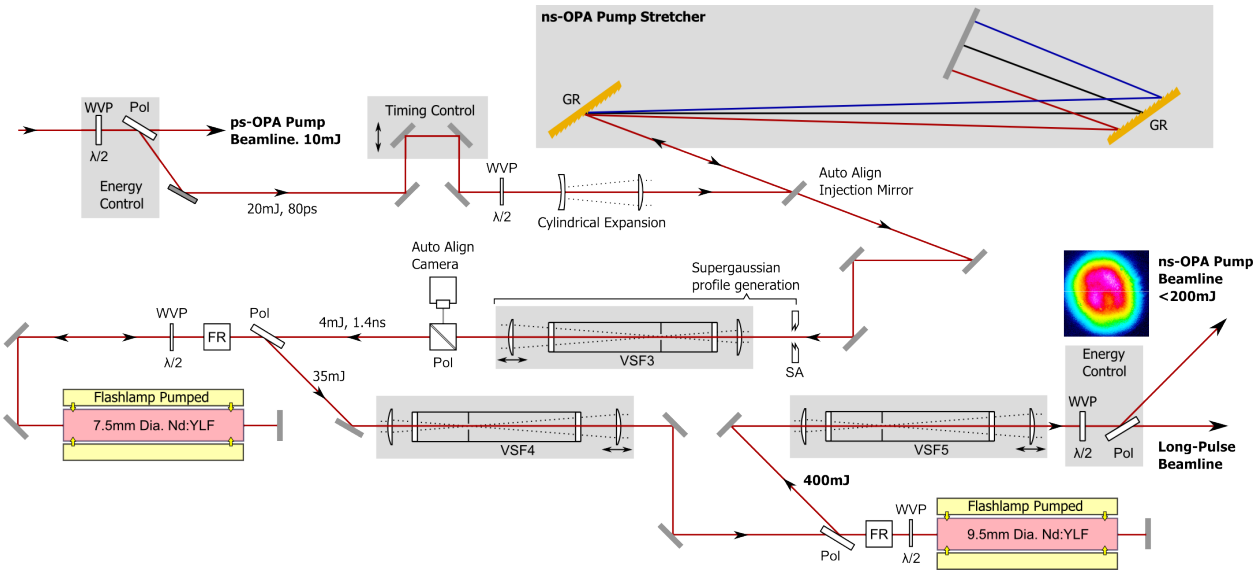


Figure 2.24: Optical layout of nanosecond OPA pump beamline. Pulses from the regenerative amplifier are further stretched to ~1.4 ns duration from a parallel grating pair stretcher and amplified through two double-passed Nd:YLF rod amplifiers to $\leq$ 400 mJ. Spatial filtering and image relay of the super-Gaussian beam between amplifiers reduces B-integral and images a super-Gaussian beam for pumping the ns-OPAs.

circular beam on the diffracted beam close to the grating and create a near circular beam at the output of the grating stretcher. For the current implementation, a pulse duration of ~1.4 ns has been measured, shown in figure 2.25, using an 80 ps rise fast photodiode with ~25 % transmission efficiency of the stretcher optical setup. A planned upgrade to this system using a Martinez geometry, described in §7.1.3, will be implemented to allow for a longer stretch factor and the inclusion of a discrete Fourier plane which a spatial light modulator (SLM) can be added to for temporal control of OPA pump and laser shock driver pulses.

After stretching to 1.4 ns, a serrated circular aperture, producing high spatial frequency content beyond the fundamental circular spatial mode, and vacuum spatial filter, removing most of these high spatial frequencies, produce a super-Gaussian beam that is image-relayed through two double-passed Nd:YLF amplifiers. The double-pass is achieved with a Faraday isolator optical setup that maximises the energy extraction from the ~x4 single-pass gains available from these rods when operating at 1053 nm. Pulses are amplified by the first double-passed 7.5 mm Nd:YLF amplifier from 4 mJ to ~40 mJ. The pulses are spatially filtered between amplifiers to remove minor beam imperfections, suppress self-focussing and image-relay and expansion of the super-Gaussian beam profile (5.5 mm FWHM, 6.5 mm beam waist diameter) for final amplification from a double-passed 9.5 mm

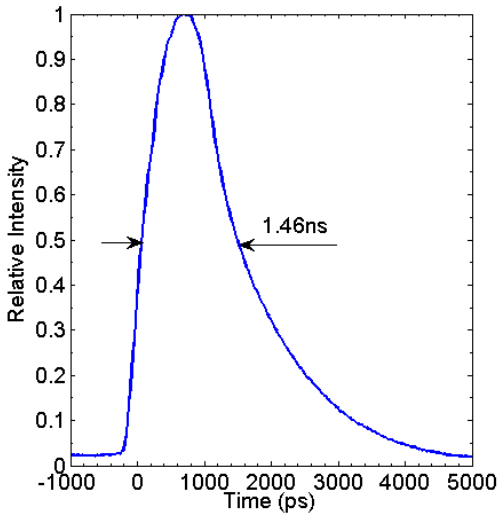


Figure 2.25: Measured 1.46 ns FWHM pulse duration, using a fast 80 ps rise photodiode and 50 Gs/s oscilloscope, from the Nd:YLF CPA beamline after stretching in a parallel grating pair stretcher and amplified to 200 mJ at 1053 nm. This output is frequency-doubled to pump the ns-OPAs.

Nd:YLF rod amplifier up to 400 mJ with 0.6% standard deviation energy stability. The damage threshold and B integral limit of the final amplifier is estimated to be ~700 mJ and therefore 400 mJ is considered a sensible operational limit. Currently only 180 mJ is required for optimal pumping of the ns-OPAs. Alternatively these high-energy pulses can be used to seed the long-pulse Nd:Glass amplification beamlines for MAGPIE and the multi-terawatt target chamber for applications including driving X-ray sources used to diagnose pulsed power experiments, or to drive shocks in solid materials.

2.7.2 *Nanosecond OPA Results*

Using similar optical methods to the ps-OPAs,the ns-OPAs use two sequential BBO non-linear gain stages with high gain in the first stage (ns-OPA2) and low gain in the final amplifier (ns-OPA2) to produce an energetic and stable output. The 180 mJ 1053 nm, 1.4 ns pulses from the Nd:YLF CPA beamline is frequency-doubled with a 30 mm long KDP, cut for type-II interactions, that produces ~80 mJ 526.5 nm, 1 ns pump light for the ns-OPAs. Residual 1053 nm light is removed using a combination of dichroic mirrors and Pellin-Broca prisms. After transmission losses, 25 mJ is used to pump the first ns-OPA1 stage using a 12 mm long BBO and 50 mJ for pumping ns-OPA2. Seed pulses with up to 9 nm FWHM pulse bandwidth from the ps-OPAs are stretched with 200 ps/nm chirp

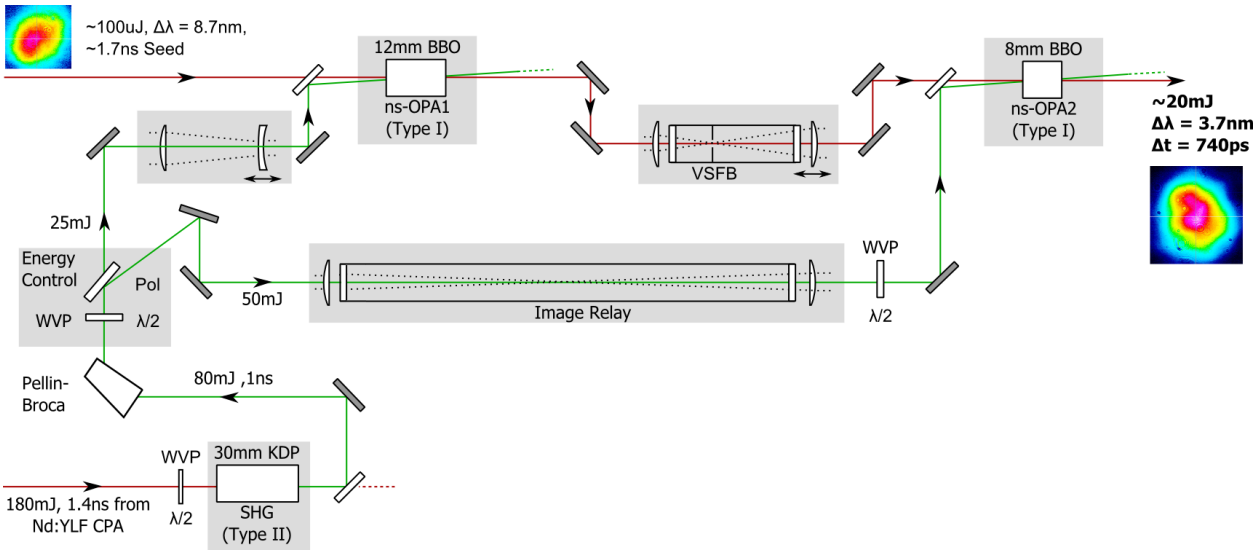


Figure 2.26: Optical layout of the ns-OPA beamline that uses the 180 mJ, 1053 nm pulses from the Nd:YLF CPA beamline to pump a pair of OPA crystals (BBO) seeded with the stretched output from the ps-OPAs. The ns-OPAs generate 20 mJ, 3.7 nm bandwidth pulses for seeding Nd:Glass amplifiers and are compressible to ~440 fs.

are then amplified in the ns-OPAs with maximum pump depletion before the onset of back-conversion for optimal energy extraction, bandwidth and stability, which require ~0.9 GW cm $^{-2}$ pump intensities. The BBO damage threshold at the pump duration and wavelength is expected to be ~2.5 GW cm^{-2}, estimated from scaling of manufacturer coating specifications scaled to our operating conditions using (2.16).

The first ns-OPA stage produces 10 mJ of signal energy, which is then amplified to 20 mJ with 1% standard deviation stability in the final OPA stage of the Cerberus front end with 3.7 nm bandwidth, corresponding to ~740 ps stretched pulse durations with a minimum transform-limited duration after compression of 440 fs. Since the original design of the stretcher-compressor system, based around a ~4 nm seed from the master oscillator, the actual seed bandwidth for the ns-OPAs in the region of 8.7 nm, due to the significant gain broadening from optimal seed/pump pulse duration ratio and pump-depletion from the ps-OPAs, which creates ~1.7 ns seed pulses for the ns-OPAs. This chirped seed duration is thus too long in comparison with the ~1 ns duration pump pulse, leading to the spectral wings of the seed to see significantly less gain and therefore spectral narrowing that is not offset by greater energy extraction or stability.

The amplification of oscillator pulses through the ps-OPAs and ns-OPAs represents the entirety of the "front-end". The 20 mJ pulses output from this OPCPA front-end, with ~10^7 net gain, has demonstrated the generation of a high energy seed that improves upon the

gain narrowing limitations of gain-storage amplification and contrast limitations, which we present in chapter 5.

2.8 ND:GLASS AMPLIFICATION AND COMPRESSION

The Cerberus front-end pulses next seed a flash-lamp pumped Nd:Glass amplification chain that add the final ~10^2 gain to boost the pulse energy to the multi-joule level to produce multi-terawatt peak-pulse powers after compression.

The Nd:Glass rod amplification chain for the terawatt beamline is composed of two 7 mm diameter rod amplifiers, each with ~x4 single pass gain, and a single 16 mm diameter rod amplifier with up to x15 single-pass gain. All of the amplifiers are single-passed to avoid pre-pulse generation from co-aligned surface reflections of transmissive optical surfaces. A central, flat-top, section of the beam profile of the 20 mJ Gaussian pulses from the ns-OPAs is selected with a serrated aperture and spatially filtered under vacuum to produce a super-Gaussian beam for optimal energy extraction from the Nd:Glass amplifiers. Between each Nd:Glass amplifier, additional vacuum spatial filtering between amplifier stages is used to suppress self-focussing and formation of hot-spots from any dusty/slightly damaged optics that may imprint high spatial frequencies on to the beam profile. Up to 1.2 J is typically extracted from this set of amplifiers in the Terawatt lab with optimal front-end operation. These pulses can be compressed in a double-passed parallel diffraction grating pair in the Terawatt lab, using 22 cm wide, 1740 lines/mm gold holographic gratings (Jobin Yvon) and measured to have 14 nm spectral acceptance and ~65% total efficiency, to deliver ~750 mJ, 500 fs (1.5 TW) pulses on target.

Alternatively, the pulses can be diverted with a waveplate-polariser to the Multi-Terawatt lab for further amplification using a 50 mm diameter rod amplifier before compression with state-of the-art 28.5 cm, wide, 1740 lines/mm multilayer dielectric coated diffraction gratings (Plymouth Grating Laboratories), which were chosen over gold/metallic substrate gratings because of their ~x4 higher damage thresholds for 500 fs pulses, and greater diffraction efficiency [67]. Although ~30 TW peak-power pulses can be output from the compressor, the peak-power on target is currently limited by B-integral accumulation from propagation through air and the glass window into the target chamber. Nevertheless, a high-quality Gaussian 5 μm FWHM focal spot size is achievable using an

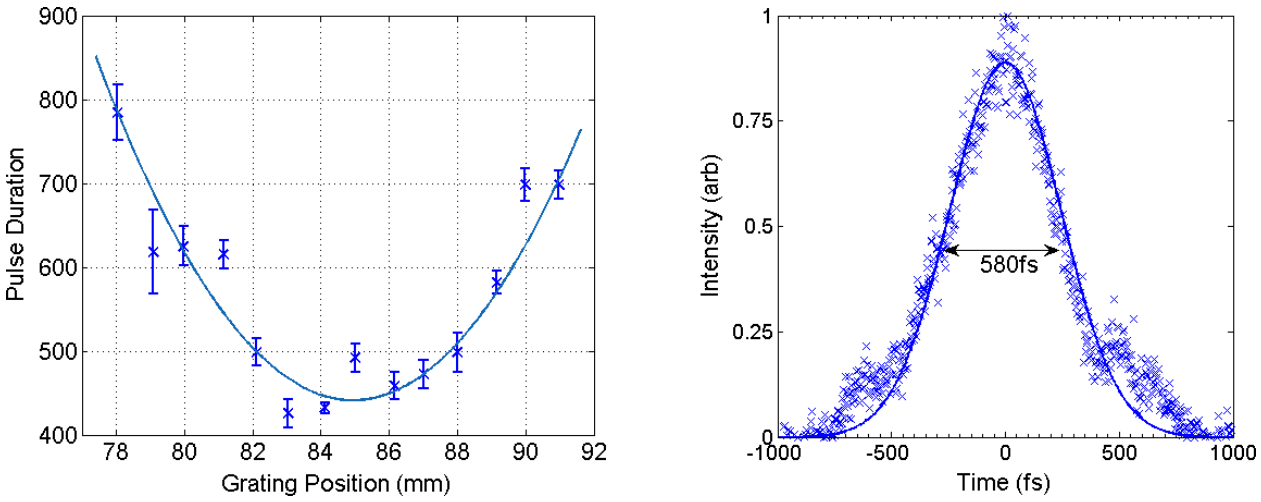


Figure 2.27: (Left) Measured compressed pulse duration scan of amplified 3.7 nm bandwidth front-end pulses through the complete short-pulse optical system using a single-shot autocorrelator and adjusting grating separation to identify the optimum grating position. (Right) Minimum pulse duration of a 1 TW pulse with the same single-shot autocorrelator. The increased pulse duration is likely due to gain narrowing or a small drift in the ns-OPA bandwidth on this shot, which the spectrum is not currently monitored on-shot.

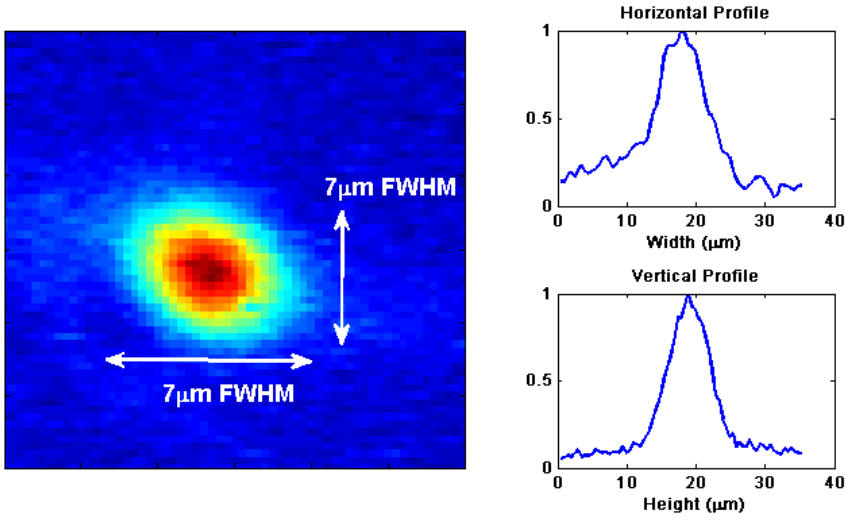


Figure 2.28: Measured focal spot of the Cerberus Laser System with an f/5 GRIN (Gradient-Index) lens, which minimises spherical aberration, and using a calibrated microscope objective for image magnification onto a CCD camera. A 600 mJ, 500 fs pulse focused to this small area will produce ~1.8 $\times$ 10^{18} W cm^{-2} peak-intensities.

f/3 off-axis parabolic mirror without the need for adaptive optics techniques, producing ~10^{19} W cm^{-2} intensities on target at the ~4 TW B-integral limit.

2.9 SUMMARY

In this chapter we have described the development and characterisation of a hybrid OPCPA/Nd:Glass multi-terawatt laser system capable of producing >10^{19} W cm^{-2} intensities on target. We have shown through modelling and experimental results how the broad parameter space of OPCPA may be tailored to provide a combination of high-gain, bandwidth broadened and high-stability output pulses through careful selection of the nonlinear crystals and its length, pump vs. seed durations and pump-depletion effects. The all-optical synchronisation between the OPCPA pump and seed pulses provides a robust approach towards high energy amplification without the need for synchronisation electronics, which will also become important for any future pump-probe style experiments using the long and short-pulse sources.

The Cerberus OPCPA front-end currently produces a stable, high quality 20 mJ train of pulses at up to 10 Hz from ns-OPAs, leaving relatively limited gain required from Nd:Glass gain-storage amplification to reach the multi-Joule level, minimising ASE and gain-narrowing effects. Currently, the beamline performance in the Multi-Terawatt lab is limited from the B-integral from the compression of pulses in air. Small improvements such as increasing the beam diameter to 60mm after the final amplifier and using a low n_2 MgF_2 window have been made to reduce the B-integral slightly; however, the upper energy limit is still expected to be <5 J before self-focussing significantly deforms the optimal focal spot with high numerical aperture (f/3 and f/1 off-axis parabola) optics until a vacuum compressor can be constructed that can extract the full 30 J potential of the current amplifier chain..

3

HIGH-DYNAMIC RANGE DIAGNOSTICS FOR CONTRAST CHARACTERISATION

In this chapter we present the design and operation of the diagnostic systems used to experimentally characterise and understand the performance and temporal contrast results of laser oscillators, parametric amplifiers and complete OPCPA systems. The dynamic range of these diagnostics is a crucial parameter to maximise in addition to temporal resolution and their overall usability. For 10^{19}-10^{21} W cm^{-2} high-intensity laser sources, this drives a requirement for ~10^{8}-10^{11} dynamic range measurements are required to measure noise sources that can potentially ionise laser targets before arrival of the high-intensity laser pulse. This is far beyond the single-shot dynamic range of current generation CCD cameras, photodiodes and photomultipliers alone, which at best produce full–ranging 16-bit output i.e. 6.5×10^{5} dynamic range.

3.1 THIRD-ORDER AUTOCORRELATOR DIAGNOSTIC (TOAD)

The second-order autocorrelator described in §2.3 used for pulse duration measurements uses two identical intersected pulses to produce a spatially encoded symmetrical second-harmonic temporal intensity envelope i.e. it is impossible to distinguish between pre and post pulses. The autocorrelation can be modified to produce asymmetric traces and produce high dynamic-range temporal contrast characterisation of high peak-power lasers by using a shorter probe pulse. In third-order autocorrelation, this probe pulse is the second harmonic, approximately $\sqrt{2}$ shorter in duration than the fundamental pulse, and sum-frequency mixing of the fundamental and probe generate the effective third-harmonic of the input pulse [68, 69]. The third-order correlation function is given by

$$I_3(t) = \int I_1(t-\tau)\, I_2(t)\, dt \tag{3.1}$$

where the subscripts denote the harmonic number. This concept is shown in figure 3.1, where the second-harmonic is approximately $\sqrt{2}$ shorter in time than the pulse to

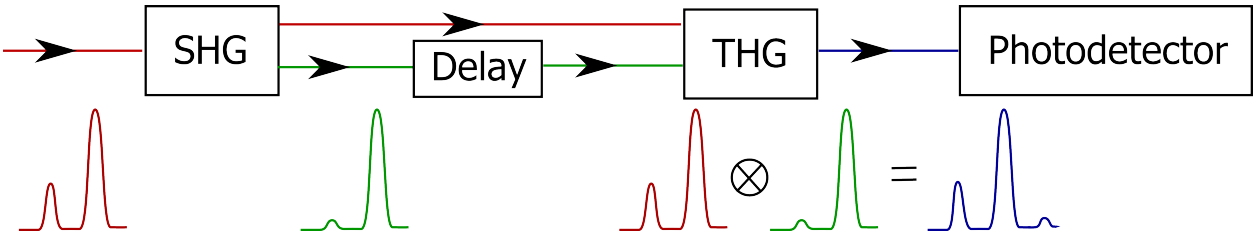


Figure 3.1: Simplified illustration of the sum frequency process used in third-order autocorrelators. Post-pulses in the input beam may still produce "ghost" pre-pulse artefacts in the retrieved third-harmonic signal, which will need to be analysed after the measurement scan to determine if they are real pre-pulses or diagnostic artefacts.

be measured, allows higher-resolution measurement of the fundamental pulse temporal intensity envelope and crucially there no longer time symmetry in the correlation.

It should be noted that the sum-frequency process can produce unwanted artefacts such as "ghost" pre-pulses from the measurement process as post-pulses in the second harmonic probe can potentially produce a symmetric pre-pulse ghost in the third-order signal due to the convolution process in the interaction. Therefore, analysis of the trace may involve matching any measured pre-pulses to a measured symmetric temporal location post-pulses. When there is no temporal matching to a well defined post-pulse, these measured pre-pulses are presumed to represent real features in the laser pulse or a post-pulse that is only added in the probing arm of the autocorrelator. Fortunately, the second-harmonic process, whose intensity scales as the square of the input intensity, also reduces the relative intensity of satellite pulses, which are capable of producing weaker artefacts oppositely equidistant from the temporal intensity maximum and therefore its real temporal position may be discerned. For example, a 10^{-4} relative intensity post-pulse produced from the double internal reflection of a polariser will produce a 10^{-8} relative intensity post-pulse after SHG into the scanning probe and therefore the autocorrelation/-convolution process will produce a 10^{-4} post-pulse and 10^{-8} pre-pulse artefact. The third-harmonic signal trace retrieved from the autocorrelation is conveniently linearly proportional to the fundamental and second-harmonic input intensity at the input of the sum-frequency crystal, as only one photon from each input harmonic is required per third-harmonic photon generated.

This type of measurement also produces significantly less background noise from unwanted non-linear processes from individual input beams into the third harmonic non-linear crystal. The third-harmonic sum-frequency signal can be well isolated from the ejected input beams by introducing a non-collinear geometry to separate the output pulses

to produce a background-free signal i.e. there is no third-harmonic signal when either the fundamental or second-harmonic pulses are individually incident on the mixing crystal or are not temporally overlapped.

The third-order autocorrelator diagnostic (TOAD) described here was optimised for maximum sensitivity to the input pulse power and therefore was designed to use focused non-linear interactions to maximise the optical intensities from low power sources such as laser oscillators. The non-linear interaction strength was also optimised by careful design of the non-linear crystal lengths, to optimise conversion efficiency against phase-matched bandwidth (2.13), and focal lengths to match the phase-matched angular acceptance of the crystal lengths.

The generated 351 nm third-harmonic signal was measured with a high-gain photomultiplier tube (PMT, ET-Enterprises 9124B), which is a near single-photon sensitive detector. The PMT is contained in a light-tight housing and is spectrally and spatially filtered to see only third-harmonic light. A custom signal amplifier, with switchable x10, x100 and x1000 gain with ~100 μs integration time, is linked directly to the output of the PMT and amplifies the PMT signal to increase the dynamic range of the measurement and improve signal to noise such that the noise floor is limited by the PMT rather than the noise level of the signal readout electronics.

For strong third-harmonic signals that may saturate the photomultiplier signal, a calibrated set of twelve density filters attenuate the emitted UV light and active control of this filter wheel enhances the dynamic range of the measurement. These filters are housed in a motorised filter wheel and have been calibrated by identifying the linearity range of the photomultiplier and measuring the attenuated signal voltage with each step in neutral density, typically a factor of ~10.

The second-harmonic signal acts as a probe of the fundamental in the frequency mixing process, as it has a shorter pulse duration than the first harmonic. This allows a more direct measurement of the temporal intensity of the first harmonic as a function of time delay, which in the ideal case requires a delta-function probe for complete recovery of all temporal information. This second harmonic probe is scanned through the temporal intensity profile of the fundamental laser pulse under characterisation with a position encoded motorised translation stage (Thorlabs LTS300/M), which has 30 cm travel, equivalent to 2 ns time delay when double passed and a temporal step size as short as 5 fs.

The neutral density filter wheel and translation stage can both be operated manually or through a computer interface. The computer software, developed by the author, is

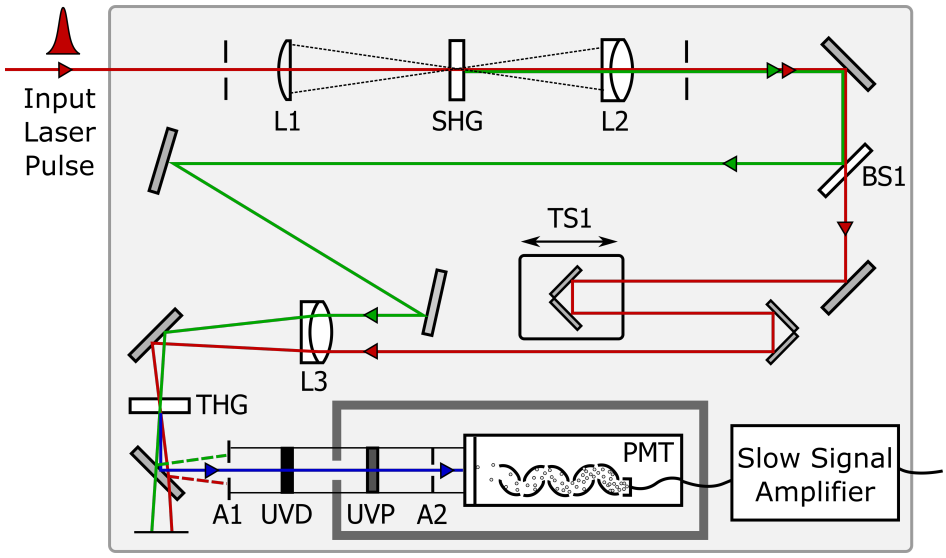


Figure 3.2: Optical layout of the third-order autocorrelator diagnostic (TOAD) for high-dynamic range characterisation of laser pulses. L1, L2: Focussing and re-collimation optics used to maximize the intensity onto an SHG crystal, a 1.5 mm thick BBO (type I). BS1: A wedged dichroic beam-splitter separates the fundamental and second harmonic pulses. TS1: Translation stage for temporal scanning. L3: An achromatic doublet lens used to focus the fundamental and second-harmonic beamlets and maximize the intensity onto the THG crystal, a 1 mm thick BBO (type II). A1, A2: Apertures are used to spatially filter THG light from residual fundamental and second-harmonic. UVD: Calibrated UV density filters in a twelve-slot filter wheel. UVP: UV coloured glass bandpass filter (UG11). PMT: Photomultiplier tube (ET Enterprises 9124B) used for single-photon sensitivity detection of the third-harmonic signal.

capable of communicating with both these devices as well as a Tektronix Oscilloscope to record the photomultiplier signal. With computer control of all the scanning components of the TOAD, it is possible to set-up and perform a fully automated scan of the temporal intensity profile of the laser pulse, which greatly reduces measurement time of the many thousands of data points required for "full" characterisation of a light pulse. However, a full scan may still take many hours to complete for a high resolution and large temporal delay range using low repetition rate (1-10 Hz) laser systems, which demands the laser remains stable with minimal drift in pulse energy and beam alignment for the duration of the measurement.

The maximum dynamic range of the instrument is limited both by optical damage thresholds and optical scattering of the individual first and second harmonic beams used to produce the third-harmonic signal. The optical damage threshold of the focused pulses

on the second and third-harmonic crystal is estimated, from manufacturer specifications at longer, ~100 ps, pulse duration and the scaling law (2.16), to be approximately 150 GW cm^{-2} for 500 fs 1054 nm pulses, which corresponds to maximum practical input energies of less than 2 μJ. Operation above this energy will increase the dynamic range but with increased risk of damaging the non-linear crystals, which have redundant aperture in the event this occurs.

Given its low input energy requirements, the TOAD is able to directly measure the laser contrast to high-dynamic range from even weak laser sources, such as laser oscillators and pre-amplifier stages operating at the few nJ-μJ level. We show in chapters 4 and 5 the contrast characterisation of oscillators and OPCPA front-ends which demonstrate that the TOAD is able to measure laser pulses with 1:10^{11} dynamic range across a 2 ns temporal scanning window. This is broad enough to assess most of the key contrast features of optical parametric chirped-pulse amplification (OPCPA) front-ends such as parametric fluorescence, secondary "ghost" pulses from multiple reflections, Fourier domain artefacts arising from spectral clipping/incomplete compression and high-order phase error effects.

3.2 SEEDED OPA FLUORESCENCE DIAGNOSTIC

The parametric fluorescence from an OPCPA laser system can be one of the dominant sources of noise against the primary high-power laser pulse. For example, the first generation petawatt OPCPA front-ends used solely nanosecond pulse pumping of the OPA gain stages, which led to nanosecond duration pedestals at ~10^{-6} relative intensity [29, 70]. A widely adopted method of parametric fluorescence characterisation measures the fluorescence intensity generated with an unseeded, yet still pumped, OPA [64, 71–73]. Results from this type of measurement can be misleading, as it is a fundamentally different mode of operation compared to that of a system delivering light to an experiment, and has led to publications advising methods to reduce parametric fluorescence by reducing the optical gain per amplifier and avoiding OPA saturation effects [71–73]. Without comparisons between the seeded and unseeded OPA fluorescence, this type of measurement should only be used to provide an upper limit of the parametric fluorescence expected to be generated from the laser amplification system. For example, Dorrer et al. presented a high-contrast OPCPA pre-amplifier system, generating energies of ~100 μJ with <20 μJ

of fluorescence in an unseeded mode of operation, where the main laser seed is blocked and the non-linear crystals are still optically pumped [64]. They were also able to measure the contrast post CPA compression with a third-order autocorrelation, which showed the fluorescence intensity level in the seeded OPA mode of operation was in fact much weaker at 10^{-4} relative intensity. This previous study demonstrates a need to better understand the behaviours of parametric fluorescence and identify the key physical mechanisms that may reduce the parametric fluorescence intensity in the seeded mode of operation in an OPA. Crucially, if further evidence arises that show the parametric fluorescence is vastly different between the unseeded and seeded modes of operation, previous recommendations on OPA design and operation based upon unseeded parametric fluorescence measurements will become unreliable.

Although the temporal contrast characterisation of high peak-power laser systems are typically performed using third-order autocorrelators [69], their dynamic range rapidly decreases for low input powers i.e. in the unseeded to partially seeded modes of OPA operation. Critically, empirical measurements of the behaviour of parametric fluorescence from unseeded to fully seeded OPA operation have not been reported to date in the literature prior to the work reported in this thesis; particularly due to the lack of a high dynamic range measurement method that is more sensitive than third-order autocorrelation. Other drawbacks of third-order autocorrelators include the requirement to use compressed pulses to temporal resolve the incompressible parametric fluorescence; however, the additional optics required for this will potentially introduce their own noise sources on similar intensity and timescales that may then make parametric fluorescence noise unresolvable. Additionally, robust third-order autocorrelator setups are typically based upon a scanning system to build-up the temporal intensity envelope over many data acquisitions, whereas the low level parametric fluorescence is likely to be an inherently noisy process from the statistical decay of pump photons to the fluorescence signal and idler photon pairs. Third-order autocorrelators are a very good general tool but do not easily permit detailed measurements of the behaviour of parametric fluorescence or investigations of single-shot processes, e.g. the shot-to-shot changes in the distribution and wavelength of noise photons.

We demonstrate the ability to measure and distinguish the parametric fluorescence intensity simultaneously with the OPA signal for the full range of unseeded to strongly seeded operation. The diagnostic we present here and in [36] does not rely upon nonlinear processes or the temporal characterisation of parametric fluorescence. Instead, we

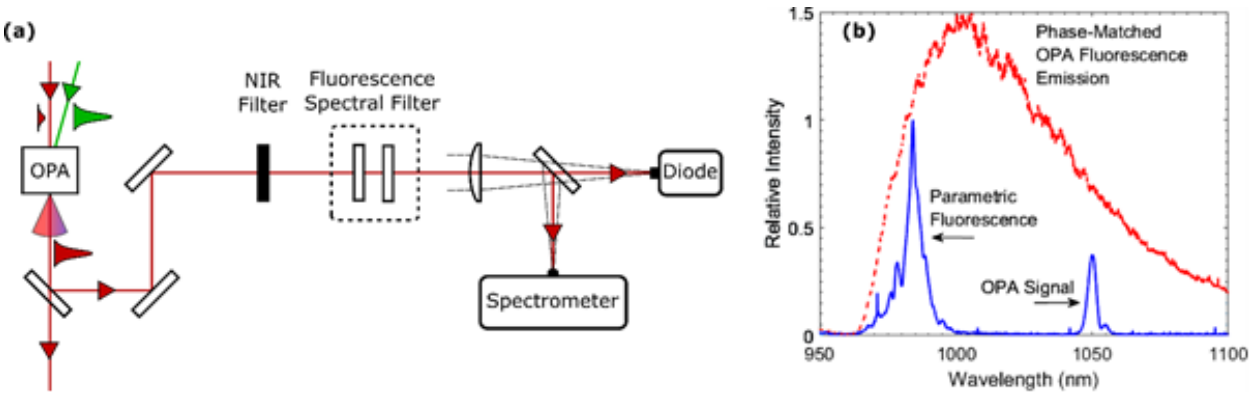


Figure 3.3: a) Optical layout of the parametric fluorescence diagnostic. Broadband mirrors are used to transport and avoid spectral distortion of the OPA output. The main amplified signal is spectrally attenuated using stacked short-pass filtering. The effectiveness of the filters was determined using a spectrometer before the energy characterisation was performed using a photodiode. A long-pass filter was used to block residual shorter wavelength pump or weak SHG generation from the OPA. b) Experimental data showing effectiveness of spectral filtering using two stacked filters to simultaneously resolve the intense OPA signal spectrum and fluorescence without saturating the spectrometer. Additional filters were placed in the stack to fully extinguish the OPA signal to characterise the fluorescence from the seeded OPAs.

have utilised the very broad fluorescence emission bandwidth (red curve in figure 3.3b) of the broadly phase-matched OPA processes to spectrally distinguish it against the relatively narrowband signal of the primary laser pulse. The optical setup is presented in figure 3.3a), a simple setup that focusses the optical emission from an OPA onto a spectrometer and photodiode. The measurement method of parametric fluorescence we present here uses entirely linear detection methods and therefore should be much more sensitive than the cascaded non-linear processes required in third-order autocorrelation. Normally, the OPA signal will completely saturate, potentially damaging, the spectrometer. However, use of appropriate short-pass filtering will act to only attenuate the primary laser signal. In figure 3.3b), two sequential short-pass filters each provided ~10^3 attenuation of light >1000 nm, such that a small section of the parametric fluorescence below this wavelength is still observable by the spectrometer in addition to a fully resolved OPA signal of the primary laser pulse in the high-gain seeded OPA mode of operation used for laser-matter experiments. For characterisation of parametric fluorescence, additional filters were added to further attenuate the laser OPA signal far below the fluorescence

intensities characterised. The methods and findings we present in this chapter have contributed towards a publication [36].

A key assumption of the measurement is that changes in the spectral intensity of parametric fluorescence slightly outside of the seed bandwidth also reflect the wavelengths overlapped within the OPA seed/signal that cannot be directly measured. As noise photons are uncorrelated and the phase-matching conditions of the amplifier should not change between unseeded to seeded operation i.e. the shape of the fluorescence spectrum in figure 3.3b) should not change, we believe this to be a robust hypothesis.

A critical requirement for this characterisation method is that the parametric fluorescence bandwidth exceeds the bandwidth of the main OPA laser seed to allow the use of an edge-pass filter stack to attenuate the significantly stronger seeded OPA signal. While this is aided by using a non-collinear geometry to offset the peak emission wavelength of fluorescence observed, this method will most likely become more difficult to implement for ultra-broadband OPCPA systems designed for few-cycle amplification which utilise several hundred nanometres of bandwidth. In such a scheme, the parametric fluorescence may need to be observed at a different viewing angle to the seed/signal with optical scatter minimised to allow the weak fluorescence emission to be resolved.

A conceptually similar technique has been applied using a dazzler to produce a spectral hole in the OPA seed and measured the fluorescence generation at a comparable intensity to the OPA signal [74]. However, for high dynamic range contrast characterisation, such a device will need to completely attenuate the seed bandwidth to levels less than the few tens of photons of the fluorescence seed, which is unrealistic for any active electro-optic device. The spectral-hole technique is not able to strongly attenuate the fluorescence relative to the signal, therefore only low dynamic-range measurements ($\sim 10^2$) are possible. Measuring the fluorescence outside of the seed bandwidth, as we demonstrate here, allows far higher-dynamic range characterisation without the requirement to add an extra optical setup to completely remove part of the seed bandwidth e.g. a dispersive system with a fully opaque Fourier plane mask.

The experimental determination of the noise term found in the OPAs and its mechanism of amplification will be of benefit to modelling OPCPA system performance and in assessing the potential impact of parametric pre-pulse in high-intensity laser interaction experiments when used in conjunction with third-order autocorrelation characterisation.

3.2.1 *Experimental Setup*

The parametric fluorescence diagnostic was positioned after the pair of ps-OPA stages of the Cerberus laser system front-end, with a block diagram of experimental setup shown in figure 3.4. The Cerberus ps-OPA stages produced 335 μJ of amplified signal from the 1.2 nJ, 1.25 ps stretched seed from the Nd:Glass short-pulse oscillator. Under normal operating conditions, optimal energy, bandwidth and stability is achieved when each stage saturates the available pump energy at the temporal intensity centre, which is monitored in real-time with a spectrometer. Beyond this point, further amplification will result in back-conversion of energy from the signal to the pump.

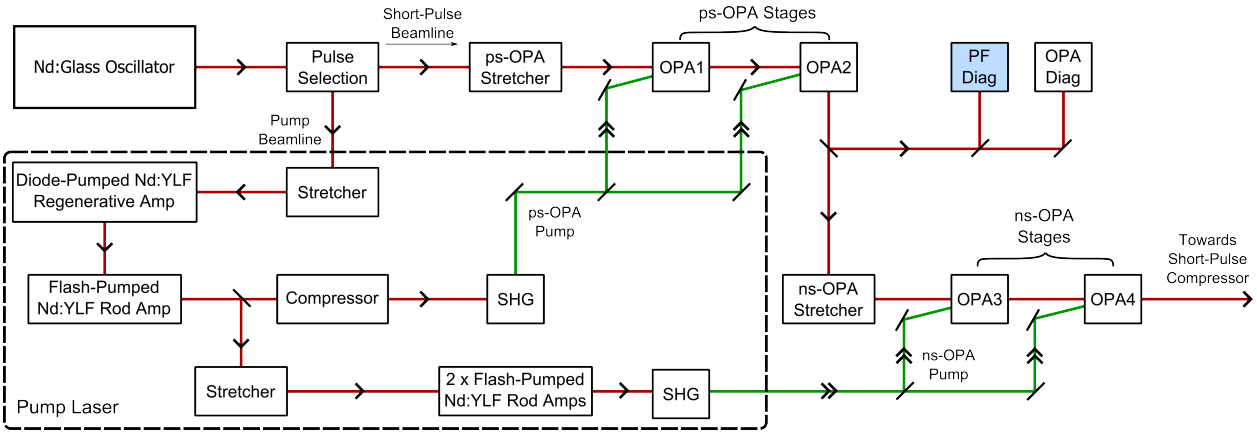


Figure 3.4: Simplified setup of the Cerberus OPCPA laser front-end used for the parametric fluorescence characterisation. "PF Diag" indicates where the unseeded and seeded parametric fluorescence was measured unless otherwise stated.

The amplified signal is then stretched again to 1.6 ns in a reflective Öffner grating system, with 35% transmission efficiency within the 1054±10 nm spectral bandwidth acceptance for the primary laser pulse. The stretched output of ~110 μJ is used to seed a pair of nanosecond-regime OPAs (ns-OPA). The ~20 mJ ns-OPA signal then seeds an Nd:Glass amplifier chain before compression to ~500 fs.

The ps-OPAs have been designed to reduce contrast degradation from parametric fluorescence by ensuring the seed pulse slightly overfills the spatial profile of the pump, whilst the temporal profile is optimised to provide a balance between bandwidth enhancement and energy extraction from the pump. Each stage is single-passed to avoid pre-pulse generation from stray reflections, with spatial filtering between the stages to eliminate wide-angle propagation of parametric fluorescence.

When both ps-OPAs are pumped with the main laser seed blocked, approximately 1 nJ of parametric fluorescence is observed after the Öffner stretcher before injection into the ns-OPAs. If the laser were to be compressed at this stage and assuming the fluorescence will be of order the pump pulse duration of ~6 ps FWHM, the temporal intensity contrast of the 110 μJ primary laser pulse versus the unseeded ps-OPA parametric fluorescence laser would be ~10^6. This method of characterisation represents the current status of fluorescence characterisation of OPCPA systems to date, which gives an upper-bound to the real parametric fluorescence temporal contrast in the seeded mode of operation.

The broadly phase-matched fluorescence spectrum in figure 3.5 was measured by focussing the combined fluorescence from OPA1 & 2 that is emitted in the same direction as the seed into a spectrometer (Ocean Optics USB4000) approximately one metre downstream from OPA2. In figure 3.5 we see the instantaneous fluorescence emission (red curve) produces an apparently random distribution of signal and idler photons but these average to produce a smooth distribution centred at 995 nm (blue curve) with ~200 nm bandwidth. In comparison with the 1054 nm laser pulse, this peak emission wavelength offset is thought to be a consequence of momentum conservation and the 0.6 ° non-collinear angle between the pump and seed pulses [27]. It should be noted that the fluorescence from OPA1 could not be detected on its own and the removal of the spatial filter between the OPA stages had no noticeable effect on the shape or intensity of the fluorescence spectrum.

In our case, an ideal transform-limited 250 fs Gaussian mode-locked laser seed pulse centred at 1054 nm will have a relative spectral intensity of 10^{-110} at the maximum 995 nm fluorescence emission peak i.e. it provides essentially zero seed photons at this wavelength. High-reflectivity 0 ° incidence Nd:YAG laser-line dielectric mirrors (CVI Laser Optics) acted as a 980-1170 nm spectral band-stop filter in the parametric fluorescence diagnostic, with a high damage threshold able to withstand the strong seeded OPA signal with the system in full operational mode. As these mirrors are also used to transport the pulses in the laser beamline, the OPA seed will be significantly attenuated outside of this bandwidth acceptance e.g. residual CW/spontaneous emission from the mode-locked oscillator. This provides further discrimination between seed and fluorescence wavelengths.

The amount of attenuation expected from a single filter is of the order 10^3, therefore multiple filters stacked in series were needed to block the >10^5 more intense seeded OPA signal compared to the fluorescence. The photodiode used for retrieval of the absolute fluorescence energy was first calibrated with a power meter against the ~70 MHz seed

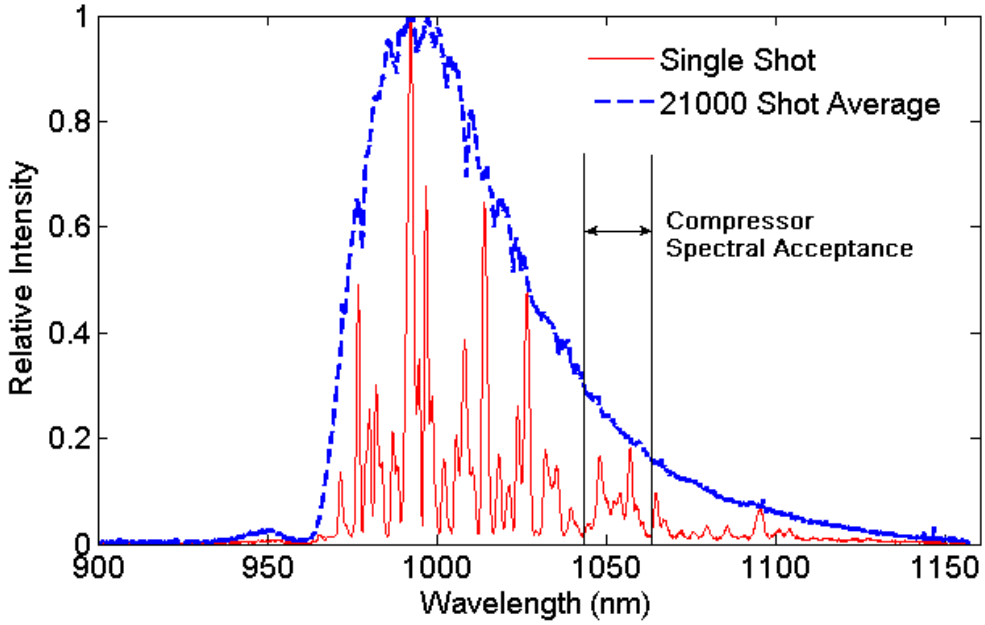


Figure 3.5: Unseeded parametric fluorescence spectrum emitted in the seed direction of the ps-OPAs with a 0.6 ° non-collinear angle. (Red solid line) Instantaneous fluorescence from a single shot, illustrating the random probabilistic nature of the parametric down-conversion and subsequent amplification. (Blue dotted line) Averaged parametric fluorescence over 21,000 shots, highlighting the broad phase-matching achieved and the peak wavelength offset of parametric fluorescence in non-collinear geometries. In this case the seed is centred at 1054 nm and the fluorescence at 995 nm, which acts to improve contrast for narrowband OPCPA schemes.

oscillator pulses without any filtering. The attenuation factor from the spectral filter stack was then determined using the unseeded fluorescence photodiode signal to give a final system calibration.

3.2.2 *Key Seeded OPA Fluorescence Results*

A common method used to rapidly diagnose the potential impact of fluorescence on the compressed temporal contrast is to measure the unseeded OPA output and its behaviour as a function of the pump energy. Figure 3.6 shows the unseeded parametric fluorescence energy plotted alongside the fully seeded case as a function of pump energy for the Cerberus ps-OPA amplifiers. The unseeded and seeded fluorescence generated from the ps-OPAs both rise exponentially with increasing pump energy, though with different coefficients, which is expected for small signal gain as a function of pump energy. When the

ps-OPA stages are operating in saturation with 2.05 mJ total pump energy, the unseeded and seeded fluorescence intensities are 20 nJ and 0.4 nJ respectively.

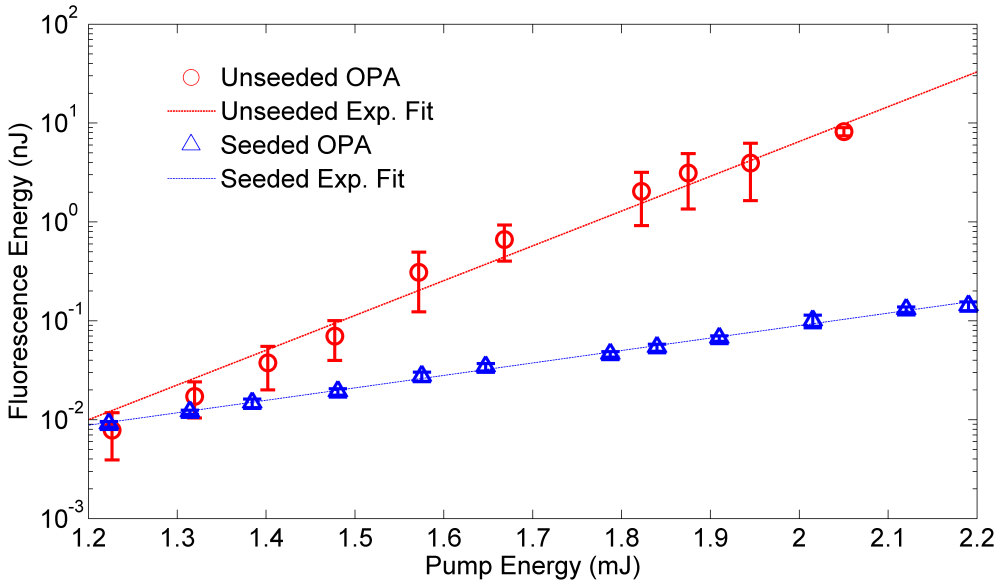


Figure 3.6: Parametric fluorescence energy generated from the ps-OPAs as a function of the total pump energy for the unseeded amplifier (red circles) and the fully seeded case (blue crosses). The seeded ps-OPA fluorescence is expected to always be less than or equal to the unseeded case and so we assume there is a systematic error of ~15 pJ is present at low pump energy, where the fluorescence levels approach the detection limit of the photodiode.

The characterisation of the fluorescence generated in these ps-OPAs represents a significant step towards understanding its impact on temporal contrast. With such a device, the fluorescence emission from the OPAs can be quantified to a higher dynamic range than with an autocorrelator, as the dynamic range is directly related to the number of spectral filters added. The fast single-shot acquisition from the photodiode detector enables optimisation of the parameters of the laser that affect the parametric fluorescence intensity and also allows the statistics of the noise photon spectral distribution to be explored in §3.2.5.

The results in figure 3.6 show the fluorescence is in competition for amplification with the laser seed, as increasing the pump energy to the OPAs produces significantly less parametric fluorescence for the seeded OPA compared to the unseeded case. The results agree with the common assumption that the fluorescence intensity decreases when the amplifiers are seeded and figure 3.7 quantifies this relationship in detail. Evidence for the physical mechanism behind this behaviour is best illustrated in figure 3.7a), which

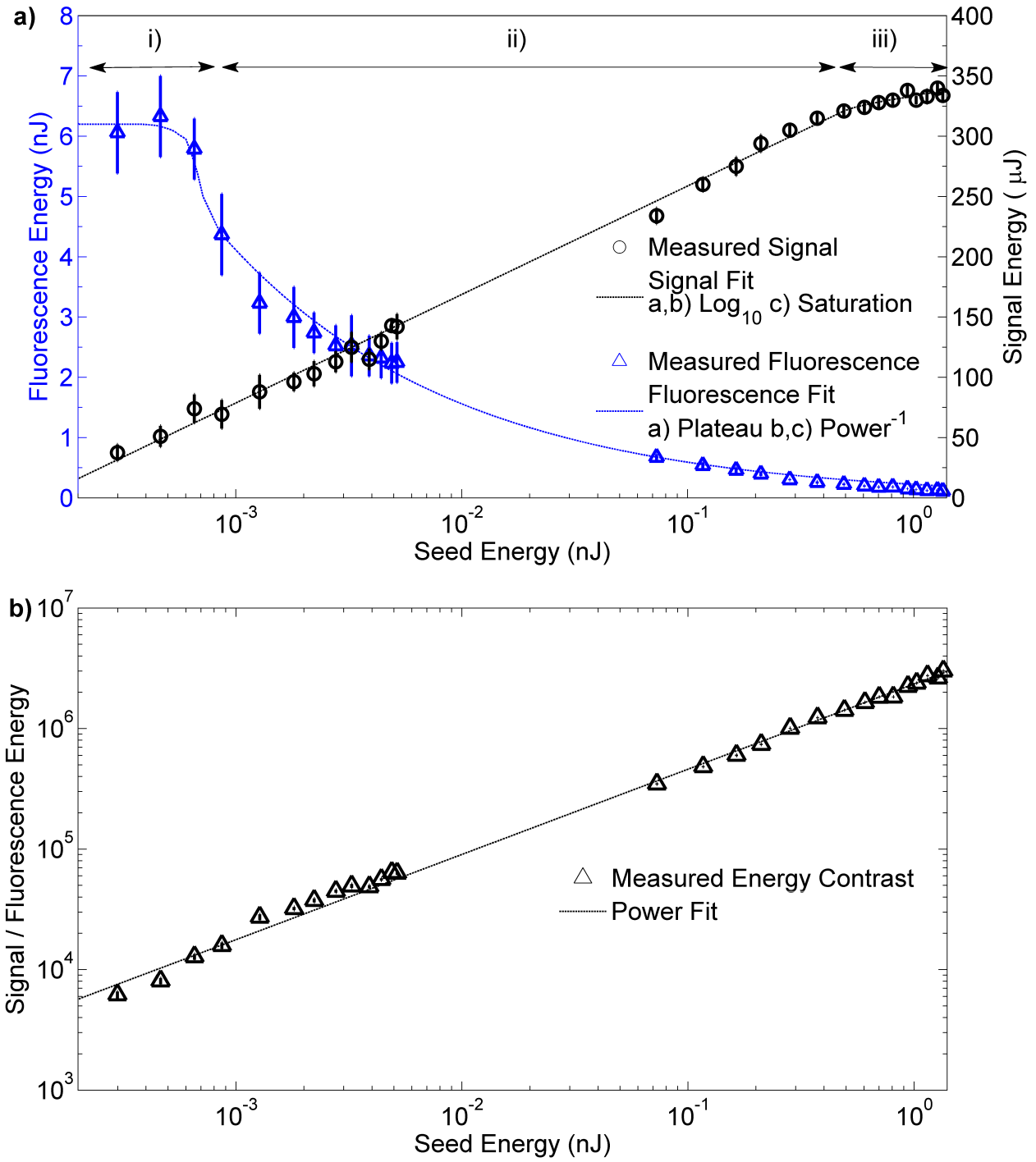


Figure 3.7: a) Measured parametric fluorescence (blue crosses) in competition with the OPA seed (black circles). Three regions of amplification behaviour are identified, from i) the undepleted pump regime, where fluorescence is broadly similar to the unseeded case, ii) the onset of pump depletion, where the fluorescence intensity becomes strongly quenched with less available pump, and iii) strong pump depletion, where the pump intensity centre becomes comparable to them main laser signal, creating a gain saturation effect. b) Energy contrast between the ps-OPA signal and fluorescence as a function of the seed energy.

investigates the total fluorescence from both stages as a function of the seed energy into the first ps-OPA stage.

At low seed levels, the OPA operates in the undepleted pump regime for seed energies <0.7 pJ (case i). As the residual pump temporal profile is difficult to retrieve, the amount of pump depletion was cross-checked against a 1D OPA code used previously to design the ps-OPA stages [40], which predicts a pump depletion of >0.5 % at the temporal maxima for seed energies >1 pJ. The level of pump depletion increases with greater seed energies (case ii) until the amplified signal reaches the maximum saturation point of 335 μJ, i.e. before significant energy back-conversion at the temporal intensity centre (case iii). A key point is that the fluorescence in the undepleted pump regime for a seeded OPA agrees with the fluorescence generated for the unseeded case with equal pump energy.

For larger seed energies, the greater pump depletion leads to less fluorescence generation, following an inverse power relationship. In the saturation regime (case iii), there is little change in net available pump energy and so the observed fluorescence remains approximately constant. At the saturation point, the combined ps-OPA stages generate 335$\pm$5 μJ of signal energy with 320$\pm$20 pJ fluorescence averaged over 500 shots at 10 Hz repetition rate. The pump and seed pulse energies both have root mean square stabilities (RMS) of 1 %.

From these measurements, the energy contrast, shown in figure 3.7b), between the OPA signal and fluorescence is seen to be improved considerably by a factor of ~1000 from $2\text{x}10^3$ to $2\text{x}10^6$ with greater pump depletion, producing a maximum total gain of $2.7\text{x}10^5$ for the primary laser seed. Although we have no analytical proof of the underlying scaling law, we observe the relationship between increasing seed energy E_s (i.e. more pump depletion) and energy contrast is found to be $\propto E_s^{-1/\sqrt{2}}$.

3.2.3 *Analysis: Seeded OPA Fluorescence Contrast*

A cross-correlation of the parametric fluorescence intensity from OPA1 amplified in OPA2 as a function of pump timing and measured by a photodiode yielded yields a ~2.1 ps pulse duration of the parametric fluorescence generated in the ps-OPAs, which agrees well with Dorrer et. al. [64], who use similar ps-OPA parameters.

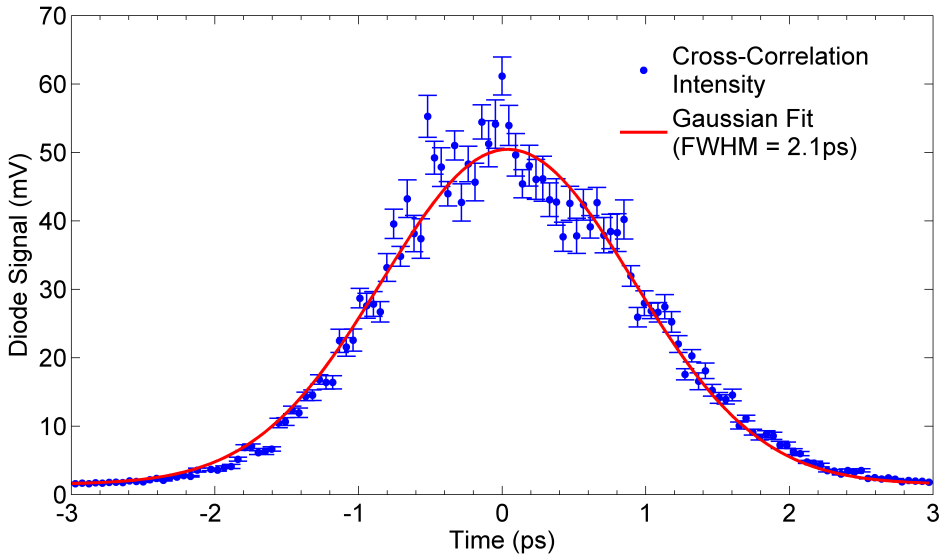


Figure 3.8: Cross-correlation as a function of time-delay between the OPA2 pump and parametric fluorescence generated in OPA1. A 2.1 ps FWHM pulse is retrieved after a $\sqrt{2}$ deconvolution factor for Gaussian pulses is applied.

After compression, the incoherent parametric fluorescence is expected to have a negligible residual chirp of 0.152 ps^2, as it does not pass through the bulk material stretcher for the ps-OPA seed.

The spectral offset between fluorescence and laser seed for non-collinear OPA helps to reduce contrast degradation, as any fluorescence produced outside of the down-stream stretcher of final compressor spectral acceptance windows will be filtered out very efficiently. The ns-OPA stretcher and final compressor used here both have a finite bandwidth acceptance of 20 nm from 1044 nm to 1064 nm. Thus, only 8% of the energy of the broadband fluorescence from the ps-OPAs will propagate through the system. Therefore, the parametric fluorescence contribution from the ps-OPAs have been modelled in figure 3.9, showing an estimated temporal intensity contrast of ~7x10^9 at 1.3 ps before the peak of the primary laser pulse after compression.

Pump depletion can therefore be seen as a highly desirable characteristic in an OPA in order to maximise the temporal contrast with respect to parametric fluorescence. This experimental analysis agrees with numerical modelling of fluorescence in the pump depletion regime by Manzoni et al. [75] together with a theoretical study by Ross et al. who also recommend operating in the pump depletion regime to minimise contrast degradation from pump intensity noise effects [65].

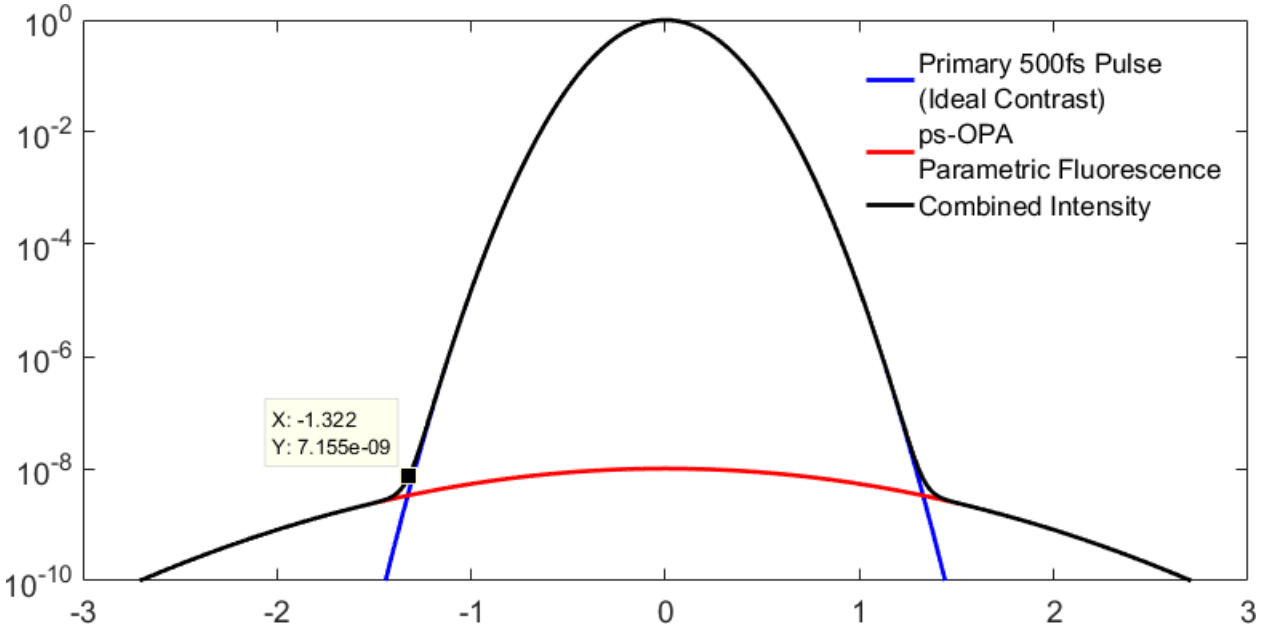


Figure 3.9: Modelling of the temporal profile on a log scale of an ideal 500 fs compressed high-power laser pulse from the Cerberus laser (blue) against the parametric fluorescence intensity envelope (red), whose energy and duration have been determined with the seeded OPA fluorescence diagnostic. The combined intensity envelope shows the contrast to be limited to ~7x10^9 at ~1.3 ps before the arrival of the primary pulse and therefore well optimised for enabling high-contrast laser matter interaction experiments.

3.2.4 *Analysis: Parametric Fluorescence Input Noise*

The semi-classical origin of parametric fluorescence is generally accepted to be the zero-point fluctuations of the electromagnetic field acting as a seed source for OPA in the non-linear crystal. The absolute number of background seed photons can be estimated using the known small-signal gain values of the OPA stages in the undepleted pump regime. This gain value can be extracted from the experimental data in figure 3.7, where the undepleted pump regime exists for very low laser seed energies, and is found to be 1.30$\pm$0.2x10^8 for the Gaussian temporal and spatial profiles of the pulses. It should be noted that this value fits well with an analytical value of 2.12x10^8 for the small signal gain in (2.9) using a plane-wave approximation analysis.

In the undepleted regime, 18$\pm$2 nJ of fluorescence is observed directly downstream from the OPA, meaning that 870$\pm$160 seed photons, or 2.1$\pm$0.4 photons ps^{-1} nm^{-1} were needed to produce this amount of fluorescence in the OPA process at these wavelengths.

The absolute level of spontaneous fluorescence seed in an OPA amplifying a 532 nm CW laser in BBO was determined experimentally by Homann and Riedle to be ~58 photons

across a 50 nm fluorescence emission bandwidth pumped by a 150 fs pulse [76]. This agreed within a factor of 1.4 to a formula adapted from stimulated Raman scattering theory to determine the effective number of noise seed photons N_{eff} in its parametric fluorescence analogue in OPA [76]:

$$N_{eff} = \frac{n^2 \triangle \lambda c \tau}{\pi \lambda^2} \tag{3.2}$$

where n is the refractive index of the signal in the non-linear amplifier medium, λ and $\triangle\lambda$ is the central wavelength and observable bandwidth of fluorescence produced respectively, c is the speed of light and τ is the fluorescence pulse duration. It should be noted that this equation matches very closely with those reported in[18, 29]. When applied our ps-OPA observations of 200 nm bandwidth centred at 1 μm with 2.1 ps pulse duration, (3.2) yields a value of 98 photons, or 0.23 photons ps^{-1} nm^{-1}. This value agrees within a factor of ten to the measured 2.1$\pm$0.4 photons ps^{-1} nm^{-1} fluorescence seed above. Possible discrepancy between the two values may be due to measurement error of the small signal gain, as the 0.3 pJ seed in the undepleted regime and is more prone to systematic error of the photodiode calibration with a very weak signal.

3.2.5 *Analysis: Shot-to-Shot Fluorescence Intensity Statistics*

The fluorescence energies reported above have so far only considered average values measured over >500 shots. The shot-to-shot fluorescence signal from the OPA stages, shown in figure 3.10, has been observed to fluctuate significantly, with ~63% RMS deviation, compared to the 1% RMS deviation of the OPA pump and laser seed pulses. This indicates that the large fluorescence fluctuations observed are an unavoidable consequence of the exponential photon distribution of the vacuum fluctuations [77]. The observed Poisson-like distribution of the fluorescence energy supports the case for a randomly fluctuating seed term.

The significance of these large fluctuations on experiments sensitive to the temporal contrast of the laser is the relatively small shot-to-shot probability of the fluorescence contribution to the temporal contrast increasing to an unacceptably high level. For our ps-OPA system, there is a 1.5% probability of fluorescence becoming five times greater than the mean and a 0.3% chance for a ten-fold increase in fluorescence on a single shot.

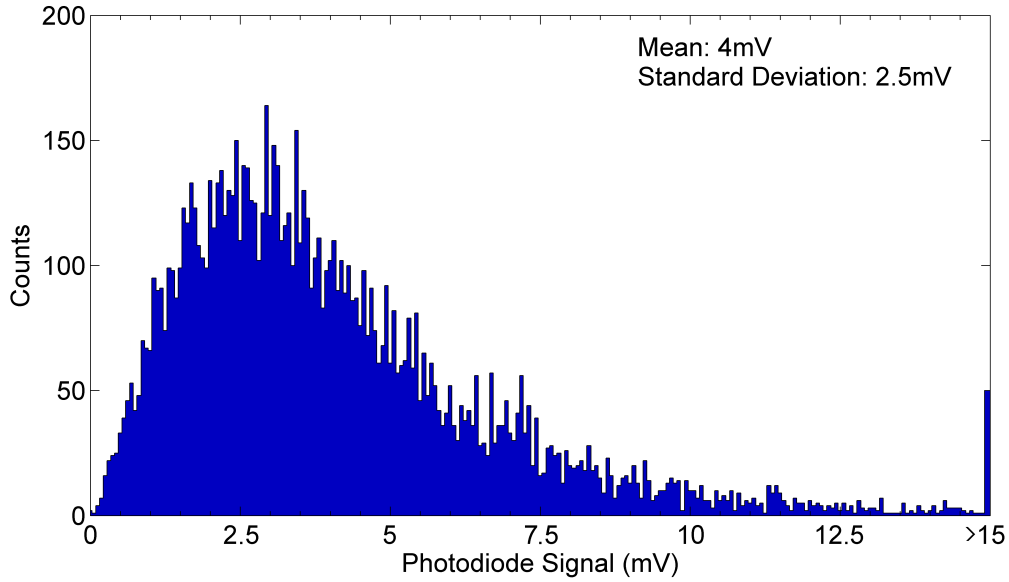


Figure 3.10: Measured photon statistics of the parametric fluorescence producing a Poisson distribution, demonstrating the random nature of the fluorescence seed, which can occasionally produce much brighter fluorescence background from shot-to-shot as a result.

3.2.6 *Conclusions*

We have demonstrated a simple and effective method to directly characterise the parametric fluorescence emission from a seeded picosecond-regime OPA system operating with ~10^8 small-signal gain and ~10^5 saturated signal gain without requiring additional amplifiers or a chirped-pulse compressor to resolve the weak fluorescence signal. This method can in principle be applied to any OPA system that generates fluorescence bandwidth that is not contained in the seed and can be spectrally filtered to clearly discriminate it from the amplified seed light.

We have determined that the fluorescence emission intensity is directly linked to the pump intensity in the non-linear crystal. The only competition effects we have observed with the seed are due to the depletion of the available pump energy. We observed that the fluorescence energy decreases by a factor of ~60 when achieving pump-depletion for pump pulses five times longer in duration than the seed, yielding a contrast enhancement factor of ~500 from undepleted to maximum pump depletion modes of operation at the intensity centre. It is expected that the fluorescence can be reduced by increasing the seed duration to further increase pump depletion in the temporal wings of the pump pulse, improving energy extraction at the cost of bandwidth amplification.

The determination of the laser seeded OPA absolute fluorescence energy, bandwidth and duration is sufficient to determine the contrast limitation after compression. When applied to our ps-OPA system, we have estimated the fluorescence emission from these OPAs to contribute a 2.1 ps pedestal with $7x10^{-9}$ temporal intensity contrast at 1.3 ps before the peak of the primary laser pulse after compression. In addition to pump-depletion in the OPAs, blocking the broadband fluorescence bandwidth outside of the laser bandwidth in the downstream pulse stretcher and compressor contributes a significant factor in reducing fluorescence and improving intensity contrast on target.

The mean absolute level of the incoherent fluorescence seed source has been experimentally determined to be 2.1 ± 0.4 photons ps^{-1} nm^{-1}. The random intensity fluctuations of the fluorescence seed will contribute to a population of 1.5% of shots with five times greater fluorescence intensity and 0.3% probability of a ten-fold increase in the mean fluorescence intensity. This diagnostic and experiment findings have been published in a peer-review journal [36].

4

CONTRAST CHARACTERISATION OF OSCILLATORS THAT SEED HIGH-POWER LASERS

The temporal intensity contrast of the short-pulse laser oscillator pulse that seeds a high-intensity laser system sets a baseline noise level for amplification to terawatt to petawatt peak-powers. In addition to a high-contrast output, sources that are suitable for seeding high-energy, high peak-power laser systems are typically <500 fs in duration and their emission bandwidth is selected to be compatible with large aperture amplifiers, for example Nd:Glass, to achieve terawatt to petawatt peak-powers.

All short-pulse mode-locked oscillators use non-linear effects to preferentially select and amplify an intense pulse above the CW spontaneous background emission. The optical Kerr effect is most commonly used in Ti:Sapphire lasers [78–80], whilst semiconductor saturable absorbers are used for many >40 fs systems [61, 62, 81]. Partial and all-fibre laser oscillators using the broad 1030 nm ytterbium laser transition typically use the "non-linear polarisation evolution" (NPE) scheme [82–84], essentially non-linear elliptical rotation from the Kerr effect, over long fibre lengths. Large advances have also been made in synchronously pumped optical parametric oscillator (OPO) technology [85, 86]. All these techniques can be used to create sources that seed Ti:Sapphire or Nd:Glass amplifier chains at 800 nm or 1054 nm respectively. The round trip frequency of short-pulse oscillators are typically around 70 MHz, and therefore all noise components will be emitted at that frequency if the cavity is in a steady state, i.e. within ~10 ns window of the primary pulse, generally a safe approximation for steady-state mode-locked cavities.

Previous investigations into the temporal contrast of short-pulse oscillators in 1995 by Braun et al. compared Kerr Lens (KLM) and saturable absorber mode-locked sources using a high dynamic range second-order autocorrelator [87]. They observed that cavities employing saturable absorbers generated $>10^8$ contrast pulses, with the observable noise floor limited by the measurement dynamic range. The KLM sources were found to produce considerably greater optical noise, with pedestals observed at the 10^{-5} intensity level.

With recent advances in laser technology, particularly with the emergence of compact turn-key fibre-based ytterbium lasers and femtosecond-pumped OPOs, a broader and more detailed comparison of these laser sources was undertaken to re-assess the performance of "older" systems at higher dynamic range, and benchmark them against new technologies to determine which mode-locking techniques best lend themselves to high contrast operation. The methods and findings we present in this chapter have contributed towards a publication [37].

Our investigations in this chapter used third-order autocorrelation techniques to allow observation of asymmetric processes with 10^8-10^{10} dynamic range between measurements across a greater scope of mode-locking techniques, with a list of oscillators characterised presented in table 4.1. The temporal intensity contrast characterisation of the laser oscillators were carried out using the TOAD correlator system, as described in §3.1, providing unambiguous time-asymmetric traces with 10^7-10^{10} dynamic range. The laser sources investigated all emitted pulse trains ranging from 2-35 nJ per pulse and 50-300 fs in duration. In each case, the TOAD was aligned to the laser source with minimal beam delivery optics to avoid the introduction of external-cavity secondary pulses, e.g. from multiple internal reflections in a parallel-faced transmissive optic, such as a waveplate. As previously mentioned in §3.1, the temporal resolution of the TOAD was determined to be ~200 fs, limited by the group velocity dispersion through the length of the sum-frequency crystal, as it was optimised for complete system characterisation of the Cerberus 500 fs OPCPA front-end pulses. This limitation only prevents accurate measurement of pulse duration, which is more routinely achieved with second-order autocorrelation techniques. However, the increased crystal length and optimal focal length allowed greater dynamic range from measurements on >200 fs timescales, allowing improved observations of low-intensity noise features.

As far as we are aware, this is the first time a broad review of oscillator contrast performance has been conducted using a third-order autocorrelator and also the first time the temporal contrast of NPE fibre and OPO sources suitable for seeding high-energy laser systems has been measured directly alongside saturable absorber and KLM oscillators from using a common diagnostic to characterise these sources to provide reliable informative comparisons.

The results presented in this chapter includes the characterisation of existing oscillator sources used for seeding OPCPA and Nd:Glass terawatt and national facility petawatt laser systems throughout the UK. This includes the Orion petawatt laser facility (AWE

Laser Oscillator	Gain Medium	Mode-locking Mechanism	Pulse Energy	Pulse Duration	Location
Time-Bandwidth GLX-200HP	Nd:Glass	SESAM	5 nJ	250 fs	Imperial College (Cerberus)
Time-Bandwidth GLX -100	Nd:Glass	SESAM	2 nJ	300 fs	STFC Central Laser Facility (Vulcan)
Spectra Physics Tsunami	Ti:Sapphire	KLM	5 nJ	120 fs	STFC Central Laser Facility (Vulcan) + AWE Aldermaston (Orion)
Coherent MIRA 900-F	Ti:Sapphire	KLM	5 nJ	120 fs	Queens University Belfast (TARANIS)
Light Conversion FLINT 2.0	Yb:KGW	KLM	25 nJ	100fs	Imperial College (Laser Consortium)
Coherent Fidelity-2	Yb-doped Fibre	KLM	30 nJ	50 fs	Queens University Belfast (TARANIS)
Spectra Physics Insight DS+	Non-linear Crystal	OPO	12.5 nJ	120 fs	STFC Central Laser Facility (Vulcan)

Table 4.1: Oscillator sources characterised by the TOAD for contrast investigations described in [37].

Aldermaston) [4], Vulcan petawatt national laser facility (Central Laser Facility, STFC) [2], TARANIS (Queen University Belfast) 20 TW [88] and the Cerberus 2 TW beamline (Imperial College London) short-pulse laser oscillators. Further contrast characterisation of these laser system front-ends or complete beamline characterisation are presented in chapter 5.

4.1 SHORT PULSE GENERATION VIA MODE-LOCKING

The mode-locking mechanism inside a laser pulse cavity typically operates by introducing a non-linear (intensity dependent) mechanism to preferentially amplify stronger pulses. The loss or gain effect is usually very small per round trip but over many round trips inside the cavity, high-contrast ultrafast pulses can be generated and be sustained. Various methods exist to passively mode-lock the cavity, ranging from saturable absorbers, Kerr-lens cavities and soliton generation that all preferentially propagate and amplify a short-pulse over the continuous spontaneous emission background.

4.1.1 *Saturable Absorber Mode-Locking*

Saturable absorption occurs from the finite absorption capacity of a material. A suitable material will absorb light across the laser bandwidth and start to become saturated at higher intensities, producing a non-linear absorber that becomes more transparent to higher-intensity pulses when in this saturation regime. Semiconductors are typically used to engineer a well-defined band-gap energy with fast transition rates between the valence and conduction bands. The mode-locked pulse durations will be of order of the relaxation time of the transition [62] For lasers emitting around 1 μm, typical for solid-state petawatt laser systems, InGaAs is often used as a quantum well absorber, with varying Indium content to control the band-gap energy [61]. This semiconductor absorber layer is then deposited on to a highly reflective mirror, giving their name as semiconductor saturable absorber mirrors (SESAM). The modulation depth between the unsaturated and saturated states are typically around 1-2% and are therefore only suitable for intra-cavity use in various oscillator designs.

When used intra-cavity, these devices first produce pulses from very small noise fluctuations of the ASE and are thus “self-starting” in principle. The fast, few hundred femto-

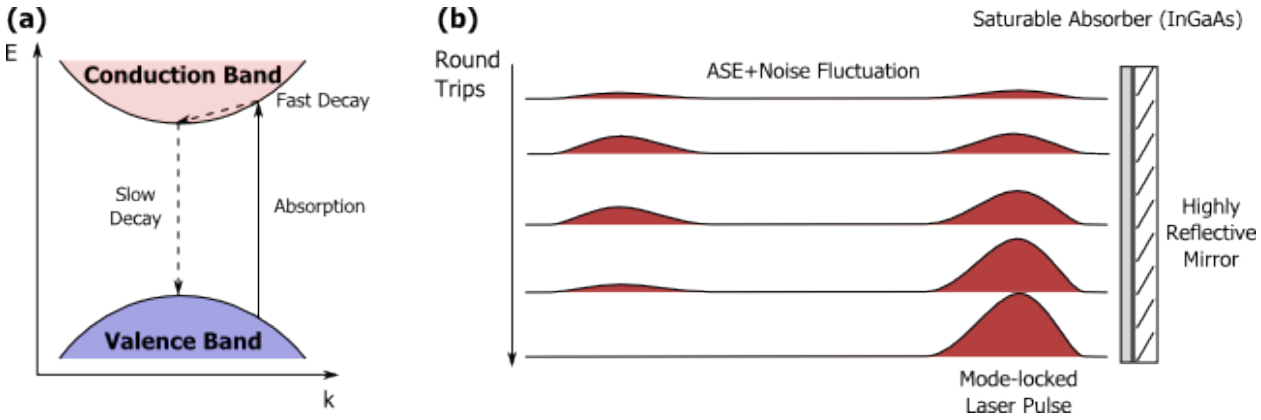


Figure 4.1: Non-linear saturable absorption method to produce mode-locked laser pulses. (a) Valence electrons are excited to the conduction upon absorption of laser light. Limited carriers in conduction band produce saturable absorption effect, which quickly decay of order 10-200 fs via intra-band relaxation and more slowly over 1-10 ps from recombination back to the valence band. (b) The effect over multiple round trips to gradually accentuate the formation of a short-pulse.

seconds, impulse response combined with modest <1% modulation depth in the absorber effectively suppresses ASE [61, 81]. The relatively slower recovery of available absorbers, tens of picoseconds, has little effect on contrast once the pulse has extracted the available gain in the steady-state mode of operation, further suppressing ASE.

The mode-locked pulse duration is mainly determined by the SESAM impulse response, the gain medium emission bandwidth, the cavity mirrors' reflectivity bandwidth and the degree of intra-cavity dispersion management.

The contrast of SESAM mode-locked Nd:Glass lasers were previously found to exhibit $>10^8$ contrast [87], limited by the dynamic range of the diagnostic used to investigate their performance.

We were similarly able to measure the temporal contrast from two SESAM mode-locked oscillators at high dynamic range with the TOAD. Their close-in ($\pm$8 ps) contrast is shown in figure 4.2. The first was the Cerberus oscillator (Time-Bandwidth GLX 200HP), described in §2.5, which can emit 5 nJ, 250 fs, 70 MHz pulse trains and showed a near ideal contrast up to the maximum 2.5×10^9 dynamic range of the measurement, limited by the available pulse energy. This was achieved with the oscillator operating slightly below optimum during the measurements, producing only 3.7 nm bandwidth, able to support a Fourier-transform limited duration of 315 fs from (1.2). The other system investigated is a similar design SESAM mode-locked laser oscillator (Time-Bandwidth GLX-100) of the Vulcan laser system at the Central Laser Facility, producing similar pulse durations

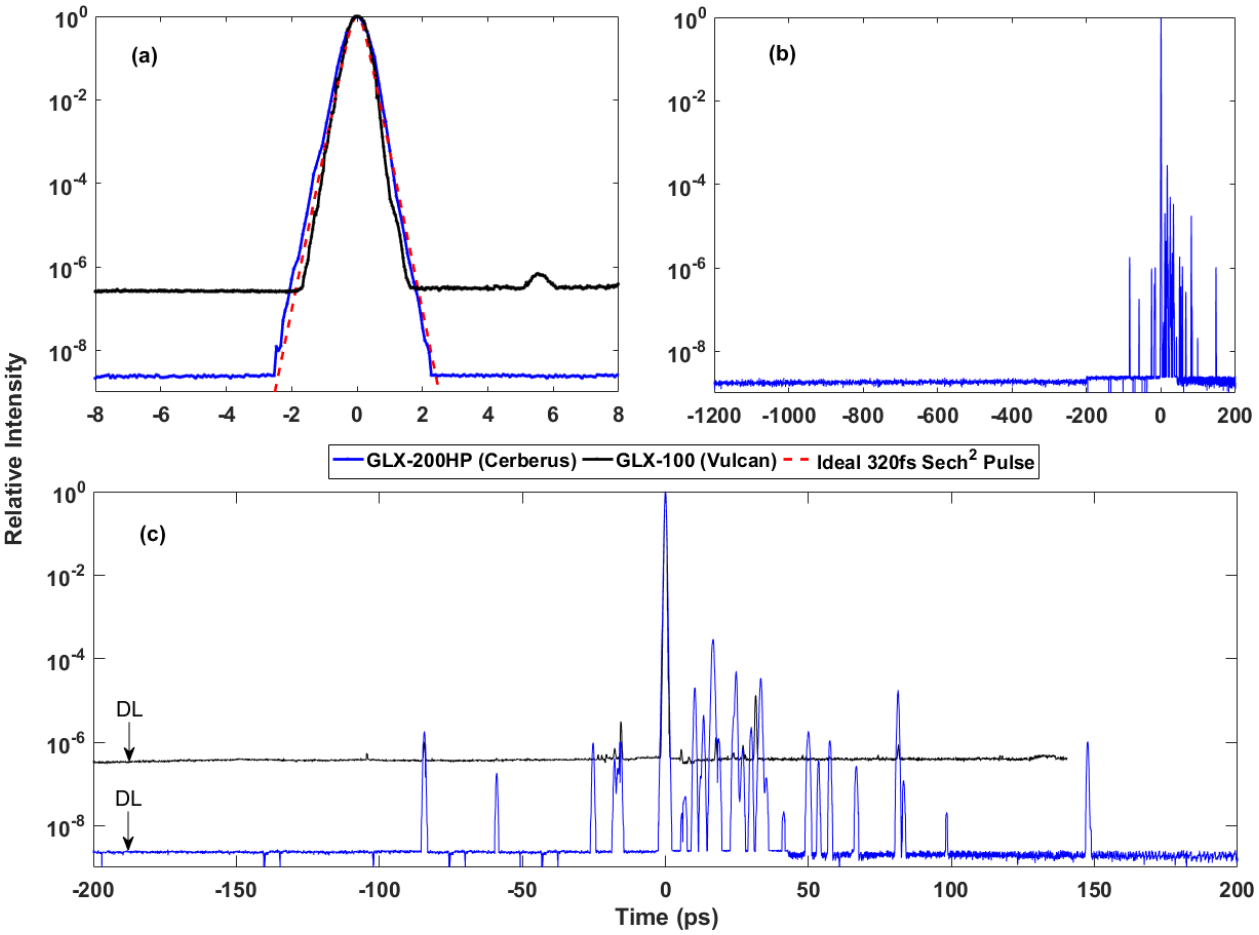


Figure 4.2: Measured third-order autocorrelations of SESAM mode-locked Nd:Glass oscillators: Cerberus GLX-200HP (blue), Vulcan GLX-100 (Black). (a) Close-in contrast showing emitted pulses fitted against an ideal 320 fs FWHM sech^2 pulse (red dashes, deconvolution factor applied), showing high-contrast operation and highly effective ASE noise suppression from the saturable absorber. (b) Long range contrast of the Cerberus GLX-200HP oscillator, showing no pre-pulse generation, real or artefact, beyond ~100 ps. (c) Mid temporal range plot of same contrast scans of both SESAM oscillators. The pre-pulses observed are thought to be measurement artefacts, as they are common features in all scans with the TOAD. DL: The detection limit of the TOAD that ultimately limits the maximum dynamic range with each scan, which is primarily dependent upon the pulse energy into the diagnostic.

with less pulse energy and used to seed the "Target Area West" CPA Nd:Glass short-pulse beamline. This oscillator displayed a near ideal close-in pre-pulse contrast within the 2.5×10^7 dynamic range of the measurement.

Laser pulses as short as 60 fs can be achieved with this technique [62] and even 40 fs pulses have been achieved from Nd:Glass SESAM oscillators with the use of mixed gain media [89]. Such a source, in combination with bandwidth broadening amplification from optimization of OPCPA [90] offers an attractive high-contrast seed that can potentially produce bandwidths able to support <20 fs amplified pulses. The useful self-starting properties of saturable absorbers have also been used in conjunction with Kerr-lens mode-locked cavities [40, 91].

4.1.2 *Kerr Lens Mode-Locking (KLM)*

Kerr lens mode-locked (KLM) lasers utilise intensity dependent self-focussing, introduced in §2.4.1, to produce an intensity-dependent spatial cavity mode or cavity length that is most stable for a more intense pulse. For a simple two mirror cavity, the stability of a cavity can be determined by the following equations:

$$\begin{aligned} g_1 &= 1 - \frac{L}{R_1} \\ g_2 &= 1 - \frac{L}{R_2} \\ 0 &< g_1 g_2 < 1 \end{aligned} \tag{4.1}$$

Where L is the cavity length and $R_{1,2}$ is the radii of curvature of the cavity optics. It is therefore possible to design a cavity that is unstable for short lengths and stable for slightly longer, intensity dependent lengths from the Kerr effect. The temporal Kerr effect non-linearly increases the refractive index of materials (e.g. the gain medium of the laser), and hence the cavity length, or spatially it creates a positive lens, introducing a third term in (4.1) with an intensity-dependent radius of curvature. If we consider the more simple temporal case and a planar mirror, with $R_1 = \infty$, the cavity is only stable for $0 < g_2 < 1$. This is satisfied when $L > R_2$. If we denote the shorter, low-power, cavity length as L_{low} and the longer high-power threshold length as L_{high}, the cavity can therefore be mode-locked when$L_{low} \leq R_2$ and $L_{high} > R_2$.

The optical Kerr effect is most notably used for passive mode-locking of Ti:Sapphire oscillators, frequently achieving <20 fs pulse durations at 800 nm and <120 fs for 1 μm

operation when matched with careful dispersion control. These laser sources offer an attractive route to quickly achieving ultrafast amplified pulses. For stable operation, the mode-locked cavity length, or mode, is sufficiently separated from the CW mode such that the cavities do not exhibit self-starting properties. Active mechanisms to initiate mode-locking such as moving a cavity mirror forward and backwards or the use of an acousto-optic modulators (AOM) to initially Q-switch the cavity are usually employed. Alternatively, hybrid mode-locking schemes that utilise the self-starting and ASE absorption advantages of a SESAM inside a KLM cavity have been reported, producing 6.5 fs pulses at 800 nm with Ti:Sapphire gain media [92, 93].

The investigations by Braun et al. [87] and Jung et al. [92], using second-order autocorrelators, found short-range noise pedestals from laser oscillators attributed to a combination of self-phase modulation, the temporal dependence of the Kerr effect, and third-order dispersion (TOD).

We have similarly characterized a range of KLM oscillators that lase at 1054 nm central wavelength that are suitable for Nd:Glass amplification. These sources deliver pulses ~120 fs in duration with up to 5 nJ pulse energy. The first sources we investigate are two nominally identical models of KLM Ti:Sapphire oscillators (Spectra Physics Tsunami). The KLM is not self-starting and therefore these cavities are initially actively mode-locked using an acousto-optic modulator (AOM) to effectively q-switch the cavity.

In figure 4.3a-c we present the measured contrast performance of these KLM lasers when using the TOAD. The measurements of these notionally identical laser sources displayed very different noise pedestal features, both starting at ~10^{-6} intensity level. A large asymmetric pre-pulse foot is seen in figure 4.3a, indicative of negative net higher odd order dispersion. Although not modelled here, self-phase modulation may also be contributing to low intensity spectral wings that produce temporal pedestals after dispersion effects. However, modest increases in the pumping power of the Vulcan oscillator when under test had no effect on the pedestal observed. Although we do not present the results here, a similar KLM Ti:Sapphire laser design (Coherent MIRA) was characterized and showed similar symmetric pedestal intensities and temporal extents to the Vulcan Tsunami, indicating these pedestal features are not device specific and are characteristic of Ti:Sapphire and/or KLM operation.

Kerr lens mode-locked sources can also be produced from other gain media. We were able to observe similar pedestal features from a KLM Yb:KGW oscillator (Light Conversion Flint), which has a specified pulse duration of 80 fs with up to 12 nJ energy per

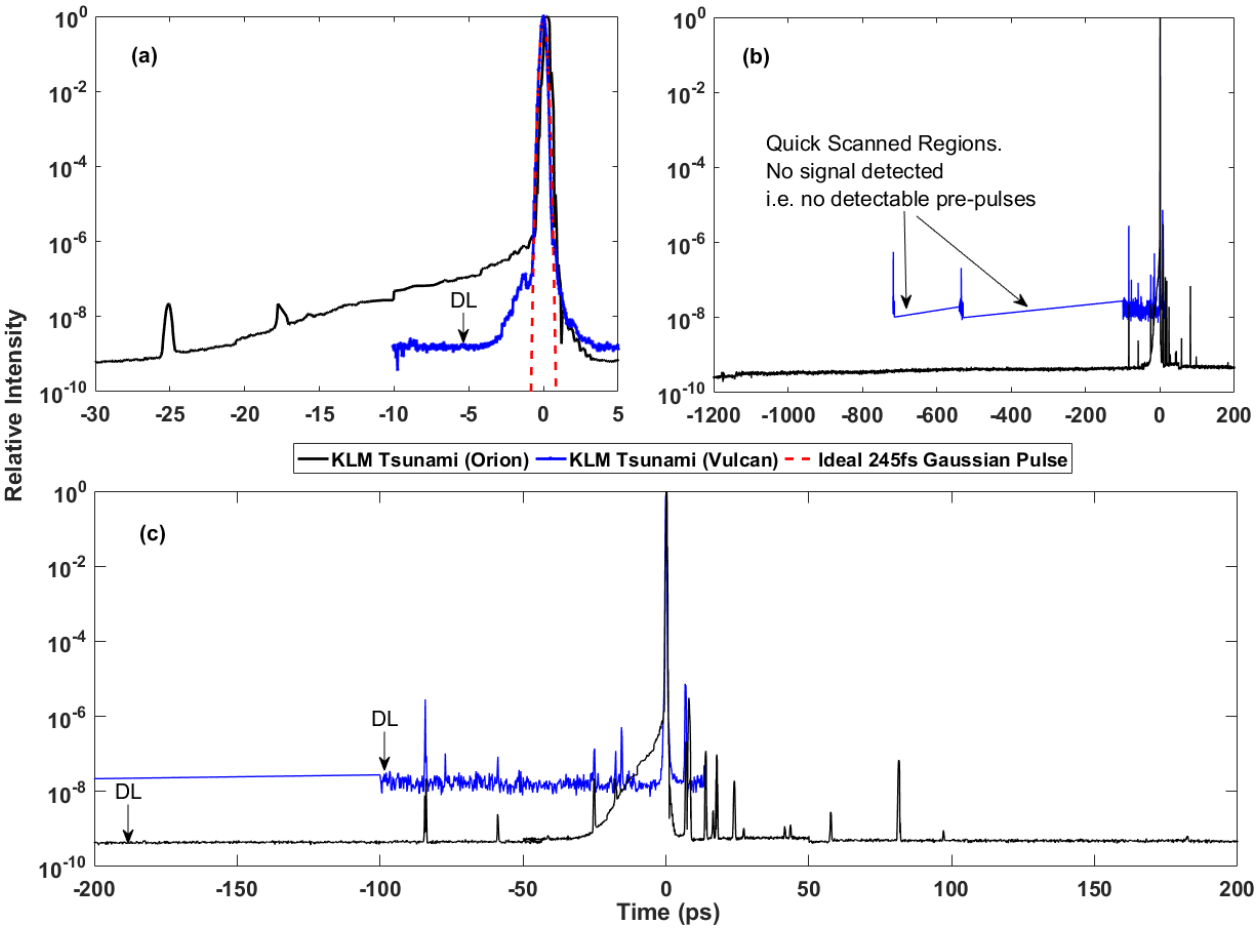


Figure 4.3: Measured third-order autocorrelations of Kerr-lens mode-locked (KLM) laser sources: Orion Tsunami (black), Vulcan Tsunami (blue). (a) Close-in contrast showing emitted pulses fitted against an ideal 245 fs FWHM Gaussian pulse (red dashes, deconvolution factor applied). Short-range pedestals starting at 10^{-5} to 10^{-6} relative intensity appear to be a common feature of KLM lasers. Although these laser systems are notionally identical models, there are large differences in the pedestal shape and temporal extent, which may be due to the large number of degrees of freedom available when aligning and optimising the cavity. (b) Long range contrast of the two sources. The Orion Tsunami pulses show a long-range contrast greater than the 4×10^{-10} dynamic range of the measurement; however, discrete pre-pulses of ~5×10^{-7} relative intensity at 717 ps and 535 ps ahead of the primary pulse appear to be generated from the Vulcan Tsunami, which can be introduced from the oscillator or from external cavity laser optics. (c) Mid temporal range plot of same contrast scans of both KLM oscillators. Prepulses observed are thought to be measurement artefacts, as they are common features in all scans with the TOAD. DL: The detection limit of the TOAD that ultimately limits the maximum dynamic range with each scan, which is primarily dependent upon the pulse energy into the diagnostic.

pulse at 1030 nm wavelength. Although the data is incomplete, as the source became inoperable mid-way through the characterisation experiments, we are able to see the appearance of asymmetric pedestals acting in the opposite time direction to the Orion KLM Ti:Sapphire laser, which is characteristic of positive higher-order dispersion. This result indicates these pedestal origins are from the KLM mode-locking mechanism rather than a characteristic of the Ti:Sapphire gain medium. In figure 4.4 we show the preliminary dataset against resolution limit of the TOAD.

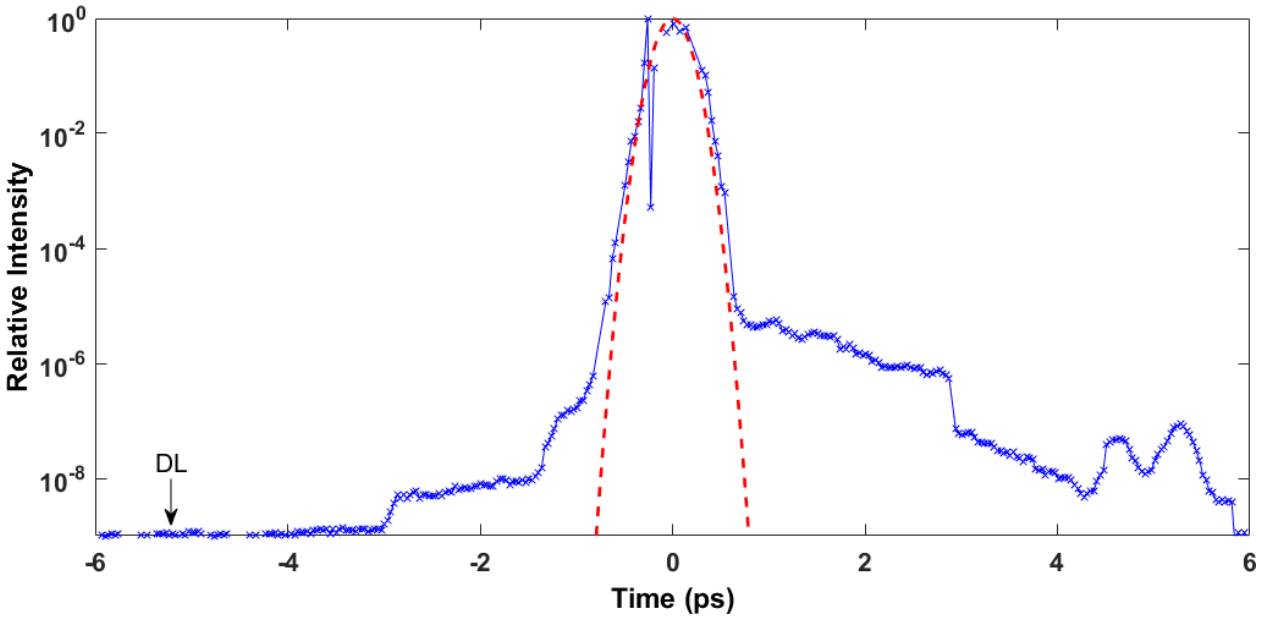


Figure 4.4: Measured third-order autocorrelation of a KLM Yb:KGW oscillator (Light Conversion Flint, blue) against the TOAD resolution limit (red), showing preliminary contrast results and the observation of asymmetric pedestal features at similar intensity found in the Ti:Sapphire sources.

As the 1030 nm central wavelength of this laser is slightly offset from the normal 1054 nm operation, the density filtering on the TOAD required re-optimisation and calibration to capture the entire envelope. We can only show the dataset without optimal filtering, which has been stitched together and fitted to the 245 fs TOAD resolution limit found previously, showing an expected 10^9 dynamic range. A large asymmetric foot was observed behind the primary pulse starting at an estimated 10^{-5} level and extending behind the main pulse to a few picoseconds, which is comparable to the results seen with the Ti:Sapphire KLM oscillators. Notably this pedestal acts in the opposite direction, attributed to positive odd higher-order phase, when compared to that seen with the Orion Ti:Sapphire Tsunami KLM oscillator, which has net negative odd-order phase.

Recreating these pulse pedestals via the Taylor expanded spectral phase in (1.7) requires non-convergent amounts of increasing higher order phase and therefore the current mathematical formalism we use for the modelling the spectral phase and temporal envelope of the ultrashort pulse is not valid in these asymmetric pulse foot scenarios where the ultrashort pulse envelope is also affected by other cavity effects of the non-linear mode-locked oscillator, such as self-phase modulation (SPM) and the mode overlap between KLM and CW operation. These third-order processes are automatically phase-matched and therefore it becomes difficult to disentangle these from each other in the experiment.

Self-phase modulation occurs as a temporal manifestation of the Kerr effect, where the time varying intensity envelope of an optical pulse produces a temporal phase accumulation. Without the presence of dispersion, addition of phase without modification of the pulse duration must therefore be compensated by an enhancement of the spectral content. Pulses which have been influenced by this effect typically have characteristic spectra with enhanced side-lobes and modulations. Dispersion first acts to translate these spectral modulations into temporal modulations, although it is still possible to recreate a high-contrast pulse from elimination of dispersion after SPM. However, an intermediate non-linearity can also occur from excessive SPM acting at the same time as dispersion. Known as "optical wave-breaking" [94], dispersion acts to mix the frequency components of the non-monotonic temporal/spectral phase of the pulse and non-linearly interfere to produces strong side-lobes that destabilise the pulse, eventually splitting a single pulse into multiple sub-pulses [95].

4.1.3 *Non-linear Polarisation Evolution (NPE) Yb-Fibre Laser*

Recent advances in mode-locked laser technology have led to the development of compact, robust mode-locked lasers with >10 nJ outputs using all normal dispersion scheme and external compression [96]. However, long glass propagation lengths inherent in a fibre laser lead to significant accumulation of higher-order phase, particularly positive third-order phase.

The long material propagation lengths permit utilization of third-order processes over long interaction lengths to achieve mode-locking. The Kerr effect does not meaningfully alter the spatial characteristics within a single mode fibre and therefore these lasers typically utilize elliptical polarization rotation from the Kerr effect in a scheme known as

"non-linear polarization evolution" (NPE). Various dispersion control schemes may be used to further enhance or maintain short-pulse generation. In the anomalous dispersion regime, temporal soliton formation is possible, where self-phase modulation and dispersion oppositely and equally counteract each other. However, the direct amplification of the ultrashort pulse in the small mode area of optical fibres typically limits pulse energies to ~0.1 nJ. "Self-similar" operation, which is depicted in figure 4.5, uses equal amount of anomalous and normal dispersion to produce a chirped pulse able to be recompressed in free-space between the fibre ends. Initial anomalous dispersion produces soliton-like propagation and Kerr elliptical rotation over long interaction lengths before amplification through normal-dispersion fibre, which also prevents "wave-breaking" that acts to destabilise the ultrashort pulse envelope [97]. In fibre, amplification can be performed on the chirped pulse and therefore provides improved energy scaling. The output is therefore chirped and external compression required. Sub-100 fs pulses with >10 nJ energies are possible using this scheme [84, 96, 98].

Here, we consider the laser oscillation with and without an intensity dependent term to show extinction of the weak CW mode. Additionally, as NPE depends upon the optical Kerr effect to produce elliptical rotation, self-phase modulation also strongly acts to modulate the pulse spectrum [98].

A proposed upgrade for the TARANIS laser at Queen's University Belfast will incorporate a newly developed commercial oscillator emitting shorter pulses at higher pulse powers. The Coherent "Fidelity 2" NPE mode-locked fibre laser emits pulses of 55 fs duration with ~2 W average power at 76 MHz repetition rate i.e. 26 nJ and therefore highly likely to operate in the self-similar regime. The TOAD is only able to phase-match to ~200 fs of the broad bandwidth of these pulses, which limits the dynamic range in the measurement. The contrast characterisation of this oscillator is presented in figure 4.6, showing the strong presence of a post-pulse foot indicative of positive higher odd order phase.

Use of prism-grating compressor geometries (sometimes known as "Grisms" when combined in a single optical element) and careful choice of prism material has been shown to potentially nullify the typical $>10^5$ fs^3 uncompensated third-order phase present in Yb-fibre lasers [82]. However, this study did not measure the temporal contrast and it is unclear if higher phase orders are nullified for high-contrast output.

Although we have not been able to model the physical origins of these noise sources, the similar asymmetric pedestal features seen here compared to the KLM sources may

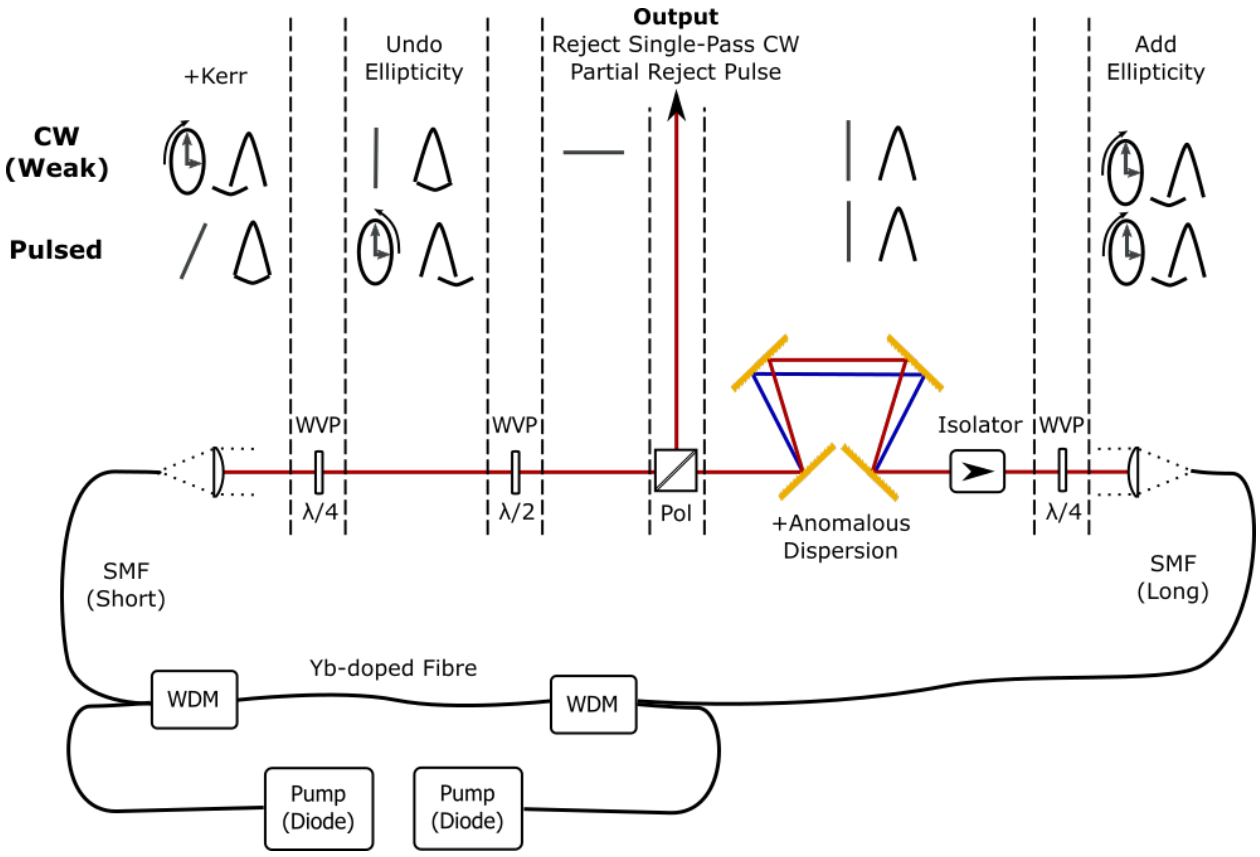


Figure 4.5: Schematic of an all-normal dispersion Yb-doped fibre laser. Top: Polarisation map showing with and without the intensity dependent polarization "evolution" from the Kerr effect. Initial unpolarised spontaneous emission is produced from an optically pumped Yb-doped fibre. All optical fibres used are polarization maintaining. Some of this light will leak through the output coupler and become polarized. Small elliptical polarization from a quarter-waveplate produces a weak "CW" beam and a stronger component that forms the mode-locked pulse through soliton formation in the first few metres of the long single-mode fibre (SMF). Additionally, a small amount of intensity dependent birefringence is produced between these two beams (quarter-wave rotation is shown here for simplicity). The second quarter-waveplate acts oppositely to the first and produces the same input polarization and therefore a half-waveplate is used to rotate this linear polarization by 90 ° to reject oscillation of the weak CW beam. The stronger beam's polarization is therefore not matched to the output polariser and some of the higher intensity light leaks through, creating an intensity dependent amplifying cavity. A Faraday isolator is used to ensure single-way propagation. WDM: wavelength-division multiplexer.

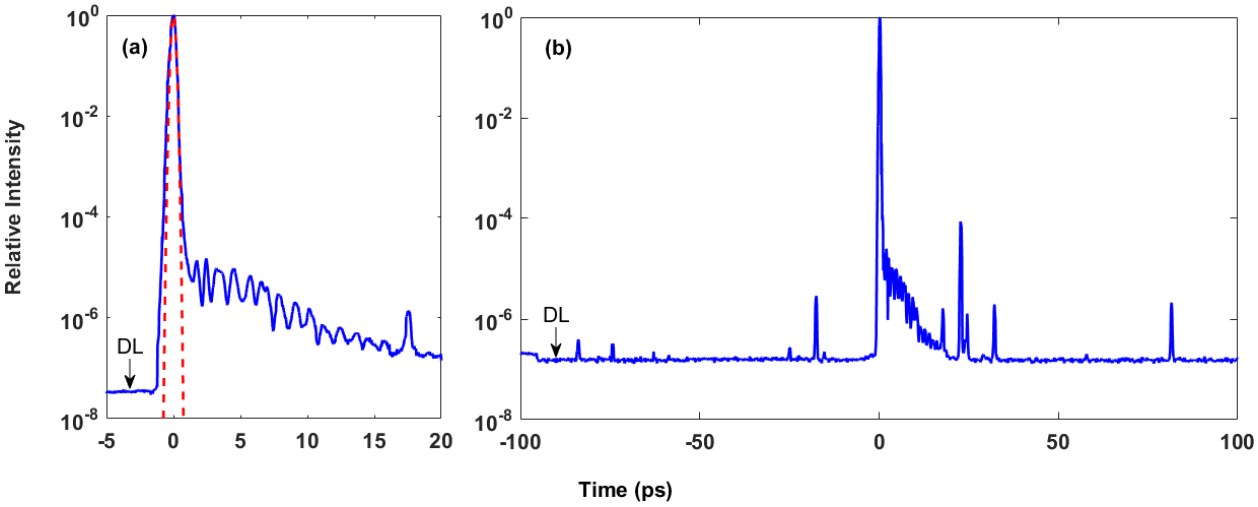


Figure 4.6: Measured third-order autocorrelations of an NPE mode-locked Yb-doped fibre laser (Coherent Fidelity 2), emitting 55 fs FWHM pulses at 1054 nm central wavelength with up to 1 W input average power into the TOAD. (a) Close-in contrast (blue) compared against an ideal Gaussian pulse with a duration of the TOAD resolution limit (red) showing a clean pre-pulse edge with greater than 3×10^8 contrast, limited by the dynamic range of the measurement. A strong asymmetric post-pulse tail is seen in the measurement. (b) Mid-range contrast showing location of secondary pulses, of which the early time pulses are thought to be diagnostic artefacts. DL: The detection limit of the TOAD that ultimately limits the maximum dynamic range with each scan.

indicate these originate from the common Kerr non-linearity between these two mode-locking methods and possible wave-breaking limits. Wave-breaking is generally accepted to be the main power limitation for energy scaling of short-pulse fibre lasers [99], and therefore it is reasonable to expect this fibre laser to also have small amounts of wave-breaking contribution with our high dynamic range measurements.

4.1.4 *Optical Parametric Oscillators (OPOs)*

The duration of the pulse being amplified in a cavity can also be directly controlled if the pumping source is another mode-locked laser, in a scheme known as "synchronous pumping". One particular non-linear optics example of this is an "optical parametric oscillator", where a difference frequency/OPA process is confined within a cavity with a repetition rate locked to the repetition rate of the mode-locked pump pulse. The DFG process from the optical intensities available from typical solid-state mode-locked oscillators can realistically achieve between x2-100 gain of the semi-classical background optical field

per pass. To produce measurable, and usable, laser sources a much greater total gain is required and therefore a cavity is used for cascaded DFG/OPA to eventually produce an optical field of similar intensity to the pump. The pulse produced from an OPO will have an ultimate transform-limited duration directly proportional to the gain window in the DFG/OPA process, which is primarily linked to the pump pulse duration. This may initially appear counter-productive, as there is little change in pulse duration. However, it becomes possible to generate broadly tunable laser sources able to operate from 0.5-7 μm by optimisation of the DFG process [86, 100] by simultaneously satisfying the phase-matching relationship

$$\frac{n_{pump}}{\lambda_{pump}} = \frac{n_{signal}}{\lambda_{signal}} + \frac{n_{idler}}{\lambda_{idler}} \tag{4.2}$$

and energy conservation

$$E_{pump} = E_{signal} + E_{idler} \implies \frac{1}{\lambda_{pump}} = \frac{1}{\lambda_{signal}} + \frac{1}{\lambda_{idler}} \tag{4.3}$$

For instance, a KLM Ti:Sapphire oscillator is restricted to ~100 fs output at 1054 nm, as this wavelength lies towards the edge of the material gain profile; however, it is entirely possible to generate 1054 nm 10-20 fs seed pulses at this wavelength from a non-degenerate OPO pumped by 10-20 fs duration 800 nm central wavelength pump pulses and using BBO as the non-linear gain medium. Using (4.3), the idler in this case would be centred at 3300 nm, also 10-20 fs in duration. Driving this process in a cavity resonant to either the signal or idler wavelength at MHz repetition rates can approach 10 % conversion efficiency [101–103]. There are also potentially significant implications regarding the pulse contrast, as the gain window of the short-pulse pumped DFG/OPA process acts as an efficient temporal cleaner for dispersive and temporal instabilities such wave-breaking processes.

We present the contrast characterisation of a NPE mode-locked Yb-Fibre laser pumped OPO that produces 12 nJ, 120 fs pulses at 1054 nm wavelength (Spectra Physics Insight DS+ [86]) in figure 4.7.

The laser is tunable between 630-1300 nm and has been set for 1054 nm operation as a potential upgrade for seeding the petawatt beamline at the Vulcan laser facility (STFC, Central Laser Facility). A dynamic range of ~10^{10} was achieved in this measurement with the high output power from the oscillator.

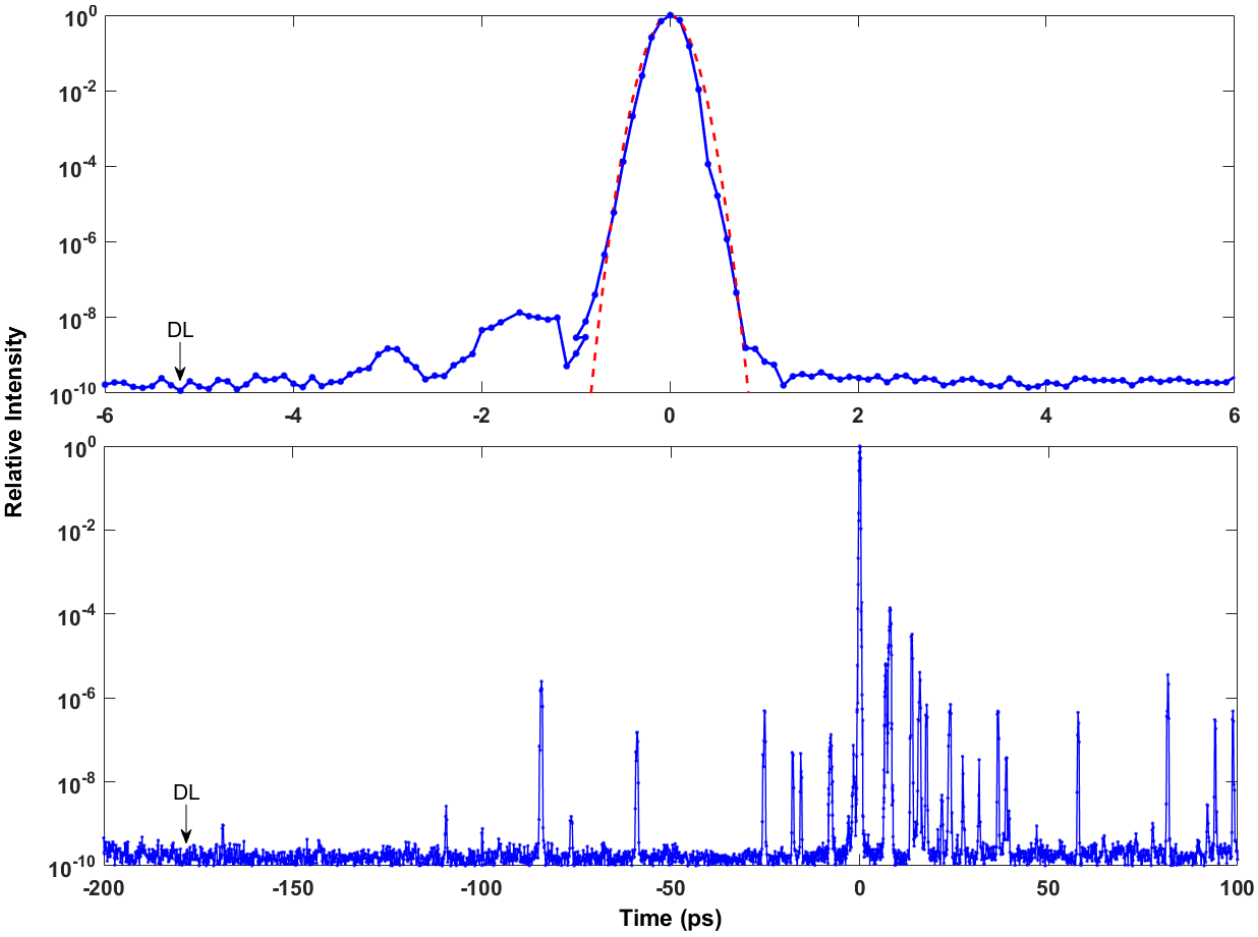


Figure 4.7: Measured third-order autocorrelation of an OPO that produces 12 nJ, 120 fs pulses (Spectra Physics Insight DS+). (a) Close-in contrast (blue) against an ideal Gaussian pulse with a 245 fs duration from the TOAD resolution limit (red). (b) Mid-range contrast showing location of secondary pulses, of which the early time pulses are thought to be diagnostic artefacts. DL: The detection limit of the TOAD that ultimately limits to ~10^{10} maximum dynamic range in this scan.

High contrast autocorrelation traces were measured with the TOAD. Pre pulse features at -1.5 ps, 10^{-8} intensity and -3 ps, 10^{-9} intensity were observed, which appear to be either residual third-order phase features or discrete pre-pulse generated by thin optics in the cavity. The contrast performance of the OPO significantly improves upon the KLM and fibre laser outputs shown in this chapter, as self-phase modulation is not phase-matched and short-gain media with ultrafast pumping reduces accumulation of higher-order phase. Their wide tunability, high output powers and comparable <150 fs pulse durations, in addition to the now confirmed high-contrast output, offers an attractive option for seeding advanced high-power lasers.

4.2 CONCLUSIONS

We have experimentally characterised the temporal intensity contrast of SESAM, KLM, NPE and OPO mode-locked laser oscillators suitable for seeding amplifier chains that operate in the 1 μm region using a single diagnostic system. The high-dynamic range of the third-order autocorrelator diagnostic (TOAD) used to characterise pulses successfully identified asymmetric noise features and allowed for direct comparison of their contrast performance [37].

In all cases the very long-range noise pedestals attributed to amplified spontaneous emission could not be detected within the 10^8-10^{10} dynamic range of the measurements. We found SESAM mode-locked laser sources produced the most ideal pulses, with no noise pedestal detected within the 2×10^9 dynamic range of the measurements, limited by the optical intensities available.

Unwanted non-linearities and higher-order phase currently limits the noise level to ~10^{-6} level in KLM lasers and ~10^{-5} in current short-pulse fibre laser technology, which may become contrast limiting when considering these sources for use in seeding short-pulse, high-power, high-contrast laser systems. Both the KLM and NPE mode-locking methods rely upon the Kerr effect, a third-order non-linear process that also produces additional changes to a light pulse in the form of self-phase modulation that is suspected to be influential in the formation of the noise pedestals. Potentially manageable pre-pulse at the 10^{-8} level was observed from an OPO source, with contrast enhancement from the limited gain time window of the pump pulse, and also offers large wavelength tunability in comparison to other mode-locked sources.

5

CONTRAST CHARACTERISATION OF UK TERAWATT AND PETAWATT LASER SYSTEMS

In this chapter we present a comparative study of the contrast performance of compressed high-power laser pulses from partial and complete optical setups of terawatt to petawatt laser systems from major laser laboratories in the UK. We have previously introduced the Cerberus hybrid OPCPA/Nd:Glass multi-terawatt laser at Imperial College, whose amplification and optical design prioritised high-contrast output to support high-intensity laser-matter interaction studies. We will also present contrast characterisations of the Vulcan and Orion OPCPA/Nd:Glass petawatt National laser facilities and also comparisons against CPA gain-storage amplifier systems at Queens University Belfast (QUB). The analysis from our studies and comparisons against published contrast characterisations of other laser systems from other authors will then be used to provide an overview of the current hurdles still to overcome in the field towards producing the ideal high-contrast temporal intensity envelope of the high-power laser pulse.

In addition to the temporal contrast, the energy stability, bandwidth and wavefront of the high-power laser pulse from OPCPA/Nd:Glass laser systems are largely influenced by the OPCPA front-end performance that provides the dominant gain mechanism before seeding the larger aperture Nd:Glass gain-storage amplifier stages. Therefore, much of the work on contrast characterisation can be performed on this part of the laser, which operates at a relatively high repetition rate (few Hz to MHz compared to shots/minute to shots/hour). This enables detailed contrast studies with measurements from the third-order autocorrelator diagnostic (TOAD), described in §3.1. The studies reported here required input from staff at a number of institutions, including Dr David Hillier and Dr Nick Hopps of the Orion laser (AWE), Bryn Parry, Alexis Boyle, Dr Marco Galimberti, Dr Pedro Oliveira and Dr Ian Musgrave of the Vulcan laser (STFC) and Ahmed Sharba, Dr Gagik Nersisyan and Prof Matthew Zepf of the TARANIS laser (QUB).

5.1 CERBERUS (IC)

An OPCPA laser will have a temporal gain window determined by the pump pulse durations, which are typically up to a few nanoseconds duration in high-power laser systems. This is significantly less than the >1 μs upperstate lifetime of most gain-storage laser media and therefore long-range optical noise from oscillators, such as ASE and the preceding pulse train, can be suppressed very effectively using this scheme without use of active gating methods such as ultrafast, low-jitter Pockels cells. Contrast measurements of the 250 fs, 2 nJ pulses from the Cerberus SESAM oscillator (Time-Bandwidth Products GLX-200HP) were described in §4.1.1, with a near ideal pulse-contrast up to the 10^9 dynamic range of the measurement. A simplified system layout is shown in figure 5.1, indicating where pulses have been measured to provide an understanding of the main contrast enhancement processes and noise sources in the Cerberus laser.

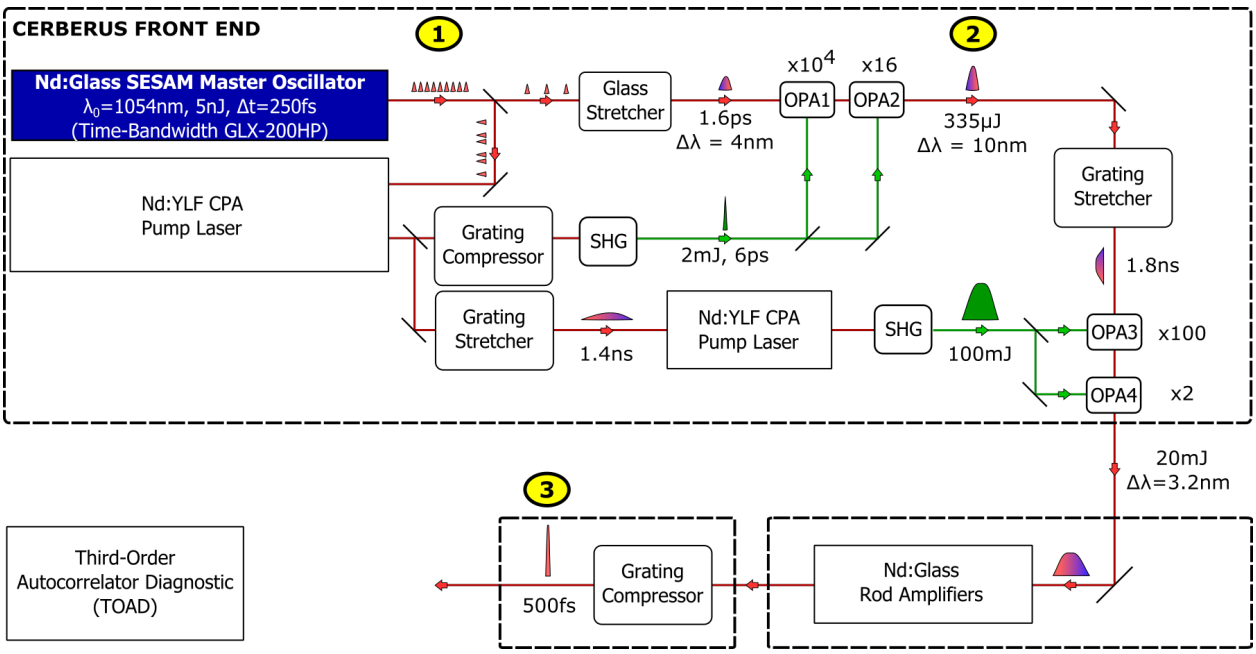


Figure 5.1: Simplified system design of the Cerberus laser. The contrast of the oscillator (position 1) has been measured in §4.1.1. Position 2: ps-OPA amplified signal that is slightly chirped to a few picoseconds duration by material dispersion. Position 3: Output from the full CPA optical system post compression, with optional amplification from the ps-OPAs, ns-OPAs and/or the Nd:Glass amplifiers for contrast characterization. Pulses are directed towards the TOAD for contrast characterisation.

The contrast is further enhanced by the use of ps-OPAs, where the seed pulses are stretched to ~1.5 ps and amplified within the gain window provided from ~6 ps FWHM

pump pulses with ~1.5×10^5 net gain to ~300 μJ energy. This is further stretched to the nanosecond regime and amplified in a pair of ns-OPAs to ~20 mJ before amplification in gain-storage Nd:Glass amplifiers that boost the energy to >1 J and finally compressed to multi-terawatt peak-power for experiments.

The energy from the ps-OPAs is highly suitable for TOAD characterisation. Figure 5.2 presents the measured pulse contrast at the direct output of the ps-OPAs and also benchmarks the contrast performance after traversal through the optical system without further amplification from the ns-OPAs or Nd:Glass amplifiers.

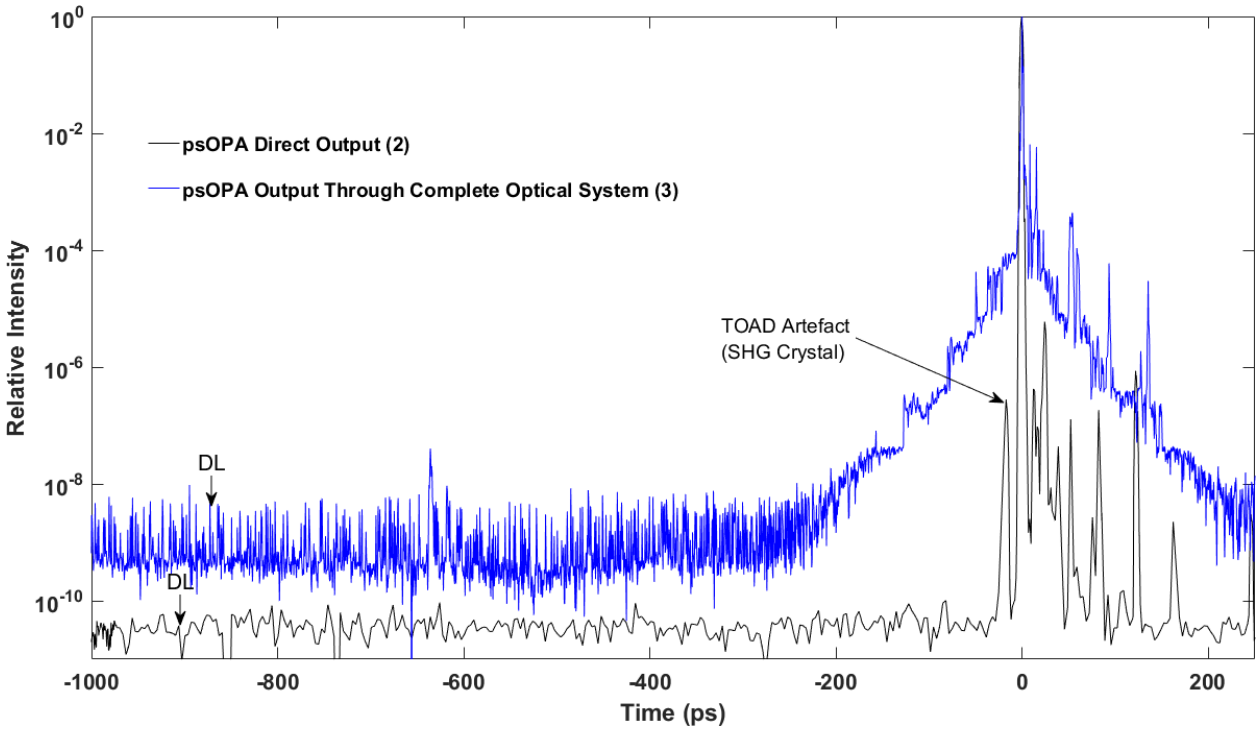


Figure 5.2: (Blue) High dynamic range scan of the compressed ps-OPA. A 500 fs Gaussian "primary" pulse has an underlying 50 ps FWHM sech^2 pedestal pulse at the 10^{-5} level resulting from spectral clipping in a CPA stretcher-compressor system. Discrete post-pulses at the 5×10^{-5} level and lower are also visible as the result of multiple reflections in AR coated optical elements within the laser chain. (Black) Uncompressed, direct output of the ps-OPAs, without the presence of the pulse pedestal seen with the complete optical system compressed output.

We see that the ps-OPAs produce extremely high contrast pulses directly after amplification; however, it is also clear that the stretcher, compressor or other optical components following the ps-OPAs produce a significant noise pedestal starting at 10^{-4} to 10^{-5} intensity level approximating a 50 ps sech-squared pulse shape. This pedestal extent does not match the spectral clipping estimates in 2.23 and did not change in shape or intensity

with artificially increased spectral clipping between the gold holographic gratings in the terawatt lab or the multi-dielectric gratings in the multi-terawatt lab. Similar noise pedestals have also been reported from other laser systems and have been attributed to surface scatter from the diffraction gratings, most likely from the stretcher [104].

In §3.2.3, we characterised the parametric fluorescence from the ps-OPAs and show this to have a contrast limitation on the 500 fs compressed primary pulse at the ~7×10^{-9} relative intensity level at 1.3 ps before the peak primary laser pulse. We were not able to resolve this noise source against the other noise sources present in the full system performance tests and this therefore reinforces the benefits of the fluorescence diagnostic in quantifying the OPA noise contribution in addition to understanding methods to reduce its impact on experiments, which has been successfully achieved here.

The contrast performance from the Cerberus ns-OPAs will build upon the noise pedestal seen from its recompressed unamplified seed from the ps-OPAs. The temporal intensity contrast has been characterised with the TOAD and a typical contrast plot is shown in figure 5.3.

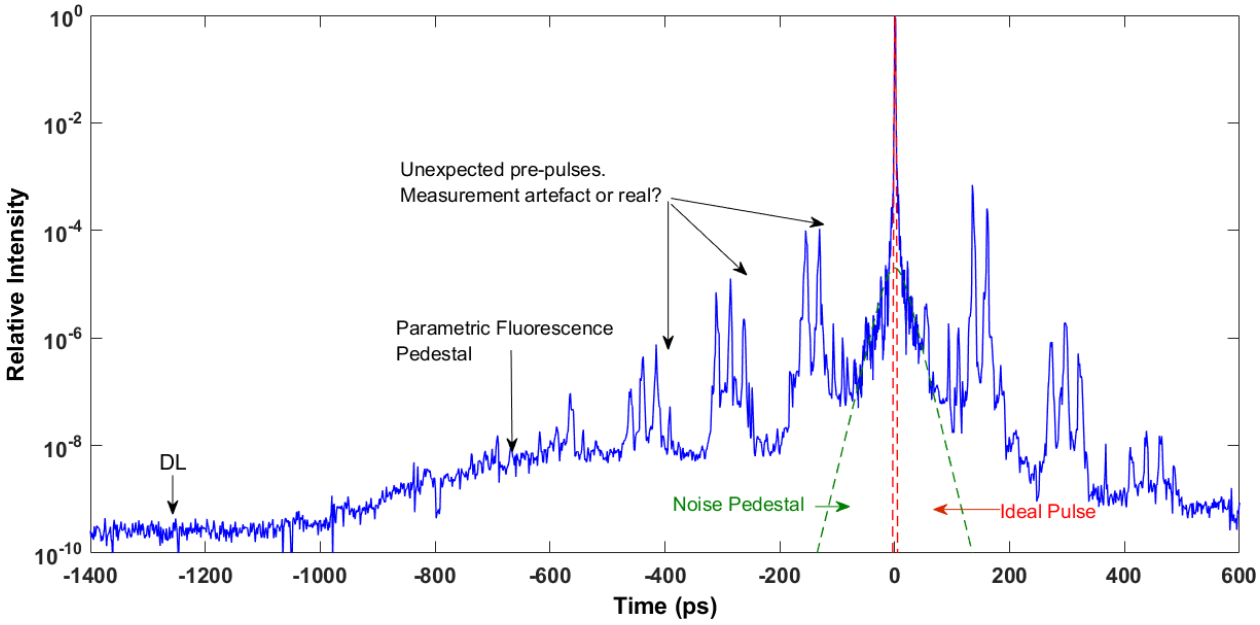


Figure 5.3: Contrast of Cerberus OPCPA front-end. Parametric fluorescence from the nanosecond OPAs is observed at <10^{-8} intensity. A series of discrete pre-pulses appear, the nature of which were unclear on first observation and could be real or artefacts due to real post-pulses in the second harmonic probe transferring onto the convolution of itself and the fundamental beam in the sum-frequency process to generate third-harmonic signal.

We found additional noise sources are generated from the ns-OPAs. A weak fluorescence pedestal is first observable above the measurement noise floor at ~900ps ahead of the primary laser pulse and is typically observed between 10^{-8} and 10^{-10} relative intensity between different scans, most likely due to day-to-day differences in pump depletion in these OPA stages.

A series of discrete pulses symmetrically distributed either side of the primary pulse are also seen. These were initially thought to be diagnostic artefacts, due to their symmetrical nature, where intense post-pulses produce a post-pulse in the second harmonic probe of the TOAD diagnostic that translate to an apparent pre-pulse in the autocorrelation process. These secondary pulses are now believed to originate from amplified internal reflections in the ns-OPA crystals, where individual OPA stages have been "turned off" to verify this, with the high gain "OPA3" stage, the first ns-OPA to be primarily responsible for their generation. Further investigations into their origin found these pulses were actually pre-pulses from a non-linear instability in the OPCPA process and their nature and methods for removing them will be discussed in §5.5.

5.2 ORION (AWE)

The Orion laser is a UK petawatt class facility that comprises ten long-pulse beamlines and two petawatt short-pulse beamlines, with these latter two derived from a common OPCPA front-end [4]. Much like Cerberus, this front-end is responsible for the generation of a high-energy, broadband and high contrast seed for further amplification in the large aperture Nd:Glass rod and disc amplifiers of Orion to deliver 500 J, 500 fs pulses on target. Ignoring optical losses, the front-end provides 99.99% of the total gain in the system, whilst the power amplifiers account for remaining 0.01% and therefore the performance of the front end has a dominant effect on overall laser performance.

A block diagram of the Orion laser front-end and contrast diagnostic setup is shown in figure 5.4. The ultra-short pulses are first derived from a mode-locked Ti:Sapphire oscillator (Spectra Physics Tsunami) generating 3 nJ, 130 fs pulses, which were characterised in §4.1.2. This pulse train is split in order to provide an optically locked OPCPA seed and pump source. The pump pulses are amplified by an Nd:YLF regenerative amplifier setup that generates a 3 ps pump pulse for a single non-linear OPA gain stage. Unlike the methods used on Cerberus, the pump pulses are not stretched before injection into

the regenerative amplifier and instead rely upon significant gain-narrowing to produce the few picosecond pump pulses. Directly amplifying a short-pulse limits the extracted energy to ~1 mJ and currently restricts the design to a single ps-OPA gain stage.

The seed pulses are pre-stretched to ~1 ps with a Martinez grating stretcher, unlike the glass block stretcher on Cerberus, and are amplified to 30 μJ after the single-stage ps-OPA [30]. The Orion system uses solely lithium tri-borate (LBO) for the SHG and OPA processes, as opposed to the preferred use of BBO in the Cerberus system. For near-degenerate OPA with a relatively modest phase-matched bandwidth requirement, there is little overall difference in the outcome of the amplified performance. BBO has a higher non-linearity yet LBO has slightly broader phase-matched bandwidth and less spatial walk-off, however require longer crystals to achieve the same amount of gain.

The ps-OPA signal energy is then equally split between two independent short-pulse beamlines, with identical design and nominally identical performance. These pulses are stretched using an Öffner triplet design with 3.25 m effective grating separation to produce a resulting chirp of 300 ps nm^{-1} and the stretcher system has an 18 nm hard clip bandwidth acceptance. The ~3.5 ns output pulses of each stretcher then seed a set of three nanosecond time domain OPA crystals operated in series and driven with increasing pump energy of 6 ns duration from a frequency-doubled Nd:YAG system to maximise energy, bandwidth, stability and minimise parametric fluorescence generation by operating each stage in the pump deletion regime [30, 36, 40]. Unlike the optically locked Cerberus pulses, the pump pulses are derived from a separate electronically synchronised custom 2 J, 6 ns Q-switched laser (Continuum Inc.) with a flat-top spatial profile that is relayed into the OPA crystals. The ~100 mJ pulse energies from each beamline are then amplified up to 500 J through large aperture Nd:Glass rod and disc amplifiers. A portion of either the 100 mJ pulses from the front-end can be redirected into an independent medium-sized compressor system identical in design to the full-system setup and therefore used for compressed pulse temporal contrast characterisation.

The contrast characterisation was based around the TOAD diagnostic described in 3.1 operated alongside a commercially available "SEQUOIA" third-order autocorrelator (Amplitude Technologies). The SEQUOIA design is similar in concept to the TOAD system with the crucial difference that it uses large aperture, collimated beams in the frequency conversion as opposed the focusing geometry in the TOAD and therefore the SEQUOIA has much higher input pulse energy requirements, typically 1 mJ as opposed to the ~1 μJ required for the TOAD and is not capable of characterising oscillator pulse trains

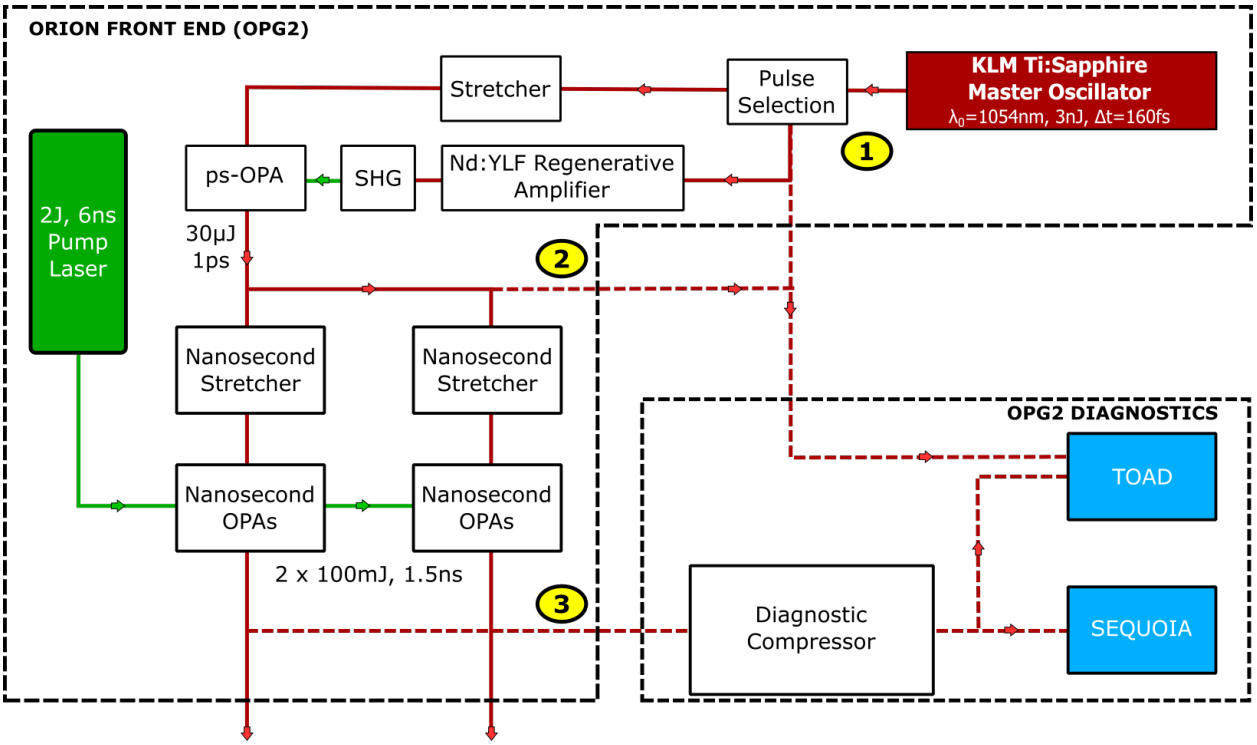


Figure 5.4: Orion short-pulse front end (Room OPG2) block diagram. Red dashes indicate the optical path used for contrast characterisation. (3) The compressed nanosecond OPA output of each beamline were measured with both the TOAD and SEQUOIA contrast diagnostics, providing useful benchmarking between these diagnostic systems (3). The TOAD is able to measure the temporal contrast of the ps-OPA (2) and oscillator output (1) for enhanced characterisation of the Orion front-end when compared to the capabilities of the more limited SEQUOIA device.

with meaningful dynamic range. The SEQUOIA is only able to perform characterisation of the compressed ns-OPA pulses and is not able to investigate contrast evolution at any point before this. Additionally, it measures across a narrower 600 ps temporal range, compared to the 2 ns range of the TOAD system.

The short-range (few hundred picosecond) contrast of the oscillator pulse train was determined in §4.1.2. to be limited to ~10^6 by a pre-pulse foot. The Orion ps-OPA will significantly improve the short-range contrast within the gain-window of the ~2 ps FWHM pump pulse. This will still capture part of the oscillator pre-pulse foot and therefore we can expect minor contrast degradation from this noise source. The contrast characterisation of the uncompressed ps-OPA compared and the compressed ns-OPA pulses from both short-pulse beamlines are presented in figure 5.5 and figure 5.6.

The SEQUOIA and TOAD measured almost identical traces above the ~10^{-8} intensity noise floor of the SEQUOIA. However, the TOAD was able to measure laser pulses with

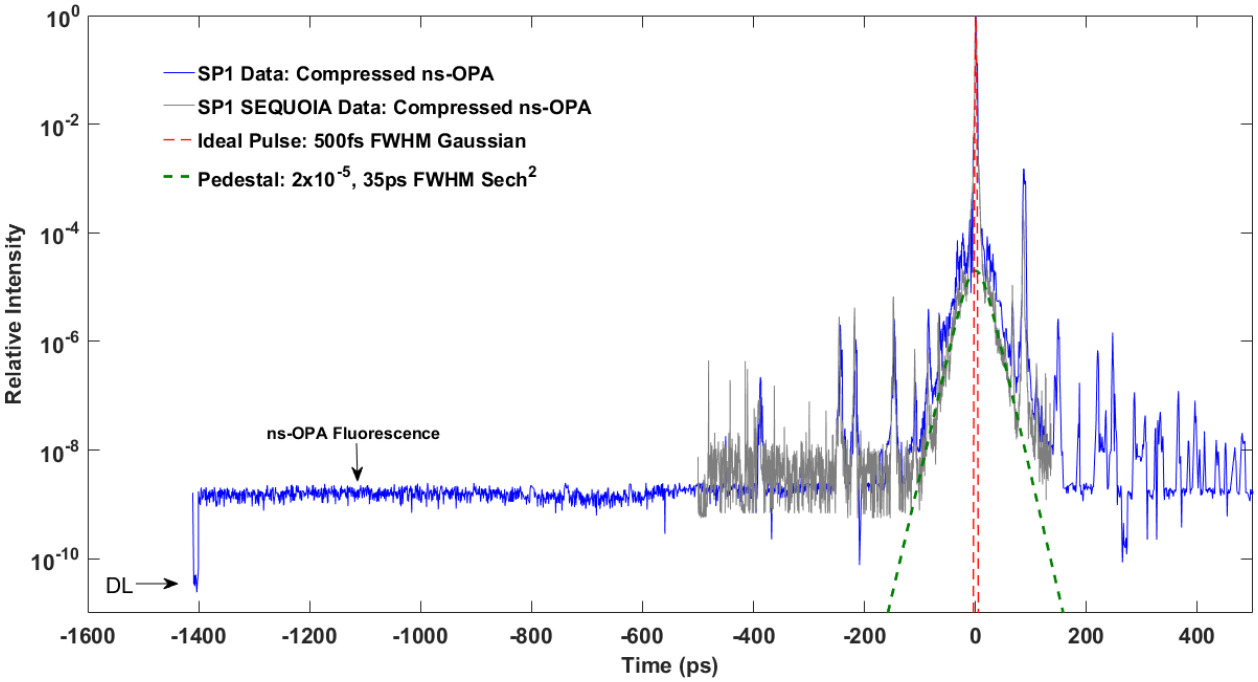


Figure 5.5: Measured contrast of the Orion front-end of the compressed ns-OPA pulses from the "SP1" beamline. (Blue) TOAD dataset with 2 ns temporal range and 3×10^{11} dynamic range. (Grey) SEQUOIA dataset with 600 ps temporal range and ~10^8 dynamic range. The significantly larger dynamic range of the TOAD is able to resolve the parametric fluorescence from the nanosecond OPAs, observed at <10^{-9} intensity. A series of discrete pre-pulses appear, similar to the Cerberus ns-OPA characterisation and an almost identical pedestal duration and intensity attributed to the diffraction grating stretcher-/compressor optical setups.

a much greater 3×10^{11} dynamic range and was able to resolve a long duration pedestal of 10^{-9} relative intensity contrast extending further than the temporal range of the diagnostic (>1.4 ns) ahead of the primary pulse. This pedestal is most likely the parametric fluorescence pedestal from the nanosecond OPAs produced by their 6 ns pump pulses.

Closer in to the main pulse, a series of pre-pulses were seen, with matching post-pulses, and were observed on both the SEQUOIA and TOAD traces. These appear to be of a similar nature to those seen in the Cerberus OPCPA contrast characterisation and are likely to result from the same underlying mechanism. The close agreement in the timing of these features between SEQUOIA and TOAD measurements strongly suggests that they are due to the laser pulse itself rather than being diagnostic artefacts.

A long duration sech-squared pedestal of 35 ps FWHM duration at 4×10^{-5} relative intensity was also observed. This pedestal is thought to arise from grating scatter in the Öffner triplet stretcher system for the nanosecond OPAs. As such, it will be difficult to

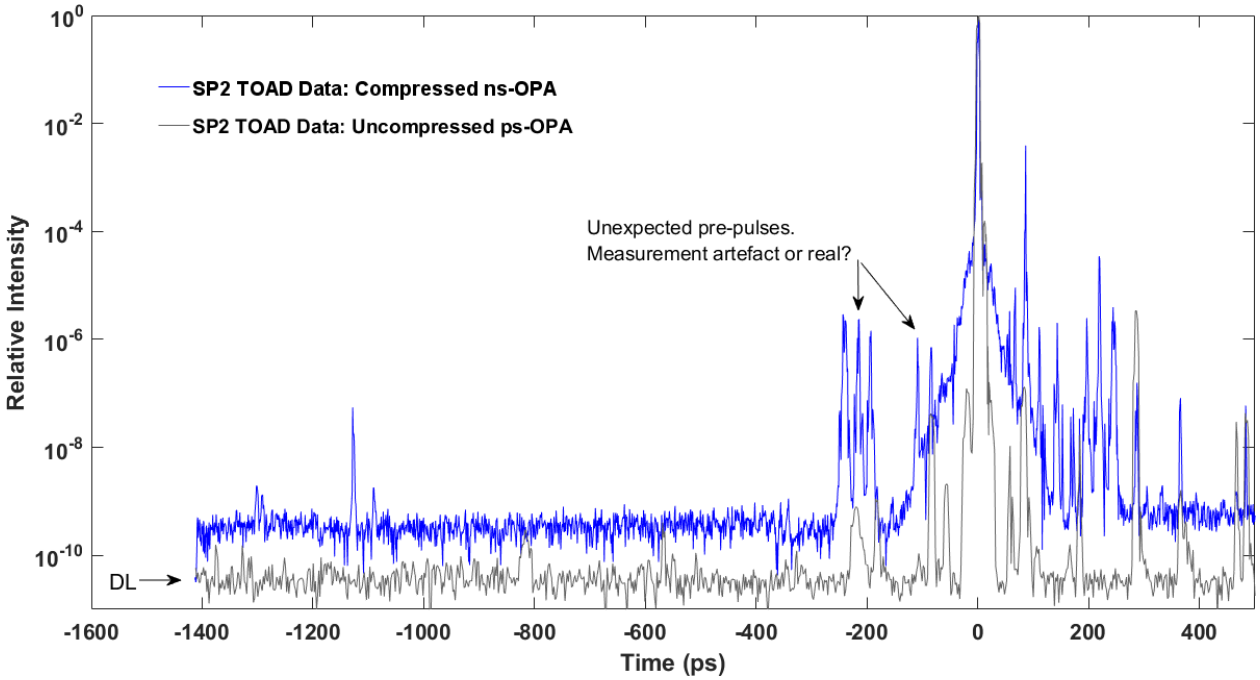


Figure 5.6: Measured contrast of the Orion front-end of the uncompressed ps-OPA pulses (grey) and the compressed ns-OPA pulses from the "SP2" beamline (blue) using the TOAD.

mitigate against this noise source in the laser system without identifying a source of "low scatter" gratings. At the present time this is not a product being offered by any manufacturer, though this may change in the future if this grating scatter effect becomes the dominant contrast limiting issues as OPCPA becomes more ubiquitous. In Orion, post compression frequency doubling will however act to significantly reduce this contrast limiting noise term, though at the expense of reduced energy on target.

Although identical in design, there are small differences in the pre-pulse locations for the two different Orion short pulse beamlines; for example, there exists a 10^{-8} intensity short pre-pulse ~1.1 ns before the arrival of the main pulse in the SP2 beamline that does not appear in SP1 pulse characterisation. The second short-pulse beamline was measured to have similar contrast characteristics as the first beamline.

5.3 VULCAN (STFC)

The Vulcan national laser facility pioneered much of the work on high-power OPCPA front-ends for amplification to petawatt pulses from its combination with Nd:Glass amplification [2, 18]. The OPCPA front-end laser design also uses a combination of picosecond and nanosecond pumped OPCPA stages to reduce the long timescale parametric fluorescence intensity [29] with a similar layout to the Orion front-end i.e. a single ps-OPA stage

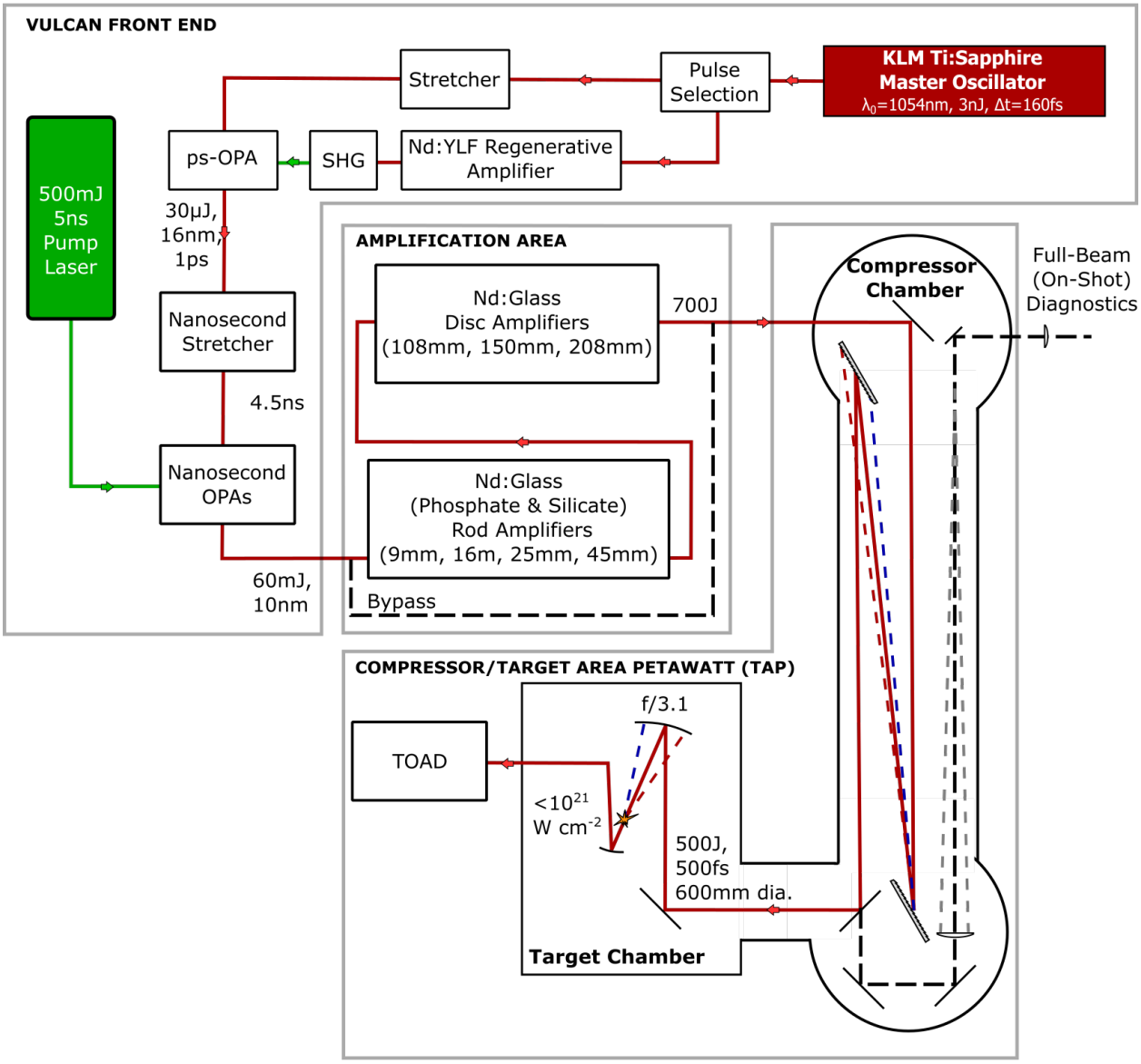


Figure 5.7: Simplified block diagram layout of the Vulcan petawatt laser and position of the TOAD for the compressed pulse contrast characterisation. Pulse wavelengths/bandwidths given in nanometres and beam size (edge to edge) in millimetres. The 2 Hz OPCPA front-end throughput can be greatly improved with the "bypass" beamline, typically used for SEQUOIA characterisation. The increased TOAD sensitivity does not need this bypass and is able to measure the full optical system contrast after re-collimation of the focused beam from the f/3.1 of-axis parabola used for the primary laser-matter interaction experiment. Future work could use the leakage through a large mirror after the compressor in the full-beam diagnostics, which is typically used for energy and pulse duration measurements.

pumped by a regenerative amplifier output and a stand-alone ns-OPA pump laser. The front-end produces ~60 mJ chirped pulses that then seed an Nd:Glass rod and disc amplifier chain up to a maximum aperture of 208 mm. Up to 700 J can be produced from the final amplifier, which is then expanded further and compressed using large aperture (~1 m scale) diffraction gratings under vacuum to produce ~500 J, 500 fs petawatt pulses that can be focused to a 5 μm FWHM spot size to produce 10^{21} W cm^{-2} intensities for laser-matter interactions.

Similar to the Orion laser, Vulcan has only been previously characterised with a SEQUOIA third-order autocorrelator with the compressed ns-OPA output. Furthermore, they do not have a stand-alone diagnostics compressor and therefore must use the main compressor output for characterisation, which is a single-passed design that reduces cost and increases energy throughput but also produces a linear spatial chirp across the diffraction axis of the output beam. With the very large aperture beams used on Vulcan, the spatial chirp is expected to have little effect on the pulse experienced by a target at best focus. Using the main compressor should produce more representative results of the pulse contrast, however there are numerous technical challenges that must be addressed in this measurement. Firstly, the beam at the output of the compressor is 60 cm in diameter and must be down-collimated to a few millimetres for the TOAD and SEQUOIA diagnostics. The design of the compressor and target chamber does not permit easy access to the beam before the focussing parabola and therefore is was re-collimated after the focus of the main parabola with ~x60 magnification with another off-axis parabola to create a beam that can be sent through a chamber window for easier coupling to diagnostics.

The second, more obstructive problem is the optical transmission through the entirety of the laser chain. The front-end produces 60 mJ pulses at 2 Hz repetition rate, easily able to be characterised with the SEQUOIA and TOAD, however only ~5 μJ of light reaches the target i.e. ~0.01% throughput, without further amplification from the Nd:Glass amplifier chain. For comparison, the Cerberus 5-30 TW beamline has ~10% throughput efficiency as it uses significantly less Nd:glass amplifier and spatial filter stages. Whilst additional losses are expected from absorption through larger volumes of Nd:Glass, it is possible much of the additional energy is lost on Vulcan through more aggressive sub-aperturing of the beam to maintain a stable super-Gaussian beam profile that better fills the laser amplifier aperture and is more robust to alignment errors. The complete optical system performance of the Vulcan laser was therefore previously beyond the sensitivity range of

the SEQUOIA, which requires ~1 mJ pulses, and therefore much of the optical amplifier chain was by-passed for contrast characterisation.

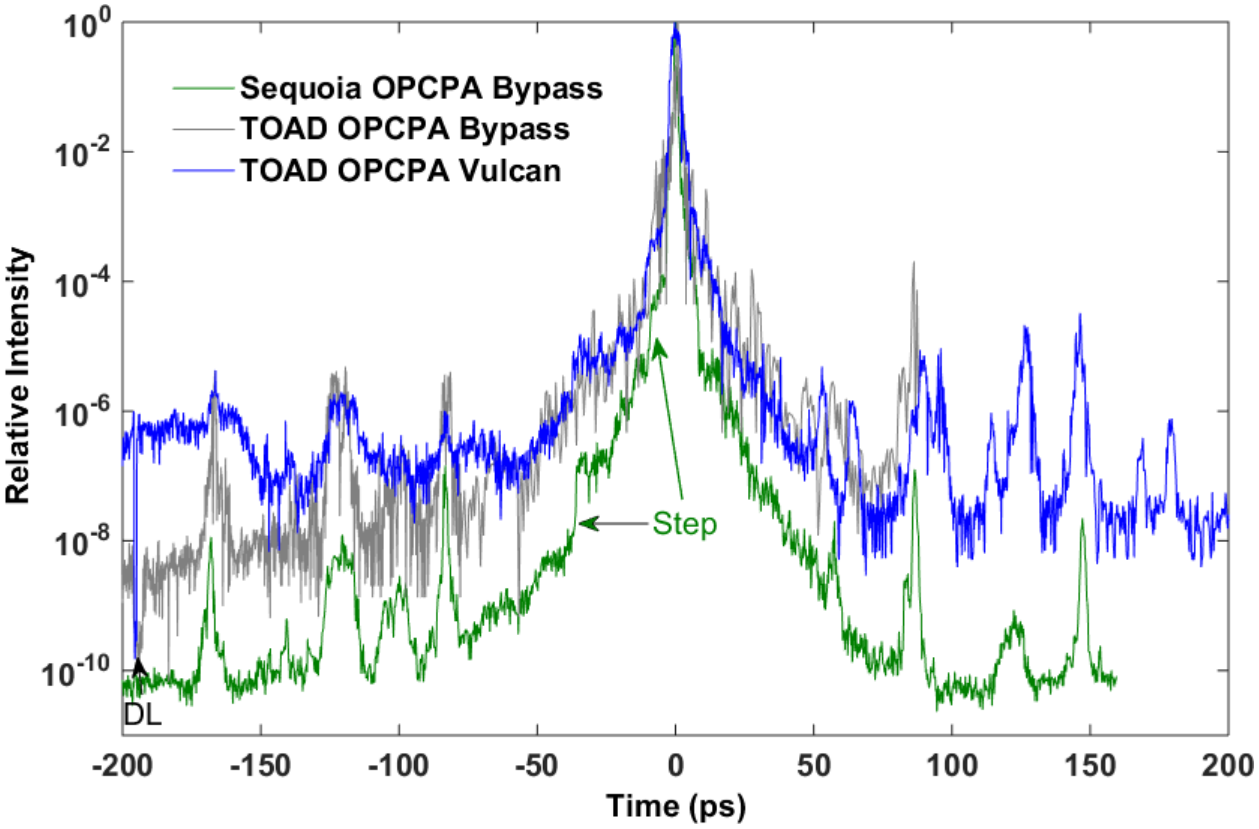


Figure 5.8: Measured contrast of the compressed 2 Hz full-system throughput (blue) and bypass beamlines of the Vulcan petawatt laser (TOAD: grey, SEQUOIA: green). The dynamic range of the two contrast diagnostics disagreed in these scans, due to suspected filter damage or miscalibration on the SEQUOIA, causing sudden "steps" in the pulse envelope trace. The SEQUOIA is not able to resolve the ns-OPA fluorescence however is easily resolved with the TOAD traces. Note: the large dip in the blue TOAD scan at -190ps from momentary blocking of the input to highlight the capture of the ns duration OPA fluorescence The noise features between the scans largely agree, although the pre-pulse fluorescence intensity is up to two orders of magnitude stronger in the full-system performance. This could be a result of the unstable ns-OPA performance during the scans, causing pump-depletion variability, known to significantly affect fluorescence generation (3.2) and also produce unstable third-harmonic signal.

The much greater sensitivity of the TOAD allows contrast characterisation of the entire optical chain of the Vulcan laser and therefore provides a useful opportunity to characterise the contrast differences between full optical system and the "reduced" by-pass beamline. The estimated damage threshold limit of the TOAD is ~2 μJ for 500 fs pulses and therefore the maximum dynamic range should be achievable from the entire optical chain

throughput. A direct comparison between the SEQUOIA and TOAD contrast characterisation is shown in figure 5.8, in addition to the complete optical chain characterisation.

5.4 TARANIS (QUB)

The TARANIS (Terawatt Apparatus for Relativistic and Non-linear Interdisciplinary Science) laser at the Queen's University Belfast is a Ti:Sapphire/Nd:Glass hybrid CPA laser system capable of producing 7 J, 750 fs (9 TW) pulses on targets [88]. A Ti:Sapphire KLM oscillator (Coherent MIRA) lasing at 1053 nm central wavelength injects a Ti:Sapphire regenerative amplifier, pumped by a Q-switched frequency-doubled Nd:YLF laser, to produce ~0.5 mJ pulses at 500 Hz repetition rate with 3% energy stability. Amplification is then performed in a series of increasing size (9 mm, 25 mm, 50 mm diameter) Nd:Glass rod amplifiers to produce up to 30 J pulses, of which 10 J may be incident on the gold-coated diffraction gratings in the pulse compressor to output 7 J, 700 fs (10 TW) pulses for experiments. Currently, TARANIS is the highest peak-power university laser in the UK, although the Cerberus laser can technically produce 10-15 J, 500-700 fs (14-30 TW) pulses in its present state except a lack of a vacuum chamber for the compressor currently limits the usefulness of such a pulse for experiments due to B-integral (self-focussing) effects.

As the TARANIS laser uses regenerative amplification in a traditional gain-storage amplifier, this is a potentially significant ASE noise source and will also introduce gain narrowing. The TERANIS system uses an "ultrafast" Pockels cell positioned after this amplifier to reduce the ASE intensity. The effectiveness of Pockels cell temporal gating will depend upon the rise time of the Pockels cell, the polarisation extinction when used in combination with a high damage threshold polariser and the random temporal jitter of the timing system for robust, repeatable results.

The contrast of the TARANIS system has previously been measured to be ~10^7 from fast (200 ps rise time) heavily saturated photodiode measurements, which are able to resolve the nanosecond to microsecond scale ASE pedestals and discrete pre-pulse generation from pre-lasing or secondary reflections from multi-passed optics [88]. This is monitored on a fast (>20 GHz, <50 ps sampling time) oscilloscope; however, the techniques to target the switch on timing position of the Pockels cell can vary by up to 5 ns depending on how well it can be defined.

Contrast measurements of the KLM and future upgrade NPE oscillators on TARANIS using the TOAD have already been presented in §4.1. The current KLM oscillator did produce any measurable ASE pedestal within the 10^9 dynamic range of the TOAD, although short-range, few picosecond, pedestals attributed to SPM instabilities limit the contrast to ~10^6 very close-in to the primary pulse envelope. In figure 5.9, we also show the compressed regenerative amplifier output.

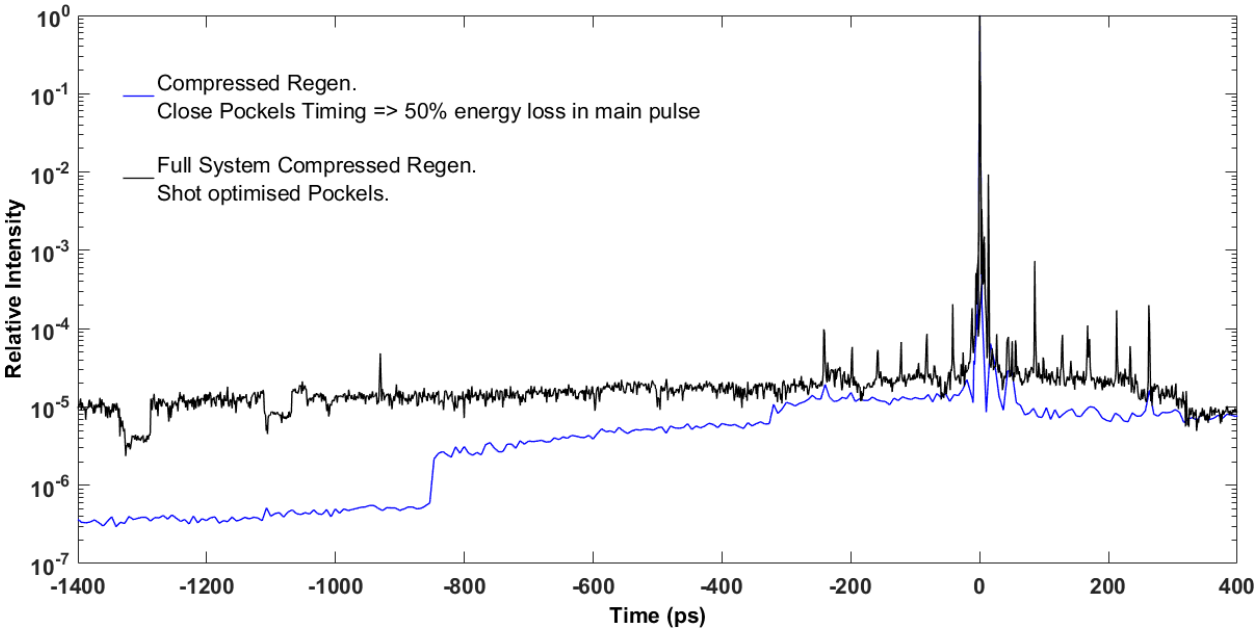


Figure 5.9: Measured contrast of the TARANIS compressed regenerative amplifier using the TOAD. (Black) Normal setting of the ultrafast Pockels cell to gate the long-timescale ASE, with 10^5 contrast due to this significant noise source beyond 1.4 ns ahead of the primary pulse.

Although "ultrafast" in name, the switch-on time of the Pockels cell showed a more typical ~1 ns rise time, possibly due to low-bandwidth cabling and cable lengths, causing half the energy to be lost when the switch-on time was positioned to start at ~850 ps ahead of the primary pulse. At this position, we see ~3×10^{-2} polarisation extinction and contrast enhancement through the Pockels cell and following polariser.

The 1 ps resolution measurements of the vacuum compressor output represent the minimum expected contrast on experiments, with the remaining uncertainty given from ASE generated in the Nd:Glass amplifiers, which have a net gain of ~ 10^4.

This measurement demonstrates the poor effectiveness of regenerative amplification and Pockels cells to actively compensate for ASE in comparison to picosecond time domain OPCPA. An improved setup with greater polarisation extinction (10^3-10^4 is realistic with precise Pockels cell alignment and higher extinction polarisers) and faster rise times

(150-300 ps have been reported in the literature [105]) and a low-jitter (<200 ps) electronic timing system are expensive but not too technically demanding to achieve. However, even with such improvements, this active method of contrast enhancement will still produce many hundreds picoseconds duration of un-attenuated ASE at the 10^{-5} level due to the rise time and timing jitter limitations.

5.4.1 *Contrast Enhancement from a Low Gain, Self-Pumped OPA*

The significant ASE noise from Ti:Sapphire CPA systems is dependent on the total gain and must therefore be counteracted with dedicated contrast enhancement setups. This is typically performed at an intermediate stage in the amplification and usually requires an additional pulse compressor and stretcher in a "dual-CPA" scheme to avoid gain narrowing [106]. This creates significant extra complexity in the optical setup of the laser system.

Unlike the small single-pass non-linear absorption from SESAMs, an effective saturable absorber for dual-CPA will need a large non-linear absorption modulation depth, which has yet to be demonstrated at 1054 nm in the literature, although RG850 glass has been used for 800 nm Ti:Sapphire laser systems [105]. Cross-polarised wave generation (XPW), a third-order non-linear linear polarisation rotation process, is an effective contrast enhancement technique. However, this weak third-order response typically achieves meaningful efficiencies close to the optical damage thresholds for 250-500 fs pulses and is therefore more routinely employed for sub-100 fs sources due to favourable damage threshold scaling [107].

Another method to enhance the contrast of the laser is to use a self-pumped, low gain OPA to produce a high-contrast idler. This was first demonstrated by Shah et al. [108], who achieved ~5% overall energy efficiency/conservation from the input pulse into the idler.

The layout of this setup shown in figure 5.10. A beamsplitter divides most of the energy to produce a pump pulse from frequency-doubling with high conversion efficiency. This second-order process produces a pump pulse window approximately $\sqrt{2}$ times shorter than the input pulse. With a transform limited input seed pulse for the OPA, a narrower gain window will produce a narrower transform-limited amplified signal and therefore is a source of spectral broadening in low pump depletion. A small angle is introduced to separate the signal and idler pulses. In the Shah et al. setup, a relatively large 4 $^\circ$ angle

was used as a compromise between large angles producing a spectral shear (spatial chirp) that degrades the focusability and small angles prone to contrast degradation from optical scatter from the signal pulse captured in the idler direction.

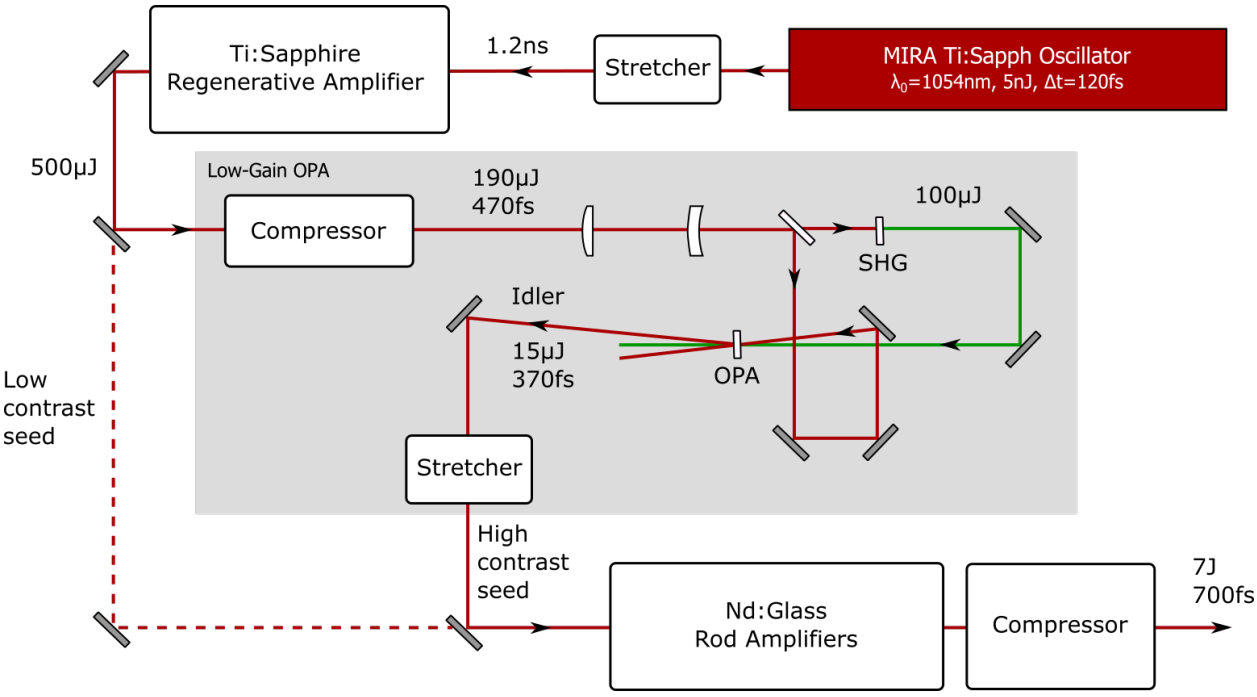


Figure 5.10: Optical setup of the low-gain OPA for contrast enhancement of compressed ~500 μJ pulses from a Ti:Sapphire regenerative amplifier

One of the projects (Ahmed Sharba) under development on the TARANIS laser implements such a low-gain OPA for contrast enhancement, with ~1.2 gain to generate a 500 Hz idler that should be a high-contrast seed for the Nd:Glass amplifiers of the TARANIS laser system. The OPA uses near transform-limited pulses after compression of the regenerative amplifier output pulses, characterised in §5.4 to have an ASE limited contrast of ~10^5, to produce a narrow gain window OPA from a ~350 fs pump pulse to "clean" the low-contrast regenerative amplifier output in a dual-CPA setup. This work builds upon the first demonstration by Shah et al. to investigate using a smaller non-collinear angle of 0.6 ° and using ~2.5 mm beam sizes to further minimise the spatial chirp of the generated idler. Contrast measurements from the TOAD developed here were therefore vital in demonstrating high-contrast outputs, as a 4 ° angle was found to be too detrimental to the high-intensity focal spots on proposed targets.

The idler from this OPA scheme has a measured contrast >10^{10} >20 ps ahead of the main pulse. As the input pulses are derived from the compressed regenerative amplifier output, measured in figure 5.9, the double-cascaded non-linear process of the SHG and OPA is estimated to produce an optical noise level of ~10^{20} for the ASE background,

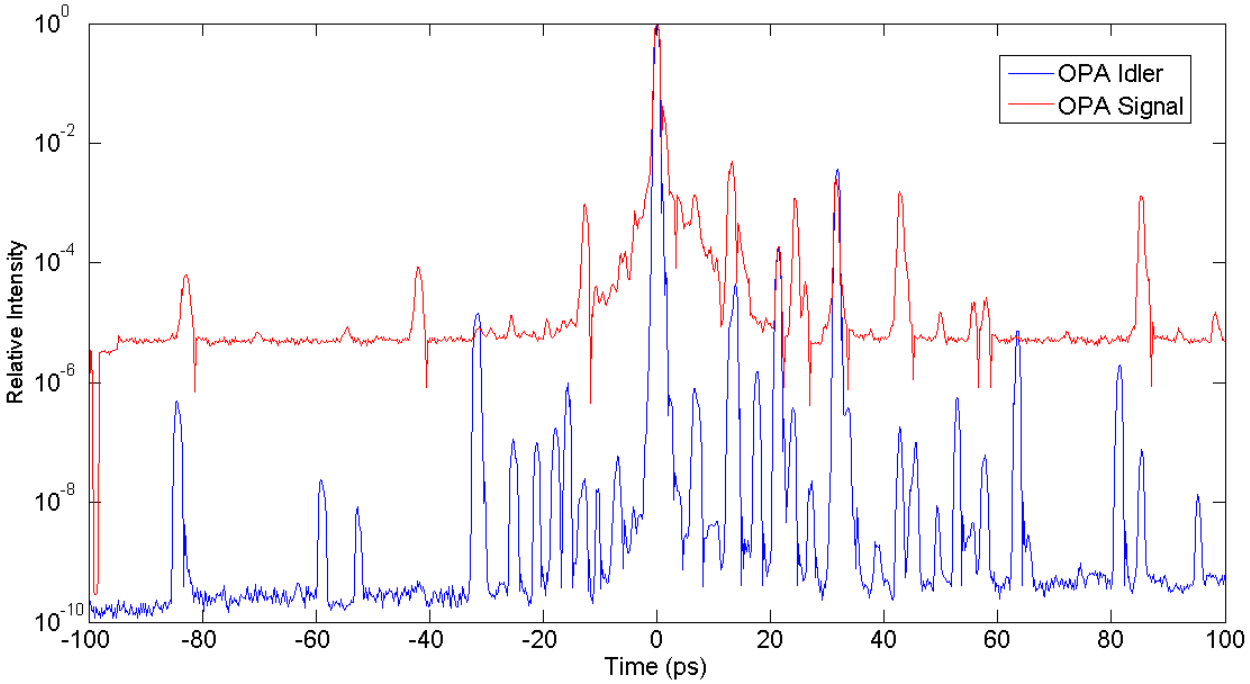


Figure 5.11: Measured contrast enhancement to a Ti:Sapphire regenerative amplifier (red) from a self-pumped low-gain degenerate OPA (blue) to produce a high-contrast idler pulse that can be stretched and injected by into the high-energy amplification beamline. The ASE contrast is improve by >10^5 to below the noise floor measurement limit of the TOAD system used to characterise these sources.

which is beyond the 10^{10} dynamic range of the measurement. This technique will prove to be a much improved high contrast seed for the Nd:Glass amplifiers of TARANIS in the near-future and is a significant improvement upon the current Pockels cell gating of the ASE noise pedestal from more traditional gain-storage amplifiers. This work has been submitted to a peer-review journal for an upcoming publication.

5.5 DISCUSSION: NON-LINEAR PRE-PULSE SYNTHESIS FROM POST-PULSES

One of the common themes of the OPCPA contrast results from the laser systems characterised are the observation of a series of discrete pre-pulses in the third-order autocorrelations, typically hundreds of picoseconds ahead of the primary pulse, with intensities up to the 10^{-3} level. Discrete pre-pulse generation within the few nanosecond window around the primary pulse are likely to originate from multi-passed optical setup employed in the laser, such as a stretcher/compressor or double-passed gain-storage amplifier. The contrast traces typically show a symmetric time-axis behaviour around the primary pulse with similar post-intensity. The sum-frequency process is a convolu-

tion between the first and second harmonic of the pulse and therefore post-pulses in the second-harmonic have the potential to produce pre-pulse artefacts. However, the contrast of these artefacts should be non-linearly weaker and therefore the precise origin of these pre-pulses seen in TOAD and SEQUOIA traces were initially unknown.

A comparison of the Cerberus full optical system performance with and without the ns-OPAs being pumped shows that these pre-pulses are most likely generated from amplification of a double internally reflected beam through the ns-OPAs. Differences between the small-signal gain and the gain of the primary-pulse in an OPA can potentially enhance the intensity of pre-pulses that originate from secondary reflections in multi-passed optical systems. However, after extensive optics changes with no contrast improvement this hypothesis was eventually ruled out. Crucial clues into their origin were found when only using the first, higher gain ns-OPA stage and swapping the BBO non-linear crystal between 8 mm and 12 mm length. The results are shown in figure 5.12. The rough position of the pre/post-pulse locations match very well with the internal reflection optical path length when accounting for refractive index of the OPA crystal and changing the crystal length moved the temporal position of these secondary pulses.

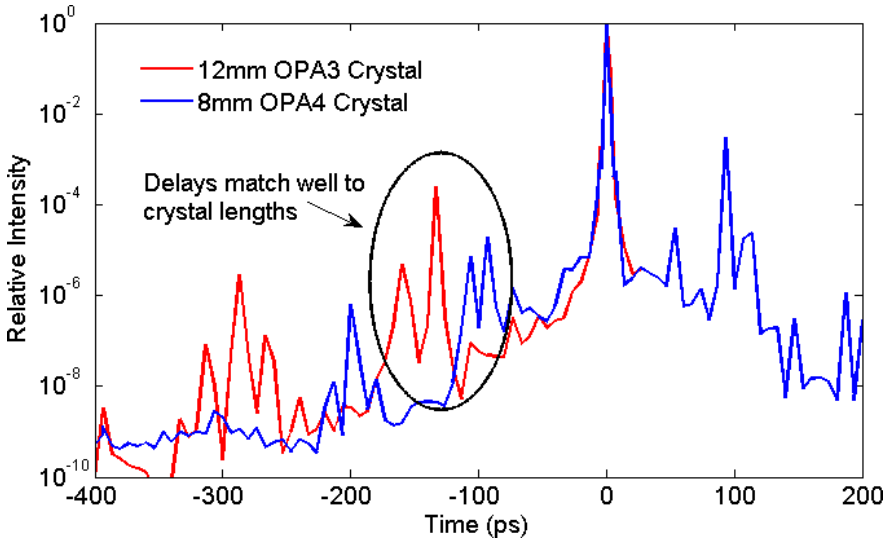


Figure 5.12: Contrast of the compressed ns-OPAs with different length amplifier crystals.

It is clear that internal secondary reflections of the amplified pulse are a likely source of post-pulses. A study by Didenko et al., which studied regenerative amplifier contrast, previously showed how the third-order non-linearity of self-focussing (B integral) can produce a sinusoidal self-phase modulation across the chirped pulse from interference between the main pulse and the overlapping secondary pulses [109]. After compression the Fourier transform of the sinusoidal modulation produces a symmetrical temporal pro-

file that converts these post-pulses into additional pre-pulses, accompanying the more intuitive appearance of post-pulses.

The non-linear phase is accumulated when the post-pulse and primary pulse are significantly chirped such that their electric fields overlap in time and can interfere. The superposition of the chirped primary pulse and post-pulse replica with time delay τ and relative intensity r can be expressed in the frequency domain as

$$E(\omega) = \left(E_0(\omega) + \sqrt{r}E_0(\omega)\exp(i\omega\tau)\right)\exp(i\phi''/2) \tag{5.1}$$

The intensities of the post-pulses are typically too weak to resolve the resulting spectral interference driven modulation on a spectrometer; whose spectral intensity is given by

$$I(\omega) = |E(\omega)|^2 = I_0(\omega) + rI_0(\omega) + 2\sqrt{r}I_0(\omega)\cos(\omega\tau) \tag{5.2}$$

A strongly chirped laser pulse will have a temporal intensity shape that maps the spectral intensity, which is the case for the ns-OPA operation. The accumulated B-integral is therefore

$$B = \frac{2\pi n_2}{\lambda} I(\omega) L \tag{5.3}$$

Where L is the length of the non-linear medium. We have considered a constant intensity here for simplicity; however, a complete model would account for of the amplifier exponential gain profiles. We see from this expression three separate sources of non-linear phase accumulation, with a modified electric field of the form

$$E(\omega) = \left(E_0(\omega) + \sqrt{r}E_0(\omega)\exp(i\omega\tau)\right)\exp(i\phi''/2)\exp(iB) \tag{5.4}$$

An ideal compressor will negate the chirp spectral phase in (5.4) but will not compensate for the B-integral phase. The co-sinusoidal phase accumulation generates an additional pre-pulse whose intensity is linked to its parent post-pulse intensity and B-integral. The analysis by Didenko et al. found the relative intensity of the generated pre-pulse and the primary pulse to be [109]

$$\frac{I_{-1}}{I_0} = rB_0^2 \tag{5.5}$$

where $B_0 = 2\pi n_2 I_0(\omega)L/\lambda$. The Cerberus and Orion OPCPA ns-OPA contrast characterisations frequently showed similar intensity pre/post-pulse intensities, which is satisfied in

(5.5) when $B_0 = 1$ and the pre-pulse intensity is non-linearly dependent on the B-integral accumulation. The very nature of the non-linear amplification requires high pump pulse intensities that approach the damage thresholds of the optical coatings. We estimate the B-integral accumulation through the 12mm BBO OPA3 crystal is ~0.2 from cross-phase modulation of the ~1 GW cm^{-2} pump pulse intensity. From (5.5) we see the generated pre-pulse will be ~25× weaker than its parent post-pulse, which is approximately what was observed in figure 5.12 and therefore shows good agreement with theory.

The contrast traces of the compressed ns-OPA pulses from all the systems characterised showed incrementing number of pre/post-pulses from each internal reflection of the OPA crystal, with the first "order" producing two pre/post-pulses. We believe these extra pulses to be the additional idler pulses generated from the internally reflected signal pulses that are then collinear with the primary signal pulse, lustrated in figure 5.13.

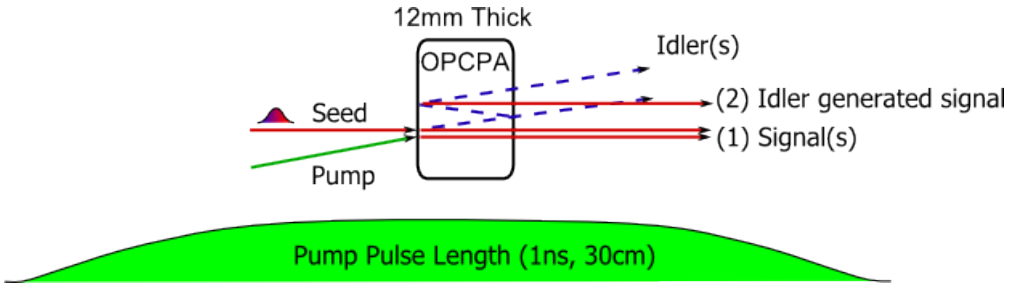


Figure 5.13: Schematic overview showing the mechanism of generation of additional collinear post-pulses in an OPCPA process that may then interact with the main pulse to produce pre-pulses after compression.

5.5.1 *Improved Cerberus Nanosecond OPAs*

The generation of pre-pulses from interference with the internally reflected post-pulses in an OPA crystal presents a significant contrast limitation to OPCPA systems. Methods to mitigate this effect are therefore of critical importance for high-contrast laser-matter experiments using OPCPA laser systems.

The generation of pre-pulses are directly linked to the co-propagation of post-pulses inside the OPA crystal that are overlapped with the pump pulse gain window of the amplifier. The internally reflected beam inside the OPA crystal are the most intense secondary pulses, as they experience the OPA pump pulse gain window twice and therefore even standard anti-reflection coatings (typically <0.2% reflectivity per surface for a dichroic

anti-reflection coating) are not sufficient to minimise their intensity. We therefore require geometries that mitigate co-propagation of the internally reflected post-pulses, which are shown in figure 5.14. Using wedged i.e. non-parallel entrance and exit, surfaces of the non-linear crystal will walk-off any internally reflected pulses, minimising interference and will also not be phase-matched for OPA gain. A wedge angle of 0.5-1 °is typically sufficient to prevent phase-matching of the post-pulses. This will produce a spatial chirp and therefore a compensating prism will likely be needed further downstream, at least half the length of the OPA gain window to prevent post-pulse amplification and non-linear pre-pulse generation. Another configuration uses a non-linear crystal whose crystal axis has not been cut optimally for OPA phase-matching and therefore needs to be tilted at a large angle until the electric field of the pump pulse see the correct phase-matched crystal orientation for OPA gain. For large crystals with small beam sizes, this will laterally walk-off the internally reflected pulses in the off-axis direction such that the post-pulses may be spatially filtered with an aperture after the OPA crystal.

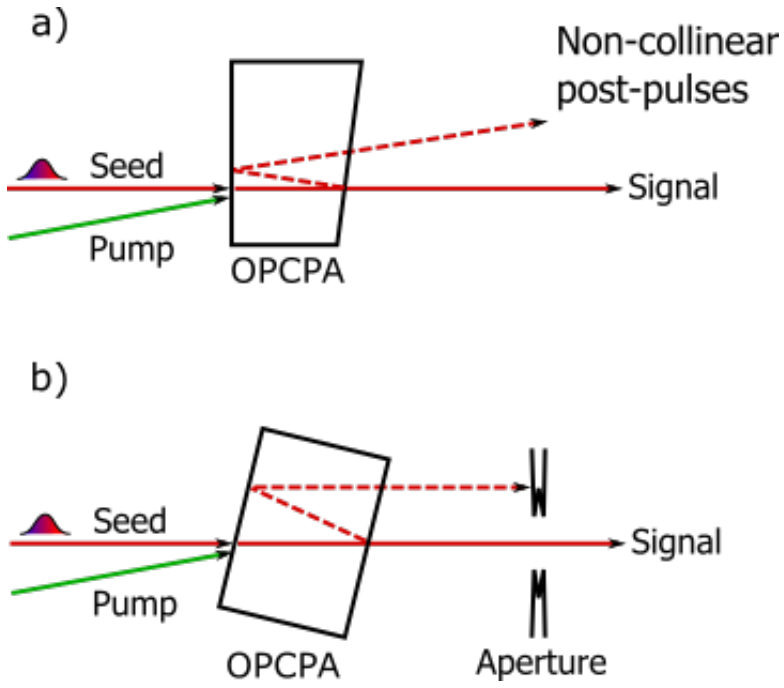


Figure 5.14: Non-linear crystal configuration that negates/minimises non-linear pre-pulse generation.

The expected ideal solution would use a wedged crystal design to separate the post-pulses from internal reflections. The off-axis crystal configuration of figure 5.14b) was the only available solution for our tests from a loan of 15 mm BBO crystals from the Vulcan laser, Central Laser Facility (STFC). We found the off-axis phase-matched angle to be ~15 °, producing a ~4 mm lateral translation of the internally reflected post-pulse. Only a 3 mm

diameter portion is selected with a serrated aperture and up-collimated for injection into the Nd:Glass amplifiers and therefore only ~0.5 mm of the post-pulse will overlap with the primary pulses, i.e. 10% area overlap between the two beams. Additionally, the lateral offset will also cause the an offset with the OPA pump pulse, further reducing it's intensity in comparison to the on-axis, parallel faced crystal configuration. In figure 5.15, we present the improved Cerberus compressed ns-OPA contrast using the TOAD from changing the OPA3 (first and highest gain ns-OPA) to this 15 mm BBO with ~15 ° off-axis phase-matching angle, without changing any other parameters.

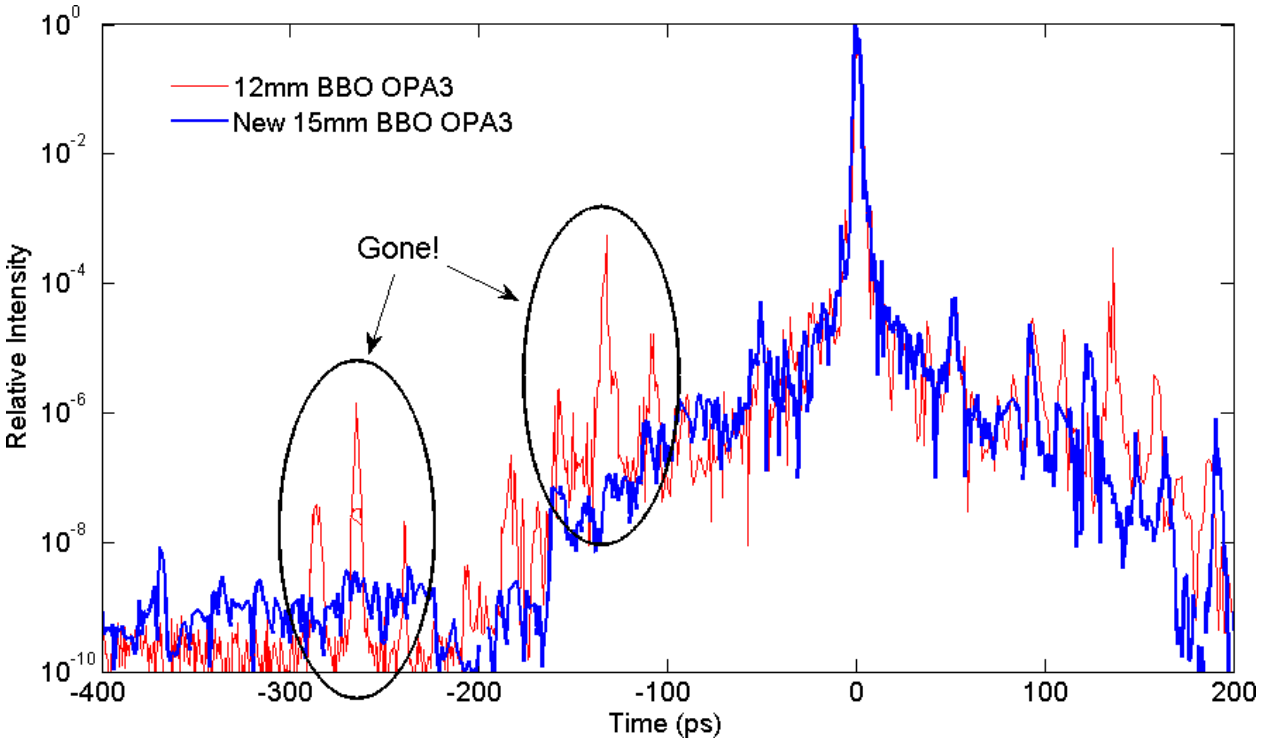


Figure 5.15: Improve Cerberus compressed ns-OPA that removes the interference between the internally reflected post-pulses generated in the OPA crystal, which has removed the non-linear pre-pulse formation.

We found the pre-pulses attributed to non-linear phase-modulation from the internally reflected post-pulses were substantially reduced in intensity to below the noise level of the TOAD and the mid-range pedestal commonly found in the CPA systems characterised. The substantial improved results from this new crystal configuration strongly supports the case that these pulses were indeed produced from non-linear effects from the co-propagation of the internally reflected post-pulses. Although these findings is not newly discovered physics, only in a different environment to the regenerative amplifiers characterised in the original findings by Didenko [109], this information has been dis-

seminated to the UK high-power laser community and will inform future OPCPA laser designs, upgrades and other application involving non-linear crystals.

5.6 DISCUSSION: MID-RANGE CPA PEDESTAL

With the elimination of the discrete pre-pulses found in the OPCPA laser systems using parallel faced on-axis OPA crystals, the dominant contrast limitation is from a "mid-range" pedestal that appeared in all laser systems with ~30-50 ps FWHM duration at ~10^{-4}-10^{-5} peak relative intensity to the primary laser pulse. The focused laser intensity of these pedestals will still create >10^{11} W cm^{-2}intensities at up to 200 ps ahead of the peak-intensity of the primary laser pulse for highest intensity interactions at petawatt laser facilities, significantly influencing target ionisation and plasma scale lengths that may be critical for laser-matter interaction experiments under investigation.

From our studies with the stretched ps-OPA pulses to ~1.6 ns FWHM durations that are then recompressed to ~500 fs FWHM duration, the pulse contrast with this noise pedestal, shown in figure 5.2, strongly indicates this noise pedestal to be a result of the stretcher/-compressor optical setups. We may also disregard the picosecond OPA parametric fluorescence, as this has already been characterised in §3.2.3 to have >10^8 contrast. These noise pedestals have also been explicitly observed in a Ti:Sapphire CPA laser and investigated by Hooker et al. [104], who also attributed these noise pedestals to the large stretch factors in high-power laser systems and imperfect diffraction grating operation from scattering processes and surface flatness errors and empirically found lower scatter gratings ($\times$6.5 weaker) with $\times$2.5 factor improved substrate flatness produced ~$\times$10 reduction in the pedestal intensity.

The design of stretcher/compressor systems typically involves ray tracing and analytical solutions provided in §1.2.2 to determine the required grating groove densities, incidence angle, grating aperture size and imaging optic focal lengths and aperture size to optimise between chirp factor, energy throughput, bandwidth acceptance and cost. For example, an in-house advanced 3D ray tracing program (CPTrace by Mike Mason [48]) was used to model the optical components of the Cerberus stretcher and compressor setups. One of the critical assumptions of ray tracing is that at every interface there exists a single incoming ray and a single reflected or transmitted ray i.e. diffraction is not included. The inclusion of diffractive effects is crucial in the operation of a diffraction grating but poten-

tially complex and expensive to implement in a numerical model. The angular intensity distribution from N slits, with slit size a, slit spacing d and incidence angle θ, is well known and given by

$$I(\theta) = I_0 \left(sinc \left(\frac{\pi a}{\lambda} \sin(\theta) \right) \right)^2 . \left[\frac{\sin\left(\frac{N\pi d}{\lambda} \sin(\theta) \right)}{\sin\left(\frac{\pi d}{\lambda} \sin(\theta) \right)} \right]^2 \tag{5.6}$$

where I_0 is the intensity of the central maxima. Unlike the ray tracing result, this produces a broad angular intensity distribution that becomes narrower with increasing slits. This is presented in figure 5.16 for different wavelengths, orders and number of slits. Larger beams produce much narrower angular spread of discrete wavelengths diffracted from the grating. Smaller beams are typically used for stretchers, where the lower pulse energy permits smaller and cheaper optical components. The slit size is typically chosen to be close to the wavelength for maximum efficiency and therefore has little room for optimisation. This angular spread in the diffracted beam that acts across the bandwidth of the ultrashort pulse can potentially be a source of noise. For spectrometers and monochromators, the optical setup has a detector or aperture at the image of the grating, thereby removing the effect of diffraction. However, stretcher setups by their very principle of operation output the beam away from this image, which is the point of zero chirp. In this case, these diffractive effects will become increasingly prevalent for larger chirp factors. The typical compressor geometry, which uses a parallel grating pair, is not an imaging system and therefore is immediately prone to this effect, although much larger beam sizes are used. We have not yet modelled the relative strengths of this process and therefore are not so far able to say at this point if this effect is the dominant mechanism and if the stretcher or compressor is the dominant source. However, our empirical evidence suggests the large variation in beam sizes used between the 600 mm diameter Vulcan compressor and the 40 mm beam size in Cerberus produced similar ~10^{-4} peak relative intensity pedestals. Additionally, we studied the effect of aperturing the beam in front of the compressor from 40 mm to <5 mm and found no difference in the pedestal intensity, supporting the case the stretcher will be the more dominant source.

Reflective diffractions gratings are usually constructed by etching a groove density profile via photoresist on top of a highly reflective mirror. The groove density profile is normally “blazed” such that the beam is most strongly reflected in a particular direction, usually in the first order dispersed beam direction. This provides large amounts of chirp

and large angular separation from spectral overlap from neighbouring diffraction orders, quantified by the free-spectral range of the grating.

$$\triangle\lambda_{FSR} = \frac{\lambda_{max}}{|m|+1} \tag{5.7}$$

For few-hundred femtosecond pulses, the use of the first order diffracted beams provides high efficiency (80-95%) and sufficient angular dispersion. However, octave spanning spectra in single/few-cycle pulses are prone to spectral overlap of multiple orders because of the lack of free-spectral range.

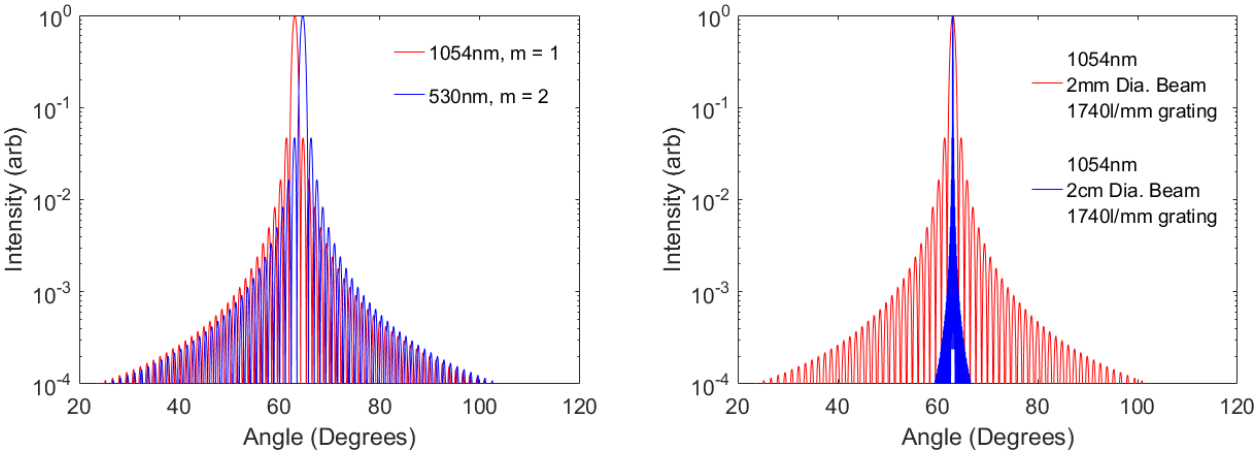


Figure 5.16: (Left) Diffracted ray intensities for a near octave spanning spectrum centred at 1053 nm using 1740 lines/mm groove density. This cross-talk between the pulse bandwidth will produce a contrast degradation proportional to the pulse spectral bandwidth, stretch factor and blazing efficiency of the grating. (Right) Influence of increased number of slits participating in diffraction grating operation. We see larger beams produce much narrower angular spread of discrete wavelengths diffracted from the grating. Smaller beams are typically used for stretchers, where the lower pulse energy permits smaller and cheaper optical components.

Stray light processes also limit the spectral contrast of the diffracted ray intensity. These can either arise from a non-uniform groove density or non-flat mirror substrate i.e. manufacture defects, or from scattered light processes due to material properties, dust and surface roughness [66]. Studies have shown that optical scatter is the most dominant mechanism by approximately an order of magnitude [66, 104]. When present in a dispersive optical setup, the entire pulse bandwidth will partially scatter and propagate through all possible paths in this optical setup, producing an incoherent pedestal. This will create an incoherent noise pedestal

A full theoretical treatment of grating scatter is given in [66], which solves the treatment the Fraunhofer diffraction from a non-ideal periodic reflective diffraction grating with a random small-scale error function σ_s from surface roughness or the RMS wavefront distortion of the grating substrate layer. The normalised field intensity of the scattered light is therefore given as

$$I_{Scatter} = \frac{\pi^2 D_x D_y \sigma_S^4 \left(\cos\left(\theta\right) + \cos\left(\phi\right)\right)^4}{L^2 \lambda^4} \tag{5.8}$$

where D_x, D_y is the horizontal and vertical beam diameter and L is the effective grating separation of the stretcher. Investigations by Hooker et al. [104] indicate the majority of grating scatter contribution is from the penultimate grating reflection of the stretcher. Using sensible values for the effective grating distance and the beam size on the final pass of the stretcher, contrast intensities of order 10^{-6} are calculated for σ_s =100 nm, a typical surface waveform flatness and roughness for diffraction gratings. If optical scatter is the main mechanism behind the pedestals observed, the strong σ_S^4 scaling indicates improvements in the surface flatness or roughness of diffraction gratings and/or internal optics has the potential to substantially reduced in the incoherent scatter pedestal intensity.

5.6.1 *Phase Conjugate OPCPA*

The empirical evidence from Hooker et al. [104] and our studies suggest the incoherent pulse pedestals originate from scattering or diffraction effects from the diffraction gratings in the dispersive optical delay systems that apply large stretch factors to produce nanosecond duration pulses from few-hundred femtosecond pulse bandwidths. To test this assertion, we can examine alternative methods to stretch these pulses that avoid the use of an imaging grating stretcher. The idler pulse generated in an OPA process contains the residual phase between the pump and signal pulse. To first order, the significantly narrower bandwidth of the pump pulses can be approximated as monochromatic, causing the phase of the idler to be a near perfect inverse of the signal. The idler is therefore "phase-conjugate" to the signal and opens the opportunity the stretch the seed of the OPA in the opposite direction, using a parallel grating pair, such that the phase-conjugate idler second-order phase is now compressible with a parallel grating pair, as before. In this configuration, figure 5.17, we therefore require two parallel grating pairs, which are not imaging systems and therefore are thought to be less prone to formation of noise pedes-

tals from diffraction grating scatter as the non-imaging geometry captures less off-axis rays.

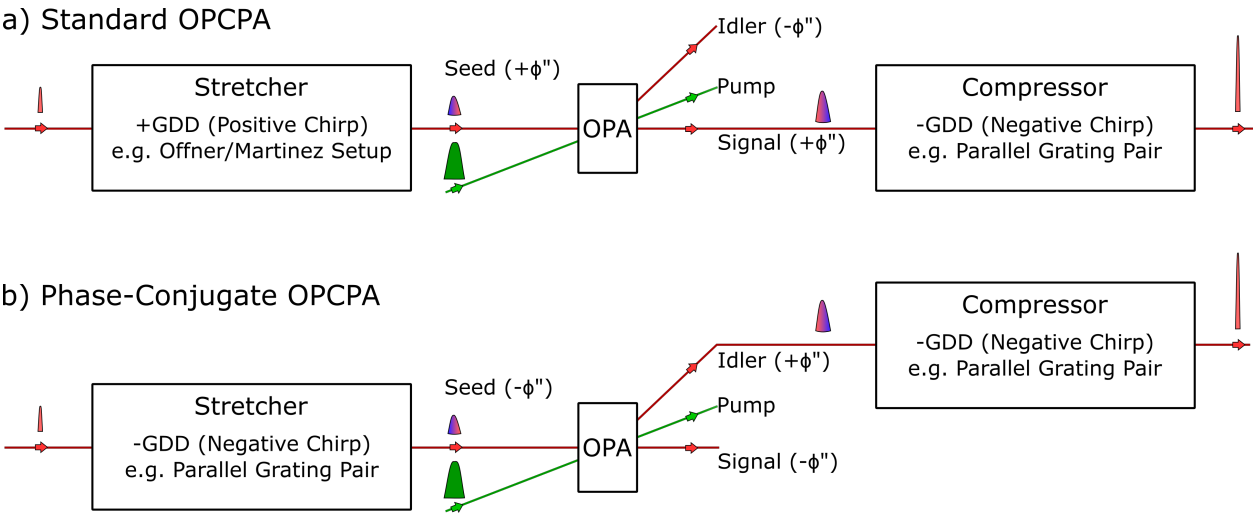


Figure 5.17: Phase-conjugate OPCPA schematic. In "Standard" OPCPA, the stretching and compressing all occurs on the seed. In phase-conjugate OPCPA, the stretching occurs on the seed using a "low scatter" parallel diffraction grating pair and the following OPCPA stages produces an idler pulse with opposing chirp from pumping with a transform-limited pulse that can also be compressed with a "low scatter" parallel diffraction grating pair.

Akahane et al. demonstrated idler compression using a single glass block to both stretch the seed and recompress the generated idler to back towards a sub-100 fs pulse duration from a single OPCPA stage using a compressed, transform-limited pump pulse [110]. Using only material dispersion to chirp the pulses in this way greatly simplifies the optical setup compared to prism or grating stretchers and compressors for low/medium power systems. However, for high-power lasers we still require large chirp factors and therefore parallel grating setups are still necessary.

For our experiments, we used two independent parallel grating pairs, from the Cerberus Terawatt lab and Multi-Terawatt Lab compressors, to afford greater flexibility due to the fact the pump pulses for the ns-OPAs are not transform-limited, and therefore the chirp of the idler will not be a perfect inverse of the seed, understood from the energy conservation relation $\lambda_{pump}^{-1} = \lambda_{signal}^{-1} + \lambda_{idler}^{-1}$. In the phase-conjugate OPCPA layout, a 0.5 nm negative chirp across the 1ns FWHM of the pump pulse will therefore only create ~1 nm FWHM negatively chirped bandwidth in the generated idler when producing a ~3 nm FWHM bandwidth signal pulse. As this idler bandwidth is generated in the same temporal window, we may therefore infer the magnitude of the idler chirp to be

approximately three times greater than the seed, which start to become unfeasible with the grating angles and separation required in the laboratory setting. To compensate for this, we shortened the parallel grating separation in the seed stretcher to produce a smaller stretch factor. However, this partially invalidates the scatter pedestal investigations, as ideally identical stretch factors to the imaging Öffner stretcher should be used in a proper comparative test. Thus far, with limited experimental time, we have yet to recompress the idler pulse below ~5 ps and observe meaningful results on this pedestal intensity and duration from the phase-conjugate OPCPA operation. In addition to the second-order phase, the idler is also prone to higher-order phase accumulation from the pump. As the phase of the pump is not tightly controlled in this system by design decisions made without reference to testing phase-conjugate OPCPA, such as using mismatched grating angles, the large amounts of material dispersion from the regenerative amplifier and successive amplifier stages, it is likely a large amount of higher order phase in transferred to the generated idler beam and used currently limits its compressibility. Spatial chirp from the non collinear angle to separate the pulses from the OPA can also have an effect, although changing this angle between 0.5 - 5 $^{\circ}$ appeared to show no observable effect on the pulse compressibility or contrast features.

5.7 CONCLUSIONS

We have experimentally studied the temporal contrast of compressed high-power laser pulses from major laser laboratories in the UK, including hybrid OPCPA/Nd:Glass system of Cerberus (IC), Orion (AWE) and Vulcan (AWE) and a gain-storage Ti:Sapphire/Nd:Glass CPA terawatt system at Queen's University Belfast. These contrast studies used the third-order autocorrelator diagnostic (TOAD) system developed by the author.

We observed a common mid-range noise pedestal of ~30-50 ps FWHM duration at ~10^{-4}-10^{-5} peak relative intensity seen across all the chirped pulse amplification laser systems characterised, whose exact origin is currently unclear but optical scattering and diffraction mechanisms are likely candidates that require further investigation to understand and eventually eliminate this source of noise. We attempted a new phase-conjugate OPCPA architecture to test the CPA scatter pedestal theory by avoiding the use of high-scatter imaging grating stretcher setups. However, higher-order phase from the pump pulse to the idler likely prevented compressibility of the phase-conjugate idler pulse. Fu-

ture investigations using this scheme must therefore address the phase management on the pump pulse, which could be introduced from the regenerative amplifier etalon or from mismatched grating angles and alignment through the stretcher systems. Alternatively, smoother optical components or wavelength scaling the contrast studies my change the observed pedestal intensity due to a high wavelength dependence on optical scatter.

The Cerberus, Vulcan and Orion OPCPA front-ends all produced pre-pulses in the third-order autocorrelation scans that have similar intensity post-pulse pairs that indicated these are non-linearly induced from post-pulse temporal overlap and interference on the strongly chirped beam producing self-phase modulation in high B-integral optics that then produce a matching pre-pulse after compression. The pre-post pulses found to originate from double internal reflections in the parallel faced ns-OPA crystals and a wedged/tilted crystal design was found to avoid this interference and generation of pre-pulses.

Additionally, the contrast of the complete Vulcan laser optical chain was able to measured for the first time and found to differ slightly to the partial optical system when measured to to ~10^{10} dynamic range, as the very high energy input sensitivity $\leq 1\mu J$ was required, which matched well to the ~5 μJ front-end energy that reaches the target without further amplification.

6

CERBERUS LASER-MATTER INTERACTION EXPERIMENTS

This chapter will showcase a number of laser-matter experiments that have benefited from access to the Cerberus laser system, both as a "driver" and a probe of extreme physical processes. The results from these experiments are largely the work of a team of colleagues who persevered with the assistance of the author in delivering laser light to target in a number of complex experimental geometries and helping to set up and operate optical diagnostics relevant to the experiments. However, before we introduce these experiments, it is useful to detail some of the key physical processes that occur when the high-intensity, time-varying electro-magnetic field of the laser pulse interacts with a target material.

6.1 HIGH-INTENSITY LASER-MATTER INTERACTIONS

The irradiation of target with intense laser light from terawatt to petawatt systems will produce a plasma state of matter, whose density, temperature and dynamics are strongly influenced by the laser parameters (particularly energy, pulse duration, contrast, spot size) and the target parameters (material, density, density profile). This wide range of parameters allows tailoring of the light-matter interaction. We therefore define a number of key plasma parameters and the nature in which they are influenced by light, or modify the propagation of light towards a target, in the following sub-sections. This will inform the dominant light-matter interaction processes that are likely to occur in the various experiments in this chapter using the laser pulse sources from the Imperial College Cerberus laser system.

6.1.1 *Free Electron Interaction in an Intense Electromagnetic Field*

At intensities greater than 10^{12} W cm^{-2} a variety of ionisation mechanisms exist that lead to formation of a plasma state of matter for highly ionised targets. An electron freed from

its parent ion in the presence of the time vary electromagnetic (EM) field of a high-power laser pulse will gain a kinetic energy from the Lorentz force

$$F = m_e \frac{d\overrightarrow{v}_e}{dt} = e\left(\overrightarrow{E} + \overrightarrow{v}_e \times \overrightarrow{B}\right) \tag{6.1}$$

Where $\overrightarrow{E}$ is the electric field and $\overrightarrow{B}$ is the magnetic field of the laser. In the non-relativistic regime, where $\left|\overrightarrow{v}_e\right| \ll c$, the forces are dominated by the electric field term. The co-sinusoidal electric field of the laser pulse drives a sinusoidal modulation of the electron velocity at the fundamental laser frequency ω_L

$$v_e(r,t) = \frac{eE}{m_e\omega_L}\sin(\omega_L t) \tag{6.2}$$

The electron "quivers" in phase with the laser electric field at a cycle-average magnitude of $v_{quiver} = {}^{eE}/_{2m\omega_L} = {}^{eE\lambda_L}/_{4\pi m_e c}$ from the ponderomotive kinetic energy of (6.2). At high-intensities (typically >10^{18} W cm^{-2}) the electron motion becomes relativistic (the electron velocity is sufficient to induce a non-negligible mass change) and the magnetic field also becomes important in determining the electron motion. We can show at which point relativistic effects become important from inspection of the Lorentz factor

$$\gamma = \left(1 - \left(\frac{v_e}{c}\right)^2\right)^{-1/2} = \left(1 - \left(\frac{eE\lambda_L}{4\pi m_e c}\right)^2\right)^{-1/2} \approx \left(1 - \frac{I\lambda_L^2}{1.4\times 10^{18} W cm^{-2}\mu m^2}\right)^{-1/2} \tag{6.3}$$

which affects the ponderomotive energy of the form $U_p \propto (\gamma - 1)\, m_e c^2$. As both the electric and magnetic fields are perpendicular to each other and the propagation vector of the laser pulse, the ponderomotive force acts to drive electrons away from the highest-intensity centre of the interaction. We also see $U_p \propto \lambda_L^2$ and for typical 1 μm terawatt-petawatt laser sources relativistic effects become important beyond ~10^{18} W cm^{-2}.

6.1.2 *Laser Propagation Through a Plasma*

A plasma is quasi-neutral ensemble of free-electrons and ions that collectively interact via electromagnetic forces. In a plasma, the electrons can be locally shielded from EM forces beyond their nearest neighbours. The extent of thermal kinetic motion and EM shielding is quantified by the Debye length

$$\lambda_D = \sqrt{\frac{\varepsilon_0 k_B T_e}{n_e e^2}} \tag{6.4}$$

where T_e denotes the electron temperature, which is determined loosely from the ponderomotive kinetic energy $U_p \sim k_B T_e$. The electrons at the edge of the plasma volume are not sufficiently shielded, contributing to a Debye sheath with an exponential fall in density of the form $n_e = n_0 \exp(e\phi/k_B T_e)$, where n_0 is the initial electron density and $\phi$is the charge-separation potential.

An electromagnetic wave propagating along the wave vector kL through a plasma follows the dispersion relation

$$\omega_L^2 = \omega_p^2 + k^2 c^2 \tag{6.5}$$

and refractive index

$$n_{plas} = \sqrt{1 - (\omega_p/\omega_L)^2} \tag{6.6}$$

,where ω_p is the electron plasma oscillation frequency. The plasma frequency is only dependent upon the electron density $n_e$from the relation

$$\omega_p = \sqrt{\frac{n_e e^2}{m_e \varepsilon_0}}. \tag{6.7}$$

From inspection of (6.5), if we consider a laser pulse with a positive k vector, the pulse is only allowed to propagate through the plasma when $\omega_p < \omega_L$ or will otherwise be reflected. Therefore, the critical density n_{crit} can be defined as the maximum electron density allowed until the plasma becomes opaque to the incoming laser EM radiation,

$$n_{crit} = \frac{4\pi^2 m_e \varepsilon_0 c^2}{e^2 \lambda^2} \tag{6.8}$$

Which corresponds to ~10^{21} cm^{-3} electron densities for 1 μm laser pulses. When the electron density exceeds this value, the laser pulse penetrates on the order of the skin depth $\delta = c/\omega_p$, which is ~170 nm at critical density for 1 μm laser pulses.

In an 'overdense' plasma, where $n_e > n_{crit}$, direct acceleration of electrons from the ponderomotive force is no longer possible. However, additional mechanisms become more dominant for energy transfer into the plasma electrons and/or ions.

An important property to consider is the expansion of the plasma electron cloud as energy is transferred from the laser photons or global electric field to a solid target, resulting

in ionisation, heating, plasma formation and hydrodynamic expansion. The spatial extent of the electron cloud over which a plasma plume is established and extends away from a solid target, or critical surface, is typically denoted as the plasma "scale length", and can be defined as the spatial extent the electron density remains approximately uniform. A very simple model is to assume isothermal expansion of the plasma from the kinetic energy of the electrons. For a one-dimension non-relativistic ideal gas and ignoring electron collisions this can be expressed as

$$L = \sqrt{\frac{2k_B T_e}{m_e}} t \tag{6.9}$$

where t is a timescale parameter, which is usually taken to be the primary laser pulse duration; however, for consideration of laser contrast this is better approximated by the time duration of the contrast limiting window, above which the intensity is sufficient to ionise the target. Shorter temporal extents therefore correspond to thinner plasma layers. Long timescale contrast features can extend the pre-plasma scale length up to many hundreds of micrometers, potentially preventing direct heating from the laser into the skin depth of the plasma volume. This scale length can be determined experimentally using optical probing of the interaction just before arrival of the laser pulse or inferred indirectly, for example measuring/calculating the X-ray source size of solid target at various X-ray energies, or by investigating the efficiency of resonance absorption as a function of angle. If we assume pre-pulses are able to generate electrons with electron temperatures between 1 eV-1 keV we can estimate that even weak pre-pulses that ionise targets before arrival of the main pulse can create a plasma that will expand at a rate of ~0.5 – 15 μm ps^{-1} between these temperature ranges. For a plasma plume extending many optical wavelengths away from the target surface, this strongly influences both the subsequent laser-plasma energy coupling mechanisms, and the position of energy deposition and subsequent energy transport into the bulk of the target.

6.1.3 *Contrast Sensitive Plasma Heating Mechanisms*

The dispersion relationship between the laser pulse and the plasma in (6.5) will cause reflection of the EM field of the laser at or close to the critical density surface. For pulses that are not normal to this interface, there is a time-varying evanescent electromagnetic field that penetrates beyond the boundary established by the critical density surface. This

evanescent field decays exponentially into the plasma volume and exists as a consequence that the electric field cannot be discontinuous at the critical surface. This evanescent field can accelerate electrons beyond the critical surface, driving collective plasma oscillations close to fundamental frequency of the laser pulse with a fractional absorption rate given by [6]

$$f_{ra} \cong \frac{\left(2.3\tau \exp\left(-2\tau^3/3\right)\right)^2}{2} \tag{6.10}$$

where $\tau = \sqrt[3]{2\pi L/\lambda_L}\sin\theta$ is a convenient parameter that includes the angle of incidence and scale length. This parameter is maximised for ~25° incidence angles and the laser pulse must be p-polarised. We see that large scale lengths exponentially decrease the energy absorption and therefore high-contrast pulses are required for efficient energy coupling close to the critical surface by resonant absorption. Greater than 20-30% energy extraction is possible for 10^{16}-10^{17} W cm^{-2} peak-intensities.

So called vacuum, or Brunel, heating relies upon very short scale lengths and steep density gradients at oblique target incidence angles such that electrons are pulled out from the plasma surface into the vacuum and subsequently re-injected into the plasma via the ponderomotive force as the electric field of the laser changes direction every half cycle [111]. The fractional energy absorbed was empirically found by Brunel to obey the relationship [111]

$$f_{vh} = \frac{2n_{plas}v_{quiver}}{\pi c \cos\theta}$$

At sufficiently high intensities when the electron quiver velocities approach relativistic speeds, the $\overrightarrow{v} \times \overrightarrow{B}$ magnetic field terms of the Lorentz force become more influential. At normal incidence, the electric field component of the quiver velocity and the magnetic field of the laser pulse are both normal to the plasma surface. Therefore, the $\overrightarrow{v} \times \overrightarrow{B}$ vector acts to drive longitudinal oscillation of electrons in and out of the plasma surface, creating an acceleration of electrons into the overdense plasma. These so called "hot" electrons are typically injected into the target at velocities substantially greater than the background thermal plasma electrons and so it is common to establish a "multi-temperature" plasma, where a small fraction of high-energy electrons do much of the "work" of ionising matter or creating energetic x-rays before they thermalise through multiple collisions.

6.1.4 *Contrast Insensitive Plasma Heating Mechanisms*

In some cases, pre-ionisation and generation of a low-density plasma before the arrival of the main pulse may be desirable for the experiment, for example to enhance energy absorption from processes that favour longer plasma scale lengths. For example, a study found a ~10^{14} W cm^{-2} pre-pulses between 2-11 ns ahead of the primary pulse produced observed up to 50 times greater X-ray flux from planar aluminium and vanadium targets when irradiated with ~10^{16} W cm^{-2}primary pulse intensities [112].

The ponderomotive motion of an electron oscillating in the Coulomb field of a more massive ion can be damped by collision with the ion which prevents complete return of the electron energy to the light field. This collisional process transfers energy to the plasma electrons, which in turn can heat the accompanying ions and, transferring energy to ions and electrons deeper within the plasma can then occur through a range of transport processes driven predominantly by the hot-tail of the electron energy distribution, or by radiation dependent on the local plasma conditions. This "inverse bremsstrahlung" collisional absorption process in sub-critical plasma can be dominant at intensities between 10^{12}-10^{16} W cm^{-2}, due to the inverse temperature scaling found in the electron-ion damping rate [6]

$$k_{ib} \propto \frac{Zn_e^2}{\sqrt{T_e^3\,(1-{}^{n_e}/_{n_{crit}})}} \tag{6.11}$$

and is also responsible for driving some continuum X-ray generation processes. This collisional absorption is strongest at "high" but sub-critical density in low temperature plasmas with heavier ions. It has also been shown that the fractional absorption increases with plasma scale length [113]. As this indirect plasma heating process scales favourably with longer plasma scale lengths i.e. poorer contrast laser pulses, this heating mechanism is also favourable for "long-pulse" sources at lower intensities.

6.2 CERBERUS SHORT-PULSE: OPTICALLY LEVITATED MICRODROPLET TARGET

This section will give a brief overview of the first experimental campaigns that used the terawatt laser output of the Cerberus laser. This was a unique target developed during the PhD works of Dr Christopher Price and is currently being further developed by Sam

Giltrap, who has recently successfully shot these targets with petawatt pulses from the Vulcan OPCPA/Nd:Glass system of the Central Laser Facility (STFC).

Trapping of transparent microdroplets is possible due to radial forces from refraction of light through the target and scattering processes that impart vertical forces, i.e. "radiation pressure", upon the droplet [114, 115]. The magnitude of the upward vertical forces that counteract gravity can be understood if we consider the photon forces acting on a partially reflecting mirror. A single photon, with momentum $h\nu/c$, that reflects at normal incidence to this mirror will impart a momentum of $2h\nu/c$ onto the mirror. If we consider a CW laser beam with an average power P_{avg} with $P_{avg}/h\nu$ photons per second aimed at the mirror, of reflectivity R, this will produce a total force per second F_{lev} equal to the momentum contribution of each photon onto the mirror multiplied by the number of reflected photons

$$F_{lev} = \frac{2h\nu}{c}\frac{P_{avg}}{h\nu}R = \frac{2P_{avg}R}{c}. \tag{6.12}$$

If we consider a 1 W CW laser beam focused onto a 10 μm droplet of 1 g cm^{-3} density and 4% reflectivity, the vertical force on the droplet will be 60 g, where g is the downward vertical acceleration from gravity and therefore levitation is possible.

The optical levitation trap is able to support a single, mass-limited ~10 μm diameter oil droplet ~ 40 mm distance from the trapping optic, allowing a very large field of view for diagnostic access and protection of the final focusing optics against plasma self-emission and scattered high-intensity laser light. These microdroplets are able to be trapped under vacuum (~0.6 mbar) and be stable for a number hours, a suitable time for alignment and eventually firing high-power laser shots on to. Mass-limited objects can couple very strongly to an intense laser field due to transient plasma resonances or Mie scattering processes and absorb substantial amounts of laser energy, whose excited electrons do not form an earth connection via a target holder/stalk, which is the case for other solid targets such as thin foils for proton acceleration experiments. This unique target differs from other mass-limited targets such as gas jet media, which produce a large volume of smaller sized (~1-100 Å) atoms/molecules/clusters that together produce a large experimental signal e.g. X-ray emission, whereas deposition of laser energy into a single target can potentially create a hotter plasma material state that will then form brighter secondary sources, such as X-rays and protons, that are also low debris.

A full detail of the target design, characterisation and performance can be found in the thesis of Dr Christopher Price [116] and instrumentation publication [39]that presents X-ray characterisation and ~x10 reduction in radio-frequency/electro-magnetic pulse (EMP) emission in comparison to a carbon solid target of similar size that was attached via a stalk to the target chamber.

6.2.1 *Experimental Set Up*

An optical layout of the microdroplet levitation trap is shown in figure 6.1. A high numerical aperture aspheric lens focuses a 50 mm diameter ~360 mW CW laser beam to ~3 μm at focus. Microdroplets of ~10 μm diameter are able to be trapped initially above this focus. large forces are required to capture and stabilise the gravity fed microdroplets and therefore the optical power could be lowered to as little as 40 mW under air and vacuum conditions, where the droplet trapping forces would stabilise closer to the laser focus. The CW laser light is fed into the target chamber trapping rig via a single-mode optical fibre, permitting minimal optic use inside the chamber and easy injection of trapping light with good beam profile quality into the trapping optics.

A high-speed position sensitive detector was also developed to observe various dynamic instabilities e.g. air/vacuum pressure, vacuum pump noise, CW laser/electrical noise and a feedback loop based upon CW power control via a Pockels cell provided correction for the significantly weaker vertical forces acting on the droplet.

Droplets nebulised from vacuum oil (KJLC 704) were initially trialled for vacuum loading for their highest compatibility, as water based sources will likely boil under vacuum conditions. To achieve trapping under vacuum conditions suitable for interaction with high-power laser pulses, the microdroplets were first trapped in air and a transparent

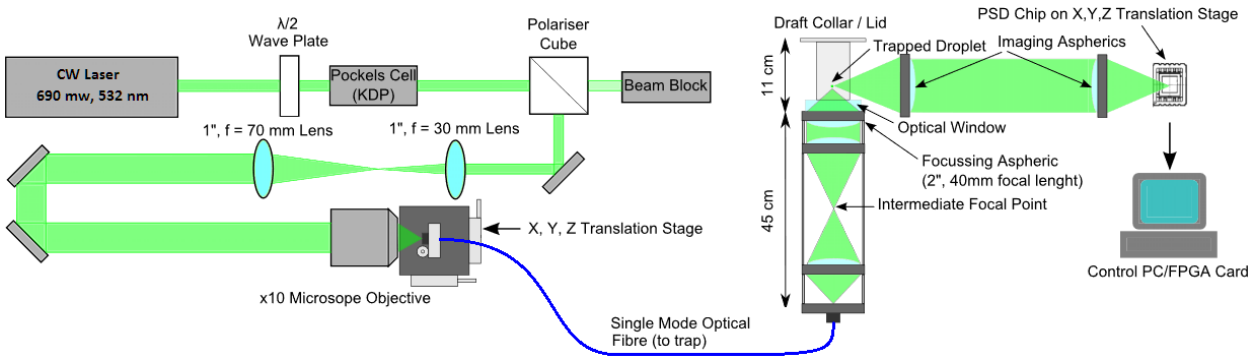


Figure 6.1: Optical layout of the levitation trap beam handling and trapping optics.

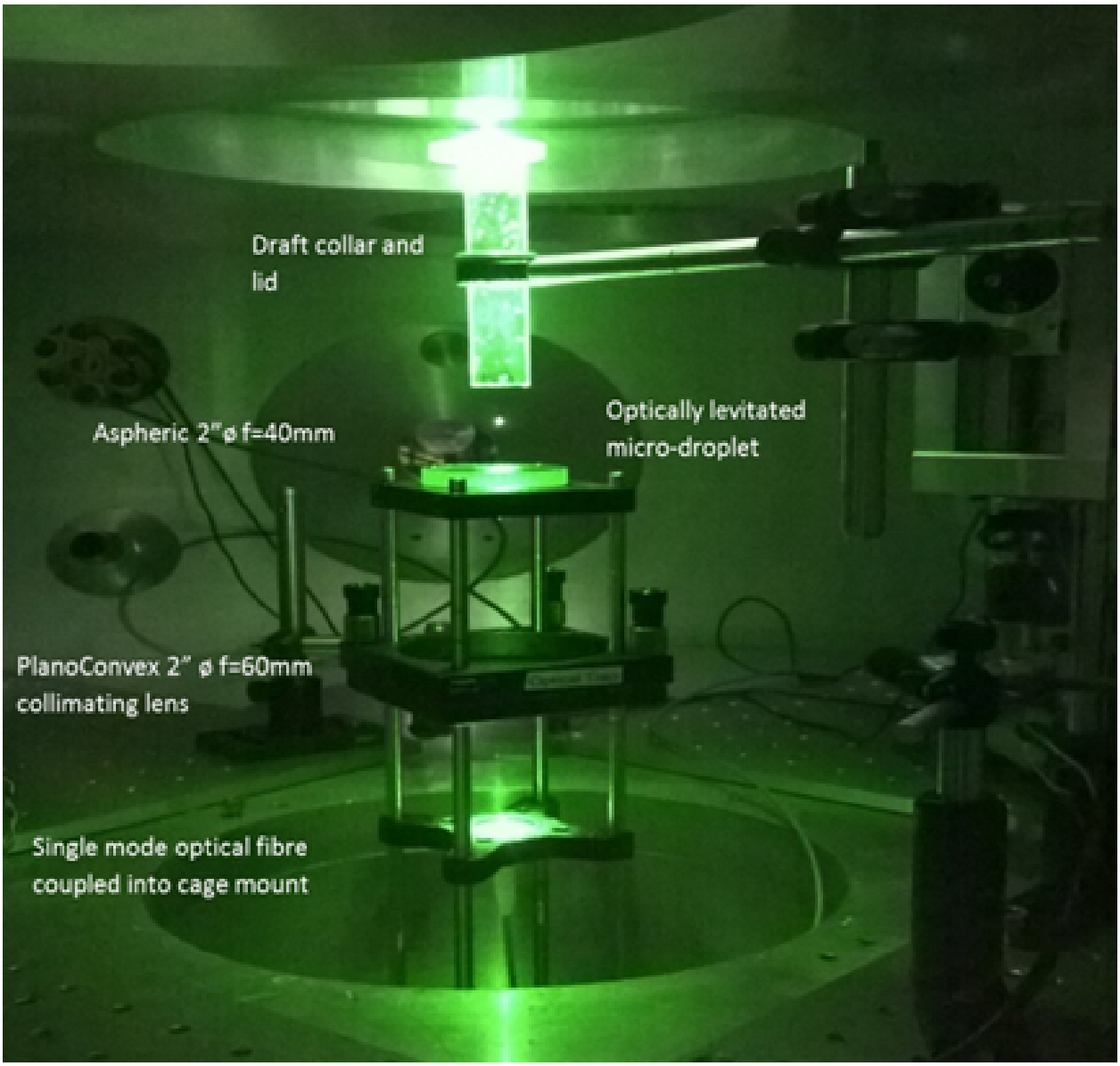


Figure 6.2: Photograph of a trapped microdroplet under vacuum inside the Cerberus Terawatt Lab target chamber.

"draft collar" lowered over the droplet to protect against air currents during pump-down of the target chamber. Once a suitable a suitably low ≤ 1 mbar pressure was achieved, the draft collar could be raised to fully expose the trapped microdroplet to alignment beams/diagnostics and the high-power laser beamline, as shown in figure 6.2. Pressures less than 0.5 mbar require turbo-molecular pumps to achieve up to 10^{-4} mbar, however their close proximity and high frequency vibrations consistently destabilised and knocked out the microdroplet. These high-vacuum pumps on the recent petawatt experiment with the Vulcan laser were very well isolated from the target location, allowing these low vacuum pressures to be achieved during trapping conditions.

A layout of the laser beam geometries and diagnostics is presented in figure 6.3. Various diagnostics were used to characterise the microdroplet source, including steel knife-edge used for penumbral X-ray source size measurements with ~x6 magnification using X-ray sensitive image plate (Fuji BAS MS2325). The generation of EMP around the high-intensity interaction can limit the number and types of diagnostics that may be fielded in close proximity on an experiment that are at risk of permanent electrical damage and therefore an RF probe, a plastic insulated 6-turn copper wire coil, was positioned inside the chamber and fed out to a 500 MHz oscilloscope to measure the EMP emission of the microdroplet source in comparison to other target types. A 25 μm beryllium filtered single-hit X-ray sensitive in-vacuo CCD camera was installed on an extended section of the chamber for spectroscopy of X-ray emission from the target.

The alignment of the isolated ~10 μm trapped microdroplet targets to the high-power laser focus was a non-trivial problem without calibrated and position-encoded high magnification alignment cameras that image the "target chamber centre" (TCC), where diagnostics and the high-power laser beamline are aligned to. On the Cerberus experiment, this was achieved with a combination of target scatter imaging cameras (Cam A and B), looking in multiple orthogonal viewing angles to align the droplet in three-dimensional space, and laser near-field profiler (Cam C on figure 6.3) through TCC that maximised obscuration of the laser light from the droplet. The scatter imaging cameras used singlet lenses and therefore the lens position could be adjusted to either view the 532 nm scattered light from the droplet trap or the 1054 nm light from scattered Cerberus light. TCC was first defined with an alignment wire, to which diagnostics and cameras are aligned to. The reference co-ordinates of the wire was then marked on the orthogonal viewing cameras. The optical trap would initially sit away from this position, so as not to hit the wire, and the wire removed and optical trap moved into position of the TCC reference with an X/Y/Z translation stage mounted to the optical trap. Once close to TCC, the 1054 nm Cerberus scatter would become visible and its intensity maximised when using the oscillator alignment beam through the entire optical system. At maximum intensity, the obscuration of the droplet would start to be visible, allowing further optimisation of the droplet position by maximising the attenuation of the near-field laser profile. At this point, the Cerberus short-pulse laser system could be switched to amplify a single Terawatt laser pulse to interact with the trapped microdroplet target. With each stage of optimisation, the oscillator power was reduced with waveplate-polarisers to avoid knocking the microdroplet out of the trapping potential, which was found to be ~1 mW at best

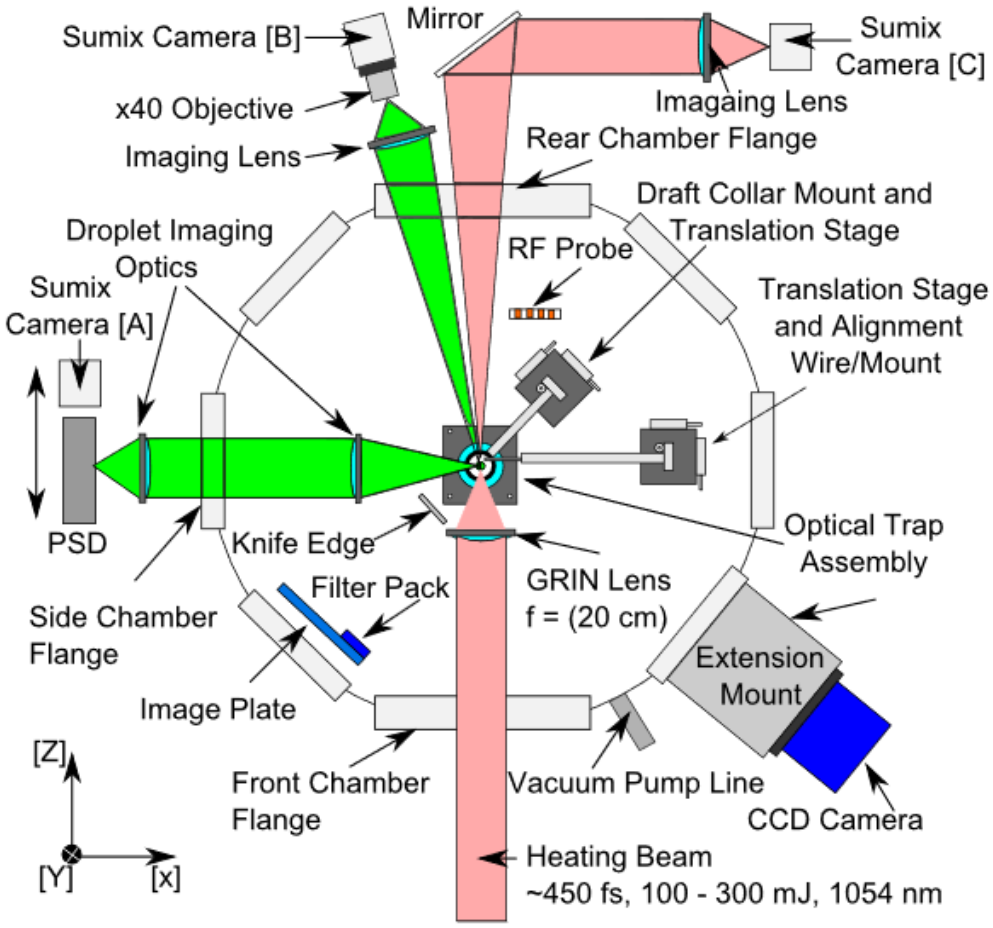


Figure 6.3: A schematic of the target chamber, alignment, and diagnostic-layout for the high-intensity laser droplet interaction experiments. Knife-edge diagnostics were used to measure X-ray source size, an Andor CCD camera used as a single hit low-resolution spectrometer for X-ray photons, and a pick-up probe deployed to measure the RF emission. Viewing angles were established to monitor the trapped droplet position (Sumix camera [A] and [B]) and also for accurate alignment with the main heating beam under vacuum (Sumix camera [C]). Image courtesy of Dr Christopher Price.

Target	Target Thickness	Horiz. Source Size	Vert. Source Size
Oil Microdroplet	~10±4 μm	20±3 μm	19±3 μm
Aluminium Foil	6 μm	49±8 μm	59±6 μm
Carbon Wire	9 μm	41±7 μm	20±3 μm
Glass Sphere	~15±5 μm	47±9 μm	20±3 μm

Table 6.1: Filtered source size measurements for various targets irradiated with 7 μm FWHM ~10^{18} W cm^{-2} intensity pulses from the Cerberus laser.

focus. The droplet trapping stability was found to be ±5 μm from the position-sensitive detector characterisation, which led to a small percentage of shots with slightly lower X-ray energies from fluctuation within the ~7 μm focal spot diameter.

6.2.2 *Results*

The apparent X-ray source size is a key parameter to minimise for high-resolution point-projection X-ray imaging techniques. This was determined by measuring the line-spread function (LSF) across the horizontal and vertical knife edge in the image plate scan, which was also compared against other target types. A single pixel of the image plate scanner (Fuji BAS 1800II) was found to be 42±2 μm, with a minimum LSF FWHM of 3.2 μm, i.e. 134 μm resolution, from placing a knife-edge directly on top of the image plate. With the ~x6 magnification of the knife-edge measurement, this resolution is reduced to ~22 μm, which is still larger than the average droplet size and the laser focus. Regardless, comparisons of X-ray source size for photon energies above ~300eV, using a 0.6μm Al filter, were made to different solid target materials and shapes in table 6.1. The results show quite clearly that the mass-limited spherical microdroplets produced the smallest source size, with measurements limited to the minimum sensitivity of the measurement determined by the image plate scanner.

Largest source sizes are seen from the extended foil targets and along the long axis of the carbon wire target of similar atomic number and thickness to the microdroplet. A glass sphere approximated the microdroplet source but the source size was increased in the direction of its mounting stalk. These measurements show a large potential for

this mass-limited target source to be a useful candidate for high-resolution X-ray point-projection.

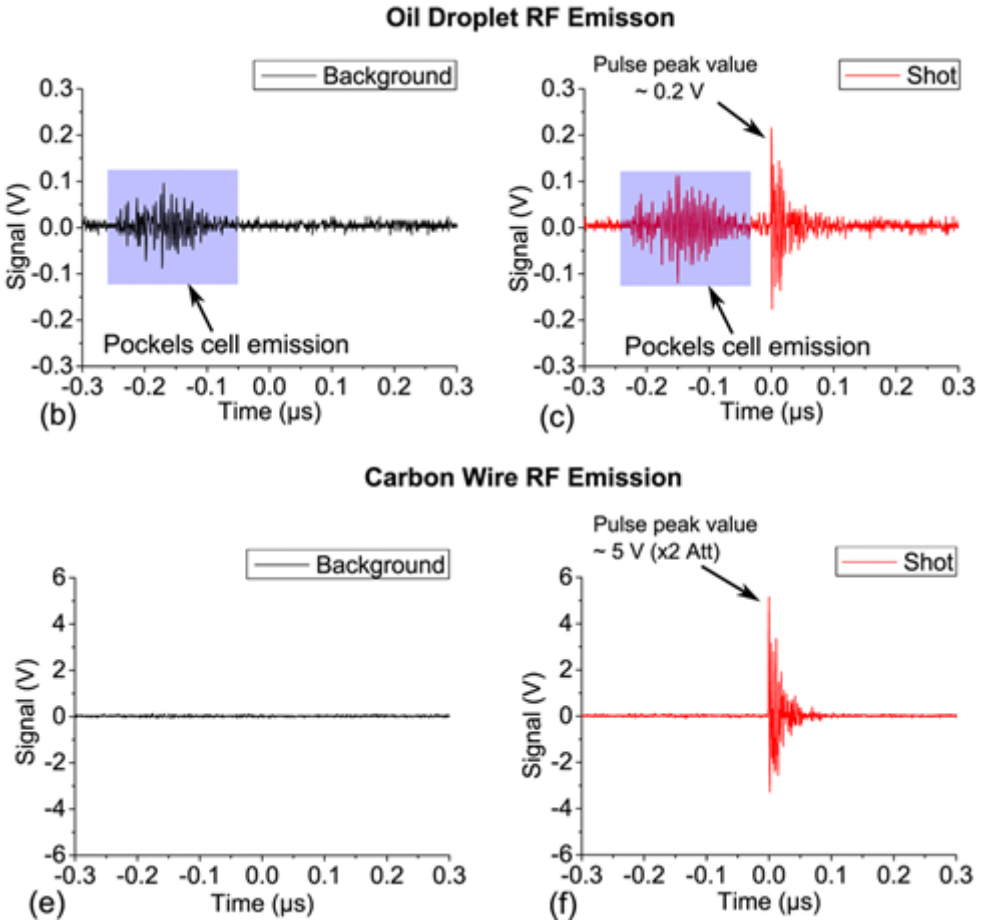


Figure 6.4: Radio-frequency signal measurements for oil droplet and carbon wire shots. Background measurements were taken to account for other noise sources within the dynamic range of each measurement; for instance, Pockels cell noise was observed with the higher sensitivity range when probing the droplet interaction. The carbon wire produced ~50 times greater RF emission, suggesting substantial EMP reductions from the mass-limited target source.

Figure 6.4 shows the RF emission intensities between the mass-limited microdroplet and carbon wire interactions. A background signal was taken within the dynamic range used for each measurement, which accounted for other noise sources not related to the laser-matter interaction, and was taken as the measured RF signal when the laser was fired into the target chamber with no target in place. We see that the carbon wire produced a peak 5 V, with x2 attenuation factor, signal versus the 0.2 V observed peak-voltage from the droplet interaction. This suggests the RF, and hence EMP emission from the micro-droplets are up to 50 times weaker from their mass-limited properties when compared against mounted solid targets of similar atomic number and size. The EMP emission is

largely thought to be due to the plasma electrons rapidly conducting back down through the target stalk into the chamber walls or from hot electrons blown off from the target that then hit the chamber walls and conduct back up the target stalk. Removal of the target stalk effectively reduces this conduction path of electrons, greatly reducing the RF/EMP emission strength.

6.2.3 *Conclusions and Outlook*

The high-power laser shots with the Cerberus laser system onto these optically levitated microdroplets are the first of its kind, presenting a variety of avenues to explore for this new target type. The results from experiment so far have identified this source to be a very useful X-ray source.

A number of developments will be explored. For example, due to the technical difficulty and time it took to trap, move out the draft collar, align and prepare for a high-power laser shot, many targets were lost within this process, leading to limited successful high-power laser shots during the campaign. Current and future trap designs will incorporate in-vacuum loading capabilities that will require significantly less time required to prepare and align the target before firing the high-power laser shots. Additionally, a variety of other target materials/sizes and geometries are envisioned, such as levitation of opaque metallic shell targets, which require a Bessel beam to produce stable trapping forces, or the combination of multiple droplets in close proximity (approximately a wavelength separation) to explore Mie resonances that enhance local electric fields.

More recently, these mass-limited microdroplets have now been shot with the Vulcan petawatt laser, producing further high-quality X-ray, EMP and proton/ion data that is currently being analysed and prepared for future publication.

6.3 DIAGNOSING MAGPIE Z-PINCH INTERACTIONS WITH CERBERUS

The Mega Ampere Generator for Plasma Implosion Experiments (MAGPIE) is a pulsed power Z-Pinch that creates high density plasmas by passing a large 1.6 MA electric current over approximately 240 ns through a material load, typically micrometer scale fine wires or metal foils [43, 44] arranged in a cylindrical geometry, known as a “radial wire array” (RWA). The pulsed-power is generated from four Marx banks, each holding 24

$\times$ 1.3 μF capacitors charged at 65 kV and discharged via dielectric breakdown through a connecting gas-filled spark gap switch. The energy deposited is over a much longer timescale, typically hundreds of nanoseconds, compared to a typical intense laser pulse. However, the deposited energy is far greater, $4 \times \frac{1}{2}CV^2$= 264 kJ, onto the load, producing terawatt peak power.

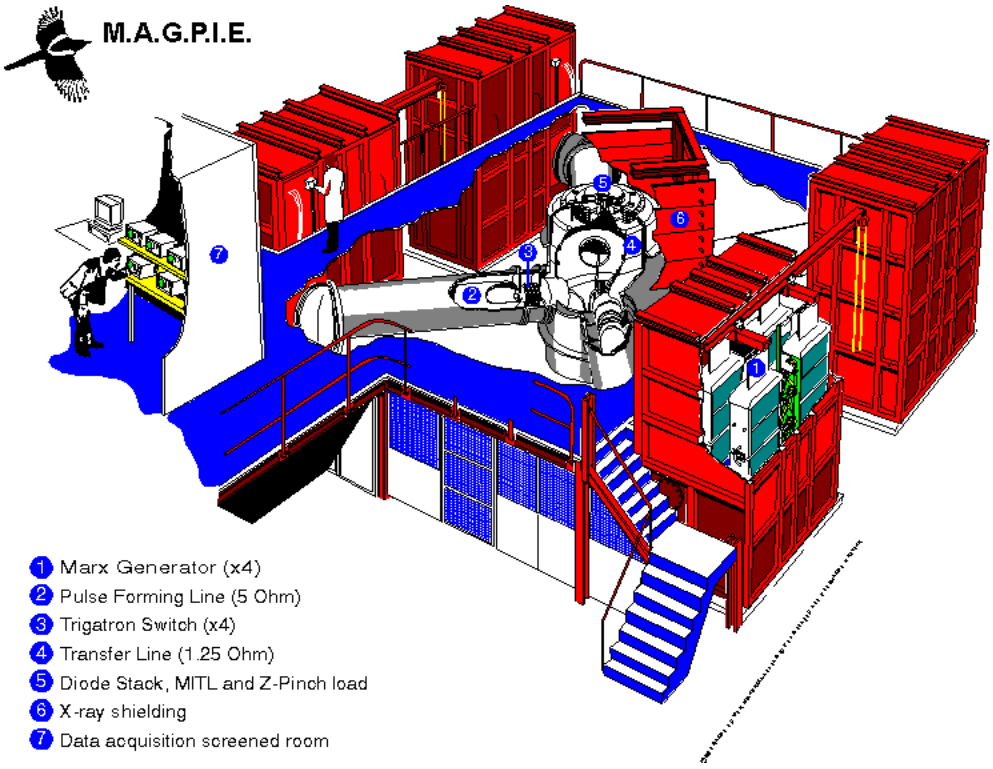


Figure 6.5: Cartoon drawing of the MAGPIE pulsed power generator main components. Each output of the four Marx banks is fed in to the high resistivity, deionised water filled pulse forming transmission lines that are that are isolated with further spark gaps, referred to as trigatrons, and therefore compress the discharge to the characteristic ~240 ns rise time of the generator. The vertical transfer lines are impedance matched to the pulse forming line and combine the four outputs in to the "magnetically induced transfer line" (MITL) which focusses the current flux from ~1.5 m from the VTl to the ~1 cm target load size. Image courtesy of the MAGPIE group.

The intense electric power that is driven through the RWAs create extreme resistive heating of the load, producing a plasma around each of the wires in the cylindrical geometry that consequently drive large magnetic fields around each wire and the corresponding $\overrightarrow{v} \times \overrightarrow{B}$ force from the conduction flow of electrons through the wire.

It is therefore possible to drive a range of plasma dynamics from these magnetic fields that can also mimic physical processes seen in astrophysical plasmas, a field known as 'Laboratory Astrophysics'. In the case of MAGPIE, it has been possible to produce highly-

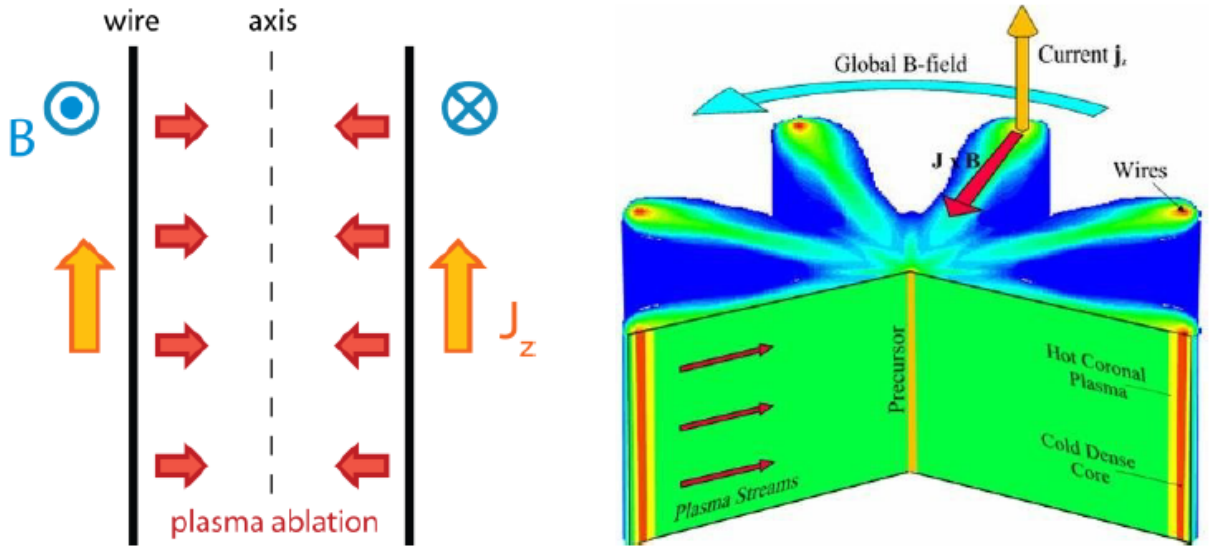


Figure 6.6: "Z-pinch" interaction from a cylindrical wire array load. Electrical current flows upwards through each wire in a cylindrical geometry. Heating of the wires creates plasma ablation from the wire surfaces, which accelerate towards and implode at the cylindrical centre from the strong $\vec{v} \times \vec{B}$ force. Reversal of the current direction creates exploding plasma ablation. Image courtesy of the MAGPIE group.

supersonic magnetically driven protostellar jets with scalable characteristics to those seen in jets and black holes [44, 117].

The Cerberus laser system was primarily built to provide greater diagnostic capability to characterise and understand interactions inside MAGPIE to significantly greater detail. The very low repetition rate of MAGPIE, one or two shots per day, requires numerous highly capable single-shot diagnostics to be as close to fully characterising each single shot. Fast time resolved optical diagnostics from pulsed laser systems are able to create snap-shots of a section of the interaction. The author was primarily responsible for delivering the Cerberus long-pulse to the target chamber and helping develop the optical diagnostic capabilities based around this source, which so far include generation of hard (1.865 keV) X-rays as a secondary source for high penetration and imaging of plasma electrons/ions in these interactions [5] and an energetic long-pulse to optically probe magnetic fields using the optical Faraday effect [35, 38, 118].

6.3.1 *X-ray Backlighter*

The use of pulsed lasers provides a tool to create a snap-shot image of the interactions of MAGPIE. As these interactions occur over many hundred of nanoseconds, even "long-pulse", nanosecond, duration laser sources provide relatively high resolution characterisation of the dynamic plasma flows. Optical diagnostics can be based around interferometry, which can measure spatial electron density profiles fringe shifts, or simply image the target interaction's shadow onto a camera, which will be sensitive to the plasma density gradients. This method is applicable only if the light that interacts with the dense plasma volumes arrives at the camera and will be completely absent for above critical electron densities in (6.8), which scales to the inverse-square of the probe wavelength. Near-infrared and visible light will therefore become ineffective tools to image the most intense part of the MAGPIE interactions and therefore development of a secondary monochromatic X-ray "backlighter" source was led by Dr Gareth Hall, based upon previous designs for Z-pinches and pulsed-power driven HEDP experiments [119–121].

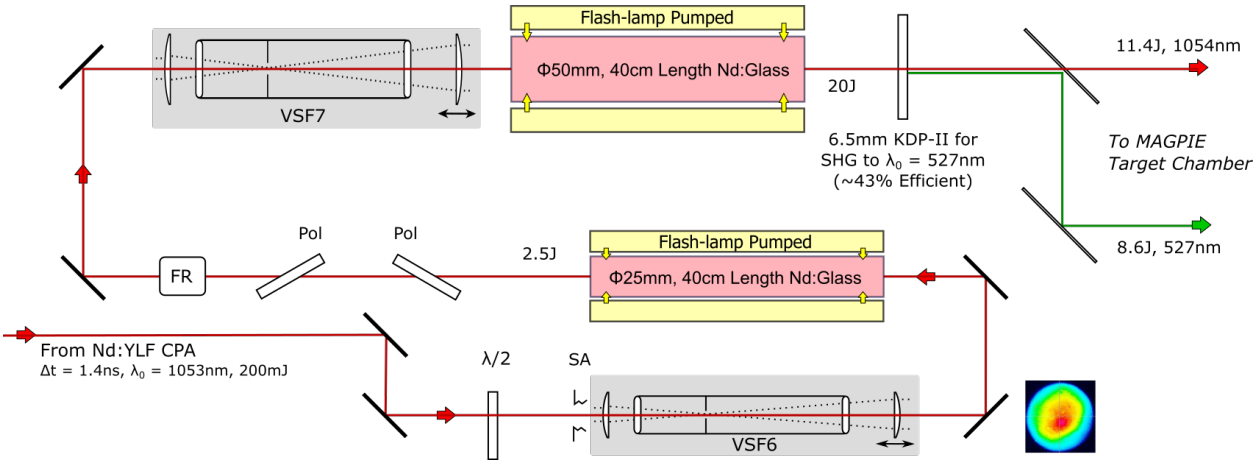


Figure 6.7: Optical layout in the MAGPIE Amplification Lab to amplify pulses from the Cerberus front-end up to 20 J energy for injection into the MAGPIE target chamber. Second-harmonic light is used for the X-ray backlighter source, while the 1054 nm beamline is used for the Faraday rotation diagnostic of magnetic fields, described in 6.3.2.

The X-ray source uses the high-energy long-pulse capability of Cerberus. The long-pulse "seed" is derived from the 10 Hz, 200 mJ, 1053 nm beamline that would otherwise pump the short-pulse ns-OPAs. This beamline is diverted with a waveplate-polariser and guided into an adjacent "MAGPIE Amplification Lab" in figure 2.3 that produces high-energy pulses from large, 25 mm and 50 mm aperture Nd:Glass (phosphate) rod amp-

lifiers, that generate up to 25 J at 1054 nm wavelength. For these experiments, between 18-20 J was produced during the early commissioning of the beamline and were able to be frequency-doubled to 527 nm wavelength with 43% conversion efficiency from a type-II, 6.5 mm thick KDP crystal.

The generation of monochromatic light utilises ionisation of the innermost electron orbital such that when the adjacent electron orbital relaxes into the vacant hole a characteristic He-α X-ray photon is produced. The silicon target material emits 1.865 keV energy X-ray photons from this He-α line. Ionisation of the innermost electrons typically occurs from collisions with hot electrons of the heated plasma target, which are heated by inverse Bremsstrahlung processes for long-pulse sources focused to ~10^{16} W cm^{-2} intensities.

The plasma electrons will also emit a continuous spectral distribution of X-rays. X-ray optics, that utilise the $m\lambda = 2d \sin\theta$ Bragg reflection condition of the [1011] orientation of quartz, reflect and image the 1.865 keV X-Rays at a 83.9° Bragg angle onto an X-ray sensitive image plate (BAS-TR) with x6 magnification.

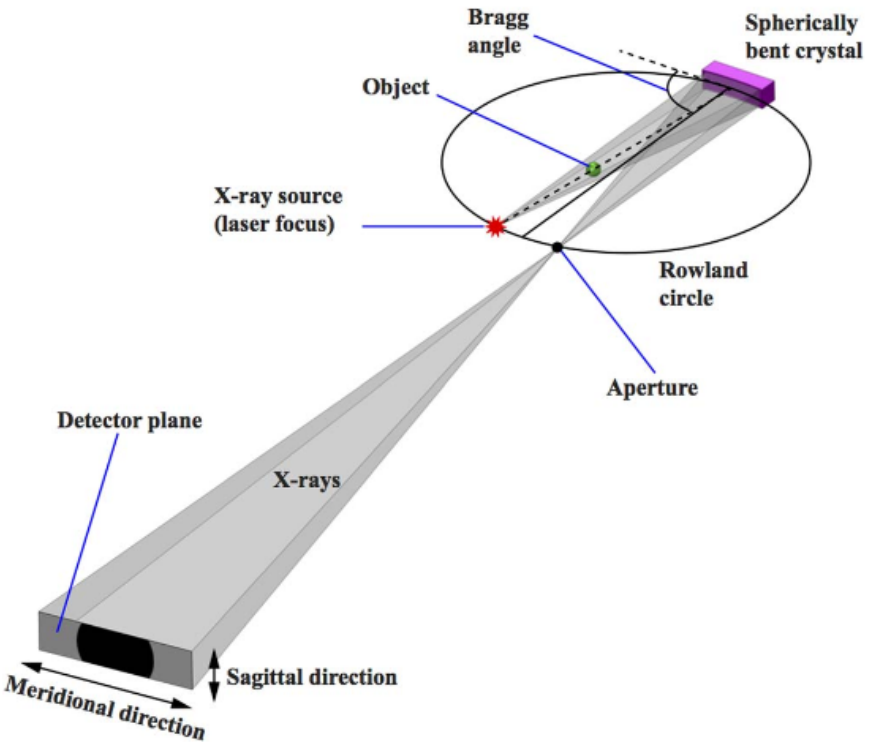


Figure 6.8: The X-ray Bragg imaging system of MAGPIE interactions. X-rays are first produced from irradiated silicon targets from the Cerberus laser and are partially captured by a bent quartz crystal that reflects the characteristic 1.865 keV photons that have traversed through the MAGPIE interaction. The light can be spatially and spectrally filtered and forms an image of the MAGPIE object plane, where the image plate is placed.

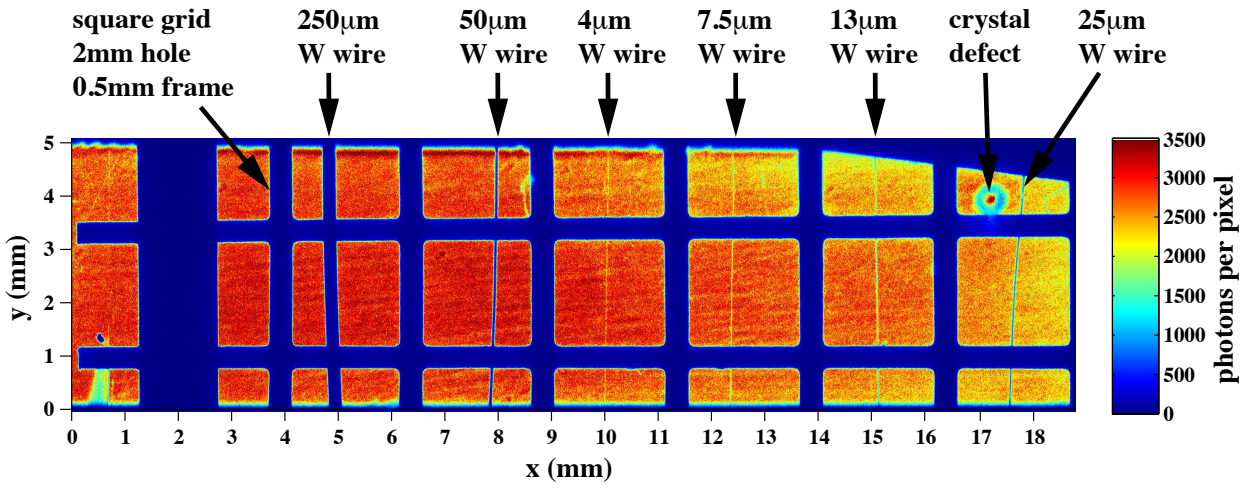


Figure 6.9: False colour X-ray image of a resolution grid. The grid was illuminated by the Si 1.865 keV K-α line. The results show that features as small as 4 μm can be discerned.

The MAGPIE interactions are also a strong source of X-rays and therefore the we require sufficient generation generation of backlighter photons to overcome this background noise and spectral filtering (25 μm beryllium to attenuate < 1 keV light) of the detector to further reduce X-ray noise from the MAGPIE interaction that may still have direct line of sight onto the detector. A test chamber was set up externally to the main MAGPIE chamber to measure if enough >1 keV X-Rays could be generated from the laser-matter target and measured with the X-ray Bragg imaging system. These initial tests saturated the image plate, allowing the Cerberus-MAGPIE experiments to commence.

The first X-ray backlighter shots in MAGPIE were laser-only shots to image static objects without MAGPIE firing. A grid formed of varying wire thicknesses gave an indication of the X-ray imaging system resolving power, which managed to resolve the smallest wire with 4 μm thickness. This value does not define the true imaging resolution, as strictly is should resolve two objects 4 μm apart.

The final experimental goal was to image plasma dynamics from a MAGPIE shot. Figure 6.10 shows the X-ray backlighter image of the plasma streams produced from a Z-pinch tungsten cylindrical wire array, using sixteen 25 μm thick wires, during the ablation phase. Known characteristic oscillations in the plasma production sites along the wires were seen, showing successful demonstration of the X-ray backlighting of MAGPIE interactions from the Cerberus laser. The X-ray backlighter signal through a range of shots was unusually low, providing poor contrast of retrieved images, potentially due to debris protection layers of the quartz reflector and laser windows.

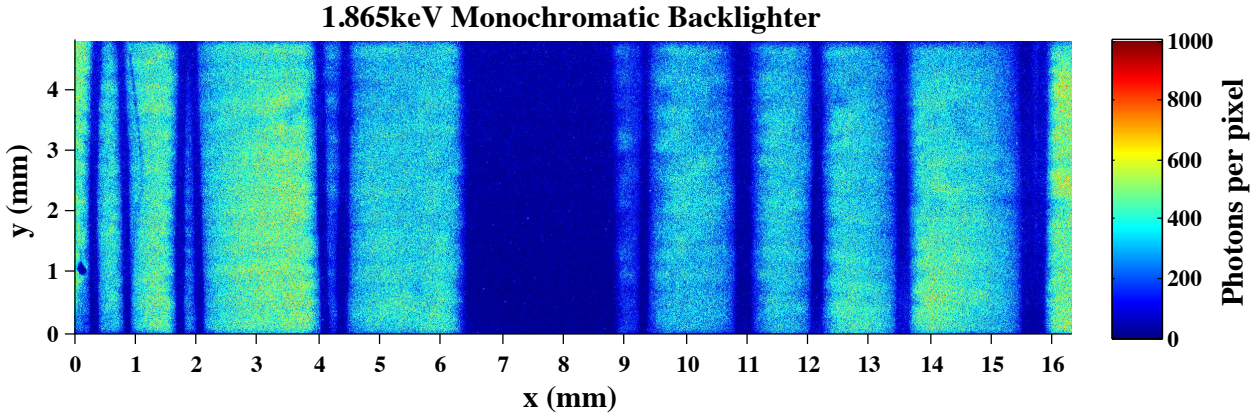


Figure 6.10: X-ray backlighter of a live MAGPIE tungsten wire array shot. Oscillations in the plasma production sites can be seen along each of the wires. The central thick column is a steel tube that quenches the Z-pinch implosion in order to reduce the emitted X-ray background light.

These first X-ray backlighter shots from the Cerberus-MAGPIE experiments represent the beginning of an experimental campaign to image plasma dynamics in the MAGPIE target chamber that were previously not detectable with visible probes alone, and have formed the basis of a publication [5]. The high energy X-rays will be able to penetrate deeper into high density plasmas before absorption or high-index refractive index gradients divert the imaging photons away from the imaging plane. Future investigations will aim to improve the collection and transmission efficiency of the X-ray imaging system.

6.3.2 *Optical Polarimetry Probe of Magnetic Fields*

The highly magnetically driven (1-10T field strength) plasma dynamics during MAGPIE shots require diagnostics that measure these fields. These magnetic fields can influence shock dynamics as well as driving particle acceleration schemes from magnetic reconnection, a process currently being investigated in MAGPIE and is responsible for astrophysical flares, where two opposing magnetic fields combine to produce bulk heating and particle acceleration [122, 123].

Magnetic induction probes are able to quantify the local magnetic field strengths along a single axis per probe; however are highly sensitive to electrically induced noise, either from interaction from hot electrons from the target or EMP generated from the experiment.

An alternative approach uses the optical Faraday effect to produce polarisation rotation of the electric field of the laser pulse from the traversed magnetic fields inside the MAGPIE interaction . The amount polarisation rotation of the laser pulse electric field through a magnetic field B of probed material length L is given by (6.13) [124].

$$\phi = \frac{\lambda^2}{8\pi^2 c^3}\left(\frac{e^3}{\varepsilon_0 m_e^2}\right)\int n_e B dL. \tag{6.13}$$

Solving for B therefore requires complimentary electron density measurements through the same optical path of the magnetic field, which were performed with an interferometry diagnostic using the same probe beam. The amount of rotation scales quadratically with the laser probe wavelength and therefore the fundamental 1053 nm wavelength of Cerberus was used to maximise sensitivity. Conversely, the critical electron density in (6.8) scales to the inverse-square to the laser probe wavelength and therefore only regions of lower electron density can be probed, which is also a function of the acceptance angle of the imaging system that is ideally maximised to collect deflected photons.

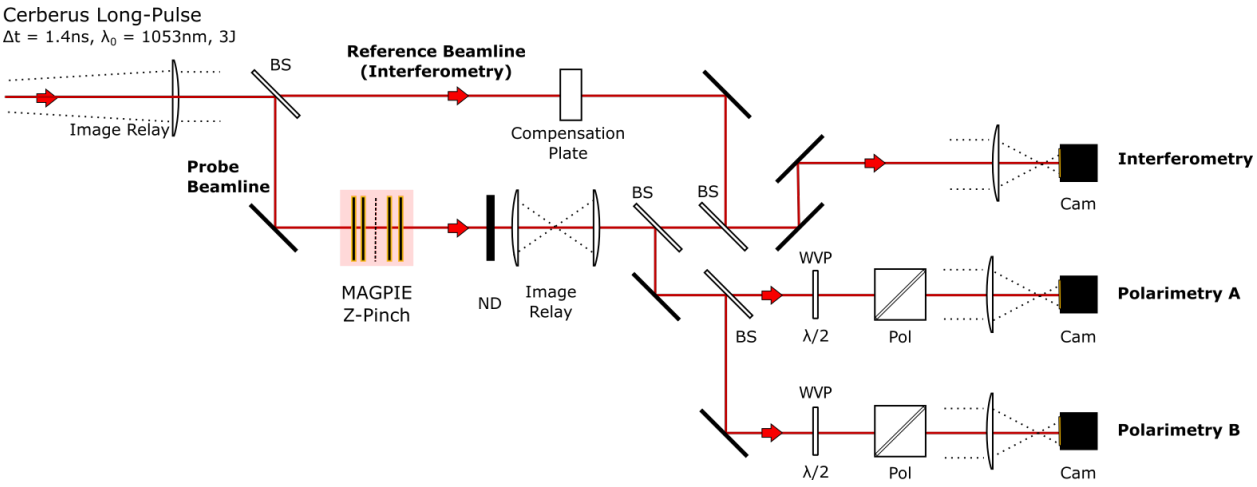


Figure 6.11: Faraday rotation optical diagnostic to characterise plasma magnetic fields. BS: beamsplitter (polarisation insensitive), ND: neutral density filter, WVP: waveplate, Pol: Polariser. Characterisation of magnetic field strength requires electron density measurement from interferometry along the same optical probe path.

An optical layout of the diagnostic is shown in figure 6.11. A ~1 J probe pulse signal is used to overcome the background self-emission noise from the MAGPIE target. The compensation plate ensures similar glass/spectral phase is added to each beam to achieve high-contrast fringes. A neutral density filter reduces background noise and signal to acceptable levels for the cameras and high-acceptance image relay optics positioned close to the chamber to collect the deflected rays into the imaging system. The magnetic field

rotation is measured as brightening/darkening of light intensity in each polarimetry channel, with each channel set to opposing ~4° static polarisation rotation with a waveplate, slightly above the upper-bound Faraday rotation expected in order to maximise dynamic range.

The interferometry uses a portion of the probe beam output after the MAGPIE chamber, whose wavefront is interfered with a reference beamline that by-passes the MAGPIE chamber. Simultaneous measurement of the polarisation rotation and electron density from interferometry analysis of the shifted interferometry fringes in the presence of high density electrons allows determination, from (6.13), of the magnetic fields probed by the Cerberus laser through the Z-pinch interactions of MAGPIE. A full analysis is given by Dr George Swadling et al. in [35] and we show the main results from this analysis in figure 6.12. The interferometry analysis shows an electron density of $n_e \sim 10^{18}$ cm^{-3}and rotation angles of up to 2°, corresponding to ~2±0.5 T magnetic fields in the plasma flow.

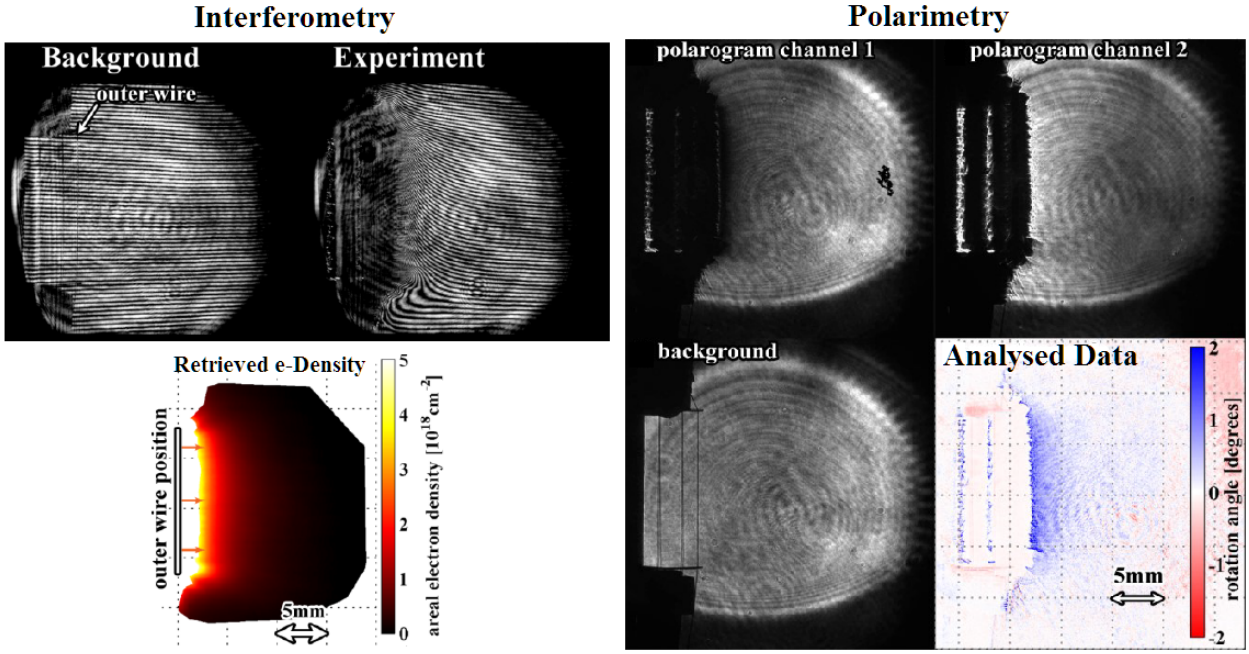


Figure 6.12: (Left) Interferometry background and on-shot images of an exploding radial wire array load and retrieved electron density in the MAGPIE target chamber. (Right) Brightening and darkening of common regions in the beam profile in the opposing polarimetry channels, corresponding to the polarisation rotation angles in the false colour analysed image, which can then be used with the simultaneous electron density measurement to calculate the magnetic field strength. Image reproduced from [35].

These results have proven the diagnostic to be capable of probing and determining a 2D snap-shot of the magnetic field map of MAGPIE Z-pinch interactions that is free from

large EMP noise sources inherent in pulsed-power machines. The successful development of this diagnostic has led to recent publication with alternative target geometries [118], including probing magnetically driven plasma dynamics [38].

7

CONCLUSIONS

The key aim of the work described in this PhD thesis was to identify, measure and investigate the physical mechanisms responsible for noise generation and corresponding temporal contrast degradation in high peak-power OPCPA pulsed lasers. As part of this study it was necessary to develop a high-contrast hybrid OPCPA/Nd:Glass multi-terawatt laser system that is capable of producing >10^{19} W cm^{-2} intensities for driving and probing laser-matter experiments.

The Cerberus multi-terawatt high-contrast laser has been configured to use a mixture of picosecond [40] and nanosecond pumped OPCPA stages to reduce parametric fluorescence, which was characterised in the picosecond domain to have ~ 10^8 contrast in a 2 ps FWHM pedestal using a high-dynamic range seeded OPA parametric fluorescence diagnostic developed and described in a peer-reviewed journal publication [36]. The nanosecond fluorescence was observed with 10^8-10^{10} temporal intensity contrast from 1 μJ input, 10^{11} dynamic range and 2 ns temporal range scanning-third order autocorrelator diagnostic (TOAD) developed by the author that can be fully computer controlled and automated. We found the widely adopted chirped pulse amplification technique inherently produces incoherent pulse pedestals of ~10^4-10^5 whose exact origin is currently unclear but optical scattering and sub-optimal diffraction mechanisms in the pulse stretcher element of the laser are likely candidates that will require further investigation to understand and eventually eliminate this source of noise. The manufacture of lower-scatter and lower waveform distortion optical components for use within the highly dispersive diffraction grating stretchers and compressors may significantly reduce this noise sources in the future.

We have experimentally studied the temporal contrast of compressed high-power laser pulses from major laser laboratories in the UK using the TOAD, including hybrid OPCPA/Nd:Glass system of Cerberus (Imperial College), Orion (AWE Aldermaston) and Vulcan (STFC Rutherford Appleton Laboratory) and a gain-storage Ti:Sapphire/Nd:Glass CPA terawatt system at Queen's University Belfast. These systems are also limited by the mid-range CPA pedestal, highlighting a requirement in the research fields under-

pinned by those laser to precisely identify its source and develop methods to mitigate its effect. Additionally, the OPCPA front-ends characterised in our work suffered from non-linear pre-pulse generation, with similar matching post-pulse intensity, from the temporal overlap and spectral modulation with post-pulses in high B-integral optics such as the internally reflected beams in the nanosecond time domain OPA crystals. The use of wedged/highly titled OPA crystals was found to eliminate this previously limiting pre-pulse source on Cerberus and also the Vulcan and Orion petawatt laser systems.

We observed a common mid-range noise pedestal of ~30-50 ps FWHM duration at ~10^{-4}-10^{-5} peak relative intensity seen across all the chirped pulse amplification laser systems characterised. We have identified optical scattering and diffraction mechanisms that could form the origin of these noise sources. We attempted a new phase-conjugate OPCPA architecture to test the CPA scatter pedestal theory by avoiding the use of high-scatter imaging grating stretcher setups. However, higher-order phase transferred from the pump pulse to the idler in this first proof of principle test likely limited the compressibility of the phase-conjugate idler pulse. Future investigations using this scheme must therefore address the phase management of the pump pulse, which could be degraded by the regenerative amplifier etalon or from mismatched grating angles and sub-optimal alignment through the stretcher systems. Alternatively, higher quality optical components or wavelength scaling studies of the laser contrast may change the observed pedestal intensity due to the strong wavelength dependence of optical scatter.

We were able to utilise the very high-sensitivity of the TOAD to measure and directly compare the contrast characteristics across a broad range of mode-locked oscillator types used for seeding high-power laser systems, including SESAM, KLM, NPE and OPO mode-locked laser sources [37]. The contrast performance these various mode-locking methods will determine which mode-locking techniques best lend themselves to high contrast operation. We found asymmetric noise features in KLM and NPE sources limited their temporal contrast to ~10^6, whilst a more attractive >10^8 contrast was measured from SESAM and OPO sources.

Finally, a multitude of short-pulse and long-pulse experiments have been performed using the high-power pulses generated from by Cerberus laser system. The X-ray backlighter [5] and Faraday rotation magnetic field [35] optical diagnostics are routinely in demand for a variety of MAGPIE investigations, producing high-quality results and furthering the understanding of magnetically driven plasma interactions[38, 118]. The high-contrast multi-terawatt pulses from Cerberus will be used for future ion acceleration ex-

periments[125], which are highly sensitive to laser contrast, and future levitated droplet [39, 116] laser-matter interactions will form a core theme of experiments in the near future that will be undertaken at Imperial College.

7.1 FUTURE WORK

In this section we shall address future works to further develop and exploit the contrast studies from this PhD project, along with a description of the upgrade path of the Cerberus laser to deliver a peak-power of up to 100 TW with modest modifications to the front-end and compressor system.

7.1.1 *Removing Pre-pulse Artefacts with X-TOAD*

Temporal contrast characterisation using third-order autocorrelators frequently identifies pre-pulse features that are of of ambiguous origin. These might be either real noise sources from the laser oscillator and amplification chain or an artefact of the measurement process where post-pulses in the second harmonic probe create "ghost" pre-pulse signals in the measurement from the convolution process of the autocorrelation.

Analysis of the third-order autocorrelator trace containing corresponding post-pulse locations with intensities approximately the square of the pre-pulse will typically lead to the inference that these these pre-pulses are in face post-pulse induced artefacts. However, there are also scenarios where this rule does not apply, for instance with the non-linear pre-pulse mechanism discussed in §5.5 does not necessarily produce this same intensity ratio between the pre-pulse and post-pulse, seen in chapter 5 from parallel-faced OPCPA crystals that used long pulse durations and allowing amplification of an internal double bounce, or if the temporal scanning range of the autocorrelator does not cover both the pre-pulse and post-pulse temporal locations. Additionally, post-pulses only produced in the second harmonic probe arm of the autocorrelator will produce a "false-positive" ghost pre-pulse signal. Many of these ambiguities can be resolved, at a monetary cost and potential increase in system complexity, by using an all-reflective optical design and minimising post-pulse generation in the laser system through reflective and wedged transmissive optics. However, where these ambiguities still remain a further refinement to the third-order autocorrelation technique is required.

The generation of ghost pre-pulse artefacts is inherently linked to real post-pulses in the fundamental harmonic input beam producing less intense, but still measurable, post-pulses in the second harmonic probe, or generation of post-pulses somewhere in the optical chain after the second harmonic generation crystal. We can therefore attempt to "clean" the second harmonic probing pulse to minimise the impact of pre-pulse artefact generation. For this application, we investigated cross-polarised wave generation (XPW) [126], a non-linear polarisation rotation effect that is driven by a combination of several effects, including self-phase modulation and cross-phase modulation, to enhance the contrast of the probing arm. The additional non-linear process reduces the probing pulse duration further, providing greater temporal resolution of the reconstructed fundamental pulse.

XPW is a third-order process typically used to enhance the ASE contrast from Ti:Sapphire lasers using the dual-CPA scheme [107, 127]. The non-linear process exploits the anisotropy of the $\chi^{(3)}$ tensor in the BaF_2 cubic crystal, with effective coefficient $\chi^{(3)}_{eff} = -1.2$ and whose efficiency η_{XPW} is determined by the relation [126]

$$\eta_{XPW} = \frac{I_\perp}{I_\parallel} = 4\left(\frac{\gamma_\perp}{\gamma\parallel}\right)^2 \sin^2\left(\frac{\gamma_\parallel I_0 L}{2}\right) \tag{7.1}$$

where $\gamma_\perp$ and $\gamma\parallel$ are coefficients that depend upon the crystal orientation and $\chi^{(3)}_{eff}$, I_0 is the input intensity and L the crystal length. In the case where self-phase modulation is negligible, the efficiency simplifies to (7.2), which is quadratically dependent upon the input intensity[126]

$$\eta_{XPW} \propto (\gamma_\perp I_0 L)^2 . \tag{7.2}$$

An experimental setup to test the XPW efficiency for cleaning the second-harmonic 527 nm pulses is shown in figure 7.1.

The XPW efficiency as a function of distance from the focussing lens is plotted in figure 7.2. The maximum XPW efficiency was limited by the damage threshold of the crystal surfaces, which is estimated to be ~2×10^{11} W cm^{-2} for ~350 fs, pulse durations of 527 nm central wavelength. An exponential increase in XPW efficiency was observed up to this limit, indicating that SPM is acting within the XPW process.

We also observed a much greater (>29%) conversion efficiency of the non-linear XPW interaction at 527 nm, in comparison to the ~15% efficiency limit reported for 800 nm

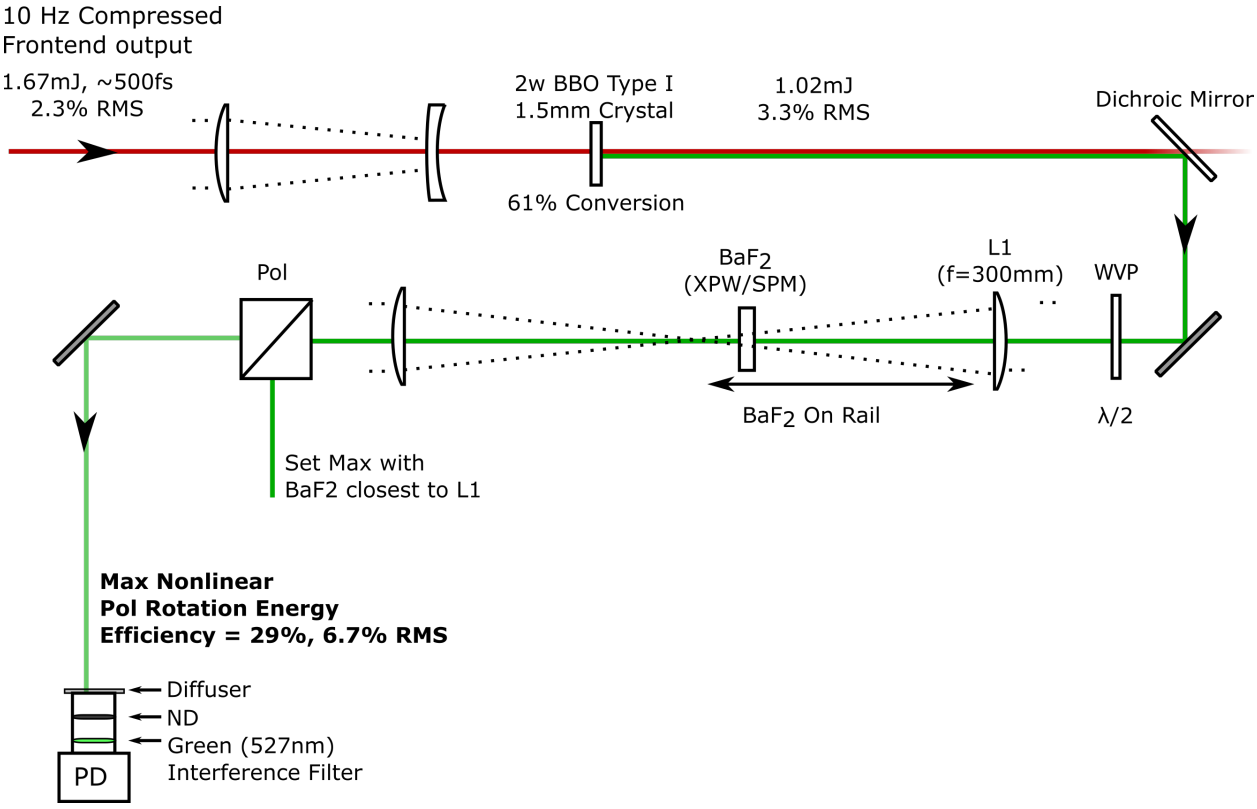


Figure 7.1: Experimental setup to test the XPW efficiency for the second harmonic of the ~500 fs, few millijoule, 10 Hz pulses emitted from the complete optical chain of Cerberus. The beam size/intensity is optimised for use with a BBO type-I SHG crystal to produce ~1 mJ, 527 nm pulses for XPW testing. A polished, uncoated BaF_2 crystal, cleaved to the [111] orientation, is variably positioned between a 1:1 positive lens telescope. The input pulses are set for maximum extinction through a polariser at low-power, with the BaF_2 crystal set closest to L1, which also account for static birefringence of the crystal. Increasing the intensity incident on the BaF_2 crystal, by translating closer to the crystal focus, increases the non-linear polarisation rotation efficiency for a given crystal orientation. A maximum energy efficiency of 29% was achieved for 527 nm pulses, with increasing rotation efficiency also producing more stable outputs.

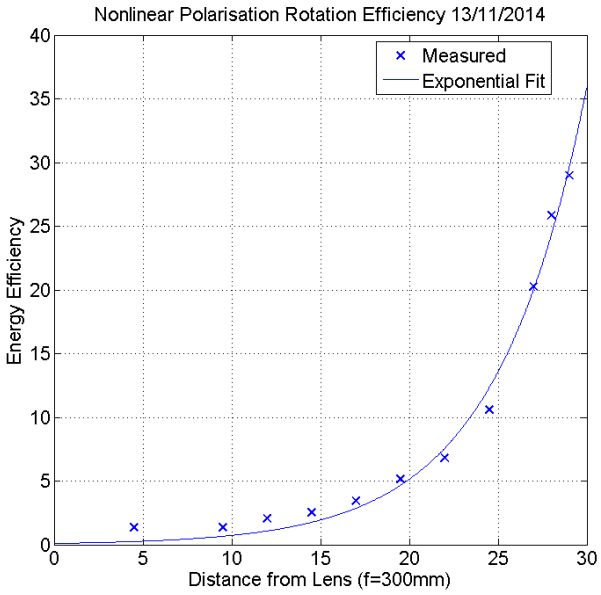


Figure 7.2: XPW efficiency of 527 nm pulses as a function of distance from the focussing lens. We observe an exponential behaviour, indicating self-phase modulation is likely acting within the XPW interaction to improve efficiency.

pulses [107], which further aids the applicability of this process for efficient pulse cleaning of the SHG probe beam in third-order autocorrelators.

Finally, we have implemented a preliminary upgrade to the TOAD, described in §3.1, to include an XPW pulse cleaner in the probe beam path. We have tested the XPW cleaning effect by adding an uncoated 5 mm thick etalon to the probing arm of the diagnostic, which introduced a well-defined pre-pulse at ~50 ps ahead of the primary pulse. This pre-pulse was observed with no XPW interaction (blue curve in figure 7.3) and with ~10% XPW rotation efficiency (red curve in figure 7.3) attenuated this artefact by a factor of >200 to reduced the intensity of this pre-pulse artefact below the CPA pedestal noise limit of the observation. The maximum contrast enhancement is directly linked to the polarisation extinction and therefore up to 10^5 extinction of pre-pulse artefacts is possible with this technique.

We only observed XPW extinction of the inserted 50 ps artefact and therefore are more confident the pre-pulses seen in data between 100-200 ps ahead of the primary pulse are in fact real features that arise from the non-linear pre-pulse generation in the ns-OPAs of the Cerberus laser system, and are likely to be present in other comparable laser chains that employ nanosecond time-domain OPCPA without careful optimisation of the OPA crystal wedge angle .

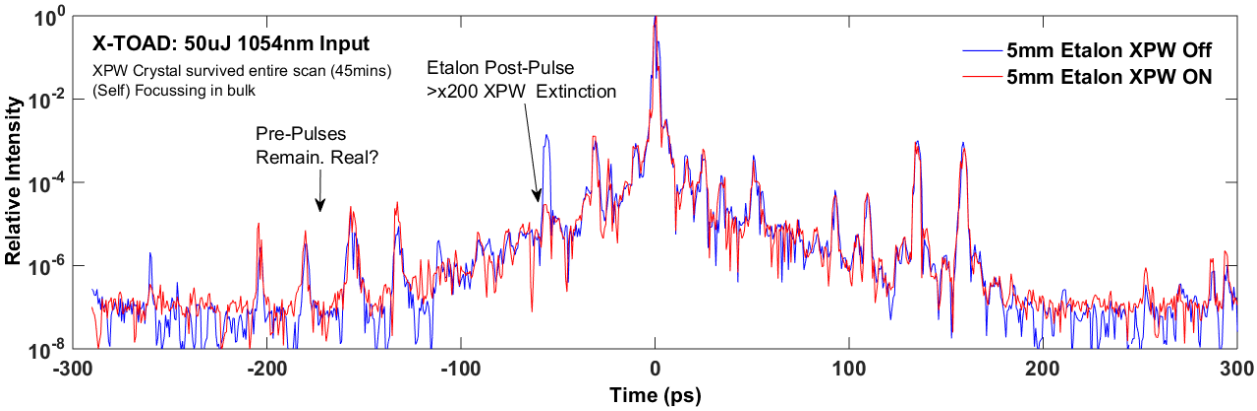


Figure 7.3: Proof-of-principle operation of XPW filtering of the probe pulses in a third-harmonic autocorrelator to effectively identify and remove diagnostic artefacts from the autocorrelation signal. (Blue line) A post-pulse introduced into the probe beamline produces a diagnostic artefact ~50 ps ahead of the primary pulse. (Red line) With no change to the optical configuration, the XPW filter is engaged (by crossed-polarisers and a BaF_2 XPW polarisation rotator moved into the focus of the probe pulse), removing the diagnostic artefact from the autocorrelation trace. All other pre-pulses remain and are therefore real features in the temporal profile of the laser pulse.

For robust operation of XPW, methods to reduce the likelihood of optical damage on the BaF_2 were addressed. We achieved >45 minute operation, the duration of the scan, from operating the XPW interaction at the crystal focus i.e. peak intensity within the crystal bulk of higher damage threshold, and adjusting the 527 nm energy until the required XPW efficiency was achieved. The energy input to the was partially optimised to 50 μJ, an increase on the original TOAD design due to the required energies to achieve the desired XPW efficiency, however still much less than the ~1 mJ input energy required by commercial scanning third-order autocorrelators. As a result of this successful proof-of-principle design and observation, we aim to create a full featured "X-TOAD" system in future as part of a knowledge transfer secondment with AWE, and then deploy this new instrument on the Orion petawatt laser system and publish the design and results once any IP protection issues have been dealt with.

7.1.2 *Scaling of OPCPA Contrast Studies to the Mid-IR*

Future laser development at Imperial College will explore "mid-infrared" laser sources that exploit the strong $I\lambda^2$ wavelength-scaling of the electron ponderomotive energy, (1.1), that is a fundamental feature which lies behind many high-intensity laser matter experi-

ments. This work will form part of a MURI (Multidisciplinary University Research Initiative) held jointly between a number of US universities and Imperial College as a formal UK collaborator. Although we are limited in what we can say regarding the laser design and experiment proposals for this project, we can extend some of the contrast analysis developed in this thesis for use at ~1 μm and determine useful wavelength scaling from current operation at 0.8-1 μm to mid-infrared (1.5-10 μm) high-power lasers that will drive these experiments.

We have concluded that the CPA pedestal is the primary contrast limitation across all current generation high-power laser systems. In the absence of active cleaning techniques such as second-harmonic generation and plasma mirror technology, high-power mid-infrared laser, which will likely use CPA and OPCPA techniques, and will also be prone to the same pedestals. These pedestals are largely thought to originate from scattering processes, which potentially scale very strongly with the laser wavelength as $I_{Scatter} \propto \lambda^{-4}$ in (5.8). We should therefore expect these CPA pedestals to be drastically reduced in intensity, as long as the surface error is maintained to similar manufacturing capabilities as is presently possible in visible/near-infrared when scaling to mid-infrared substrates/coatings. Given that "standard" optical flatness for high-quality optics, e.g. of order $\lambda/10$ is typically specified at the visible 632 nm He:Ne laser wavelength, one would expect the quality of optics for mid-IR systems to be substantially higher relative to the wavelengths at which they will be used, e.g. 1.5-10 μm. Observation of the CPA pedestal intensity through a modified mid-IR third-order autocorrelator will therefore be an informative result to determine whether or not scattering processes are the root cause of the reported incoherent CPA pedestals .

Mid-infrared laser technology will likely use non-linear techniques i.e. DFG, OPA, OPCPA, to generate and amplify pulses. Parametric fluorescence is therefore a likely limitation to contrast, which was determined by Ross et al. to also scale strongly in (1.16) as $I_{PF} \propto \lambda^{-4}$. We therefore also hope to use the seeded parametric fluorescence diagnostic we have developed to achieve very high dynamic range measurements and characterisation of the fluorescence intensity when generating/amplifying these mid-infrared fields to confirm this attractive scaling.

7.1.3 *High Energy OPCPA and Cerberus 100TW Design*

In chapter 2, we successfully demonstrated an experimental OPCPA system that generates 20 mJ, 700 ps pulses at 10 Hz repetition rate that is then amplified to in an Nd:Glass amplifier chain and compressed to 750 mJ, 500 fs in the Terawatt lab. The Multi-Terawatt lab is currently limited to ~2 J after compression due to B-integral accumulation in air, where ~>15 J is feasible in the current optical setup if this limitation was circumvented and the dielectric grating damage threshold then set the maximum energy throughput. Additionally, during the process of the OPCPA pump and signal beamline development a number limitations arose for ns-OPA operation which conspired to produce significant gain narrowing effects from mismatched pulse durations. Here we address the design for planned optics upgrades to the Cerberus ns-OPAs to overcome these limitations as well as the possibility for generating 100 TW pulses using the existing Nd:Glass amplifiers and compressor gratings.

We start by addressing the balance between pulse duration and compressor optics sizes. If sufficient additional bandwidth can be generated with near linear phase, shorter pulse durations offer a route to higher peak-power without the need for additional Nd:Glass amplification beyond 20 J. The compressor must be able to handle this extra bandwidth such that spectral clipping does not produce its own problematic contrast pedestal. We also know the pulse contrast is unfortunately limited at the moment by the incoherent CPA pedestal attributed to grating scatter and therefore the degree of spectral clipping can be optimised against pulse bandwidth. The spectral acceptance of a parallel grating pair is limited by the second grating width in the dispersion dispersion direction and therefore the minimum grating size to accept a given edge-to-edge bandwidth $|\lambda_R - \lambda_B|$ for a small input beam can be calculated from solving the diffracted angular spread $|\gamma_R - \gamma_B|$ using the grating equation (1.9) for the edge-edge acceptance and using the simple geometrical relation to find the required grating width x with separation L

$$x = 2L \tan\left(|\gamma_R - \gamma_B|\right) \tag{7.3}$$

If we consider the current Cerberus parameters, with a 500 fs transform limited pulse with ~3.3 nm bandwidth centred at 1054 nm, we can model the spectral acceptance required to match the CPA contrast pedestal of 10^{-5} intensity and ~35 ps FWHM duration. This can be achieved simply by applying the Fourier transform of the Gaussian spectrum

with a spectral mask function. This mask function will in practice be a super-Gaussian, with smaller beams likely to have sharper edge responses and larger beams will have a smoother edge response i.e. lower-order super-Gaussian. In §2.7, we measured the spectral mask function of the Öffner stretcher to approximate closely to a 5^{th}-order super-Gaussian, which uses a considerably smaller input beam than the compressors. We therefore conservatively assume a 20^{th}-order super-Gaussian for the spectral clipping mask of the compressor.

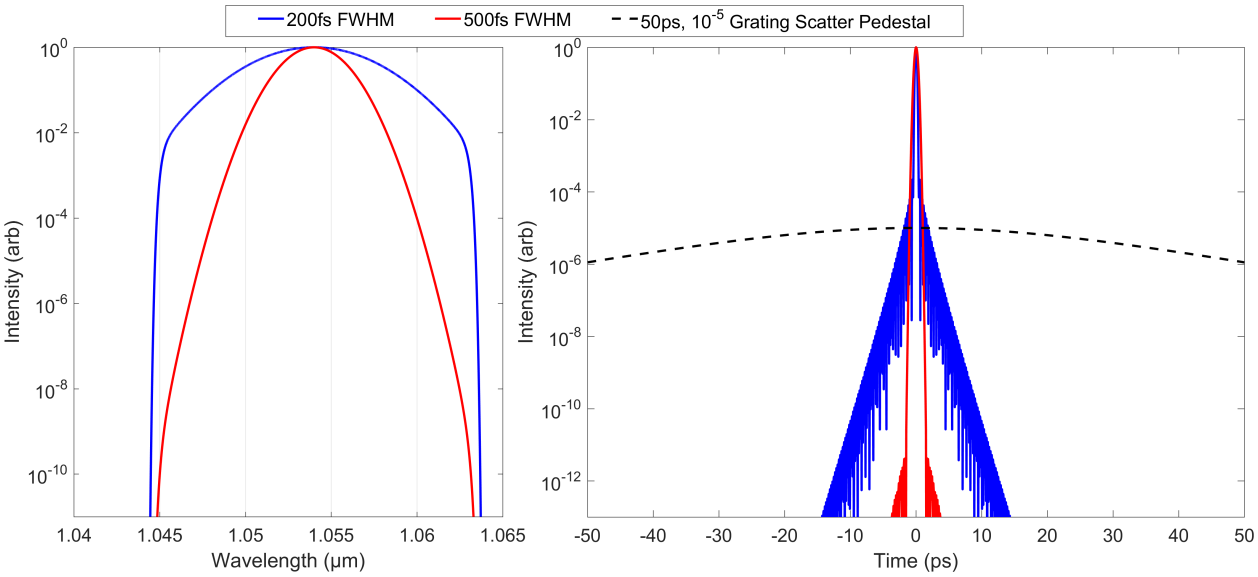


Figure 7.4: Compressor spectral clipping impact (20^{th}-order 18 nm FWHM super-Gaussian) on the compressed pulse contrast for varying pulse durations (blue) 200 fs FWHM Gaussian bandwidth, producing ~10^{-4} relative intensity pedestal (red) 500 fs FWHM Gaussian bandwidth, producing ~10^{-11} relative intensity pedestal. We have also plotted the mid-range CPA pedestal for comparison of timescales, showing in both spectrally clipped cases the temporal noise duration is negligible compared to this current limitation.

For the Cerberus pulse and compressor parameters, a grating size of ~1.56 cm is required per nanometre bandwidth with 2.3 m grating separation. The current terawatt gratings are 22 cm wide and have been measured to have 14 nm spectral acceptance and the multi-terrawatt high damage threshold dielectric gratings expected to have ~18.2 nm edge-edge spectral acceptance from their increased 28.5 cm grating width. We show in figure 7.4 that the current 500 fs bandwidth experiences negligible spectral clipping contrast effects and even 200 fs pulse bandwidths can be used without further impact on the temporal contrast. Producing a 200 fs pulse with the maximum 22.5 J currently obtained from the 50 mm diameter Nd:Glass amplifiers (1.4 ns pulse duration in this test) will pro-

duce ~100 TW pulses after compression with the measured 87% efficiency of the dielectric compressor.

Given that the current Cerberus short-pulse CPA optics are capable of handling 200 fs pulses, the other major challenge is the OPA optimisation required to generate the >8.2 nm bandwidth required to compress to these durations. Fortunately, this bandwidth can already be produced from the ps-OPAs and handled by the stretcher system but is then effectively lost from the shorter seed/pump pulse duration ratio used in the ns-OPAs, which are currently only able to maintain ~3.5 nm bandwidth at maximum pump depletion. The relatively short pump pulse duration is determined by the parallel grating pair stretcher geometry currently used, that outputs 1.4 ns, 1053 nm pulses. The second-order OPA process shortens the output signal pulse, producing ~700 ps OPA signal durations, which also reduces the energy extraction possible from the large aperture Nd:Glass amplifiers from reduced fluence damage thresholds; for example, currently 22.5 J, 1.4 ns performance is possible on the long-pulse beamline. This grating pair stretcher can be improved in two ways: firstly, by switching to an imaging stretcher that adds positive chirp, as the input is already slightly positively chirped over ~80 ps and therefore we require less dispersion. Secondly, the current gratings used have limited efficiency at the steep angles required to achieve the large stretch factors and therefore switching to more "modern" gratings will produce much greater efficiency at high dispersion.

Doubling the pump pulse duration therefore seems a natural choice to approximately double the OPCPA pulse bandwidth and produce a 1.4 ns OPCPA pulse than can be faithfully amplified to 22.5 J in the 50 mm rod amplifier. We also identified limitations with the current parallel grating stretcher for the long-pulse/ns-OPA pump, including the extra work required to undo the chirp from the preceding Martinez stretcher, and the cylindrical expansion that degrades long-throw beam profiles and spherical collimation. A new four-pass Martinez stretcher has been designed using a 1740 lines/mm gold holographic grating and a custom 75 mm aperture f = 3.5 m lens with 58.7° diffraction grating incidence angle. Using (1.10) and an effective single-pass grating separation of 3.2 m, this four-pass stretched pulse is expected to be ~3 ns FWHM with 0.5 nm bandwidth, which accounts for minor gain-narrowing of the 0.6 nm regenerative amplifier output through the Nd:YLF chain.

Cerberus upgrades that will accompany the move to a Martinez stretcher geometry for the OPA pump beam will include the installation of an additional pair of Nd:YLF amplifiers with 7.5 mm and 9.5 mm rod diameters, With the increased long-pulse duration

and vastly greater optical gain available it should be possible to extract up to 750 mJ from each of the two final 9.5 mm amplifiers, of which 1.2 J can potentially be used to pump an improved set of ns-OPAs with wedged crystal design that should be able to produce 100-150 mJ signal energies from the final OPA at 10 Hz repetition rate, while eliminating Fourier pre-pulse features seen with un-wedged OPA crystals. If these pulses are compressible to the above 200 fs design goal this should create a highly desirable 0.5-0.75 TW at 10 Hz capability for high repetition rate target systems and faster data acquisition from small-scale laser-plasma experiments.

We have therefore remodelled the ns-OPAs in OPA.FOR with these new input parameters and present a small summary of the modelling results. Increasing the pump pulse duration will reduce the intensity threshold by $\tau^{1/2}$ scaling in (2.16) and thus require longer crystals to produce the same optical gain. We shall also assume 150 mJ and 300 mJ pump pulse energies into the first and second ns-OPA stage respectively, with up to 300 mJ, 2.8 ns that can be used for simultaneous long-pulse amplification and experiments. Key input and output pulse characteristics of the 1D modelling are presented in table 7.1. The OPAs require a fixed amount of gain with the available pump energy so general results are presented and we identify suitable beam sizes and intensities which are reported separately for each crystal length. Using the 8 nm bandwidth from the ps-OPAs, 200 ps/nm chirp on the seed and increased pump pulse energies a 140 mJ, 9.5 nm bandwidth OPA signal is expected from the final ns-OPA. Optimal amplification maximises pump depletion before the onset of back-conversion introduces unwanted modulations on the signal spectrum, which is also expected to be a highly stable mode of operation. These pulse bandwidths should be compressible to ~170 fs and therefore the 200 fs goal is a realistic target. The 1D code assumes flat-top beam profiles and therefore the conversion efficiency is an upper estimate.

The damage thresholds for AR coated BBO crystals is 300 MW cm^{-2} for 10 ns, 532 nm pulses (Castech), which scales with (2.16) to 700 MW cm^{-2} for 2 ns, 526.5 nm expected from the Martinez stretcher upgrade and therefore optimal crystal lengths should be kept such that the required pump intensity is at least half the expected damage threshold, and ideally one-quarter of the damage threshold. The crystal aperture is adjusted to accommodate the available pump energy and intensity for non-linear gain. To produce the same gain with lower pump intensity a 17 mm long BBO would serve as a suitable direct replacement to replace the 12 mm long BBO currently in the first ns-OPA stage. The maximum length able to be grown by crystal manufacturers is currently 20 mm. Additionally,

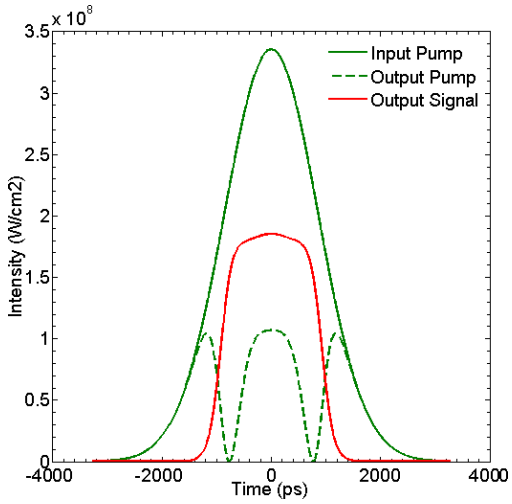


Figure 7.5: OPA.FOR Temporal profiles of pump and signal from optimised ns-OPAs.

	ns-OPA1 Seed	Pump	ns-OPA2 Signal	ns-OPA2 Signal (Old)
Wavelength	1054 nm	526.5 nm	1054 nm	1054 nm
Bandwidth	8 nm	0.4 nm	8 nm	3 nm
Pulse Duration	1.6ns	2ns	1.6ns	600ps
Energy	100 μJ	150 mJ (ns-OPA1) 300 mJ (ns-OPA2)	140 mJ	20 mJ

Table 7.1: Pulse parameters for re-optimised ns-OPAs using an improved pump pulse stretcher and additional amplification.

7×7 mm aperture 15 mm BBO crystals have been donated by RAL that could be refurbished with wedged surfaces and retasked for the Cerberus OPAs for this upgrade. With these current 8 mm, 12 mm and 15 mm long crystal already available we may assess their applicability in this upgrade from the pump intensity and beam size requirements to produce to required OPA gain in table 7.2.

The other engineering requirement for this potential upgrade lies with the already limiting factor of the in air compression of the multi-terawatt beamline. B- integral accumulation from propagation in atmospheric air and the necessity to transmit through a ~7 mm thick M_gF_2 optical window into the vacuum chamber adds significant levels of B-integral that limits current operation to 1-5 TW, although ~35 TW pulses should be possible if this were not a limiting factor. The only solution for this limitation is to house the compressor

BBO Length	ns-OPA1 (150 mJ, 2 ns Pump)	ns-OPA2 (300 mJ, 2 ns Pump)
8 mm	-	340 MW cm^{-2}, 10.4 mm dia.
12 mm	640 MW cm^{-2}, 5.4 mm dia.	150 MW cm^{-2}, 16.0 mm dia.
15 mm	390 MW cm^{-2}, 7.0 mm dia.	
17 mm	310 MW cm^{-2}, 7.8 mm dia.	
20 mm	250 MW cm^{-2}, 8.6 mm dia.	

Table 7.2: Required pump intensities and beam diameters for optimal ns-OPA gain. Beam diameters conservatively given as I_0/e^2 width for a Gaussian intensity profile and therefore super-Gaussian beams will fill a smaller area.

gratings under vacuum, permitting even near-zero B-integral accumulation if reflective optics are used to guide these pulses to target.

BIBLIOGRAPHY

BIBLIOGRAPHY

[1] T. H. Maiman. 'Stimulated Optical Radiation in Ruby.' In: *Nature* 187.4736 (1960), pp. 493–494 (cit. on p. 1).

[2] C. Danson et al. 'Vulcan petawatt: Design, operation and interactions at $5X10^{20}W/cm^2$.' In: *Laser and Particle Beams* 23.1 (2005), pp. 87–93 (cit. on pp. 1, 27, 33, 51, 92, 114).

[3] C. J. Hooker et al. 'The Astra Gemini project – A dual-beam petawatt Ti:Sapphire laser system.' In: *Journal de Physique IV (Proceedings)* 133 (2006), pp. 673–677 (cit. on pp. 1, 32).

[4] N. Hopps et al. 'Overview of laser systems for the Orion facility at the AWE.' In: *Applied Optics* 52.15 (2013), pp. 3597–3607 (cit. on pp. 1, 27, 51, 92, 110).

[5] G. N. Hall et al. 'Monochromatic radiography of high energy density physics experiments on the MAGPIE generator.' In: *Review of Scientific Instruments* 85.11 (2014), p. 11D608 (cit. on pp. 1, 19, 22, 26, 150, 154, 159).

[6] S. C. Wilks and W. L. Kruer. 'Absorption of ultrashort, ultra-intense laser light by solids and overdense plasmas.' In: *IEEE Journal of Quantum Electronics* 33.11 (1997), pp. 1954–1968 (cit. on pp. 1, 139, 140).

[7] S. P. D. Mangles et al. 'Monoenergetic beams of relativistic electrons from intense laser–plasma interactions.' In: *Nature* 431.7008 (2004), pp. 535–538 (cit. on p. 1).

[8] F. Albert et al. 'Laser wakefield accelerator based light sources: potential applications and requirements.' In: *Plasma Physics and Controlled Fusion* 56.8 (2014), p. 084015 (cit. on p. 1).

[9] H. W. Doyle. 'Creating and Probing Warm Dense Matter and High Energy Density Blast Waves.' PhD Thesis. Imperial College London, 2012 (cit. on p. 1).

[10] M. Koenig et al. 'Progress in the study of warm dense matter.' In: *Plasma Physics and Controlled Fusion* 47.12 (2005), B441 (cit. on p. 1).

[11] A. G. MacPhee et al. 'Limitation on Prepulse Level for Cone-Guided Fast-Ignition Inertial Confinement Fusion.' In: *Physical Review Letters* 104.5 (2010) (cit. on p. 1).

[12] G. H. Miller, E. I. Moses, and C. R. Wuest. 'The National Ignition Facility.' In: *Optical Engineering* 43.12 (2004), pp. 2841–2853 (cit. on pp. 1, 32).

[13] A. B. Bullock and P. R. Bolton. 'Laser-induced back ablation of aluminum thin films using picosecond laser pulses.' In: *Journal of Applied Physics* 85.1 (1999), pp. 460–465 (cit. on p. 2).

[14] L. V. Keldysh. 'Diagram technique for nonequilibrium processes.' In: *Sov. Phys. JETP* 20.4 (1965), pp. 1018–1026 (cit. on p. 2).

[15] N. B. Delone and V. P. Krainov. 'Tunneling and barrier-suppression ionization of atoms and ions in a laser radiation field.' In: *Physics-Uspekhi* 41.5 (1998), pp. 469–485 (cit. on p. 2).

[16] J.-P. Chambaret et al. 'Extreme light infrastructure: laser architecture and major challenges.' In: *SPIE Conference on Solid State Lasers and Amplifiers IV, and High-Power Lasers*. Vol. 7721. 2010, pp. 77211D–77211D–15 (cit. on p. 3).

[17] G. A. Mourou et al. 'Exawatt-Zettawatt pulse generation and applications.' In: *Optics Communications* 285.5 (2012), pp. 720–724 (cit. on p. 3).

[18] I. N. Ross et al. 'The prospects for ultrashort pulse duration and ultrahigh intensity using optical parametric chirped pulse amplifiers.' In: *Optics Communications* 144.1 (1997), pp. 125–133 (cit. on pp. 6, 14, 15, 86, 114).

[19] C. N. Danson et al. 'High contrast multi-terawatt pulse generation using chirped pulse amplification on the VULCAN laser facility.' In: *Optics Communications* 103.5 (1993), pp. 392–397 (cit. on p. 7).

[20] B. Stuart et al. 'Nanosecond-to-femtosecond laser-induced breakdown in dielectrics RID A-4480-2009.' In: *Physical Review B* 53.4 (1996), pp. 1749–1761 (cit. on pp. 7, 44, 45).

[21] D. Strickland and G. Mourou. 'Compression of Amplified Chirped Optical Pulses.' In: *Optics Communications* 56.3 (1985), pp. 219–221 (cit. on p. 8).

[22] P. Maine et al. 'Generation of Ultrahigh Peak Power Pulses By Chirped Pulse Amplification.' In: *Ieee Journal of Quantum Electronics* 24.2 (1988), pp. 398–403 (cit. on p. 8).

[23] M. E. Faldon. 'A high intensity, short pulse neodymium laser.' PhD Thesis. Imperial College London (University of London), 1992 (cit. on p. 12).

[24] O. Martinez. '3000 times grating compressor with positive group velocity dispersion: Application to fiber compensation in 1.3-1.6 um region.' In: *IEEE Journal of Quantum Electronics* 23.1 (1987), pp. 59–64 (cit. on p. 12).

[25] P. A. Franken et al. 'Generation of Optical Harmonics.' In: *Physical Review Letters* 7.4 (1961), pp. 118–119 (cit. on p. 13).

[26] A. Dubietis, G. Jonušauskas, and A. Piskarskas. 'Powerful femtosecond pulse generation by chirped and stretched pulse parametric amplification in BBO crystal.' In: *Optics Communications* 88.4 (1992), pp. 437–440 (cit. on p. 14).

[27] D. A. Kleinman. 'Theory of Optical Parametric Noise.' In: *Physical Review* 174.3 (1968), pp. 1027–1041 (cit. on pp. 15, 79).

[28] R. Glauber and F. Haake. 'The initiation of superfluorescence.' In: *Physics Letters A* 68.1 (1978), pp. 29–32 (cit. on p. 15).

[29] I. Musgrave et al. 'Picosecond optical parametric chirped pulse amplifier as a preamplifier to generate high-energy seed pulses for contrast enhancement.' In: *Applied Optics* 49.33 (2010), pp. 6558–6562 (cit. on pp. 16, 51, 74, 86, 114).

[30] D. I. Hillier et al. 'Contrast enhancements to petawatt lasers using short pulse optical parametric amplifiers and frequency doubling.' In: *Applied Optics* 53.29 (2014), pp. 6938–6943 (cit. on pp. 16, 51, 111).

[31] C. Dorrer et al. 'High contrast optical-parametric amplifier as a front end of high-power laser systems.' In: *Optics Letters* 32.15 (2007), pp. 2143–2145 (cit. on p. 16).

[32] S. Patankar. 'High-Power Laser Systems for Driving and Probing High Energy Density Physics Experiments.' PhD Thesis. Imperial College London, 2013 (cit. on pp. 18, 29, 61).

[33] K. Hadjicosti. 'Modelling of an OPCPA system for high energy ultrashort femtosecond pulses.' Masters Thesis. Imperial College London, Physics - Quantum Optics & Laser Science, 2010 (cit. on pp. 18, 56).

[34] N. G. R. Leblanc. 'Designs of parametric setups to be used in OPCPA systems.' Masters Thesis. Imperial College London, Physics - Quantum Optics & Laser Science, 2011 (cit. on pp. 18, 56).

[35] G. F. Swadling et al. 'Diagnosing collisions of magnetized, high energy density plasma flows using a combination of collective Thomson scattering, Faraday rotation, and interferometry.' In: *Review of Scientific Instruments* 85.11 (2014), 11E502 (cit. on pp. 19, 22, 26, 29, 150, 156, 159).

[36] N. H. Stuart et al. 'Direct fluorescence characterisation of a picosecond seeded optical parametric amplifier.' In: *Optics Communications* 336 (2015), pp. 319–325 (cit. on pp. 19, 20, 75, 77, 88, 111, 158).

[37] N. Stuart et al. 'Comparative study on the temporal contrast of femtosecond modelocked laser oscillators.' In: *Optics Letters* 41.14 (2016), p. 3221 (cit. on pp. 19, 20, 90, 91, 105, 159).

[38] L. G. Suttle et al. 'Structure of a Magnetic Flux Annihilation Layer Formed by the Collision of Supersonic, Magnetized Plasma Flows.' In: *Physical Review Letters* 116.22 (2016), p. 225001 (cit. on pp. 19, 24, 150, 157, 159).

[39] C. J. Price and T. D. Donnelly. 'An in-vacuo optical levitation trap for high-intensity laser interaction experiments with isolated microtargets.' In: *The Review of Scientific Instruments* 86.3 (2015), p. 033502 (cit. on pp. 19, 22, 142, 160).

[40] D. Bigourd et al. 'Spectral enhancement in optical parametric amplifiers in the saturated regime.' In: *Applied Physics B* 113.4 (2013), pp. 627–633 (cit. on pp. 20, 56, 83, 95, 111, 158).

[41] K. Mecseki et al. 'Flat-top picosecond pulses generated by chirped spectral modulation from a Nd:YLF regenerative amplifier for pumping few-cycle optical parametric amplifiers.' In: *Applied Optics* 53.10 (2014), p. 2229 (cit. on pp. 21, 54).

[42] S. Patankar et al. 'Multiwavelength interferometry system for the Orion laser facility.' In: *Applied Optics* 54.36 (2015), p. 10592 (cit. on p. 23).

[43] I. H. Mitchell et al. 'A high impedance mega-ampere generator for fiber z-pinch experiments.' In: *Review of Scientific Instruments* 67.4 (1996), p. 1533 (cit. on pp. 26, 148).

[44] F. Suzuki-Vidal et al. 'Formation of episodic magnetically driven radiatively cooled plasma jets in the laboratory.' In: *Astrophysics and Space Science* 322.1 (2009), pp. 19–23 (cit. on pp. 26, 29, 148, 150).

[45] M. J. Norman et al. 'Multipass Reconfiguration of the HELEN Nd:Glass Laser at the Atomic Weapons Establishment.' In: *Applied Optics* 41.18 (2002), p. 3497 (cit. on p. 27).

[46] J. H. Kelly et al. 'OMEGA EP: High-energy petawatt capability for the OMEGA laser facility.' In: *Journal de Physique IV (Proceedings)* 133 (2006), pp. 75–80 (cit. on p. 27).

[47] T. Ditmire, E. Gaul, and M. Martinez. *Conceptual Design Report for the Texas Petawatt Laser at the Texas Center for High Intensity Laser Science*. University of Texas, Austin, 2004 (cit. on p. 27).

[48] M. Mason. 'A sub-60 fs Titanium Sapphire Chirped Pulse Amplification System.' PhD Thesis. Imperial College London, 2000 (cit. on pp. 29, 61, 128).

[49] S. Hooker and C. E. Webb. *Laser physics*. Oxford University Press, 2010 (cit. on pp. 31, 32, 47).

[50] G. New. *Introduction to Nonlinear Optics*. Cambridge University Press, 2011. 257 pp. (cit. on pp. 31, 35, 43).

[51] Schott. *Schott - Active & Passive Laser Glasses*. In: *Schott - Active & Passive Laser Glasses*. 2013 (cit. on pp. 31, 33).

[52] J. D. Bonlie et al. 'Production of $>10^{21} W/cm^2 from a large aperture Ti:Sapphire laser system$.' In: *Applied Physics B* 70.1 (2000), S155–S160 (cit. on p. 32).

[53] E. W. Gaul et al. 'Demonstration of a 1.1 petawatt laser based on a hybrid optical parametric chirped pulse amplification/mixed Nd:glass amplifier.' In: *Applied Optics* 49.9 (2010), pp. 1676–1681 (cit. on p. 33).

[54] I. N. Ross, M. Trentelman, and C. N. Danson. 'Optimization of a chirped-pulse amplification Nd:glass laser.' In: *Applied Optics* 36.36 (1997), pp. 9348–9358 (cit. on p. 33).

[55] V. Bagnoud et al. 'High-energy, high-average-power laser with Nd:YLF rods corrected by magnetorheological finishing.' In: *Applied Optics* 44.2 (2005), p. 282 (cit. on p. 34).

[56] K. Mecseki. 'An ultrafast optical parametric laser for driving high energy density science.' PhD Thesis. Imperial College London, 2013 (cit. on p. 34).

[57] I. Nobuhisa. 'Development of Optical Parametric Chirped-Pulse Amplifiers and Their Applications.' PhD Thesis. Ludwig-Maximilians University, Munich, 2006 (cit. on p. 36).

[58] P. Bates. 'Optical Parametric Chirped Pulse Amplification in the Few-Cycle Regime.' PhD Thesis. Imperial College London, 2008 (cit. on p. 36).

[59] V. Pyragaite et al. 'Parametric amplification of chirped optical pulses under pump depletion.' In: *Optics Communications* 283.6 (2010), pp. 1144–1151 (cit. on p. 37).

[60] W. Rudolph et al. 'Femtosecond autocorrelation measurements based on two-photon photoconductivity in ZnSe.' In: *Optics Letters* 22.5 (1997), p. 313 (cit. on p. 42).

[61] D. Kopf et al. 'Diode-pumped mode-locked Nd:glass lasers with an antiresonant Fabry-Perot saturable absorber.' In: *Optics Letters* 20.10 (1995), pp. 1169–1171 (cit. on pp. 47, 89, 92, 93).

[62] U. Keller et al. 'Semiconductor saturable absorber mirrors (SESAM's) for femtosecond to nanosecond pulse generation in solid-state lasers.' In: *IEEE Journal of Selected Topics in Quantum Electronics* 2.3 (1996), pp. 435–453 (cit. on pp. 48, 89, 92, 95).

[63] H. Yoshida et al. 'High-power and high-contrast optical parametric chirped pulse amplification in BBO crystal.' In: *Optics Letters* 28.4 (2003), p. 257 (cit. on p. 51).

[64] C. Dorrer. 'Analysis of pump-induced temporal contrast degradation in optical parametric chirped-pulse amplification.' In: *Journal of the Optical Society of America B* 24.12 (2007), p. 3048 (cit. on pp. 51, 74, 75, 83).

[65] I. N. Ross, G. H. C. New, and P. K. Bates. 'Contrast limitation due to pump noise in an optical parametric chirped pulse amplification system.' In: *Optics Communications* 273.2 (2007), pp. 510–514 (cit. on pp. 56, 84).

[66] M. R. Sharpe and D. Irish. 'Stray light in diffraction grating monochromators.' In: *Optica Acta* 25.9 (1978), pp. 861–893 (cit. on pp. 57, 130, 131).

[67] M. D. Perry et al. 'High-efficiency multilayer dielectric diffraction gratings.' In: *Optics Letters* 20.8 (1995), p. 940 (cit. on p. 67).

[68] G. Albrecht, A. Antonetti, and G. Mourou. 'Temporal shape analysis of Nd3+: YAG active passive model-locked pulses.' In: *Optics Communications* 40.1 (1981), pp. 59–62 (cit. on p. 70).

[69] S. Luan et al. 'High Dynamic-Range 3rd-Order Correlation-Measurement of Picosecond Laser-Pulse Shapes.' In: *Measurement Science & Technology* 4.12 (1993), pp. 1426–1429 (cit. on pp. 70, 75).

[70] D. Hillier et al. 'Ultrahigh contrast from a frequency-doubled chirped pulse amplification beamline.' In: *Applied Optics* 52.18 (2013), pp. 4258–4263 (cit. on p. 74).

[71] J. Moses et al. 'Highly stable ultrabroadband mid-IR optical parametric chirped-pulse amplifier optimized for superfluorescence suppression.' In: *Optics Letters* 34.11 (2009), p. 1639 (cit. on p. 74).

[72] X.-L. Li et al. 'Control of the superfluorescence for compact optical parametric chirped pulse amplification.' In: *Journal of Modern Optics* 55.11 (2008), pp. 1795–1800 (cit. on p. 74).

[73] F. Tavella, A. Marcinkevicius, and F. Krausz. 'Investigation of the superfluorescence and signal amplification in an ultrabroadband multiterawatt optical parametric chirped pulse amplifier system.' In: *New Journal of Physics* 8 (2006), p. 219 (cit. on p. 74).

[74] X. Gu et al. 'Generation of carrier-envelope-phase-stable 2-cycle 740 uJ pulses at 2.1 um carrier wavelength.' In: *Optics Express* 17.1 (2009), pp. 62–69 (cit. on p. 77).

[75] C. Manzoni et al. 'Excess quantum noise in optical parametric chirped-pulse amplification.' In: *Optics Express* 19.9 (2011), pp. 8357–8366 (cit. on p. 84).

[76] C. Homann and E. Riedle. 'Direct measurement of the effective input noise power of an optical parametric amplifier.' In: *Laser & Photonics Reviews* 7.4 (2013), pp. 580–588 (cit. on p. 86).

[77] J. P. Gordon, W. H. Louisell, and L. R. Walker. 'Quantum Fluctuations and Noise in Parametric Processes. II.' In: *Physical Review* 129.1 (1963), pp. 481–485 (cit. on p. 86).

[78] U. Morgner et al. 'Sub-two-cycle pulses from a Kerr-lens mode-locked Ti : Sapphire laser.' In: *Optics Letters* 24.6 (1999), pp. 411–413 (cit. on p. 89).

[79] K. Wall and A. Sanchez. 'Titanium sapphire lasers.' In: *The Lincoln laboratory journal* 3.3 (1990), pp. 447–462 (cit. on p. 89).

[80] T. Brabec et al. 'Kerr lens mode locking.' In: *Optics Letters* 17.18 (1992), p. 1292 (cit. on p. 89).

[81] L. R. Brovelli, U. Keller, and T. H. Chiu. 'Design and operation of antiresonant Fabry–Perot saturable semiconductor absorbers for mode-locked solid-state lasers.' In: *Journal of the Optical Society of America B* 12.2 (1995), p. 311 (cit. on pp. 89, 93).

[82] J. R. Buckley, S. W. Clark, and F. W. Wise. 'Generation of ten-cycle pulses from an ytterbium fiber laser with cubic phase compensation.' In: *Optics Letters* 31.9 (2006), p. 1340 (cit. on pp. 89, 100).

[83] F. Ilday et al. 'Generation of 36-femtosecond pulses from a ytterbium fiber laser.' In: *Optics Express* 11.26 (2003), p. 3550 (cit. on p. 89).

[84] X. Zhou et al. 'Generation of 28-fs pulses from a mode-locked ytterbium fiber oscillator.' In: *Optics Express* 16.10 (2008), p. 7055 (cit. on pp. 89, 100).

[85] D. T. Reid, M. Ebrahimzadeh, and W. Sibbett. 'Ti:Sapphire-pumped femtosecond optical parametric oscillators based on KTiOPO4 and RTiOAsO4.' In: *Applied Physics B* 60.5 (1995), pp. 437–442 (cit. on p. 89).

[86] J. D. Kafka et al. 'Broadly tunable optical parametric oscillator.' US20110180729 A1. 2011 (cit. on pp. 89, 103).

[87] A. Braun et al. 'Characterization of short-pulse oscillators by means of a high dynamic-range autocorrelation measurement.' In: *Optics Letters* 20.18 (1995), pp. 1889–1891 (cit. on pp. 89, 93, 96).

[88] T. Dzelzainis et al. 'The TARANIS laser: A multi-Terawatt system for laser-plasma investigations.' In: *Laser and Particle Beams* 28.3 (2010), pp. 451–461 (cit. on pp. 92, 118).

[89] J. Aus der Au et al. '60-fs pulses from a diode-pumped Nd:glass laser.' In: *Optics Letters* 22.5 (1997), p. 307 (cit. on p. 95).

[90] S. Han et al. 'Generation of sub-40 fs pulses from a mode-locked dual-gain-media Nd:glass laser.' In: *Applied Physics B* 74.1 (2014), s177–s179 (cit. on p. 95).

[91] R. Fluck et al. 'Broadband saturable absorber for 10-fs pulse generation.' In: *Optics Letters* 21.10 (1996), p. 743 (cit. on p. 95).

[92] I. D. Jung et al. 'High-dynamic-range characterization of ultrashort pulses.' In: *Applied Physics B* 65.2 (1997), pp. 307–310 (cit. on p. 96).

[93] I. D. Jung et al. 'Self-starting 65-fs pulses from a Ti:sapphire laser.' In: *Optics Letters* 22.13 (1997), p. 1009 (cit. on p. 96).

[94] W. J. Tomlinson, R. H. Stolen, and A. M. Johnson. 'Optical wave breaking of pulses in nonlinear optical fibers.' In: *Optics Letters* 10.9 (1985), p. 457 (cit. on p. 99).

[95] D. Anderson et al. 'Wave breaking in nonlinear-optical fibers.' In: *Journal of the Optical Society of America B* 9.8 (1992), p. 1358 (cit. on p. 99).

[96] J. R. Buckley et al. 'Femtosecond fiber lasers with pulse energies above 10 nJ.' In: *Optics Letters* 30.14 (2005), p. 1888 (cit. on pp. 99, 100).

[97] F. Wise, A. Chong, and W. Renninger. 'High-energy femtosecond fiber lasers based on pulse propagation at normal dispersion.' In: *Laser & Photonics Reviews* 2.1 (2008), pp. 58–73 (cit. on p. 100).

[98] A. Chong, W. H. Renninger, and F. W. Wise. 'All-normal-dispersion femtosecond fiber laser with pulse energy above 20nJ.' In: *Optics Letters* 32.16 (2007), p. 2408 (cit. on p. 100).

[99] F. Ö. Ilday et al. 'Self-Similar Evolution of Parabolic Pulses in a Laser.' In: *Physical Review Letters* 92.21 (2004), p. 213902 (cit. on p. 102).

[100] Y. Chen et al. 'Generation of high beam quality, high-energy and broadband tunable mid-infrared pulse from a KTA optical parametric amplifier.' In: *Optics Communications* 365 (2016), pp. 7–13 (cit. on p. 103).

[101] S. Chaitanya Kumar et al. 'Few-cycle, broadband, mid-infrared optical parametric oscillator pumped by a 20-fs Ti:sapphire laser.' In: *Laser & Photonics Reviews* 8.5 (2014), pp. L86–L91 (cit. on p. 103).

[102] S. Chaitanya Kumar et al. 'High-power femtosecond mid-infrared optical parametric oscillator at 7 um based on CdSiP_2.' In: *Optics Letters* 40.7 (2015), p. 1398 (cit. on p. 103).

[103] Q. Fu, G. Mak, and H. M. van Driel. 'High-power, 62-fs infrared optical parametric oscillator synchronously pumped by a 76-MHz Ti:sapphire laser.' In: *Optics Letters* 17.14 (1992), p. 1006 (cit. on p. 103).

[104] C. Hooker et al. 'Improving coherent contrast of petawatt laser pulses.' In: *Optics Express* 19.3 (2011), p. 2193 (cit. on pp. 109, 128, 130, 131).

[105] H. Kiriyama et al. 'Temporal contrast enhancement of petawatt-class laser pulses.' In: *Optics Letters* 37.16 (2012), pp. 3363–3365 (cit. on p. 120).

[106] Y. Fu, E. J. Takahashi, and K. Midorikawa. 'High-energy infrared femtosecond pulses generated by dual-chirped optical parametric amplification.' In: *Optics Letters* 40.21 (2015), p. 5082 (cit. on p. 120).

[107] A. Jullien et al. 'Highly efficient temporal cleaner for femtosecond pulses based on cross-polarized wave generation in a dual crystal scheme.' In: *Applied Physics B* 84.3 (2006), pp. 409–414 (cit. on pp. 120, 161, 163).

[108] R. C. Shah et al. 'High-temporal contrast using low-gain optical parametric amplification.' In: *Optics Letters* 34.15 (2009), p. 2273 (cit. on p. 120).

[109] N. V. Didenko et al. 'Contrast degradation in a chirped-pulse amplifier due to generation of prepulses by postpulses.' In: *Optics Express* 16.5 (2008), p. 3178 (cit. on pp. 123, 124, 127).

[110] Y. Akahane et al. 'Idler Pulse Compression using an Identical Positive Stretcher/-Compressor Combination in Optical-Parametric Chirped-Pulse Amplification.' In: *Applied Physics Express* 2.7 (2009), p. 072503 (cit. on p. 132).

[111] F. Brunel. 'Not-so-resonant, resonant absorption.' In: *Physical Review Letters* 59.1 (1987), pp. 52–55 (cit. on p. 139).

[112] J. Steingruber et al. 'Prepulse dependence of X-ray emission from plasmas created by IR femtosecond laser pulses on solids.' In: *Journal of Physics B: Atomic, Molecular and Optical Physics* 29.2 (1996), p. L75 (cit. on p. 140).

[113] V. L. Ginzburg. *The propagation of electromagnetic waves in plasmas*. 1970 (cit. on p. 140).

[114] E. F. Nichols and G. F. Hull. 'A Preliminary Communication on the Pressure of Heat and Light Radiation.' In: *Physical Review (Series I)* 13.5 (1901), pp. 307–320 (cit. on p. 141).

[115] P. Lebedew. 'Untersuchungen über die Druckkräfte des Lichtes.' In: *Annalen der Physik* 311.11 (1901), pp. 433–458 (cit. on p. 141).

[116] C. Price. 'High-intensity laser interactions with optically levitated liquid microdroplets.' PhD Thesis. Imperial College London, 2014 (cit. on pp. 142, 160).

[117] A. Ciardi et al. 'Episodic Magnetic Bubbles and Jets: Astrophysical Implications from Laboratory Experiments.' In: *The Astrophysical Journal Letters* 691.2 (2009), p. L147 (cit. on p. 150).

[118] G. F. Swadling et al. 'Experimental investigations of ablation stream interaction dynamics in tungsten wire arrays: Interpenetration, magnetic field advection, and ion deflection.' In: *Physics of Plasmas (1994-present)* 23.5 (2016), p. 056309 (cit. on pp. 150, 157, 159).

[119] S. A. Pikuz et al. 'High-luminosity monochromatic x-ray backlighting using an incoherent plasma source to study extremely dense plasmas (invited).' In: *Review of Scientific Instruments* 68.1 (1997), pp. 740–744 (cit. on p. 151).

[120] Y. Aglitskiy et al. 'High-resolution monochromatic x-ray imaging system based on spherically bent crystals.' In: *Applied Optics* 37.22 (1998), p. 5253 (cit. on p. 151).

[121] D. B. Sinars et al. 'Monochromatic x-ray imaging experiments on the Sandia National Laboratories Z facility (invited).' In: *Review of Scientific Instruments* 75.10 (2004), pp. 3672–3677 (cit. on p. 151).

[122] E. G. Zweibel and M. Yamada. 'Magnetic Reconnection in Astrophysical and Laboratory Plasmas.' In: *Annual Review of Astronomy and Astrophysics* 47.1 (2009), pp. 291–332 (cit. on p. 154).

[123] M. Yamada, R. Kulsrud, and H. Ji. 'Magnetic reconnection.' In: *Reviews of Modern Physics* 82.1 (2010), pp. 603–664 (cit. on p. 154).

[124] S. N. Bland et al. 'Use of Faraday probing to estimate current distribution in wire array z pinches.' In: *Review of Scientific Instruments* 77.10 (2006), 10E315 (cit. on p. 155).

[125] G. Hicks. 'Spiral: Ion beams accelerated by laser irradiation of thin foils and their applications.' In: *Imperial College London PhD Thesis* (2015) (cit. on p. 160).

[126] N. Minkovski et al. 'Nonlinear polarization rotation and orthogonal polarization generation experienced in a single-beam configuration.' In: *Journal of the Optical Society of America B* 21.9 (2004), p. 1659 (cit. on p. 161).

[127] A. Jullien et al. '$10^{-10} temporal contrast for femtosecond ultraintense lasers by cross-polarized wave generation$.' In: *Optics Letters* 30.8 (2005), pp. 920–922 (cit. on p. 161).